Politecnico di Milano
Department of Physics
Doctoral Programme In Physics

Nonvolatile control of spin and charge transport in Ferroelectric Rashba Semiconductors

Doctoral Dissertation of:
Sara Varotto

Supervisor:
Prof. Christian Rinaldi

Tutor:
Prof. Riccardo Bertacco

The Chair of the Doctoral Program:
Prof. Marco Finazzi

2020 – Cycle XXXII

Abstract

The steep increase of the computing power offered by the downscaling of complementary metal oxide semiconductor (CMOS) electronics is reaching both physical and economical limitations. New schemes must be devised in order face the large power demand of information technology. Contrary to electric currents, pure spin currents are dissipation-less and can be used to carry information with low power consumption. In spintronics, spin currents are generated and detected through ferromagnets, whose electric switching via spin transfer torque is an energy consuming process. To avoid the use of ferromagnets, spinorbitronics exploits spin-orbit coupling in heavy metals, Rashba interfaces or topological insulators, for the electrical generation and detection via charge-spin interconversion. Rashba systems offer also the possibility of harnessing spin-orbit coupling by electric fields to control information processing (*computing*). Nonetheless, information is still typically encoded in the magnetization of a ferromagnet (*memory*).

In this thesis, we propose an innovative approach based on ferroelectric Rashba semiconductors (FERSC), in which memory is provided by ferroelectricity. The father compound is Germanium Telluride (GeTe), a CMOS-compatible semiconductor predicted to display a giant Rashba spin-orbit coupling at room temperature, that can be manipulated acting on the ferroelectric state. Calculations reveal that the spin populations of the Rashba bands are inverted upon polarization reversal. Hence, the information stored in the remanent ferroelectric state can be utilized for an efficient and electrically tuned spin-charge conversion.

Although GeTe is a highly doped semiconductor, we conceive a method for the control of the ferroelectric state by means of an electric gate. Based on spin- and angle- resolved photoemission spectroscopy, we demonstrate the link between Rashba effect and ferroelectricity. Then, we observe that spin-to-charge conversion in GeTe films is mainly due to spin Hall effect. The sign of the conversion is reversed by switching the ferroelectric polarization, providing nonvolatility and electric reconfigurability. Finally, we propose a path to exploit also the semiconductive behaviour of FERSC, by creating InGeTe alloys with reduced carriers concentration.

FERSC materials offer the possibility of both storing and processing information in a single channel of a semiconductor, so that the ferroelectric control of spin-charge conversion can be exploited for spin based reconfigurable electronics.

Contents

Introduction 3

1 Ferroelectric Rashba Semiconductors 5
1.1 Ferroelectricity . . . 5
1.1.1 Phenomenology . . . 5
1.1.2 Theoretical frameworks . . . 6
1.1.3 Interplay with piezoelectricity . . . 7
1.1.4 Characterization of ferroelectric thin films . . . 7
1.2 Rashba Effect . . . 9
1.3 Spin-charge interconversion . . . 11
1.3.1 Spin transport equations . . . 11
1.3.2 Spin-Hall effect . . . 13
1.3.3 Rashba-Edelstein Effect . . . 16
1.4 Germanium Telluride . . . 17
1.4.1 Ferroelectricity in GeTe . . . 17
1.4.2 Ferroelectric dependent Rashba effect in GeTe . . . 18
1.4.3 FERSCs based devices . . . 20
1.5 Indium doped Germanium Telluride . . . 22

2 Experimental techniques 25
2.1 Ferroelectric characterization . . . 25
2.1.1 Current-voltage methods . . . 25
2.1.2 Piezoresponse Force Microscopy . . . 27
2.2 Spin- and Angle- Resolved Photoemission Spectroscopy: SARPES . . . 33
2.2.1 Photoemission of electrons . . . 34
2.2.2 Mapping bands structure by ARPES . . . 37
2.2.3 Spin-resolved bands by SARPES . . . 38
2.3 Spin-to-charge conversion by Spin Pumping . . . 40
2.3.1 Ferromagnetic resonance . . . 40
2.3.2 Spin transfer via spin pumping at ferromagnetic resonance . . . 46
2.4 Growth of GeTe-based Heterostructures . . . 51
2.4.1 Growth by Molecular Beam Epitaxy (MBE) . . . 52
2.4.2 Decapping protocol . . . 53

3 Control of ferroelectricity in the semiconductor GeTe **55**
3.1 Ferroelectricity at the nanoscale: Piezoresponse Force Microscopy 56
3.1.1 Switching spectroscopy PFM in GeTe 57
3.1.2 Nanopatterning of domains in GeTe 57
3.2 Ferroelectric switching via macroscopic gate 59
3.2.1 Reading the ferroelectric state: bipolar resistive switching 59
3.2.2 Ferroelectric domains: a microscopic view 66
3.2.3 Performances of ferroelectric Shottky devices 69
3.3 Conclusions 71

4 Ferroelectric control of the spin physics in GeTe **73**
4.1 Ferroelectric control of the Rashba spin texture in GeTe 73
4.1.1 Control of the polarization by surface termination 74
4.1.2 Surface and bulk Rashba states in GeTe by ARPES 76
4.1.3 Spin-resolved ARPES of bulk Rashba bands 81
4.2 Investigation of spin-to-charge conversion 85
4.2.1 Growth of Fe/GeTe heterostructures 85
4.2.2 Spin pumping in Fe/GeTe bilayers 87
4.2.3 Gating Inverse Spin-Hall Effect 88
4.2.4 Ferroelectric dependent spin Hall conductivity 92
4.2.5 Comparison with calculated spin Hall conductivity 92
4.3 Conclusions 94

5 Control of the doping in FERSC: Indium doped GeTe **95**
5.1 Growth of InGeTe 95
5.1.1 Epitaxy on GeTe/Si 96
5.1.2 Epitaxy on BaF_2 97
5.2 In-doped GeTe as a FERSC 98
5.2.1 Ferroelectricity of InGeTe 98
5.2.2 Rashba effect of InGeTe 99
5.2.3 Concentration of carriers 104
5.3 Conclusions 105

Conclusions **108**

Bibliography **109**

Introduction

Today's data processing is achieved through computers based on the von Neumann architecture. The bottleneck is given by the memory and the computing units being physically separated, so that data must be transferred between the two. This process is highly inefficient. In view of increasing the working frequency and containing the power consumption, the dimensions of the Complementary Metal–Oxide–Semiconductor (CMOS) transistors have been drastically reduced in the past 50 years and the Moore's law has been mostly respected. However, the benefits from the scaling are being limited by a minimum physical size of about 10 nm [1–3]. As X. Xu *et al.* pointed out [4], "CMOS scaling does not offer much help in meeting the increasingly demanding requirements for computation density and energy efficiency, so innovations in architecture, circuit and device are required instead." In order to overcome the issues of von Neumann architecture, *in-memory computing* paradigm takes advantage of calculations performed within the memory space. In other words, the data bits are memorized exactly in the same physical space of the the transistors processing them. This removes the need for data transfer between the units increasing the throughput and reducing the power consumption.

The high computing capability and density scalability [5] required for in-memory computing sparked the discoveries of multi-functional materials and nanodevices implementing innovative physical concepts. A huge effort has been devoted to specific technologies. Resistive-switching memory (RRAM) devices [6–8] and spin-orbit heterostructures [3, 9] are marking a turning point for the realization of in-memory architectures more efficient than conventional CMOS-based ones. These approaches share a common ground. The computing capability is enhanced by exploiting materials with new functionalities, e.g. ferroelectricity, phase-change effect for RRAM or spin-orbit coupling effects as Rashba or topological states in the case of spinorbitronics. These new variables in principle would allow to relax the complexity of the circuit in terms of number of devices and operations involved, complexity that is transferred to the fundamental physics of the materials [10]. One example is the Magneto-Electric Spin-Orbit logic (MESO) designed by Intel [9], which combines a nonvolatile memory element and a spin-orbit readout logic within the unit device.

From this perspective, FErroelectric Rashba SemiConductors (FERSC) stand out with their intrinsic multi-functional nature. FERSC combine ferroelectricity, Rashba effect in a unique semiconductor [11] and they could bridge resistive memory and Spin-Orbitronics to a new approach of in-memory computing.

The discovery of FERSC dates back to 2013, when Density Functional Theory (DFT) calculations of the electronic bands structure of Germanium Telluride disclosed a giant bulk Rashba effect at room temperature intrinsically related to ferroelectricity [11, 12]. Thereafter, few other materials have been predicted, as the oxide perovskite Bi_2WO_6 Aurivillius crystal [13] or ultra-thin films of

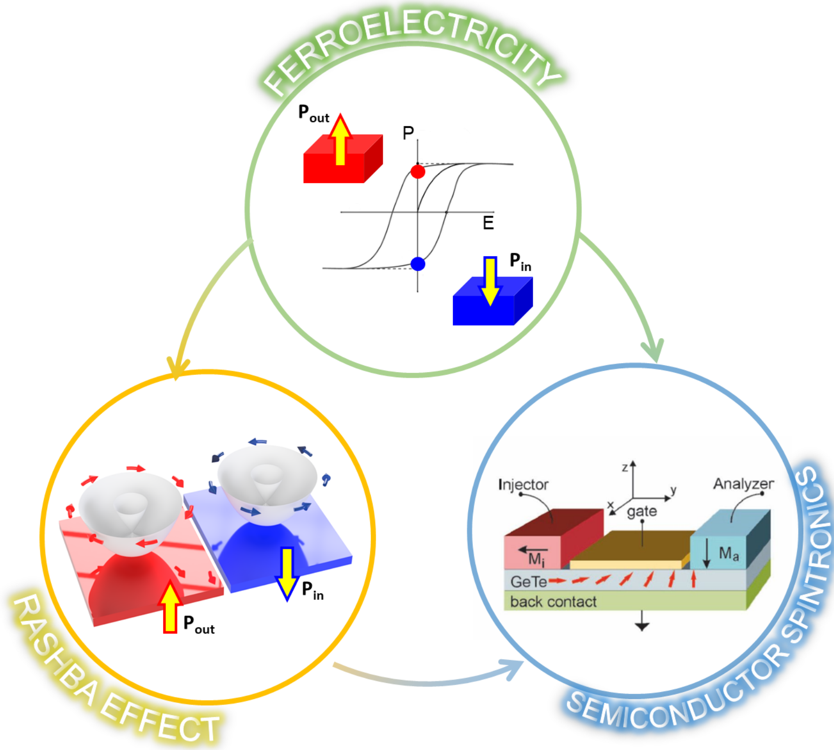

Figure 1: *Diagram of the physical properties of Ferroelectric Rashba Semiconductors.*

SnTe [14].

The essential concept of FERSC is depicted in Fig. 1. The ferroelectric material can host different polarization states without an external electric field. The non-volatility is the key ingredient of a *memory* device. The ferroelectric distortion breaks the space inversion symmetry of the crystal and the effect is persistent up to the critical transition temperature ($\sim$ 700 K for GeTe), which at the same time generates a bulk Rashba momentum- and spin-dependent splitting of the electronic bands as result of the large spin-orbit coupling. This translates into the possibility of modulating spin-orbit interaction by acting on the ferroelectric state. Indeed, the spin direction in each spin dependent sub-band is predicted to be reversed by switching the polarization vector. The ferroelectric control of the Rashba effect in FERSC has important consequences on spin-computing. Rashba spin-orbit coupling can be used for low-power spin based *computing* applications [15], as it triggers the conversion between charge and dissipation-less spin currents in non-magnetic platforms. The conversion efficiency can be tuned in amplitude and sign by means of an external electric field that modulates the spin orbit coupling and consequently the splitting and the spin texture of the electronic bands. The electric tuning of spin Hall effect was demonstrated in ultrathin Pt films [16]. The control of the spin transport was demonstrated in two dimensional Rashba surface or interfaces as well, as for example in $LaAlO_3/SrTiO_3$ [17] or $Al/SrTiO_3$ [18]. Despite these systems show spin-to-charge conversion even in absence of electric fields, the modulation of the efficiency requires the application of an external electric field (i.e the modulation is volatile). On the contrary, in a FERSC material the spin texture is persistent and the chirality is locked to the internal electric field associated to a specific ferroelectric state. This would in principle lead to spin-charge conversion with remanence and tunable with ferroelectricity. Finally, ferroelectric dependent spin-charge conversion would be achievable in a semiconductor, opening the route towards low-power transistors combining memory (ferroelectric polarization) and computing (spin-charge conversion).

The main purpose of this thesis work is to experimentally investigate the physical properties predicted for GeTe. GeTe can be grown epitaxially on Silicon substrates with process temperatures compatible with CMOS devices [19]. In this work we study the feasibility of employing this ma-

terial for spin-orbitronic and in-memory computing electronics. The manuscript is organized as follows.

In **Chapter 1**, fundamental aspects of ferroelectricity, Rashba, spin-charge conversion, together with DFT calculations performed by our coworkers J. Sławińska, S. Picozzi *et al.* of the ferroelectric dependent Rashba in GeTe will provide a more concrete picture of the concept of FERSC.

Chapter 2 explains the main techniques employed in this work. Among them ferroelectric characterization techniques as current-voltage methods and piezoresponse force microscopy (Sec. 2.1), spin- and angle- resolved photoemission spectroscopic as the a useful tool to map the spin-split Rashba bands (Sec. 2.2), and spin pumping at ferromagnetic resonance to characterize spin-charge conversion (Sec. 2.3).

Chapter 3 presents the possibility of switching the ferroelectric polarization of GeTe thin films over micrometric areas, still debated due to its pronounced conductivity related to the *p*-type degenerate doping. Furthermore, a suitable method for the reading the ferroelectric state of a strongly doped semiconductor is still lacking. We investigate the interplay between the ferroelectric polarization and the bands bending across a GeTe/gate interface, and define a strategy to read the state based on the ferroelectric resistive switching of the junction. At the same time, we study the switching of the polarization in GeTe and its endurance, for the deployment of the memory functionality in devices.

Chapter 4 deals with the implications of ferroelectric switching of GeTe on its spin physics. We design an experiment to map the spin texture of the bulk Rashba bands versus the ferroelectric remanent state. For this purpose, GeTe thin films are suitably prepared with opposite spontaneous polarization (Sec. 4.1). Complemented by DFT calculations, the experiment establishes the link between Rashba and ferroelectricity, the main concept of FERSC. The possibility of gating the ferroelectric state as shown in Ch. 3 would allow to electrically reconfigure the Rashba effect, with high potential for in-memory applications. In view of an actual implementation of such concept, we study spin-to-charge conversion versus ferroelectric polarization in Fe/GeTe epitaxial bilayers by spin pumping. More specifically, we study whether a spin current injected from Fe into GeTe is converted to a charge current and how the conversion efficiency depends on the remanent ferroelectric state. With the help of theoretical calculations of the spin Hall conductivity, we distinguish between REE and SHE contributions observed in our GeTe films. The ferroelectric dependent spin-charge conversion would represent an innovative realization the MESO architecture based on a FERSC. Remarkably, the design and fabrication of the proposed architecture would be extremely simplified by using a single film of GeTe as active layer, which intrinsically combines memory and computing functionalities.

Ch. 5 deals with the possibility of reducing the strong *p* doping of GeTe, in order to exploit also the semiconductive behaviour of such a material in transistors. Reducing the free carriers density would also lead to lower currents developed during the ferroelectric switching and a less consuming electric gate. For these reasons, we study if alloying GeTe with Indium can mitigate the free carriers concentration. We characterize the effect of substitutional In on doping, ferroelectricity and Rashba effect of InGeTe films grown by molecular beam epitaxy. In this sense InGeTe could represent a new FERSC allowing the ferroelectric tuning of spin computing in a semiconducting platform.

CHAPTER 1

Ferroelectric Rashba Semiconductors

The first part of the present chapter provides some theoretical insights in the physics of ferroelectricity (Sec. 1.1), Rashba effect (Sec. 1.2) and spin-charge interconversion mechanisms, including spin Hall and Rashba-Edelstein effects (Sec. 1.3). In the second part, density functional theory (DFT) calculations of the bands structure of GeTe are presented in Sec. 1.4 and the interplay between Rashba effect and ferroelectricity is discussed from theoretical principles. Possible devices implementing a tunable spin-charge conversion are proposed in Sec. 1.4.3. Finally, the possibility of compensating the concentration of free carriers in GeTe in Indium-doped GeTe films is discussed in Sec. 1.5. The attention will be concentrated on those physical aspects required for a deep understanding of the experimental chapters **Ch. 3-4-5**.

1.1 Ferroelectricity

Ferroelectricity was discovered in 1921 by Valasek, who observed a spontaneous dielectric polarization in crystals of the piezoelectric Rochelle salt (potassium sodium tartrate tetrahydrate) [20, 21]. The ferroelectric perovskite oxide $BaTiO_3$ became popular in the 1940s [22] and hence a large variety of other compounds were discovered, e.g. $BiFeO_3$, $PbTiO_3$, $LiNbO_3$ and $Pb[Zr_xTi_{1-x}]O_3$ [23,24]. In the recent years, metal free ferroelectric perovskites [25] and ferroelectric inorganic and organic semiconductors [26, 27] are exploited for the design and fabrication of nanoscale memory devices [28], offering high integration capabilities. Exemplarly, Ferroelectric FET were designed and implemented in devices based on ferroelectric thin films, nanowires or nanoparticles [29]. Ferroelectricity is a property of materials belonging to polar space crystallographic groups and it is accompanied by piezoelectricity and pyroelectricity (Fig. 1.1**a**). These properties further extend the applications of ferroelectrics to active devices, comprising MEMS-based sensors [30, 31], piezoelectric actuators [32] and transducers [33].

1.1.1 Phenomenology

From a phenomenological point of view, a ferroelectric crystal exhibits a spontaneous dielectric polarization (or remanence polarization, $\mathbf{P}_\mathrm{R}$) even in the absence of an external electric field. Unlike other polar materials (Fig. 1.1), in ferroelectrics the orientation of P_R can be reversed by application

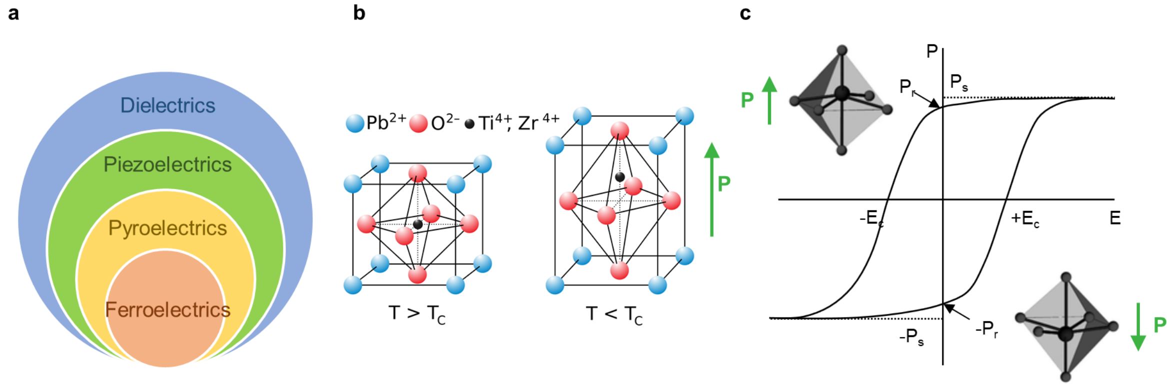

Figure 1.1: ***a*** *Diagram showing the relationship between dielectric, piezoelectric, pyroelectric and ferroelectric materials.* ***b*** *Ferroelectric distortion of the persovskite oxide Lead Zirconium Titanate, (Pb[Zr_xTi_{1-x}]O3, or PZT). The distortion occurs below the critical temperature T_c.* ***c*** *Representation of the hysteresis behaviour of ferroelectric polarization P versus an external applied electric field E. Polarization switches between two opposite saturation values ($\pm P_s$) after crossing the coercive fields ($\pm E_c$). Two remanent states at zero field ($\pm P_r$) refer to opposite ferroelectric distortions of the lattice. Adapted from Ref. [36].*

of a sufficiently intense electric field in the opposite direction. Polarization directions can be used as the logic states of a memory device, hence no backup power is required to maintain the stored information. The net electric dipole moment is due to the charge separation between the centre of positive and negative charge sublattices, with breaking of the inversion symmetry (Fig. 1.1**b**). To be more precise, below a certain critical temperature (T_c) the crystal energy is reduced by a structural phase transition from a high to a lower symmetry lattice. Such symmetry breaking reflects in the asymmetrical shift of the equilibrium ion positions and hence in a permanent polarization. This is evident from Fig. 1.1**b**, where the structural distortion of ferroelectric oxide lead zirconium titanate ($Pb[Zr_xTi_{1-x}]O_3$, or PZT) displaces the Zr^{4+} and Ti^{4+} positive ions from the O^{2-} tetrahedron with a net dielectric dipole in the unit cell. A typical value of Zr concentration is x= 0.52, which yields to a room temperature polarization of about $\sim$40 μC/cm^2. The largest values of polarization are generally obtained in oxides with distorted perovskite structures, e.g. $BiFeO_3$ with 150 μC/cm^2 in the tetragonal phase [34, 35].

The interaction between dipoles provokes a hysteresis loop behaviour of the polarization versus an external electric field (Fig. 1.1**c**). In general, the crystal is broken into ferroelectric domains with different orientations. The boundary of two neighboring domains is called a domain wall. In the absence of an electrical field, the domains are randomly oriented, with a near complete compensation of the polarization (initial point of the loop in Fig. 1.1**c**). An external electric field (**E**) increases the net polarization of the material (**P**) by aligning the domains along its direction via propagation of the domain walls. At large enough E, all the dipoles are aligned and P reaches its saturation value ($\mathbf{P}_s$). After the first alignment process, then the P-V curve follows the hysteresis. Two equivalent remanence states are allowed ($\pm\mathbf{P}_r$). The minimum value of E causing the switching of the orientation of P is called coercive field (E_c).

1.1.2 Theoretical frameworks

In analogy with the paramagnetic-ferromagnetic phase transition, the phenomenology of the paraelectric-ferroelectric one can be described at a macroscopic level in the framework of the mean-field Landau- Devonshire Theory [37, 38]. This approach can describe the appearance of ferroelectricity below the critical temperature with a hysteresis P-E behaviour. The mean-field approach is suitable for bulk materials with spatially uniform polarization.

Because of the assumption of a uniform polarization field that neglects local fluctuations, the

mean-field approach fails to describe the behaviour of ferroelectric materials in the very proximity of the critical point. In general, the functional dependencies of polarization, susceptibility, specific heat and critical isotherm that are predicted by the Landau free energy are not compatible with the experimental ones [39]. To overcome the limitations imposed by the mean-field approach, a microscopic theory relying on the softening of optical phonons was developed in the 1960s by Cochran and Anderson [40, 41].

1.1.3 Interplay with piezoelectricity

Due to the link between the polar and the structural phase transitions, any ferroelectric material displays also a piezoelectric behaviour. The link between ferroelectricity and piezoelectricity is the main idea implemented in Piezoresponse Force Microscopy (Sec. 2.1.2), that is exploited in this work in order to measure and control ferroelectricity at the nanometer scale.

In non-polar piezoelectric materials, the electric field induces a polarization $\mathbf{P} = \epsilon_0(\epsilon_r - 1)\mathbf{E}$. Therefore, the mechanical stress and the applied field are linked by the linear equation $\eta_{ij} = d_{ij}E_i$ (linear piezoelectric effect). The strain tensor η_{ij} is linked to the electric field component E_i by the piezoelectric tensor d_{ij}, expressed in m/V. The latter is strictly related to the specific crystal symmetry [42]. In ferroelectric piezoelectrics, the piezoelectric coefficient can reach much higher values than in non-polar materials [42]. The enhancement of the piezoelectric response is dramatic, especially approaching the critical temperature (T_c). In general, ferroelectrics display centrosymmetric paraelectric phases, hence they loose piezoelectricity above T_c. For tetragonal ferroelectrics, the piezoelectric response is mostly registered along the polarization axis (z) as described by the coefficient d_{33} [42]:

$$d_{33} = 2Q_{33}\epsilon_0\epsilon_{33}P_3 \tag{1.1}$$

Where ϵ_{33} and P_3 are the relative permittivity and polarization along z, ϵ_0= $8.854 \cdot 10^{-12}$ F/m vacuum permittivity. Q_{33} is the electrostrictive coefficient of the material in the paraelectric state, which relates the out-of-plane strain to the polarization through $\eta_3 = Q_{33}P_3^2$ (0.05 and 0.1 $\mathrm{m}^4/\mathrm{C}^2$ for ceramics).

If an electric field E_3 is applied along the z axis perpendicular to a film plane (thickness z_0), the thickness variation results [42, 43] :

$$\Delta z = d_{33}V = 2Q_{33}\epsilon_0\epsilon_{33}P_3V \tag{1.2}$$

Where V is the voltage drop across the film (V= E_3z_0). The surface expands ($\Delta z > 0$) or contracts ($\Delta z < 0$) when the applied field E= V/z_0 is parallel or contrary to P_3, respectively. Due to the hysteresis behaviour of P_3 with E, the vertical deformation describes a “butterfly-loop”, as represented in Fig. 1.2**a**. The strain-field curve refers to an ideal single domain ferroelectric material with a squared polarization-field loop Fig. 1.2**b**.

Therefore, the polarization state P_3 can be determined by measuring the vertical displacement Δz for a given voltage V (lower than the coercive one). Piezoresponse Force Microscopy (Sec. 2.1.2) exploits a bias tip to induce and sense the piezoelectric deformation of the sample to probe the ferroelectric state [39].

1.1.4 Characterization of ferroelectric thin films

The integration of ferroelectric thin films in electronic devices requires a fine tuning of the memory state with electric fields, long time retention and large switching endurance. Different techniques can be adopted to characterize and control a ferroelectric thin film.

The main techniques are listed below.

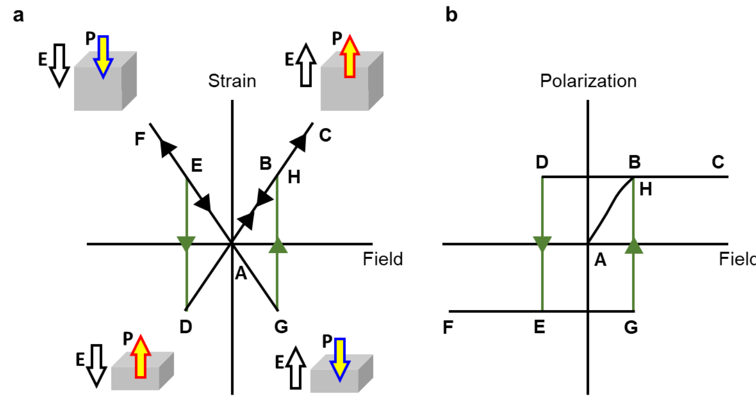

Figure 1.2: ***a*** *Dependence of the strain on the electric field for a ferroelectric material. The strain is positive when the polarization is parallel to the field, negative when antiparallel, according to Eq. 1.2* ***b*** *Polarization-electric field hysteresis loop of a single domain ferroelectric.*

- **Current–voltage measurement method** [44] allows for the ferroelectric switching of capacitor structures at a "macroscopic" scale ($\sim$ 10 μm). The hysteresis loop can be measured by sweeping the voltage applied between the top and bottom electrodes and recording the displacement current, as described more in detail in Sec. 2.1.1. The technique does not require expensive instrumentation or sample treatments. It is suitable for common insulating ferroelectric oxides but not for semiconducting films, as the conduction current hinders the measurement of the displacement one.

- **Piezoresponse force microscopy** [45] is a microscopic technique that allows for mapping of the ferroelectric domain configuration of a sample. Nowadays, 3D reconstruction of the polarization vector can be achieved by vectorial PFM. Moreover, it allows for the ferroelectric switching by voltage pulses, down to the nanoscale. PFM is suitable for both insulating and semiconducting thin films. More details can be found in the dedicated Sec. 2.1.2.

- **Infrared Raman** [46] and **terahertz spectroscopies** [47] are used to probe phonon softening in the para-to-ferroelectric transition. They are very sensitive tools to characterize the thin film quality, the transition temperature and the lattice dynamics involved by the ferroelectric distortion.

- **Environmental scanning electron microscopy** [48, 49] can be employed for imaging of ferroelectric patterns, by proper choice of the operation conditions and sample preparation. A heating stage can allow for investigation at the Curie point. A different contrast for different polarization is achieved in the back-scattered electrons which are sensitive to the local atomic packing (channeling effect), i.e. to the orientation of the atomic planes.

- **Second harmonic generation** [50] employs electromagnetic light to induce an oscillating dipole moment. In nonlinear materials with broken inversion symmetry (including polar systems), two photons of the incident are combined into a single photon at doubled frequency (second harmonic). This technique allows for imaging of ferroelectric domains and it can be employed for in-situ and real-time control of ferroelectricity during growth of a sample in ultra high vacuum clusters.

In the experimental chapters, piezoresponse force microscopy and current-voltage methods are employed for the characterization and control of ferroelectricity in GeTe thin films. Due to the significant conductivity of GeTe, a specific current-voltage method is developed thus allowing for ferroelectric switching of semiconductors over relatively large areas (tens of μm).

1.2 Rashba Effect

The Rashba effect consists in the lift of the spin degeneracy of the electronic bands with a momentum-dependent energy shift. This relativistic effect is triggered by spin-orbit coupling (SOC) of free carriers in a non-centrosymmetric system under an applied electric field. It allows for electric field tuning of spin properties of the bands, which in turn are reflected in the spin-charge interconversion (Sec. 1.3). Systems hosting Rashba effect are good platforms for low-power electric manipulation of spins, according to the paradigm of spinorbitronics [51, 52].

Rashba effect usually applies two dimensional electron gas (2DEG) systems, with inversion symmetry broken by an external applied electric field E_0 perpendicular to the plane of motion (Fig. 1.3**a**). The effect can be modulated by an external electric field.

In the following, Rashba effect is derived for the ideal case in which the two-dimensional material can be considered as a gas of free and independent electrons. Due to SOC, the relativistic charge particles that are moving with velocity **v** in an electric field **E** experience a magnetic field in their frame of motion, also called the SO field, as consequence of Lorentz transformation.

$$\mathbf{B} = \frac{\mathbf{E} \times \mathbf{v}}{2c^2\sqrt{1 - \frac{v^2}{c^2}}} \tag{1.3}$$

The magnetic field **B** of Eq. 1.3 couples to the electron's spin magnetic moment ($\boldsymbol{\mu}_s = -g_s\mu_B\boldsymbol{\sigma}$) via Zeeman interaction and it defines the spin quantization axis even in absence of an external magnetic field. The general form of the Zeeman Hamiltonian of a quantum system is:

$$H_{Zeeman} = -\boldsymbol{\mu}_s \cdot \mathbf{B} \tag{1.4}$$

Note that the spin operator can be written as $\mathbf{S} = \frac{1}{2}\boldsymbol{\sigma}$, where $\boldsymbol{\sigma}$ is the spin operator defined by the Pauli matrices. The electron's speed can be related to the momentum by $\mathbf{v} = \mathbf{p}/m$. The quantistic operator associated to the momentum is $\mathbf{p} = -i\hbar\boldsymbol{\nabla}$. Substituting the operators expressions in Eq. 1.4, the SOC Hamiltonian results:

$$H_{SOC} = \frac{e\hbar}{4m^2c^2}(\mathbf{E} \times \mathbf{p}) \cdot \boldsymbol{\sigma} = -\frac{e\hbar}{4m^2c^2}\mathbf{E} \cdot (\boldsymbol{\sigma} \times \mathbf{p}) \tag{1.5}$$

For a 2DEG, the eigenvalues of the momentum operator are $\mathbf{p} = \hbar\mathbf{k}$ and the wave-vector **k** represents a quantum number with a continuous spectrum. In this case, the Hamiltonian can be compacted as follows:

$$H_R = \boldsymbol{\alpha}_R \cdot (\boldsymbol{\sigma} \times \mathbf{k}) \tag{1.6}$$

The Rashba field $\boldsymbol{\alpha}_R$ is proportional and opposite to **E** and depends on the specific system considered through the coefficient $a_{46} > 0$:

$$\boldsymbol{\alpha}_R = -a_{46}\mathbf{E} \tag{1.7}$$

In the real case of 2DEG semiconducting quantum wells of III–V zinc-blende semiconductor heterostructures [12, 53] or perovskites oxides [54–56], a_{46} describes the contribution of the interface bands structure. The effective mass of the electron m, the energy gap E_g and the SOC in the valence band Δ_S contribute to the Rashba [51]:

$$a_{46} = \frac{\pi e\hbar^2}{m}\frac{\Delta_S(2E_g + \Delta_S)}{E_g(E_g + \Delta_S)(3E_g + 2\Delta_S)} \tag{1.8}$$

The electronic bands of a SOC-free 2DEG are parabolas with two-fold degeneracy with respect to the spin. SOC Hamiltonian term (H_R) breaks the inversion symmetry yielding a **k**-dependent

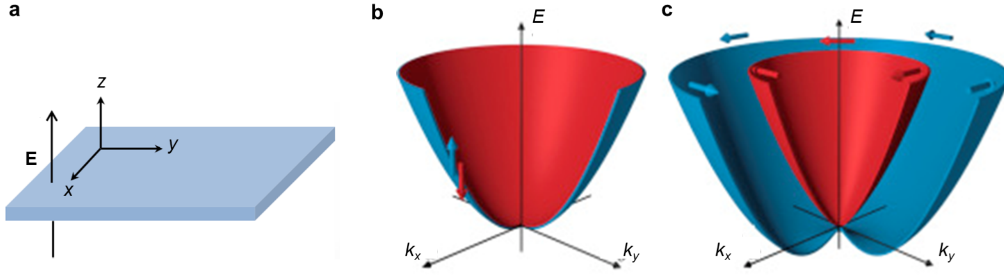

Figure 1.3: ***a*** *Space directions of the two dimensions gas.* ***b/c*** *3D representation of the parabolic dispersion of free electrons in absence/presence of Rashba SOC. Adapted from Ref. [56].*

splitting, without any external magnetic field. The spin splitting results from the solution of the eigenvalue problem of the total Hamiltonian including the Rashba term.

The energy eigenvalue can be separated between the free electrons term and the Rashba term $E = \frac{\hbar^2 k^2}{2m} + E_R$. The latter can be computed as follows:

$$det(H_R - E_R I) = 0 \tag{1.9}$$

From which the total energy eigenvalues result:

$$E^{\pm} = \frac{\hbar^2 k^2}{2m} \pm \alpha_R |k| \tag{1.10}$$

The eigenvalues of a 2DEG depend on the wave-vector, as consequence of the SOC between the momentum (i.e. **k**) and the external electric field. The result is a spin and wave-vector dependent splitting ($\Delta E_R(k) = E^+(k) - E^-(k)$). Fig. 1.3 shows how the spin degeneracy of SOC-free 2DEG (panel **b**) is removed by Rashba effect (panel **c**), through the **k**-dependent splitting.

The maximum value of $\Delta E_{R,max} = E_R$ and the corresponding wave-vector k_R indicated in Fig. 1.4**a** take the following expressions:

$$E_R = \frac{2m\alpha_R^2}{\hbar^2} \text{ and } k_R = \frac{m\alpha_R}{\hbar^2} \text{ with } \alpha_R = \frac{E_R}{2k_R} \tag{1.11}$$

Since the Rashba parameter is described by Eq. 1.7, it is clear from Eq. 1.11 that the Rashba energy splitting can be tuned by the applied electric field, thereby allowing for the electric control of the spin properties of the bands structure.

The eigenspinors are defined by a pseudo-vector $< \boldsymbol{\sigma} >^{\pm}$:

$$< \boldsymbol{\sigma} >^{\pm} = \begin{bmatrix} < \sigma_x >^{\pm} \\ < \sigma_y >^{\pm} \\ < \sigma_z >^{\pm} \end{bmatrix} \tag{1.12}$$

For each wave-vector, $< \boldsymbol{\sigma} >^{\pm}$ belongs to the *xy* plane on which the 2DEG is confined and it is perpendicular to **k**:

$$\mathbf{k} \cdot < \boldsymbol{\sigma} >^{\pm} = 0 \tag{1.13}$$

It results that quantization axis of the spin depends on **k**. As shown in Fig. 1.4**b**, the electronic Rashba split bands (E^+ and E^-) are associated with a spin texture with a chirality opposite in the two cases. Moreover, the chirality depends on the sign of **E** through $\boldsymbol{\alpha}_R$.

Unlike the Zeeman effect, the Rashba spin splitting does not lead to a net magnetization of the 2DEG, because the spin pseudo-vector averaged in the occupied in reciprocal space is equal

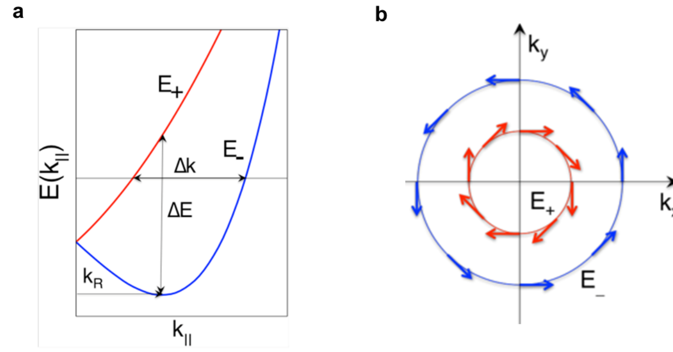

Figure 1.4: ***a*** *Projected Rashba spin splitting of the bands, along the generic direction* $k_{||}$. ***b*** *In-plane spin texture drawn on the Fermi contours of the split bands (E^+ and E^-) in the (k_x, k_y) plane. Adapted from Ref. [57].*

to zero. On the other hand, SOC produces a spin-ordered electronic structure in the **k** space, without involving external magnetic fields. The **k**-dependent effective magnetic field, causes a spin-dependent correction to the carrier's velocity, yielding to spin-charge conversion mechanisms (Sec. 1.3). The tunability with the electric field allows for development of Spin-Orbitronic devices.

The Rashba spin splitting is also an intrinsic property of few semiconducting compounds with large SOC and broken inversion symmetry. Among them BiTeI [58, 59], GeTe [11, 12, 60], *n*-GaN [61] and the oxide $BiCoO_3$ [62]. The increasing interest in bulk Rashba systems is based on their robustness with respect to interfaces and the possibility of exploiting the related spin-charge interconversion mechanisms in a paramagnetic semiconducting thin film. In this thesis work, bulk Rashba effect was controlled by means of the internal field of the ferroelectric polarization (Sec. 4.1). This property makes GeTe a nonvolatile and tunable Rashba system (Sec. 1.4.2), with promising implications in the field of spin computing.

1.3 Spin-charge interconversion

Spin orbit coupling in a non-magnetic system is the main engine that can be exploited for the generation of a spin current from a charge current and viceversa. Large spin-charge conversion can be observed in heavy metals (Pt [63] or Ta [64]), Rashba interfaces [65] and topological insulators [66]. The possibility of controlling SOC interaction in a Rashba system with external electric field is appealing for high efficiency conversion and electrically reconfigurable spin logic devices [9].

In this section, the fundamental equations governing spin transport in SOC materials will be first introduced (Sec. 1.3.1), the theoretical framework for spin-charge conversion effects. Among them spin Hall effect and Rashba Edelstein effect are described in Sec. 1.3.2 and 1.3.3, respectively.

1.3.1 Spin transport equations

In 1993 Valet and Fert [67] developed the spin drift-diffusion equations, under the *two channels approximation*. This approach treats the electric conduction by up and down spin carriers as independent channels.

Charge and spin currents

The density of charge current (J_c) is defined as the net flux of charges (eN) through a surface S:

$$J_c = \frac{e}{N}\frac{dN}{dt} \tag{1.14}$$

Similarly, a spin up (down) current is defined as the net flux of spin up (down):

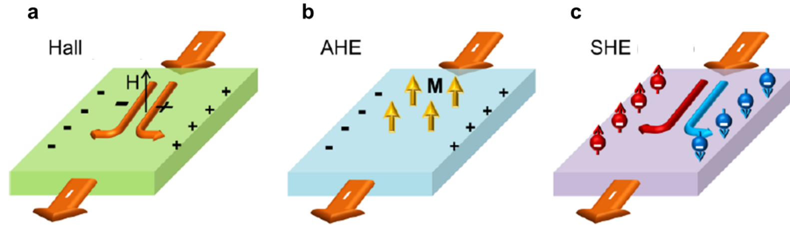

Figure 1.5: *Sketch of* ***a*** *ordinary Hall effect,* ***b*** *Anomalous Hall Effect (AHE),* ***c*** *Spin Hall Effect (SHE). Adapted from Ref. [69].*

$$J_{\uparrow(\downarrow)} = \frac{\hbar}{N}\frac{dN_{\uparrow(\downarrow)}}{dt} \tag{1.15}$$

It is clear that those quantities intrinsically have different units, however the spin up (down) current can be multiplied by the Josephson constant (2e/$\hbar$) and expressed with the same unit of the charge current. The net charge (J_c) and spin (J_s) currents are thus expressed as follows:

$$J^c = J_\uparrow + J_\downarrow \tag{1.16a}$$
$$J^s = J_\uparrow - J_\downarrow \tag{1.16b}$$

If charge current can be represented by a three components vector ($\boldsymbol{J}^c$), spin current is described by a second rank tensor (J^s_{ij}). The first index of J^s_{ij} is the direction of the spin flow, the second the spin polarization component. Both charge and spin current change sign upon inversion of the space coordinate; concerning time inversion, spin current does not invert because both spin and velocity change sign. The invariance with respect to time inversion makes spin currents dissipationless, an appealing feature for low-power consumption devices.

Coupling between spin and charge currents in SOC media

Along their path, electrons undergo scattering events due to impurities, defects or by phonon-electron interaction. During a scattering event, not only the charge velocity but also the spin direction can be modified (spin-flip event), which can be due to scattering with magnetic impurities or by SOC interaction. Both electrons scattering and spin-flip events determine a diffusive type of spin transport.

The charge current ($\boldsymbol{J}^c$) and spin polarization current density ($J^s_{i,j}$) are described by the drift-diffusion model [68]:

$$\boldsymbol{J}^c = e\mu n\boldsymbol{E} + D\nabla n + \gamma\mu\boldsymbol{E}\times\boldsymbol{P} + \gamma D\nabla\times\boldsymbol{P} \tag{1.17a}$$
$$J^s_{i,j} = -\mu E_i P_j - D\frac{\partial P_j}{\partial x_i} + \epsilon_{ijk}\left(\gamma\mu n E_k + \gamma D\frac{\partial n}{\partial x_k}\right) \tag{1.17b}$$

Where μ is the electron mobility, D the diffusion coefficient, n represents the free carriers density, **E** is an applied electric field, **P** the normalized spin polarization density (**S**= **P**/2). The quantity ϵ_{ijk} is the unit asymmetric tensor, x defines a generic direction in space.

The first two sources of charge current in Eq. 1.17 are the usual drift and diffusion in semiconductors. The following two terms describe the generation of a charge current due to spin polarization density **P**, i.e. spin-charge interconversion. The transformation between charge and spin currents is governed by the phenomenological and adimensional parameter γ, proportional to the SOC strength.

According to the expression $\gamma\mu\boldsymbol{E} \times \boldsymbol{P}$, a charge current induced by the electric field **E** couples to the spin density **P** and gives rise to a transverse charge flow (Hall current). Spin polarization density can be induced in a semiconductor by an external magnetic field, so that the ordinary Hall effect is observed (Fig. 1.5**a**). However, a non-equilibrium density can be created also by optical or spin injection, as shown by M. I. Miah in GaAs [70]. In this case, Hall effect is called anomalous because it is observed in absence of the external magnetic field. Anomalous Hall Effect (AHE) is commonly observed in ferromagnetic materials, where spontaneous uniform spin polarization is due to spin population unbalance (Fig. 1.5**b**). In addition, a charge current can be also generated by a transverse spin current associated to a inhomogenous spin density ($\boldsymbol{\nabla} \times \boldsymbol{P}$), i.e. a spin current. This effect is also called Inverse Spin Hall Effect (ISHE) and it was observed for the first time by A. A. Bakun *et al.* in $Ga_xAl_{1-x}As$ [71].

Conversely, a spin current can originate from a transverse drift ($\gamma\mu n E_k$) or diffusion ($\gamma D\partial n/\partial x_k$) charge currents, via SOC interaction (Fig. 1.5**c**). This phenomenon called Spin Hall Effect (SHE) [72] was originally predicted by M. I. Dyakonov and V. I. Perel in 1971 [73] and measured experimentally by Y. K. Kato *et al.* [74]. Spin Hall effect will be described in details in Sec. 1.3.2.

The drift and diffusion equations (Eq. 1.17) have to be completed by the continuity equation, relating the time evolution of charge and spin densities with their current. On one side charge is always conserved, however spin information can be lost due to spin-flip scattering events. The average time between two spin-flip scattering events is named spin-flip time (τ_s). The continuity equation of the spin density takes the form:

$$\frac{\partial P_j}{\partial t} = -\frac{\partial J^s_{ij}}{\partial x_i} - \frac{P_j}{\tau_s} \tag{1.18}$$

In Eq. 1.18, the time evolution of the local spin density component P_j is due to the generation of spin current flow along the direction x_i (term $-\partial J^s_{ij}/\partial x_i$) and to the spin-flip rate (term -P_j/τ_s).

The kinetic equation is here derived assuming a steady state condition ($\partial P_j/\partial t = 0$) and a homogeneous medium ($\nabla n = 0$). By substituting Eq. 1.17b into Eq. 1.18 and neglecting the term $-\mu E_i P_j$ in a paramagnetic semiconductor, a diffusion equation is obtained for the spin density P_j:

$$\frac{\partial^2 P_j}{\partial x_i^2} = \frac{P_j}{D\tau_s} = \frac{P_j}{\lambda_s^2}, \forall i, j \in x, y, z \tag{1.19}$$

Where λ_s is the characteristic length of spin in the medium, referred to as the *spin diffusion length*.

Materials with large diffusion lengths of the order 100 nm such as Al or Cu [75] are suitable for spin transport, as spin currents can be carried for long distances. On the other hand, large SOC materials such as heavy metals (Pt [63] or Ta [64]) or bulk Rashba systems in general display λ_s of few nanometers.

1.3.2 Spin-Hall effect

The generation of spin currents from charge currents in paramagnetic SOC systems in absence of magnetic field is called Spin Hall Effect (SHE) [72]. An electric current density J_x^c under the electric field E_x generates a transverse pure pure spin current, propagating along y with z-spin polarization $J_{z,y}^s$. The physical mechanism governing SHE was first described by M. I. D'yakonov and V. I. Perel [76] in terms of a "spacial separation of electrons with different spin orientations" caused by a spin-dependent scattering asymmetry due to SOC effect (e.g. a conduction electron with spin-up has a larger probability to be scattered towards $y > 0$ with respect to spin-down). The spin current produces a spin accumulation with opposite sign at the edges of the slab, but without Hall voltage [77]. The transformation from a charge to a spin current can be compared with the Magnus effect. According to Magnus effect, the deviation from a straight path of a spinning ball in

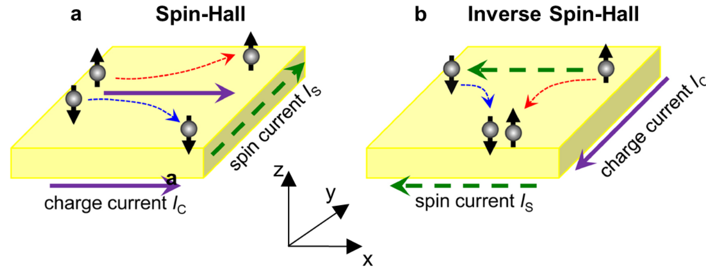

Figure 1.6: *Sketch of spin Hall effect **a** and inverse spin Hall effect **b**. Adapted from Ref. [81].*

air depends on its sense of rotation. Similarly, SOC makes electrons deviate from the direction of the current drift velocity depending on their spin [78].

Spin Hall effect is reversible, as demonstrated experimentally by T. Kimura *et al.* [79]. The inverse Spin Hall effect (ISHE) is the production of an electric charge current (J_x) from a pure spin current $J^z{}_y$ (Fig. 1.6). Direct and inverse SHE play a crucial role in spin-based technologies [80], as they allow for generation and detection of dissipation-less spin currents in a paramagnetic material [72].

The relation between charge and spin current due to SHE or ISHE can be derived from the term $J^s_{i,j} = \epsilon_{ijk}\gamma\mu n E_k$ in Eq. 1.17 derived in Sec. 1.3.1. Considering that the charge current is $\boldsymbol{J}^c = e\mu\mathbf{E}$, ISHE can be described as follows:

$$\mathbf{J}^{c,ISHE} = \theta_{SHE}\mathbf{J}^s \times \boldsymbol{\sigma} \tag{1.20}$$

The conversion efficiency is given by the Spin Hall angle (θ_{SHE}), which is proportional to the SOC constant γ. In Eq. 1.20, σ is the unit vector for the direction of the spin polarization and the Josephson constant (K_J= $2e/h$) is included in $\mathbf{J}^s$ (i.e. charge and spin current are defined with the same units, Sec. 1.3.1).

Spin Hall effect is also described in terms of spin Hall conductivity tensor σ^k_{ij}, where i, j and k indexes can take values x, y and z.

$$\sigma^z_{xy} = -\frac{J_{y,z}}{E_x} \tag{1.21}$$

Considering that the charge current J_x can be obtained from Ohm's law $J_x = \sigma_{xx}E_x$, the spin Hall angle can be calculated as:

$$\theta_{SHE} = \frac{\sigma^z_{xy}}{\sigma_{xx}} \tag{1.22}$$

The value of the spin Hall angle is intimately related to the intensity of SOC interaction [81]. Hence, high efficiency is obtained in heavy metals (e.g. Pt, Ta, Au [63, 64, 82]) and alloys. Conversion between charge and spin currents has been observed also in semiconductors, such as GaAs [74, 83], ZnSe [84], and in 2DEG such as (110)-AlGaAs quantum wells [85, 86].

Spin Hall effect can be of extrinsic or intrinsic origin. The intrinsic contribution is caused by the anomalous velocity of the electrons in the solid. On the other hand, the extrinsic SHE is driven by skew or side-jump scattering with defects or impurities in presence of SOC.

Intrinsic SHE

The intrinsic spin Hall conductivity depends only on the peculiar bands structure of the crystal, in absence of scattering with defects and impurities [77].

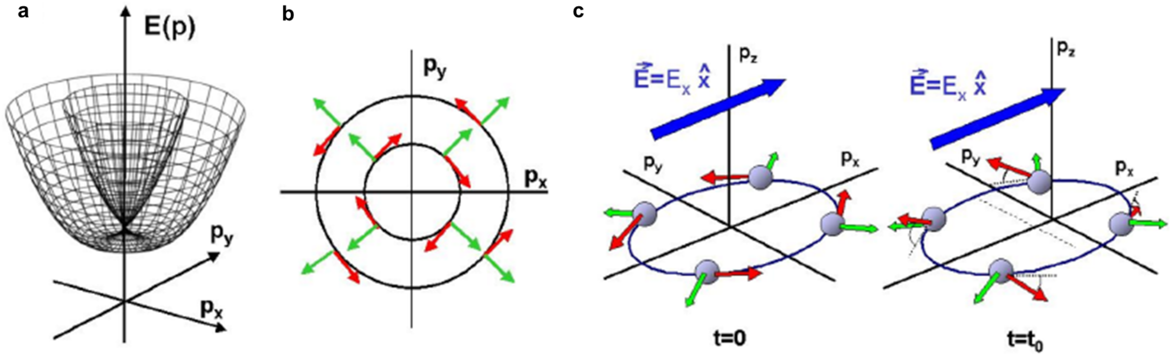

Figure 1.7: ***a*** *Representation of the Rashba bands of a 2DEG in* p_x*-*p_y *space.* ***b*** *Spin momentum locking of the Rashba contours. Green arrows represent* **p** *vector and red arrows the spin direction.* ***c*** *Generation of the spin current by intrinsic SHE. Each Fermi contour is shifted by the application of the* E_x *field (t=* t_0*). The* **p***-dependent magnetic torque gives rise to a spin current along y. Adapted from Ref. [93].*

In 1954 R. Karplus and J. M. Luttinger [87] discovered that the fundamental quantity governing the intrinsic mechanism of AHE and SHE is the Berry curvature of the system ($\boldsymbol{\Omega}$) [88]. The Berry curvature of a periodic crystal depends on $\boldsymbol{k}$ and it is a function of the particles eigenstates ($u_{n,\boldsymbol{k}}$, with n band index). When the single-band approximation is valid (i.e. negligible interband coupling), $\boldsymbol{\Omega}$ takes the form [88, 89]:

$$\boldsymbol{\Omega}_n(\boldsymbol{k}) = i\left\langle \frac{\partial u_{n,\boldsymbol{k}}}{\partial \boldsymbol{k}} \right| \times \left| \frac{\partial u_{n,\boldsymbol{k}}}{\partial \boldsymbol{k}} \right\rangle \tag{1.23}$$

Where $\times$ is the vector product operator. G. Sundaram and Q. Niu formulated the dynamics of the electrons, accounting for the Berry curvature [90]. Under a semiclassical approach, electrons in the crystal are wave-packets centred in $\boldsymbol{r}$ with momentum $\hbar\boldsymbol{k}$, obeying to the following equations of motion:

$$\begin{cases} \dot{\boldsymbol{r}} = \frac{1}{\hbar}\frac{\partial E_n(\boldsymbol{k})}{\partial \boldsymbol{k}} - \dot{\boldsymbol{k}} \times \boldsymbol{\Omega}_n(\boldsymbol{k}) \\ \hbar\dot{\boldsymbol{k}} = -e\boldsymbol{E} - e\dot{\boldsymbol{r}} \times \boldsymbol{B} \end{cases} \tag{1.24}$$

In Eq. 1.24, **E** and **B** are external electric and magnetic fields acting a force on the electron ($\dot{\boldsymbol{r}}$). The group velocity ($\dot{\boldsymbol{r}}$) contains an additional component with respect to the kinetic term ($\sim \partial E_n(\boldsymbol{k})/\partial \boldsymbol{k}$) which is orthogonal to the external force and related to the Berry curvature ($\dot{\boldsymbol{k}} \times \boldsymbol{\Omega}_n(\boldsymbol{k})$ contribution). Such orthogonal component is named anomalous Hall velocity, because a Hall velocity can arise from the 'intrinsic magnetic field' provided by the Berry curvature, directly related to the bands structure of the system. This term is associated to an off-diagonal spin dependent conductivity component.

In materials with large spin orbit splitting of the conduction bands (e.g. Pt [91]) or in Rashba systems (Sec. 1.2), the Berry curvature is spin dependent $\boldsymbol{\Omega}(\boldsymbol{k}) \sim \alpha_R\boldsymbol{\sigma}$, where α_R is a parameter dependent on SOC (or Rashba coefficient, Sec. 1.2). As a consequence, anomalous Hall velocity takes opposite sign for the spin up and spin down electrons [52, 92]. In a non-magnetic medium the two spin populations are equal so that a transverse pure spin current is formed (SHE).

The Berry curvature of a Rashba system is a $\boldsymbol{k}$-dependent effective magnetic field [93]. Indeed, the spin quantization axis is always perpendicular to $\boldsymbol{k}$ (Fig. 1.7**a**-**b**).

The formation of a spin current from the Rashba magnetic field is explained by J. Sinova *et al.* [93]. As shown in Fig. 1.7**c**, after a time interval t_0 the circular Fermi contour in the momentum space is shifted from the origin along p_x-axis by the amount $|eE_xt_0|/\hbar$. Note that t_0 must be much shorter than the relaxation time. The application of E_x makes electrons with **p**= $p_y\mathbf{u}_y$ acquire a new

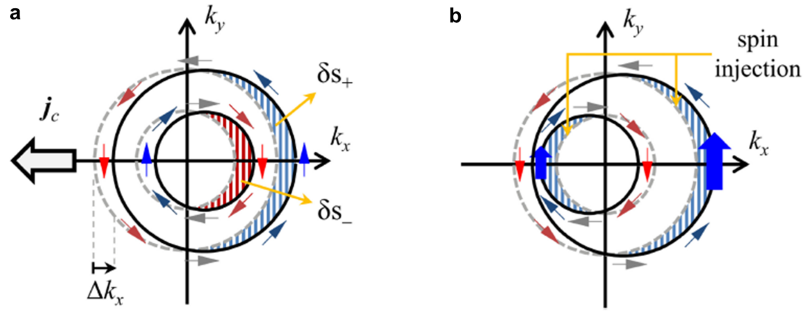

Figure 1.8: *Pictorial description of **a** REE and **b** IREE mechanisms. The shift of the Rashba contours is indicated as Δk_x. Blue and red dashed areas correspond to positive and negative spin populations (δs_+ and δs_-). Adapted from [105].*

component along x. Thus, the momentum-dependent torque acting on the electrons turns the spins (red arrows) up for positive p_y (green arrows) and down for negative p_y. A spin current is created along y and it can be seen as the result of an anomalous Hall velocity.

Extrinsic SHE

Spin Hall effect can be caused by spin dependent scattering of the carriers with impurities [94]. Similar mechanisms were found in ferromagnetic metals or in materials with magnetic impurities [95] in order to explain AHE [96]. The possible contributions are *skew scattering* [97] and *side-jump scattering* [98]. The two contributions have a different dependence on the density of scattering impurities, hence they can be tuned by controlling their type and concentration in the compounds.

The skew scattering mechanism is related to the asymmetric scattering due to SOC on the impurity, leading to a change of the direction of the wave-vector depending on the spin [96]. This mechanism was discovered by Niimi *et al.* in Cu with Ir impurities [99]. The asymmetry of side-jump scattering instead arises from a spin-dependent jump of the carriers' trajectory transverse to their wave-vector, which in turn is preserved. The side-jump SHE has been observed in AuTa [98].

1.3.3 Rashba-Edelstein Effect

Systems with locking between the carriers momentum and their spin display the so called spin galvanic effect (SGE) [100]. More recently, SGE is also referred to as Inverse Rashba Edelstein effect (IREE) [101]. In a Rashba 2DEG described by the Hamiltonian in Eq. 1.6 [52], a non-equilibrium spin density $\mathbf{S}$ generates a charge current density $\mathbf{J}_c^{IREE}$ [52]:

$$\mathbf{J}_c^{IREE} = -\frac{e\alpha_R \mathbf{z} \times \mathbf{S}}{\hbar} \tag{1.25}$$

Spin accumulation can be induced either optically or electrically [102]. However, the spin-to-charge conversion by IREE was obtained in NiFe/Ag/BiAg heterostructure [103], also by spin pumping (see Sec. 2.3.2). A non-equilibrium spin accumulation was induced at NiFe/Ag interface by the ferromagnetic resonant precession of NiFe. By IREE, the spin accumulation induces a charge current in the SOC-2DEG at the Ag/BiAg interface. The inverse spin galvanic effect (or Edelstein effect [104]) was also measured in semiconductors and 2DEG. In this case, a spin accumulation is created in the material by an electric current:

$$\mathbf{S} = \frac{\alpha_R \mathbf{z} \times J_c}{e\hbar} \tag{1.26}$$

REE manifests also in topological insulators, such as $(Bi,Sb)_2Te_3$ or Bi_2Se_3 [66].

In panels **a** and **b** of Fig. 1.8, microscopic mechanisms of REE and IREE are depicted, based on the Fermi contours of the Rashba bands (Sec. 1.2). A charge current along k_x ($\mathbf{J}^c$) shifts both contours by $\Delta k_x = -(e\tau_e/\sigma\hbar)J^c$ (σ is the conductivity, τ_e the momentum relaxation time). Due to spin-momentum locking, the spin populations are no longer equal and a net spin accumulation develops in the system (S_y): the inner band develops a negative spin density (δs_-) and the outer a larger positive one (δs_+). Conversely, a spin accumulation S_y can be host by a Rashba system only through a shift of the Fermi contours (Fig. 1.8**b**). The sign of the shift depends on the chirality of the bands. The inner constant energy contour shifts to negative k_x and the outer to positive values, so as to accommodate a positive injected spin accumulation along *y* (blue dashed areas). A shift of the Fermi energy contour ($\Delta\mathbf{k}$) is associated to an electric current density $J^c = ev_F^2\hbar N\Delta k$, with *N* the number of electrons in the conduction band and v_F the Fermi velocity. Two opposite contributions are generated by IREE (negative for the inner contour, positive for the outer), with a net current along the positive direction (the term deriving from the outer band is more intense). A different interpretation of IREE can be found in the work of K. Shen *et al.* [101], in which equilibrium/static spin accumulation and a dynamic/non-equilibrium one are treated in different ways.

Both Rashba-Edelstein and intrinsic SHE play an important role in spintronics, as they allow for the electric control of the spin-charge interconversion. Recently it has been observed that it is possible to control the amplitude and the sign of the IREE by applying gate voltage, in $LaAlO_3/SrTiO_3$ Rashba interface [17] and topological surfaces [18]. Gate-dependent intrinsic SHE was demonstrated also in graphene [106] and WS_2-graphene heterostructures [107]. All those systems are quite promising for low power spintronic devices with high spin-charge conversion efficiency. However, this effect is volatile, as it is observed only when the voltage is applied the gate. This thesis work shows that spin-to-charge conversion in the Rashba GeTe can be modulated electrically as well, in non-volatile fashion, exploiting the internal field associated to the ferroelectric polarization (Ch. 4).

1.4 Germanium Telluride

In the 1970s, chalchogenides materials such as GeTe and $Ge_2Sb_2Te_5$ were known as phase change materials [108]. GeTe undergoes a reversible transition between amorphous and crystalline phases, upon heating at $\sim$ 200 ^{o}C. The two states can be obtained by the application of specific current pulses [109] and they are characterized by different electrical and optical properties. The electrical resistivity changes by by five to six orders of magnitude (low state in crystalline phase, high state in amorphous phase), which make GeTe suitable for non-volatile resistive memory devices (PCRAMS) with large ON/OFF ratio [110].

GeTe crystalline phase displays a spontaneous ferroelectric polarization [111, 112]. The control of the ferroelectric state by means of electric fields would also allow for memory functionalities. As addressed in Ch. 3, the switching between different ferroelectric states in GeTe by metal electrodes has not been achieved so far, because of the high conductivity associated to its narrow gap nature.

In 2013, density functional theory calculations (DFT) by D. Di Sante, S. Picozzi *et al.* [11, 12] predicted that the ferroelectric distortion is accompanied with a giant Rashba splitting of the bulk electronic bands. Rashba and ferroelectricity are linked by the lattice distortion, so that a sign change of the distortion causes a change of both ferroelectric polarization and the chirality of the Rashba spin texture. Calculations are presented and discussed more in detail in the following (Sec. 1.4.2). The predicted interplay between ferroelectricity and Rashba makes FERSC materials suitable for Spin-Orbitronic applications. Some device schemes implementing the ferroelectric control of spin-charge interconversion are proposed in Sec. 1.4.3.

1.4.1 Ferroelectricity in GeTe

GeTe is the simplest conceivable ferroelectric with two atoms in the primitive cell [111, 113]. At the Curie temperature of 720 K, the crystal structure undergoes a Peierls distortion from a paraelectric

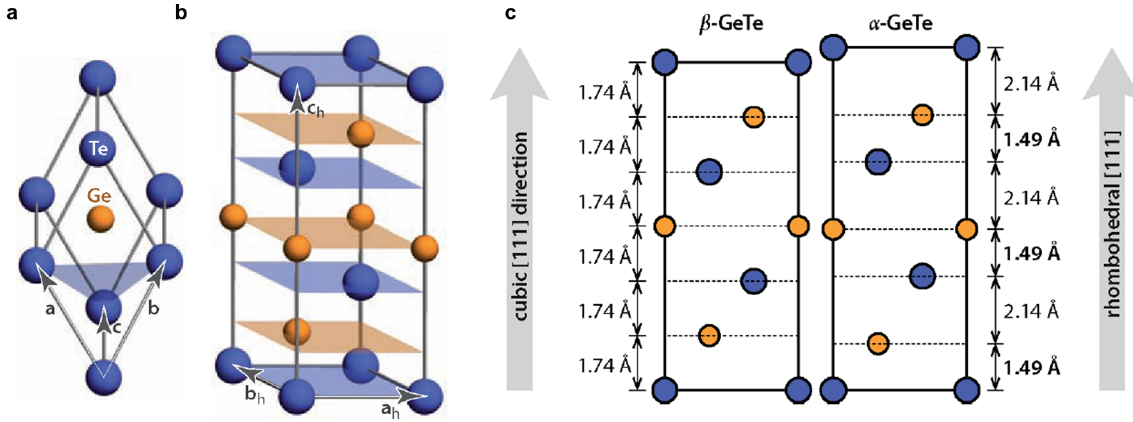

Figure 1.9: ***a*** *Distorted unit cell of α-GeTe.* ***b*** *Alternation of Ge and Te planes along the polar direction (111) direction. The unit cell vectors are named ($\boldsymbol{a}_h$,$\boldsymbol{b}_h$,$\boldsymbol{b}_h$), as they are related to the hexagonal cell.* ***c*** *Spacing between Ge and Te planes in cubic/β-GeTe and rhombohedral/α-GeTe. The stack is obtained upon projection on the unit vector $\boldsymbol{b}_h$. Adapted from [114].*

cubic (β-GeTe) to a reduced symmetry rhombohedral phase (R3m or α-GeTe) [114, 115]. In α-GeTe, a ferroelectric polarization of $\sim$ 60 μC $\cdot$ cm^{-2} results from the shift of Ge and Te atoms from the cubic positions, along the (111) direction [116] (Fig. 1.9**a**). The displacement of the Ge and Te planes were calculated theoretically in Ref. [114, 117] (Fig. 1.9**c**) and measured experimentally by high-resolution transmission electron microscopy combined with holographic polarization imaging in Ref. [118].

Experimental investigations of the para-to-ferroelectric transition were performed by first order Raman scattering in Ref. [113] and then by time-domain terahertz spectroscopy in Ref. [119]. Their observations revealed a displacive character mixed with a order-disorder type.

GeTe is also a narrow gap semiconductor ($E_{\text{gap}}\sim$ 0.8 eV), with high density of free carriers at room temperature $\sim 3 \cdot 10^{20}$ cm^{-2}. The impact of the marked semiconducting properties on the stability of the ferroelectric phase is investigated in Ref. [116, 118]. The strong internal screening of the surface polarization charges operated by free carriers minimizes the effect of the depolarization field, thus leading to a high stability of the FE state. However also external electric fields are completely screened within the first few monolayers, so that the polarization inversion should be prevented in the bulk. For such a reason, GeTe has been considered similar to a polar "metal" or an improper ferroelectric [116]. So far, the ferroelectric switching has been achieved only at the nanoscale via piezoresponse force microscopy on thin films [112] and by electrical shots in nanowires [120]. However, is GeTe a proper ferroelectric material, with tunable polarization? Our experimental investigations discussed in Ch. 3 tried to provide a solution to this outstanding question.

1.4.2 Ferroelectric dependent Rashba effect in GeTe

In FERSC materials, ferroelectricity has been predicted to be the electric key tuning the Rashba effect. Similarly, the magnetic order in multiferroics [121, 122] can be manipulated by ferroelectricity.

As discussed in Sec. 1.2, Rashba splitting commonly arises in metallic surfaces and interfaces. However, a Rashba Hamiltonian might also occur in bulk polar materials as GeTe [11, 12, 114] and BiTeI [123, 124], due to the leak of inversion symmetry. GeTe and BiTeI display a *giant* Rashba splitting compared to 2DEG, with coefficient $\alpha_R \sim 5$ eVÅ and ~ 3.8 eVÅ, respectively. The giant effect results from (i) atoms responsible for large SOC (Te), (ii) narrow gap, and (iii) same orbital character of valence and conduction bands. Bulk Rashba effect is intimately related to the crystal

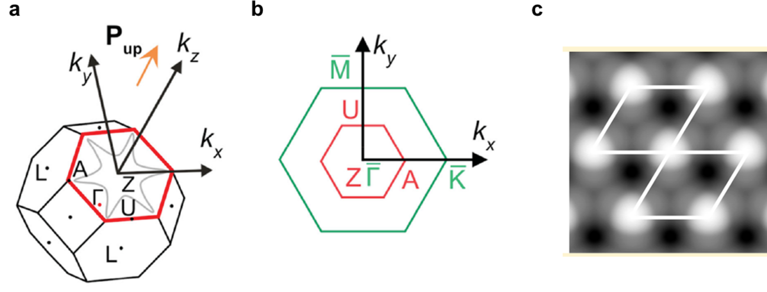

Figure 1.10: ***a*** *Bulk and* ***b*** *surface Brillouin zone of GeTe. ZA and ZU directions define k_x and k_y of the carriers. The red hexagon in panel* ***b*** *represents the projection of the bulk FBZ on the ZAU plane. The bulk direction ZA and ZU are equivalent to the surface ΓK and ΓM. Adapted from [60].* ***c*** *Hexagonal atomic patterns of a Te-terminated GeTe surface [114].*

structure, hence on the polar distortion. In the case of GeTe, the amplitude and the sign of the Rashba effect can be tuned by acting on the ferroelectric state.

Density Functional Theory (DFT) calculations of GeTe bands were performed in Ref. [12]. In the following, we explain the fundamental steps. The bulk and surface first Brillouin zones are shown in Fig. 1.10**a-b**. The six-fold symmetry arises from the hexagonal arrangement of atoms on each Ge and Te plane along the (111) direction, as clear in panel **c**. A giant Rashba splitting affects both valence and conduction bands around the *Z* point of the Brillouin zone, for carriers with wave-vectors within the *ZAU* plane (with k_x and k_y components). Note that ΓZ axis coincides with the (111) in the real space, i.e. the ferroelectric distortion.

The Rashba effective Hamiltonian of α-GeTe can be expressed in the form of Eq. 1.27, under the $\mathbf{k} \cdot \mathbf{p}$ framework. The direction k_x corresponds to ZA, k_y to ZU.

$$H_R = \alpha_k(\sigma_x k_y - \sigma_y k_x) + \lambda(k_+^3 + k_-^3)\sigma_z \text{ with } k_\pm = k_x \pm i k_y \tag{1.27}$$

Unlike conventional Rashba coefficient, in a bulk system a quadratic correction on the wave-vector *k* has to be taken into account:

$$\alpha_k = \alpha_R(1 + ak^2) \tag{1.28}$$

Thus, the Hamiltonian term arising from α_k is of the third order on *k* (cubic Rashba term). The second contribution in Eq. 1.27 is also cubic and depends on σ_z, so it is responsible for an out-of-plane spin component.

Note that the sign and amplitude of α_R depends on the internal electric field associated to the lattice distortion (i.e. the ferroelectric polarization **P**). The link between α_R and **P** is the hearth of the physics of FERSC.

The splitting of the bands (ΔE_S) solution of the eigenvalue problem is a function of the azimuth angle θ between **k** and k_x axis (i.e. $\theta = 0$ along ZA, $\theta = 90$ along ZU) as follows:

$$\Delta E_S = 2(\alpha_k^2 k^2 + 4\lambda^2 k^6 \cos 3\theta^2)^{\frac{1}{2}} \tag{1.29}$$

Such dependence leads to an anisotropic Rashba splitting (maximum along ZA and minimum along ZU), as shown in Fig. 1.11**b**. Moreover, equivalent directions in the A-Z-U plane are obtained by rotation of multiples of $\Delta\theta = \pi/3$, as clear in the six-fold symmetry of the Rashba contours shown in Fig. 1.12. The maximum energy splitting along ZA is $E_\mathrm{R}\sim$ 250 meV, with $k_\mathrm{R}\sim$ 0.1 Å and $\alpha_R \sim$ 5 eV · Å.

The eigenspinors of the Hamiltonian show a dominant in-plane component orthogonal to the wave-vector direction, according to the Rashba physics (Sec. 1.2). The expectation values of the spin are drawn on the constant energy maps in panels **a** and **c** of Fig. 1.12 for $\mathbf{P}_\mathrm{out}$ and $\mathbf{P}_\mathrm{in}$,

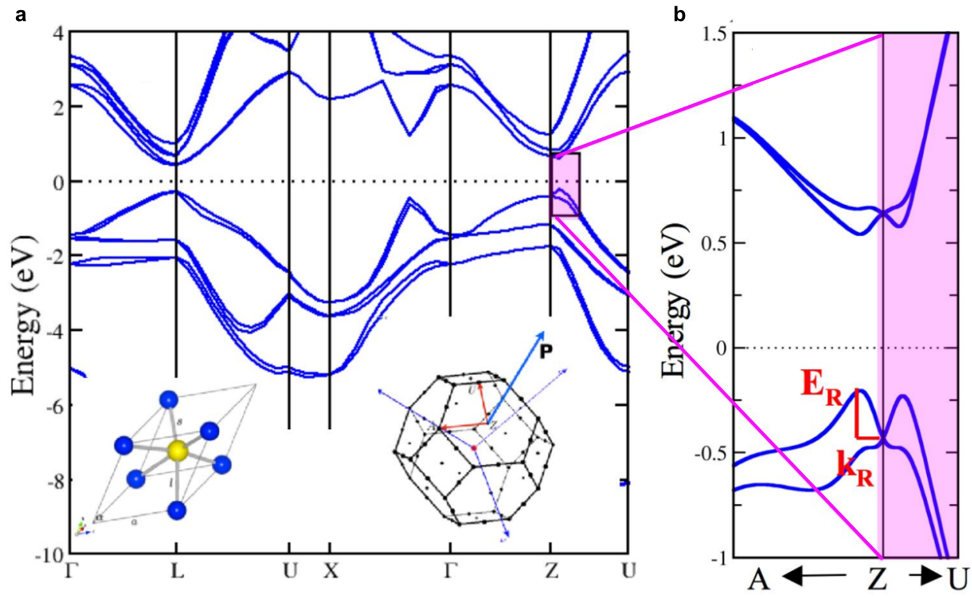

Figure 1.11: ***a*** *Bands dispersion of α-GeTe calculated by DFT in Ref. [11], along high symmetry directions. The distorted unit cell is reported in the bottom left inset, the FBZ at the bottom right.* ***b*** *Zoom of the giant Rashba effect obtained at the Z point, along ZA and ZU (i.e. in the plane perpendicular to* ***P****). The Rashba energy and wave-vector (E_R and k_R) are evidenced in red. Adapted from [11, 12].*

respectively. In both cases, a small out-of-plane spin component is also obtained (Fig. 1.12**b**-**d**). Due to the sign inversion of α_R with **P**, both in-plane and out-of-plane components of the spinors are opposite in the two polarization states. In other words, the chirality of the spin texture can be inverted by switching the ferroelectric state. The link between ferroelectricity and Rashba spin texture in actual GeTe films was the aim of the experiments described in Ch. 4. This fundamental concept would be of strong impact in view of the implementation of spintronic devices.

1.4.3 FERSCs based devices

The nonvolatile ferroelectric control of Rashba effect holds potential for low-power spinorbitronics applications. As already introduced in Sec. 1.3.2, Rashba effect triggers spin-charge conversion phenomena. In GeTe, the switching of the ferroelectric state produces an inversion of the Rashba SOC. The link between the polarization direction and the spin Hall conductivity of GeTe (Sec. 1.3.2) has been recently studied by our collaborators J. Slawinska, S. Picozzi *et al.* and the results will be discussed in detail in Sec. 4.2.5.

A wide variety of reconfigurable devices can be designed out of FERSC. The building block is composed by a thin film of a FERSC material, whose ferroelectric state can be controlled through voltage pulses applied between top and bottom electrodes (Fig. 1.13**a**).

Spin Hall Effect Transistor. A spin transistor based on SHE can be realized with a nanometric H-shaped bar made of SOC material, covered by a metallic gate (Fig. 1.13**b**). A charge current (I_{in}) can be injected in one arm (Region I). A transverse spin current is induced in the orthogonal arm by SHE (Region II). A second conversion from spin to charge current would lead to an electric current flowing in the outer arm (Region III). The output current can be sensed by means of an open-circuit voltage (V_{out}). The amplitude and sign of V_{out} can be controlled by the Rashba coefficient of the SOC material, through the gate voltage. This means that the transfer function of the logic port can be configured electrically. A spin Hall effect transistor based on a Rashba-2DEG created at the AlGaAs/GaAs interface was realized in 2010 by J. Wunderlich *et al.* [126]. More recently, W. Y. Choi *et al.* created a ferromagnetic free SHE transistor with InAs quantum-wells [125]. Adopting FERSC as SOC material the logic device would gain non-volatility (i.e. the device stores one data

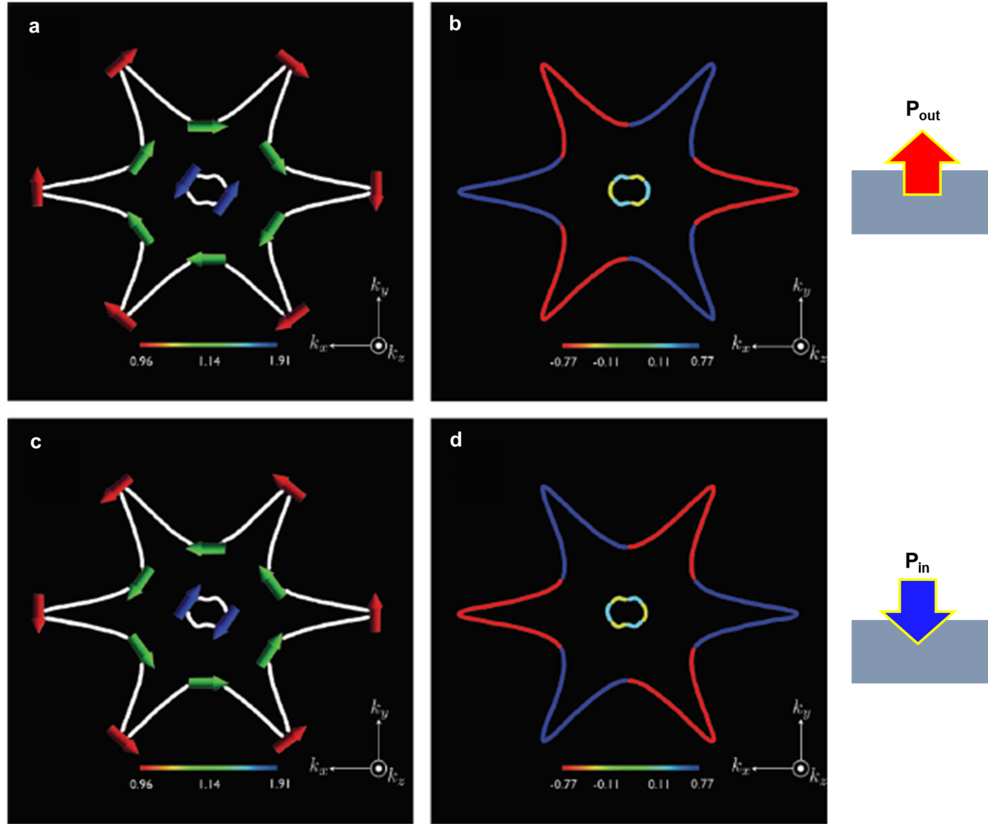

Figure 1.12: *Constant energy maps on the Z-A-U plane from cut of the bands structure at energy of -0.47 eV. Six-fold symmetry results from the hexagonal crystal structure that couples to the cubic Rashba term. The spin texture is drawn by arrows. The direction of the spin is mainly in the plane (**a**, **c**) with a small contribution out-of-plane (**b**, **d**). The sign of the spin is fully reversed comparing the outward polarization state $\mathbf{P}_{out}$ (**a**, **b**) and $\mathbf{P}_{in}$ (**c**, **d**). Adapted from Ref. [12].*

bit). Moreover, the logic function could be reconfigured by setting different ferroelectric states with a proper choice of the gate poling pulses. For saturated $\mathbf{P}_{\text{out}}$ and $\mathbf{P}_{\text{in}}$ states, V_{out} is expected to change sign so the device can implement either a NOT or a buffer function as shown in the table of Fig. 1.13**b**. Moreover, depending on the history, the duration and amplitude of the gate voltage pulses, the FERSC channel can be brought to different non-saturated polarization ferroelectric states with coexisting domains pointing in and out the growth plane. This would reflect in different possible values of V_{out}, signature of a multilevel logic device suitable for neuromorphic architectures [127]. Interconnecting different bit devices it is possible to achieve a memory unit in which the data can be processed in logic operations, thus implementing the concept of *in-memory computing*. An example of in-memory computing device based on ferroelectric spin Hall effect transistors is depicted in Fig. 1.13**c**. The two data inputs are the ferroelectric states $\mathbf{P}_1$ and $\mathbf{P}_2$, that can be manipulated by the gate voltages V_1 and V_2. When a charge current I_{in} is injected in the two input arms of the transistors, the output currents generated by the charge-spin-charge conversion sum up at the central arm of the device. The logic thus performs the algebraic sum of the inputs, as the output voltage V takes a positive value when both polarization vectors point up, negative when they point down and a zero value when they are opposite to each other.

Spin-orbit logic device. Intel has very recently proposed a prototypical scheme for a non-volatile spin-orbit logic architecture, composed by two key elements [9]. The first is a ferromagnetic memory, whose magnetization can be tuned by magneto-electric coupling with an adjacent ferroelectric material. The second element is a readout unit, capable of detecting the ferromagnetic memory state by spin-to-charge conversion in a high SOC material.By adopting a FERSC material,

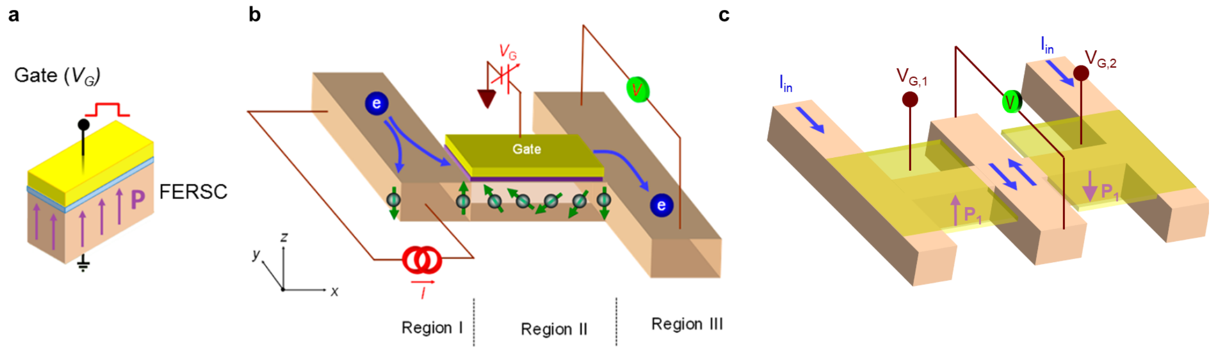

Figure 1.13: ***a*** *Sketch of the building block of made of a FERSC. The polarization state (**P**) can be controlled with a proper gate voltage pulse.* ***b*** *Illustration of a spin Hall effect transistor from Ref. [125]. The device is divided into three regions (I, II and III). The current is injected in Region I, while the spin current is generated by SHE in the SOC channel of Region II. The output voltage V of the network is measured in Region III.* ***c*** *Sketch of a in-memory computing device based on FERSC. Two gated spin Hall effect transistors are interconnected so that the output currents sum together in the central arm. The output voltage V depends on the remanent polarization states* $\boldsymbol{P}_1$ *and* $\boldsymbol{P}_2$ *of the FERSC layer set by the two gate voltages (*$V_{G,1}$ *and* $V_{G,2}$*). The device computes the algebraic sum of the two data bits (i.e. the two polarization states): when both polarization vectors point UP V> 0, when they point DOWN V< 0 and when they are opposite V= 0.*

memory (ferroelectricity) and SOC readout (Rashba) are implemented by a single layer thus reducing the complexity of the device. Similarly to the case presented for the spin Hall effect transistor, logic networks can be designed by connecting different bit devices in the memory space [9].

1.5 Indium doped Germanium Telluride

The great potential of GeTe for generation of spin logic devices on semiconducting platforms is limited by its intrinsic high doping level. Indeed, a reduction of the density of free carriers would necessarily lower the power absorbed during the ferroelectric switching by a reduction of the conduction currents, but most importantly it would allow for the full exploitation of its semiconducting behavior. In addition, it would be possible to obtain FERSCs with different doping levels and use them for novel generation of nonvolatile electronic devices, as for instance ferroelectrically tunable *p*-*n* GeTe junctions.

The goal of the work in Ch. 5 is to reduce the doping level of GeTe towards a *n* character, but keeping its ferroelectric-driven Rashba effect. To such scope, we investigate substitutional doping of GeTe with Indium. The present section provides some theoretical arguments of the effect of In expected on the doping of GeTe.

By thermodynamics, epitaxial undoped GeTe naturally shows a strong *p* carriers concentration due to the spontaneous formation of Ge cation vacancies in the lattice at room temperature, i.e. empty Ge sites in the crystal lattice formed during the film growth. Indeed, GeTe generally grows with slight off stoichiometry (from 2.5 to 10 % of Ge vacancies [128–131]) and with marked *p* doping level (from 8 to 11 $\cdot 10^{20}$ cm $^{-3}$). The relation between vacancies and holes concentrations can be understood from the Lewis diagrams in Fig.1.14: when a Ge atom is removed from the lattice, the Te 5*p* orbital is not completed and a pair of holes is left, named V_c^{2+}.

Many solutions were proposed in the literature to manipulate the amount of vacancies, such as the introduction of Bi_2Te_3 [130] or Sb_2Te_3 [131] as well as filling vacancies with other metals including Ga, In, Ag or Sn [130]. In Ref. [130], Bi_2Te_3 is used as solvent that increases the value of the solubility of metal dopants in the GeTe matrix. As depicted in Fig. 1.15, Bi_2Te_3 in GeTe lattice increases the number of vacancy sites but due to the electrical neutrality of such compound does not increase the doping concentration (V_c^0). The vacancies introduced by Bi_2Te_3 are therefore termed

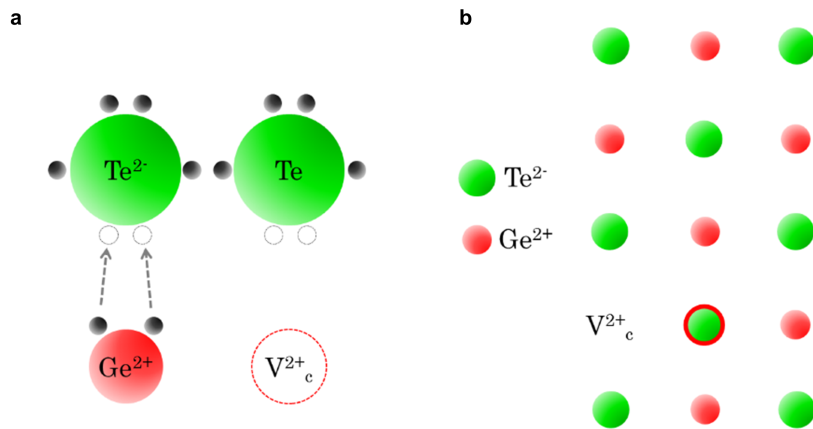

Figure 1.14: ***a*** *Lewis representation of the chemical bond between Te and Ge (left) and the formation of a holes pair with a Ge vacancy (right). The gray filled circles represent the electrons of Te5p and Ge2p orbitals, the empty ones holes.* ***b*** *Naturally formed vacancy (V_c^{2+}) in a GeTe array (100 plane). The uncompensated Te anion is circled in red.*

as "neutral". This means that a larger solubility of the metal can be achieved by increasing the number of available sites in the lattice because for every three Te ions only two Bi ions are added into cation sites. With this method, the net number of charged vacancies is decreased and a partial p doping compensation is obtained with respect to GeTe Ref. [130]. A similar approach was recently adopted in Ref. [131] by introduction of Sb_2Te_3 in the GeTe matrix which has the same cation-anion ratio as Bi_2Te_3. Nonetheless, because of the large number of chemical species involved, this technique can be applied to synthetized GeTe polycrystalline sample but hardly employed for the growth of epitaxial monocrystalline films by molecular beam epitaxy (MBE). In this work we proposed a different solution that can be realized by coevaporation of Ge, Te and In elements in a MBE machine. Following the same idea exposed before, Indium can be easily ionized into the cation In^{3+} as it tends to bond with Te. The formation of In_2Te_3 inside the GeTe matrix increases the solubility of In itself and the carriers compensation. A similar result could be achieved with Gallium atoms, even though the mismatch between Ga^{3+} and Ge^{2+} radius is larger (i.e. the solubility achievable for Ga is reduced).

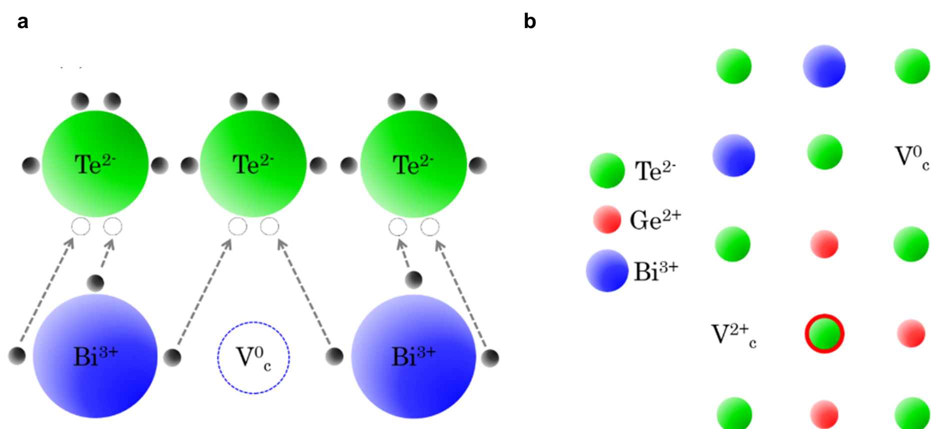

Figure 1.15: ***a*** *Lewis representation of the formation of neutral vacancy with Bi_2Te_3 denoted as V_c^0.* ***b*** *Representation of a neutral vacancy in GeTe lattice by the introduction of Bi_2Te_3 (100 plane).*

CHAPTER 2

Experimental techniques

The present chapter is devoted to the fundamental aspects of the techniques employed for the experimental work on FERSC. The intrinsic multifunctionality of these materials gives rise to the need of several diversified tools for the study and the control of their properties. In general, ferroelectricity can be accessed by means of electric or piezoelectric measurements. The most important techniques, their potentialities and limitations are discussed in the first section (Sec. 2.1), such as *I*-*V* methods (e.g. Positive Up Negative Down, PUND) and Piezoresponse Force Microscopy (PFM). Ferroelectricity in FERSC is also correlated with the Rashba bands splitting, which can be visualized by Spin- and Angle Resolved Photoemission Spectroscopy (SARPES) described in Sec. 2.2. Finally, spin-charge interconversion phenomena play a fundamental role for the application of FERSC in spin computing devices. In this work, spin-to-charge conversion is probed by spin pumping at ferromagnetic resonance discussed in Sec. 2.3. The last section of the chapter is dedicated to the growth of the samples investigated in the experiments.

2.1 Ferroelectric characterization

2.1.1 Current-voltage methods

Current-voltage (*I*-*V*) methods are commonly used for the characterization of ferroelectric materials. They are based on the Sawyer-Tower circuit, conceived in 1930 [132]. A ferroelectric film is grown between a top and a bottom electrodes. The application of a voltage among them induces a change of the polarization state, which can be tracked by means of the displacement current. Indeed, a given polarization (P) is associated with a proper distribution of charges (surface σ_P, and bulk ρ_P distribution). In the case of a homogeneous ferroelectric material, only surface polarization charges $\sigma_P = \mathbf{P} \cdot \mathbf{n}$ are developed at the top and the bottom surfaces of the film. Thus, any time variation of P gives rise to a current J_P.

The expression of J_P can be derived from Maxwell equations. In the case of a material with polarization axis along the capacitor structure (i.e. perpendicular to the film surface), the amplitude of the displacement field D is:

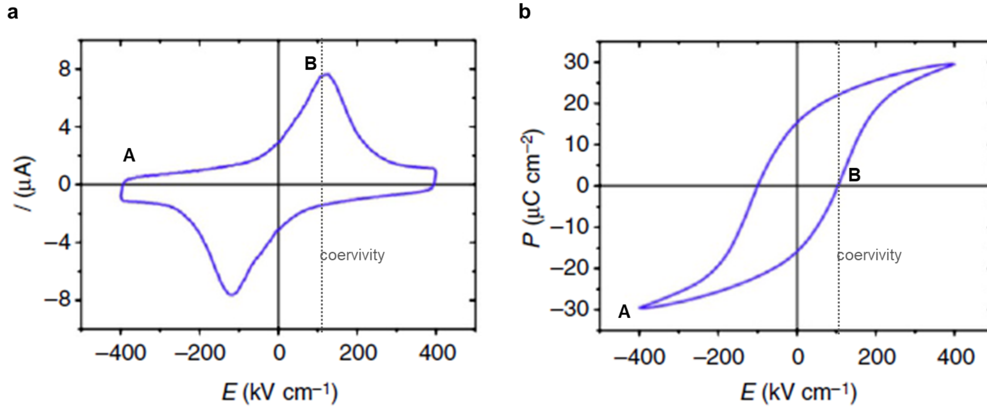

Figure 2.1: ***a*** *Current-field (I-E) loop of a BTO/LSMO/STO heterostructure.* ***b*** *Polarization-field loop (P-E) retrieved by time integration of the curve in panel* ***a****. Adapted from Ref. [133].*

$$D = \epsilon_0 E + P \tag{2.1}$$

And the total displacement current is the time derivative of D:

$$J = \frac{\partial D(t)}{\partial t} = \epsilon_0 \frac{\partial E(t)}{\partial t} + \frac{\partial P(t)}{\partial t} \tag{2.2}$$

For a paraelectric material $P = \epsilon_0 \chi E$, with χ the dielectric susceptibility of the material. In this case, Eq. 2.2 reduces to the capacitor fundamental equation $J(t) = \frac{\epsilon_0 \epsilon_r}{d} \frac{dV}{dt}$, with d the thickness of the film.

A ferroelectric material instead shows a remanent polarization (P_r), with a hysteresis loop behaviour versus the applied field (Sec. 1.1).

$$P = P_r + \epsilon_0 \chi E \tag{2.3}$$

In this case, an additional polarization current term arises (J_P):

$$J_P = \frac{\partial P_r}{\partial t} \tag{2.4}$$

By integrating Eq. 2.4, the polarization variation in a specific time interval t_i-t_f can be related to the area of the measured current peak:

$$\Delta P_r = \int_{t_i}^{t_f} J_P dt \tag{2.5}$$

Eq. 2.5 allows to recover the ferroelectric hysteresis loop from the measurement of the current. Typically the experiment consists in the application of a voltage ramp to the capacitor with a fixed rate, so that the electric field is $E(t) = Kt$. In Fig. 2.1 this method is applied to a $BaTiO_3$ thin film. For large negative electric field values (e.g. point A in Fig. 2.1**a**-**b**), the film is polarized with negative saturation polarization ($-P_{sat}$). In panel **a**, the total current in this region is dominated by a constant displacement current $J = \epsilon_0 \epsilon_r K$, that results from Eq. 2.1 and Eq. 2.2 with a fixed value of the remanent polarization ($-P_{sat}$). Integrating in time the displacement current, the retrieved value of the polarization (panel **b**) follows a linear increase with the field corresponding to the dielectric response. When E increases up to the coercive value (point B, in this case around 100 kV cm^{-1}), the ferroelectric material is forced to switch from negative P_r to a positive value, with the generation of a current peak (panel **a**). This current peak is translated into a switching of the polarization (panel **b**) by means of Eq. 2.5. Then, the full loop is recovered by sweeping the electric field back

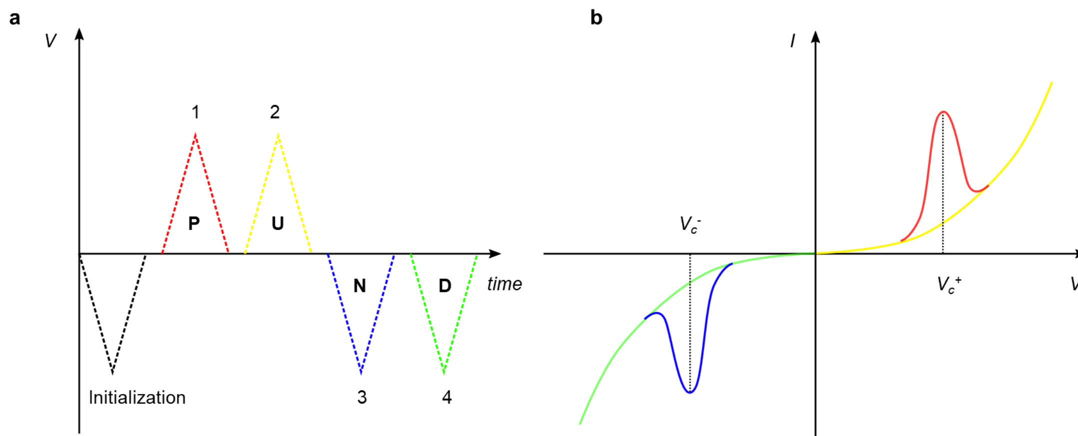

Figure 2.2: *Sketch of a Positive Up Negative Down (PUND) measurement.* ***a*** *Sequence of triangular voltage pulses. The first (dashed line) is used to initialize the polarization state (negative pulse), the following four pulses are used to perform the measurement: 'P' switches the polarization to the other state, 'U' is used to probe the dielectric and leakage currents during a positive slope, 'N' switches polarization back to the initial state and 'D' registers the contributions not related to ferroelectric switching of a negative pulse (same role as 'U').* ***b*** *Example of behaviour of the capacitor current versus voltage obtained with the pulses in panel* ***a****. An exponential leakage behaviour is assumed.*

from positive to negative saturating values and registering the current peak at the negative electric coercive field.

Polarization switching current allows then for monitoring the change of the ferroelectric state when the external field is applied. Lossy dielectrics can also develop a non-negligible leakage current through the capacitor during poling. Leakage and other spurious contributions to the total current can be subtracted during the measurement, by adopting a pulsed technique called Positive Up Negative Down (PUND). The concept of the measurement is sketched in Fig. 2.2**a**. First a polarizing voltage pulse **P** is applied to the capacitor in order to induce the switching of the polarization from the starting state (pre-polarized in the opposite direction). During this pulse, the current through the capacitor develops both leakage, displacement and polarization switching contributions (red curve in Fig. 2.2**b**). Then, a second identical pulse **U** is applied to record only the leakage and displacement contribution, as the system is kept at the same saturation (yellow curve in panel **b**). Therefore, the pure polarization current peak can be extracted by subtracting the current recorded during **P** and **U**. The same procedure is then performed with two opposite voltage pulses (**N** and **D**), leading to a negative switching current peak (blue curve in Fig. 2.2**b**). After the correction, the integral of the current is calculated to obtain the ferroelectric loop according to Eq. 2.5. This trick is not applicable to the case of strongly doped semiconductors, as the polarization switching peak is hindered by the Ohmic current density.

2.1.2 Piezoresponse Force Microscopy

Piezoresponse Force Microscopy (PFM) was invented by M. Abplanalp *et al.* in 1998 [45], as a tool for mapping ferroelectric domains in space with nanometric resolution [134]. A conductive tip of an Atomic Force Microscope (AFM) is used to measure the out-of-plane piezoelectric coefficient (d_{33}), exploiting the link between the ferroelectric polarization and the piezoelectric response (Sec. 1.1.3). Differently from I-V methods, PFM senses a mechanical deformation rather than a current and it is applicable to both semiconducting and insulating ferroelectrics. Note that the contact area is defined by the nanometric size of the tip, which limits the current flow and the related sample damage (especially in strongly doped films). For those reasons, PFM represents a less destructive technique for characterization of semiconducting thin films.

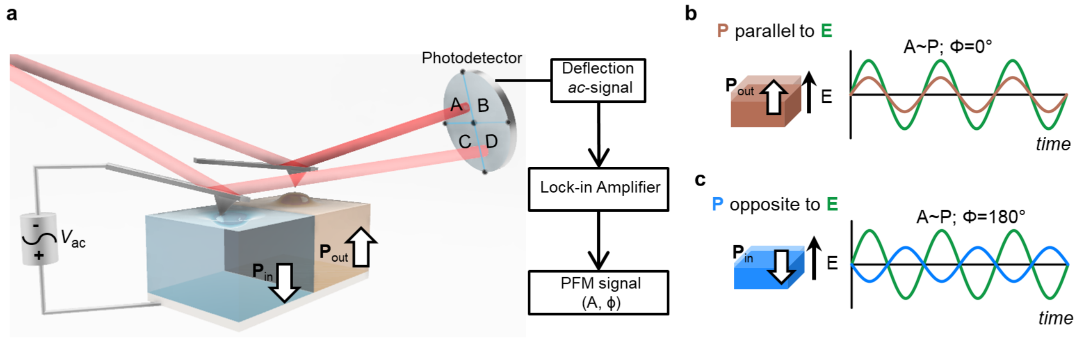

Figure 2.3: *Working principle of Piezoresponse Force Microscopy.* ***a*** *Sketch of the setup. A contact AFM setup is endowed by an ac voltage supplier, connected between the sample back-electrode (positive) and the conductive tip (negative electrode). The deflection of the cantilever probed as the laser position on the photodetector depends on the ferroelectric state. When V_{ac}> 0 is applied to the back-electrode, the deflection is positive for $\mathbf{P}_{out}$ regions, by piezoelectric expansion. On the opposite a $\mathbf{P}_{in}$ domain results in a negative deflection signal. The tip oscillates at the frequency of V_{ac}, resulting in an oscillating deflection signal demodulated by a lock-in-amplifier (LIA). The PFM amplitude A and phase ϕ are retrieved from Eq. 2.8.* ***b*** *Piezoelectric oscillation of outward regions is in-phase with respect to V_{ac} (ϕ= 0°), because polarization (**P**) is always parallel to the electric field **E**.* ***c*** *The oscillation of the inward domain is out-of-phase (ϕ= 180°), because **P** is opposite to **E**.*

Working principle

The measurement of the out-of-plane ferroelectric response (vertical PFM [135]) is performed with a biased conductive AFM tip, in physical contact with the sample. A voltage is imposed between the tip and a bottom electrode (placed underneath the ferroelectric film), and the mechanical change of the sample height (Δz) is recorded simultaneously as the corresponding tip deflection signal of the four quadrants detector, computed as (A+B)-(C+D). According to Eq. 1.2 discussed in detail in Sec. 1.1.3, the sign of the height change (i.e. tip deflection) is signature of the polarization orientation (P_3) with respect to the imposed electric field (i.e. the sign of the voltage V):

$$\Delta z = d_{33}V = 2Q_{33}\epsilon_0\epsilon_{33}P_3V \tag{2.6}$$

As shown in Fig. 2.3**a**, the deflection is positive when the sample expands ($\Delta z > 0$), or negative when it contracts ($\Delta z < 0$). If a voltage V> 0 is applied to the sample back-electrode with the tip at ground, expansion and contraction correspond to outward ($\mathbf{P}_{\text{out}}$) and inward ($\mathbf{P}_{\text{in}}$) polarization, respectively.

In addition, also the lateral deformation associated to a in-plane polarization component can be detected from the torsion of the cantilever (lateral PFM [136]). Hence, a three-dimensional reconstruction of the polarization vector can be obtained by vectorial PFM [137]. In this study we will focus on Vertical PFM.

Typical values of d_{33} of ferroelectric oxides are in the range 50-500 pm/V [138], while the vertical sensitivity of the tip is of 100-200 nm/V (the stiffness of the cantilever is of the order of 1 N/m). Due to the small mechanical deformation, a lock–in technique [139] is required. As sketched in Fig. 2.3**b**, an alternating driving voltage ($V_{ac} = V_0 \cos(\omega t)$) causes an oscillation of the sample height:

$$\Delta z = |d_{33}|V_0 \cos(\omega t + \phi(d_{33})) \tag{2.7}$$

Driving voltages typically have frequencies of about $f \sim 10$ kHz - 1 MHz and amplitude of $V \sim 1 - 10$ V. The tip cantilever bends following the surface, so that also the deflection signal at the detector oscillates in time ($D(t)$). The amplitude (A) is proportional to the absolute value of P_3, averaged over the tip-sample contact area. The phase signal (ϕ) is ideally either 0° or 180°, if the net polarization is parallel or antiparallel with respect to the applied electric field (Fig. 2.3**b-c**).

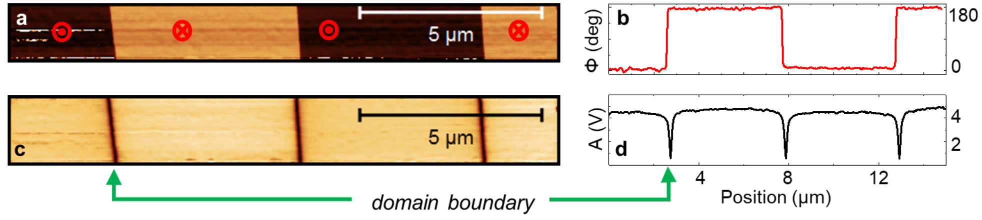

Figure 2.4: *Example of domains reading in $LiNbO_3$ periodically poled single crystal.* ***a*** *PFM phase map and* ***b*** *phase profile.* ***c*** *PFM amplitude map and* ***d*** *amplitude profile. Profiles have been integrated over the lines of the scans.*

Hence, the sign of the ferroelectric state P_3 can be measured from the phase of the tip deflection signal.

A and ϕ are measured by demodulating $D(t)$ at the driving frequency with a lock-in amplifier (LIA) and combining X and Y output signals as follows:

$$\left.\begin{aligned} X &= A\cos(\phi) \\ Y &= A\sin(\phi) \end{aligned}\right\} \iff \begin{cases} A = \sqrt{X^2+Y^2} \\ \phi = \arctan\dfrac{Y}{X} \end{cases} \tag{2.8}$$

From the amplitude A it is possible to extract the associated value of the piezoelectric coefficient d_{33} as:

$$|d_{33}| = \frac{S}{GV_{ac}}A \tag{2.9}$$

Where S is the sensitivity of the optical lever at the detector expressed in pm/V that can be obtained from a proper calibration of the AFM. The sensitivity describes how much the tip has to move along z to cause a change of 1 V of the deflection signal at the detector. G is the amplification factor of the LIA.

Scanning the tip over a ferroelectric sample it is then possible to map A and ϕ and visualize FE domains. An example of periodical alternation of ferroelectric domains in $LiNbO_3$ is shown in Fig. 2.4. The values of the phase signal takes alternatively 0° or 180° values, corresponding to outward and inward polarizations (panels **a**-**b** of Fig. 2.4). The amplitude instead has approximately the same value in the two types of domains, as the absolute value of the polarization is ideally the same for opposite domains (panels **c**-**d** of Fig. 2.4). At the domain walls A is drastically reduced. Ideally the tip amplitude goes to zero, because the oscillations induced to the tip by neighbouring up or down domains cancel each other (i.e. they are out-of-phase). It is usually convenient to represent the output of the LIA as a phasor in the (X, Y) plane. In the ideal case described before, outward and inward polarizations are phasors on the X axis with a 180° phase jump (Fig. 2.5**a**). In practical situations, a rigid rotation of the vectors axis can be induced by delays in the acquisition line. Moreover, E. Soergel *et al.* demonstrated that the phase shift between the ferroelectric phasors can be significantly smaller than 180°, due to a system inherent background noise and/or tip-sample electrostatic interaction [139, 140] (Fig. 2.5**b**). The origin of the background noise in PFM is the presence of multiple mechanical resonances of the AFM head (comprising of tip, cantilever, piezoelectric actuators and other mechanical parts), which could be excited during the *ac* measurement [139]. The background strongly depends on the frequency of V_{ac}, on the stiffness of the tip-sample contact on the specific cantilever [140]. It can be removed by subtracting to the phasors measured by the lock-in their mean vector **B** (indicated by violet vector in panel **b** of Fig. 2.5), and the PFM image can be recovered.

The PFM signal of materials with small piezoelectric coefficients can be enhanced by choosing the driving frequency at the tip-sample contact resonance. As any oscillator, the amplitude of

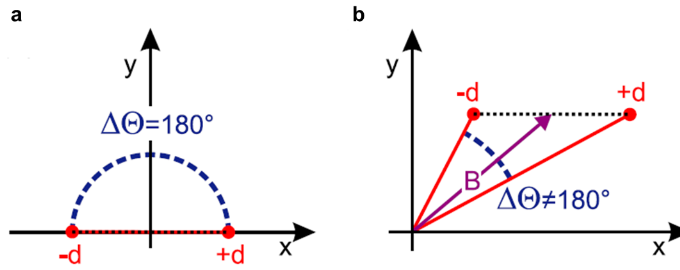

Figure 2.5: *Phasors representation of the ferroelectric states (+d and -d).* ***a*** *Ideal measurement, the phase shift is 180° and the vectors' lengths are the same.* ***b*** *System inherent background and tip-sample electrostatic effects alter the detection of the piezoelectric response. The two phasors have different lengths and a reduced phase shift. The background phasor is identified by the vector* ***B****, which must be subtracted from the measurement. Adapted from Ref. [139].*

the system response increases by the quality factor of the resonance. This is the case of GeTe ($d_{33}\sim$ 1 pm/V), for which resonance-enhanced PFM was chosen by A. V. Kolobov *et al.* to get domains maps [112]. The amplitude of d_{33} can be estimated as in Eq. 2.9 and accounting for the amplification Q provided by the mechanical tip resonance:

$$|d_{33}| = \frac{S}{GV_{ac}Q}A \tag{2.10}$$

Where Q is the quality factor of the resonance. The major drawback of resonant PFM is related to the enhanced sensitivity to any other external excitation, including changes of topography during the scan, electrostatic tip-sample interaction and background noise.

Finally, the AFM can be used also to write ferroelectric domain patterns at the micro- and nanoscale, through a large enough *dc* bias voltage between the scanning tip and the back-electrode. Writing and reading domain patters by PFM is useful to investigate the switchability of the polarization. Ferroelectric patterns on GeTe thin films have been realized in this thesis work.

Switching spectroscopy

The ferroelectric hysteresis loop can be measured in a specific location of the sample (point or switching spectroscopy). Spectroscopy provide information on the local mechanism of domain nucleation and the thermodynamic parameters of the switching process [134]. The PFM signal is recorded as a function of the applied poling voltage (*dc*). In the so called 'continuous *dc* mode', the *dc* voltage ($V_{\rm dc}$) sweeps linearly with time, between a negative and a positive saturating values (Fig. 2.6**a**). The *ac* voltage is constantly added to the tip, so as to record the PFM signal during the voltage sweep. The continuous mode is suitable especially for insulating ferroelectrics with consistent piezoelectric coefficient and low conductivity, for which the mechanical response is higher compared to tip-sample electrostatic contributions. An example of measurement on a Lead Zirconate Titanate (PZT) thin film is reported in Fig. 2.6**b-f**.

The *ac* voltage is applied to the sample back-electrode, the *dc* one to the tip. The X and Y components of the LIA are in panels **b** and *c*, respectively. The deflection signal is mostly contained in X (Y is negligible), which means that the tip oscillation is either in-phase or out-of-phase respect to $V_{\rm ac}$. Indeed, the two ferroelectric states belong to the X axis on the (X,Y) plane (panel **d**). X follows a hysteresis loop, which is ascribed to the ferroelectric one as result of converse piezoelectric effect. The two saturation states correspond to outward and inward polarization ($\mathbf{P}_{\rm out}$ and $\mathbf{P}_{\rm in}$), respectively stabilized with $V_{\rm tip}< 0$ and $V_{\rm tip}> 0$. The vectors $\mathbf{P}_{\rm out}$ and $\mathbf{P}_{\rm in}$ are reported in the (X,Y) plane. The influence of the system inherent background is marginal, because the two ferroelectric phasors have equal amplitude and belong to the X axis, as expected for the noise-free measurement (Fig. 2.5**a**). In this case the complete information of the piezoelectric behaviour is retained in the

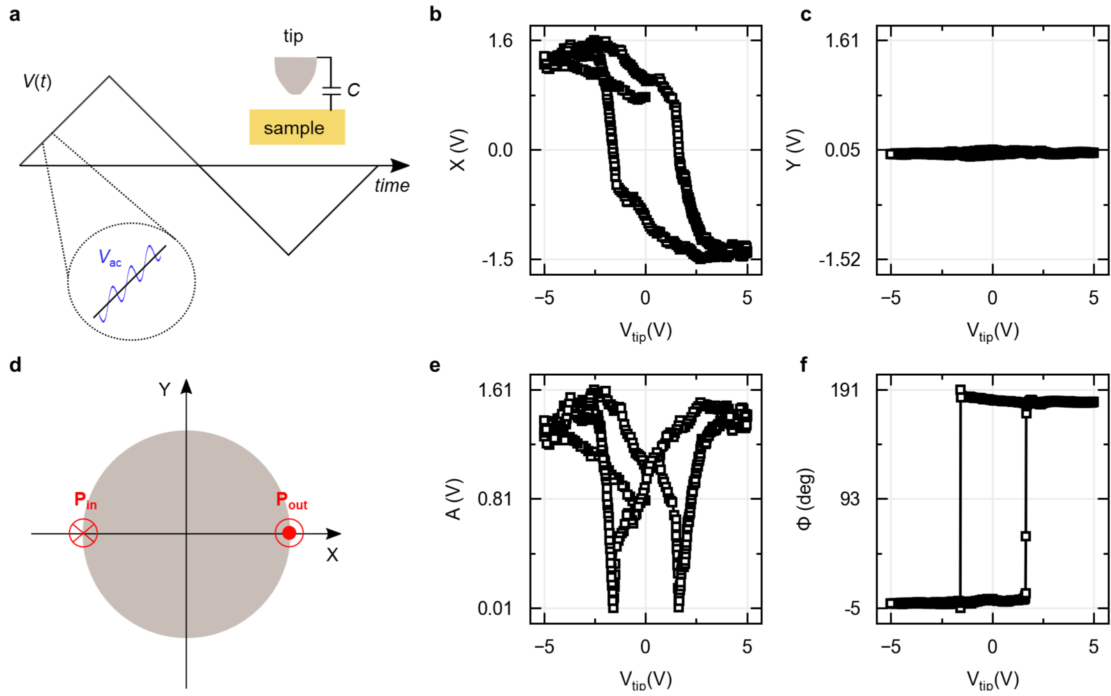

Figure 2.6: *Continuous dc point spectroscopy.* ***a*** *Schematics of the measurement. The linear slope followed by the poling bias (V_{dc}) is superimposed to the driving voltage (V_{ac}). The amplitude of V_{ac} is usually smaller than V_{dc}.* ***b-c*** *and Y signals from LIA versus the tip voltage (V_{tip}), acquired in the continuous dc mode on a film of PZT (20 nm).* ***d*** *The vector representation in the (X,Y) plane of the two saturation states of measurements* ***b-c****. Outward polarization ($\mathbf{P}_{out}$) is stabilized by negative V_{tip}, whereas inward state ($\mathbf{P}_{out}$) is obtained with V_{tip}> 0. Note that the two states have negligible Y component, they have the same amplitude (i.e. same distance from the origin) and they are separated by a phase shift of 180 °.* ***e-f*** *PFM amplitude (A) and phase (ϕ), respectively. The signals are computed from X and Y according to Eq. 2.8.*

signal X (also referred to as PFM signal). The A and ϕ representation can be obtained from X and Y by Eq. 2.8 (panels **e** and **f**). The amplitude is proportional to the average $|d_{33}|$ below the tip. The maximum value is obtained when the polarization is saturated; the minimum is observed at the coercive voltages, when the sample is broken into domains ($V_c \sim \pm 2$ V). On the other side, the phase takes 0° and 180° values depending on the orientation of the polarization vector ($\mathbf{P}_{out}$ and $\mathbf{P}_{in}$).

For materials with low piezoelectric coefficient and non-negligible conductivity, such as ferroelectric semiconductors, a different approach is needed. In those cases, the piezoelectric signal can be comparable or possibly overwhelmed by the deflection signal caused by the electrostatic interaction between the tip and the sample. Indeed a charged tip induces a opposite charge distribution at the sample surface, with the formation of a capacitor ($C(z)$, with z the tip-sample distance). The electrostatic force between the tip and the sample alters the loop shape causing artifacts [134, 141]. The force between the capacitor plates is:

$$F_{el}(z) = \frac{1}{2} V \frac{\partial C}{\partial z} \tag{2.11}$$

The tip-sample contact can be treated as a spring with stiffness k, so that the tip displacement can be written as:

$$\Delta z = \frac{1}{2k} \frac{\partial C}{\partial z} V^2 \tag{2.12}$$

In a spectroscopic measurement $V = V_{dc} + Vac$, so the displacement signal derived from Eq. 2.12 results:

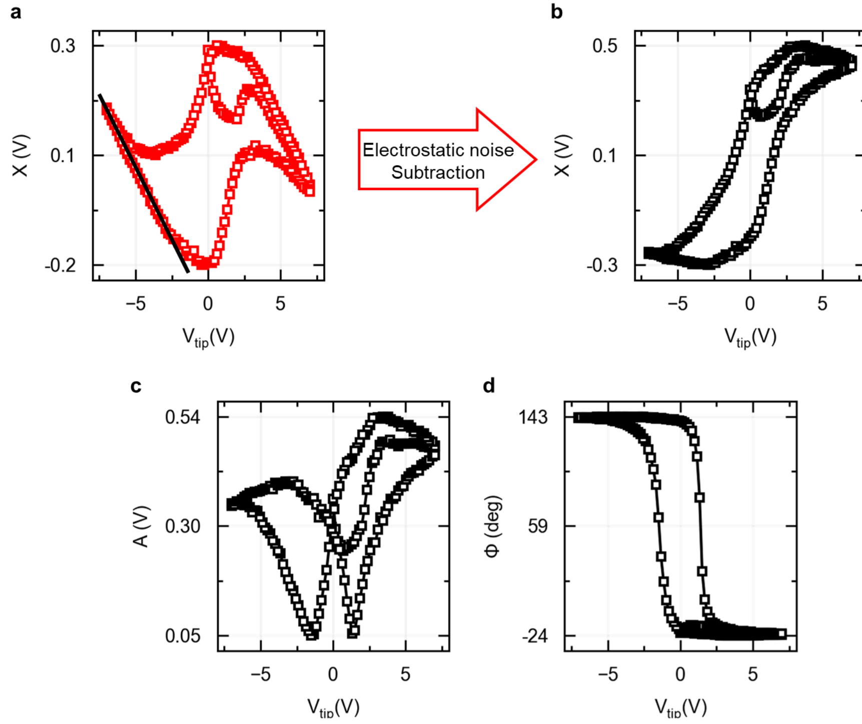

Figure 2.7: *Effect of electrostatic forces on the continuous dc loop of a PZT film.* ***a*** *X component of continuous dc loop. The linear contribution to the deflection signal (black line) results from the electrostatic tip-sample interaction (Eq. 2.13). The subtraction of the electrostatic linear background yields to the signal in panel* ***b****, the reproduction of the ferroelectric hysteresis loop. A similar procedure has to be done on Y, that could be different from zero due to system inherent background or delays (data not shown).* ***c-d*** *Amplitude (A) and phase (ϕ) obtained from the X and Y signals after the subtraction of the electrostatic signal.*

$$D_{el,ac}(V_{dc}) = \frac{1}{k}\frac{\partial C}{\partial z} V_{dc} V_{ac} \propto V_{dc} V_{ac} \tag{2.13}$$

The electrostatic contribution linearly increases with the applied *dc* voltage and it sums to the PFM signal $D_{piezo}(V_{dc}) = d_{33}(V_{dc})V_{ac}$ (Eq. 1.1).

In wide gap semiconductors as for example PZT, the electrostatic noise can be estimated by a linear fit of the saturation arm of the X and Y channels of the LIA. The linear slope can be subtracted and the corrected amplitude and phase can be computed. The correction procedure performed on PZT is shown in Fig. 2.7.

In GeTe however, the electrostatic interaction with the tip is way more intense due to the high density of free carriers (i.e. large $\partial C/\partial z$). Consequently, the electrostatic linear contribution typically overwhelms the PFM signal, which is more than 100 times lower than in the case of PZT ($d_{33,PZT}$/ $d_{33,GeTe} \sim 100$). The subtraction procedure is not applicable in this case, because of the strongly reduced signal-to-noise ratio.

As follows from Eq. 2.13, the electrostatic contribution can be avoided if the PFM signal is recorded at with V_{dc}= 0 (with a V_{ac} applied), i.e. at remanence. As shown in Fig. 2.8, the sample can be poled by a voltage pulse with varying amplitude ('on' time), following a triangular waveform similar to the one used in continuous mode. The PFM signal is read immediately after the pulse ('off' time), by sensing the piezoelectric deformation induced by the driving voltage V_{ac}. This technique is called pulsed *dc* spectroscopy, as conceived by S. Jesse *et al.* in Ref. [142] (or switching spectroscopy or continuous pulsed mode). Typical pulse duration are of the order of 1 μs-1 ms. Pulsed *dc* approach is preferred for gathering high-quality hysteresis loops and it becomes mandatory for semiconducting samples, especially those with poor piezoelectric properties and

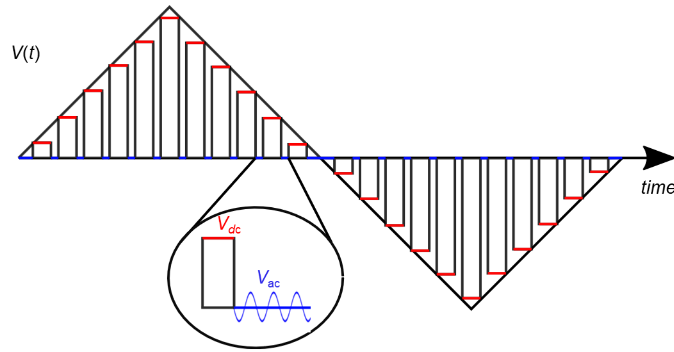

Figure 2.8: *Measurement principle of the pulsed dc voltage point spectroscopy. The poling voltage V_{dc} is a train of rectangular pulses. The amplitude of the pulses follows the triangular envelope used in the continuous dc mode. The sample is poled by V_{dc} in the 'on' state (red), while the PFM signal is recorded in the 'off' state (blue) through V_{ac}.*

marked conductivity as GeTe. Pulsed *dc* spectroscopy of GeTe thin films is discussed in Sec. 3.1.1. The acquisition of PFM loops on different positions of the sample provides information about the spatial distribution of the FE properties, as the pristine polarization state and the coercive voltages. The pulsed approach also permits to limit the local heating of tip and sample, because the *dc* component of the voltage is applied only for relatively short times and is turned off during the reading step. A different scenario is found for domains writing, because the current is always flowing between the sample and the biased tip during the scan, provoking a fast degradation of the tip quality and damages of the sample surface (burning, electrochemical reactions). Given those arguments, voltage point spectroscopy maps were recorded throughout the thesis for the characterization of the ferroelectric properties of GeTe thin films, with spatial information.

2.2 Spin- and Angle- Resolved Photoemission Spectroscopy: SARPES

Photoemission spectroscopy techniques play a leading role in the characterization of the chemical composition and the electronic properties of a material. Among others, Spin- and Angle- Resolved Photoemission Spectroscopy (SARPES) leverages the simultaneous detection of angle, energy and spin polarization of photoemitted electrons to map the spin dependent electronic bands structure of solid-state materials in the momentum space. High resolution maps allow to obtain information about the collective behaviour of correlated electrons systems, as superconductors [143, 144], density waves and magnetic orders, about the topological surface states [145] and map bands of semimetals (i.e. materials with no bandgap) [146]. In Ch. 4, the large Rashba splitting of bands of GeTe(111) and the spin texture are measured by SARPES. This technique helped the investigation of the effect of In doping of GeTe on the Rashba effect and on the conduction properties (Ch. 5).

This section aims to provide the reader with the fundamental principles of SARPES.

When the sample is irradiated by photon beam with energy $h\nu$, electrons can be photoemitted. If the energy absorbed from the photon overcomes the binding energy and the potential barrier at the surface, the excited electron can be emitted from the sample and behave as free particles. The angle of emission, the kinetic energy and the spin polarization of the photoemitted electrons are linked to the electronic state before the emission (wave-vector, binding energy and spin). Filtering electrons based on their kinetic energy and emission angle is performed by an electron analyser. The intensity is then recorded by a detector at the exit of the analyser, which could also add spin resolution (spin detector). The dependence of the spin intensity with kinetic energy is also called photoemission spectrum. As any photoemission technique, ultra-high vacuum environment (UHV chamber) is needed, so as to minimize the scattering of electrons with the atoms and ions in the atmosphere and at the same time preserve the sample surface quality from oxidation or contamination.

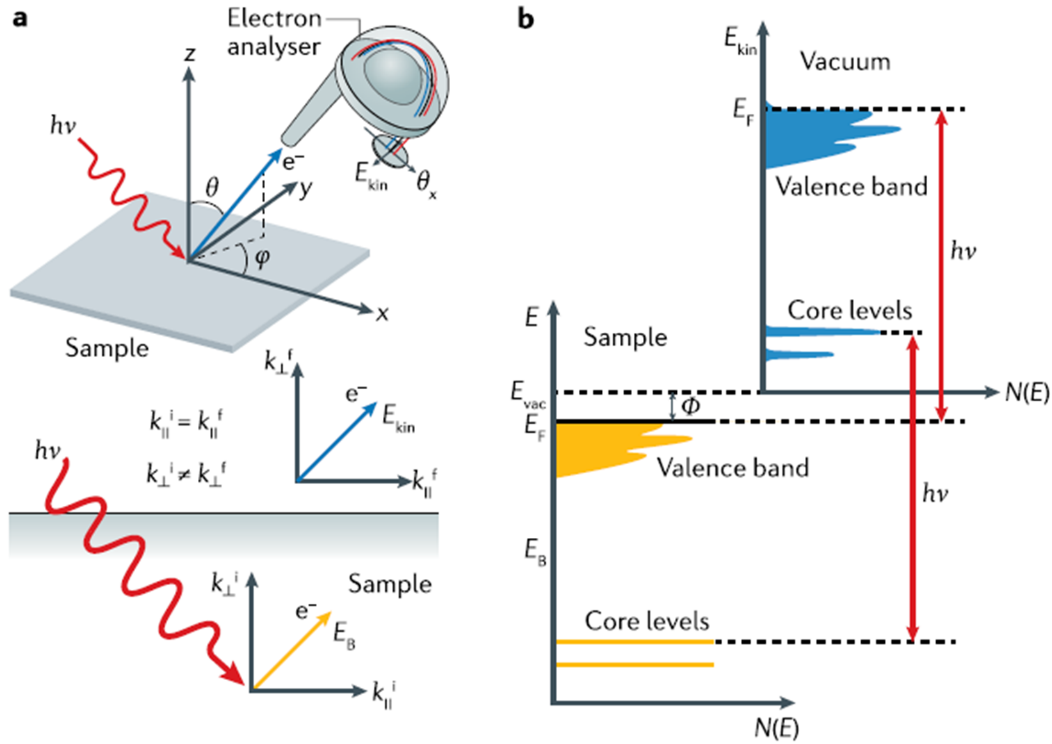

Figure 2.9: ***a*** *Geometry of Angle- Resolved Photoemission Spectroscopy (ARPES). The electron emission angles θ and ϕ are defined with respect to the electron analyser. In the bottom panel, the momentum conservation laws are reported. The parallel component $k_{||}$ is conserved, while the perpendicular one $k_{\perp}$ is not because of the translation symmetry breaking produced by the surface.* ***b*** *Conservation of energy during a photoemission process. $E_{kin} = h\nu - \Phi - E_B$, where E_B is the binding energy. N(E the density of states, $h\nu$ the photon energy and Φ the work function of the material. E_F, E_{vac} are the Fermi and vacuum levels [147]. The intensity spectrum of the photoemitted electrons can be therefore mapped to the electronic density of states inside the material.*

The photoemission process will be described in Sec. 2.2.1, then ARPES mapping of the bands structure will be explained in Sec. 2.2.2. Lastly, Sec. 2.2.3 will be dedicated to spin detectors and SARPES.

2.2.1 Photoemission of electrons

The physical mechanism at the basis of ARPES measurements is the photoelectric effect, discovered by Hertz in 1887 and explained in 1905 by Einstein in terms of absorption of photons by electrons in the solid. Photoemission process can be treated as a sequence of three independent steps (three-steps model):

- Electron optical excitation;
- Propagation to the surface;
- Emission in vacuum.

The subdivision simplifies the description of the process, although in principle the problem should be treated within a single step. The photoelectron intensity can be formulated as a product of three independent probabilities, one per each step, which will be derived in the following.

Photoexcitation

For non-interacting electrons system, the probability that a single electron is promoted from an initial state ψ_i with energy E_{i} to a final state ψ_f with energy E_{f}, by interaction with an electromagnetic

wave is described by the Fermi Golden rule. For electrons in a periodic crystal, the wave-functions are Bloch states dependent on the wave-vector **k**. The transition probability per unit time (W_{if}) takes the form:

$$W_{if} = |M_{if}|^2 \delta(E_f(\boldsymbol{k}_f) - E_i(\boldsymbol{k}_i) - h\nu) \tag{2.14}$$

Where the δ function establishes the conservation of the total energy: $E_{\text{f}}= h\nu- E_{\text{i}}$. In the following we will consider $E_{\text{i}}= E_{\text{B}}$ with E_{B} the binding energy of the electron. Therefore, the photoemitted electrons reproduce the image of the energy distribution in the sample, shifted by the photon energy (Fig. 2.9**b**). In Eq. 2.14, $|M_{if}|$ is the matrix element of the Hamiltonian (*H'*) describing the interaction between the electron and the photon:

$$|M_{if}| = \langle \psi_i(\boldsymbol{k}_i) | H' | \psi_f(\boldsymbol{k}_f) \rangle \tag{2.15}$$

The interaction Hamiltonian can be expressed as the scalar product between the electromagnetic vector potential $\boldsymbol{A}$ and the electronic momentum operator, according to the dipole approximation:

$$H' \sim \frac{e}{m} \boldsymbol{A} \cdot \boldsymbol{p} \tag{2.16}$$

It results that the matrix element depends on the polarization of the photon (through $\boldsymbol{A}$) as well as the symmetry of the initial and final states, which can be related to the orbital character of the Bloch states.

In Eq. 2.14 the momentum of the photon is neglected with respect to those of electrons in the valence band. The latter is then conserved in the crystal up to a vector of the reciprocal lattice (**G**), as consequence of the periodic potential of the solid. It follows that $\boldsymbol{k}_i = \boldsymbol{k}_f \pm \mathbf{G}$. The transition is vertical, namely $\boldsymbol{k}_i = \boldsymbol{k}_f = \boldsymbol{k}$.

This approximation is valid for ARPES, in which $h\nu$ is chosen in the VUV regime (6 eV - 124 eV) up to the soft-X rays (124 eV - 5 keV).

The integration of the transition probability over the bands structure of the system yields to the expression of the internal photocurrent:

$$I(E_{\text{i}}, \nu, \boldsymbol{k}) = \sum_{i,f} |M_{if}|^2 \delta(E_f(\boldsymbol{k}) - E_i(\boldsymbol{k}) - h\nu) \tag{2.17}$$

Concerning spin information, the photon does not directly couple to the electron spin which is preserved during the optical transition.

Propagation

The photo-excited electrons travel as free particles. Several elastic and inelastic scattering mechanisms with other electrons, ions, phonons in the solids can reduce the intensity of the photocurrent ($I(E_{kin}, \nu, \boldsymbol{k})$). The average length between two subsequent inelastic scattering events is called inelastic mean free path, which is a function of the electron kinetic energy ($\lambda_{IMFP}(E_{kin})$). Most materials show the same $\lambda_{IMFP}(E_{kin})$ dependence, described by the "universal curve" [148] (Fig. 2.10). The general expression is:

$$\lambda_{IMFP}(E_{kin}) = \frac{A}{E_{kin}^2} + B\sqrt{E_{kin}} \tag{2.18}$$

Where *A* and *B* coefficients are different for elements, organic or inorganic compounds. For elemental samples, *A*= 143 and *B*= 0.054, if λ_{IMFP} is in nm and E_{kin} in eV. The decay of the photoelectron intensity is given by the exponential Lambert law. The transport probability factor *D* as function of the travel distance *x* reads:

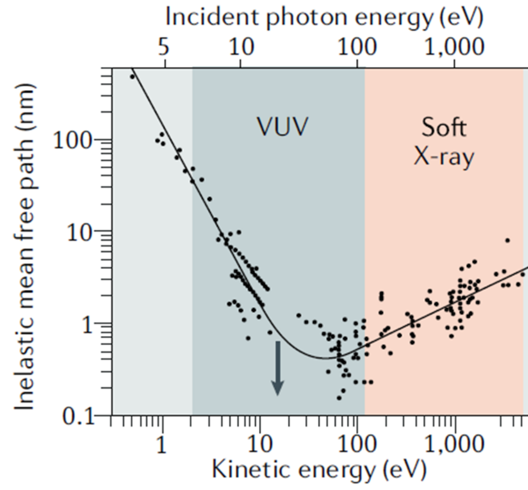

Figure 2.10: *Universal dependence of the electron inelastic mean free path on the kinetic energy (bottom axis). The top axis refers to the photon energy (the work function is assumed about 4 eV for all materials). VUV and soft-X ray regimes are indicated by blue and pink areas. Adapted from Ref. [147].*

$$D(E_{kin}, x) = e^{-\frac{x}{\lambda_{IMFP}(E_{kin})}} \tag{2.19}$$

Which multiplies the photocurrent. It follows that the outgoing photoemitted electrons are only those generated at the surface of the sample, within a very confined layer with thickness comparable to λ_{IMFP} (also named escape depth). Note that the escape depth of electrons is of the order of 1 nm for VUV and soft-X beams, much smaller than the excitation depth, as the penetration distance of the photon beam is of the order of 1 μm.

Escape into vacuum

For escaping into vacuum, the excited electron has to overcome the energy barrier of the surface, given by the work function. The work function is the energy separation between vacuum and Fermi levels, $\Phi = E_{vacuum} - E_F$. Thus, the kinetic energy has to be corrected as follows:

$$E_{kin} = h\nu - \Phi - E_B \tag{2.20}$$

The energy shift due to photoemission is shown in Fig. 2.9**b**. The surface barrier truncates the periodicity of the crystal potential along the direction normal to the surface (z). Hence, only the component of the wave-vector parallel to the surface is conserved in the Brillouin reduced scheme. For an electron emitted with in plane wave-vector component $\boldsymbol{k}_{||}$ forming an angle θ with respect to the normal to the surface, an in-plane angle ϕ (Fig. 2.9**a**), and a kinetic energy $E_{kin} = \hbar^2(k_{||} + k_{\perp})^2/2m$, one obtains:

$$\boldsymbol{k}_{||} = \sqrt{\frac{2mE_{kin}}{\hbar}^2}(\sin\theta\cos\phi\boldsymbol{k}_x + \sin\theta\sin\phi\boldsymbol{k}_x) \tag{2.21}$$

The normal wave-vector component $k_{\perp}$ instead is not conserved. For photon energies larger than 10 eV, the initial value $k_{\perp,i}$ can be related to that of the final free electron as follows:

$$k_{\perp,i} = \sqrt{\frac{2m}{\hbar^2}(E_{kin}\cos^2\theta + V_0)} \tag{2.22}$$

The quantity V_0 is the inner potential of the solid, representing the effect of the translation symmetry breaking along z. This constant can be determined from theoretical calculations or extracted

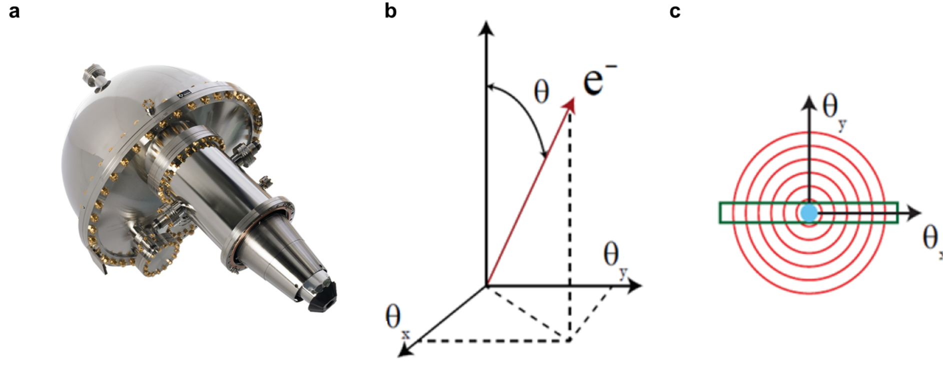

Figure 2.11: ***a*** *Picture of ScientaOmicron DA30 hemispherical analyser employed in the APE beamline of Elettra (Basovizza, Italy).* ***b*** *Reference angle coordinates for the photoemitted electron. θ is the angle between the electron and the normal to the surface, θ_x and θ_y are the two orthogonal in-plane projections.* ***c*** *Top view of the in plane projections; θ_x is the dispersion direction of the analyser.*

from the measurement [147]. In ARPES, the normal component is always larger than the probed in-plane one (small angle approximation). Under such condition, the dependence on θ is only at the first order and $k_{\perp,i}$ is determined by the photon energy:

$$k_{\perp,i} = \sqrt{\frac{2m}{\hbar^2}(h\nu - \Phi - E_B + V_0)} \tag{2.23}$$

It follows that the electron state in the solid with binding energy E_B and wave-vector $\boldsymbol{k}_i$ can be traced down by the kinetic energy E_{kin} and the emission angles (θ and ϕ) after photoemission. ARPES is the technique which exploits an energy and angle dispersion analyser to retrieve information on the electronic state in the solid.

The overall photocurrent is further reduced by the probability of transmission through the surface ($T(E_i, \boldsymbol{k}_{||})$):

$$I_{final} = I(E_{kin}, \nu, \boldsymbol{k}_{||})D(E_{kin}, x)T(E_{kin}, \boldsymbol{k}_{||}) \tag{2.24}$$

Note that the outgoing intensity is a function of the three measurable quantities photon energy, the kinetic energy and parallel wave-vector component.

2.2.2 Mapping bands structure by ARPES

In ARPES measurements, a source of VUV or soft X-rays is employed in order to probe valence band electronic states close to the Fermi level. As derived in Sec. 2.2.1, the dispersion of the energy bands in the wave-vector space can be detected by filtering the photoelectron intensity by the emission angle and the kinetic energy of the electrons with a suitable electron analyser. The kinetic energy reflects the binding energy in the solid, which is shifted by the photon energy and the work function. Concerning the wave-vector, $k_\perp$ is fixed by the the photon energy (Eq. 2.23), while $k_{||}$ is related to the photoemission angle. The output of a ARPES measurement is thus the dispersion of electronic states along $k_{||}$, around the point $k_\perp$. It is clear that by changing $h\nu$ and the angle between the surface and the electron analyser, bands dispersion can be mapped at different points of the reciprocal space. Information about the orbital character of the electronic bands can be also obtained by adopting photons with different polarizations, because the photoelectron intensity is modulated by the electric dipole matrix element (Eq. 2.15).

Experimental conditions

Experiments are usually performed exploiting synchrotron radiation in UHV.

The ARPES measurements discussed in Ch. 4 and Ch. 5 were performed at the Advanced Photoelectric Effect experiments (APE) beam-line of Elettra synchrotron (Basovizza, Italy).

A clean and ordered surface is crucial, being ARPES a surface sensitive technique (the escape depth of the electrons is of the order of 1 nm). The sample is usually kept at low temperatures by liquid Helium (77 K in our experiments), in order to minimize electrons scattering events in the sample and the Fermi broadening that reduce the *k*-resolution of the spectrum.

Measurement of a ARPES spectrum

The fundamental working principle of the electron analyzer is briefly described here, in order to understand how an ARPES spectrum is formed.

The APE beam-line is endowed with a high-resolution hemispherical analyser (Scienta Omicron DA30, Fig. 2.11**a**), that separates electrons according to their kinetic energy and the propagation direction. For a fixed value of the kinetic energy, the analyser simultaneously disperse electrons with different angle component along a fixed axis (θ_x, with k_x the corresponding wave-vector component), as shown in Fig. 2.11**b**-**c**. Internal deflectors can also be used in order to shift the dispersion axis to a certain value θ_y (with related k_y component). The angular acceptance of the analyzer is of 30° for both θ_x and θ_y directions. This value can be translated into the probed ranges for k_x and k_y respectively, by using Eq. 2.21 and Eq. 2.23.

An ARPES spectrum $I(E, k_x)$ is built by the acquisition of the photocurrent dispersion along θ_x by scanning the selected kinetic energy. The selection of the energy is operated by suitable electrostatic lenses placed in front of the analyser. Furthermore, the 3D data-set $I(E, k_x, k_y)$ can be obtained as a sequence of spectra $I(E, k_x)$ for different values of θ_y. Three dimensional maps provide a complete picture of the bands dispersion, which is relevant especially for high-symmetry points of the FBZ. The symmetry of the bands can be appreciated from sections at fixed binding energy (Constant Energy Maps, CEM).

2.2.3 Spin-resolved bands by SARPES

Spin and Angle-Resolved Photoemission Spectroscopy (SARPES) is a powerful tool used for mapping bands dispersion with spin resolution. The increasing number of SARPES studies in the last years enabled the recent discoveries of highly spin-polarized electronic bands in SOC systems and correlated materials (e.g. Rashba, topological insulators).

In this work we investigate the the interplay between ferroelectricity polarization and Rashba states spin chirality in GeTe, combining SARPES with PFM (Ch. 4).

Spin resolution is provided by feeding the photocurrent from the exit of the electron analyser to suitable spin detectors, filtering the intensity by the spin polarization on a given axis. The 3D reconstruction of electrons spin is obtained by combining spin detectors with orthogonal axes.

Mott spin detector is a widely employed solution [149], which however reduces the intensity of the photocurrent by a factor 10^4 [150]. Mott scattering is extremely inefficient, as it results from SOC of electrons with a target magnetized material. Often the problem is overcome by increasing the bandpass energy of the beam-line above 100 meV to increase the number of counts consequently.

In the the last decade, a Very Low Energy Electron Diffraction (VLEED) type of spin detector has been designed and developed, with an improvement of SARPES efficiency by 10^2 [151–153]. The APE beamline is equipped with a Very Efficient Spin Polarization Analysis (VESPA) 3D spin detector [154]. VESPA exploits two identical VLEED polarimeters with orthogonal axes (Fig. 2.12). The electron beam is split by two apertures connected to the VLEED reflectometers by proper electrostatic lenses. Each polarimeter is made of a scattering target of Fe(001)-p(1×1)O. The magnetization fixes the quantization axis of the measurement of the spin state. The spin polarized beam reflected by the polarimeter is detected by a Faraday cup collector. By properly setting

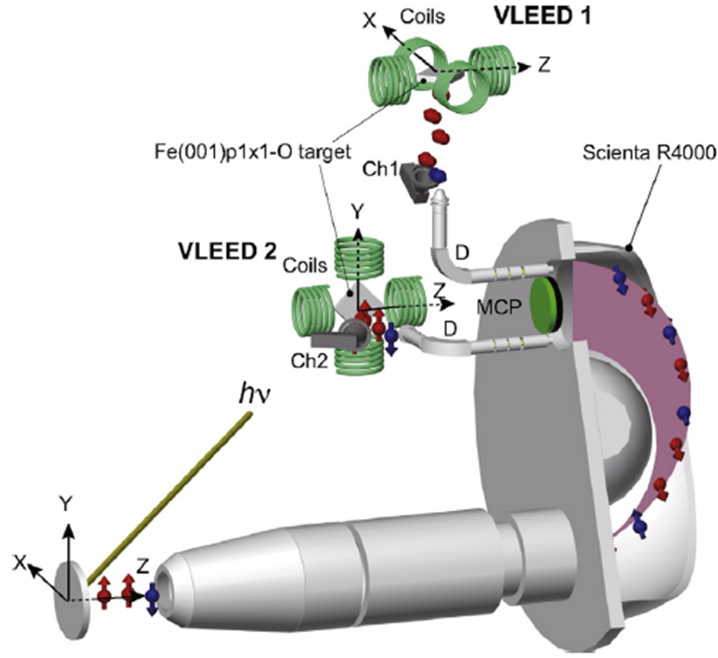

Figure 2.12: *Picture of the angle and energy dispersion analyser, completed by a 3D VLEED spin detector. Adapted from Ref. [155].*

the magnetization of the targets by electromagnetic coils, all the three components of the spin polarization can be measured. The electrons reflected are detected by a channeltron (Ch1 and Ch2 in Fig. 2.12).

The working principle of a VLEED polarimeter is based on the asymmetric scattering of spin-up and spin-down collimated low energy electron beam ($\sim$10 eV) from a magnetic target, made of a thick epitaxial Fe(001) film (> 3000 Å) passivated by a single ordered monolayer of oxygen (Fig. 2.13). The asymmetry is caused by the exchange splitting of the bands of the ferromagnet and the resulting unbalance of the spin populations at the Fermi level. Consequently, electrons polarized as majority (minority) carriers will be preferentially reflected (absorbed) from the target.

The efficiency of the spin detector is also called analysing power or Sherman function (S) and it is proportional to the exchange scattering asymmetry (A_{ex}). The latter can be determined experimentally as follows. The intensity of a reference electron beam with polarization $\mathbf{P}_0$ is measured after the reflection from the VLEED polarimeter. The intensity I_{P} is collected with $\mathbf{M}$ parallel to $\mathbf{P}_0$, I_{AP} when the magnetization is reversed. The analysing power is hence proportional to the spin asymmetry, which takes the form:

$$S \sim A_{ex} = \frac{1}{|\mathbf{P}_0|} \frac{I_P - I_{AP}}{I_P + I_{AP}} \tag{2.25}$$

The value of S is used in order to extract the spin polarization of an unknown electron beam with polarization $\mathbf{P}$. The component P_{i} of the polarization is obtained setting the magnetization along the i-axis. It can be computed from the detector intensities corresponding to positive and negative magnetization (I_+ and I_-):

$$P_i = \frac{1}{S} \frac{I_+ - I_-}{I_+ + I_-} \tag{2.26}$$

The Sherman function of the VLEED system available at APE has been determined to be of the order of 0.3 [154]. An example of measurement of spin polarization of a Rashba 2DEG formed the Au(111) surface can be found in Ref. [156].

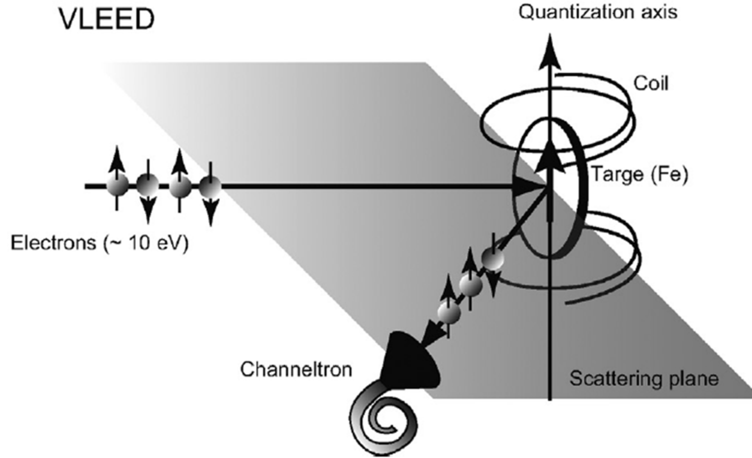

Figure 2.13: *Schematics of the spin dependent scattering process by a VLEED target. The reflection probability is spin dependent. The scattering plane (grey area) is perpendicular to the magnetization and the surface of the target. Two coils are employed in order to reverse the magnetization of the target. Adapted from Ref. [155].*

The fundamental principles of (S)ARPES introduced in this sections will be exploited in the discussion of the experimental work in Ch. 4 and Ch. 5.

2.3 Spin-to-charge conversion by Spin Pumping

The excitation of a ferromagnetic material at its ferromagnetic resonance can be exploited as a source of pure spin current, pumped into an adjacent non-magnetic material (NM). Thus, spin-to-charge conversion in the NM material related to ISHE (Sec. 1.3.2) or IREE (Sec. 1.3.3) can be investigated from the generated charge current. Spin pumping by ferromagnetic resonance has been performed in this work on Fe/GeTe bilayers in order to probe the spin-to-charge conversion efficiency and its modulation with ferroelectricity. The results are discussed in Ch. 4.

The present section is dedicated to the fundamental concepts of FerroMagnetic Resonance (FMR) and spin pumping. For both techniques, the setup employed in the present work is shown and theoretical explanation of the involved physical effects is proposed. As discussed in Sec. 2.3.1, FMR is a powerful magnetometry tool for ferromagnetic films providing both static and dynamic quantities. FMR can be also employed as source of pure spin currents. The origin of spin injection and the evaluation of spin-to-charge conversion efficiency from spin pumping measurement are discussed in Sec. 2.3.2.

2.3.1 Ferromagnetic resonance

Equilibrium magnetization

The orientation of the equilibrium magnetization of a ferromagnetic body with an external applied magnetic field can be calculated by variational method based on Brown equation [157]. Within this approach, equilibrium is derived by minimizing the Landau free energy (G_L), which is a functional of the magnetization vector ($\mathbf{M} = M_s\mathbf{m}$) and the external applied magnetic field $\mathbf{H}_0$. G_L accounts for the Zeeman interaction with an external field, the exchange, anisotropy and the demagnetizing energy terms.

G_L integrated in the volume *V* results:

$$G_L(\mathbf{M}, \mathbf{H}_0) = \int_V \Big[-\mu_0 M_s \mathbf{m} \cdot \mathbf{H}_0 + A(\nabla \mathbf{m})^2 + f_{an}(\mathbf{m}, \mathbf{u}\,(\mathbf{r})) - \frac{\mu_0}{2} \cdot M_s \mathbf{m} \cdot \mathbf{H}_D \Big] \, dV \tag{2.27}$$

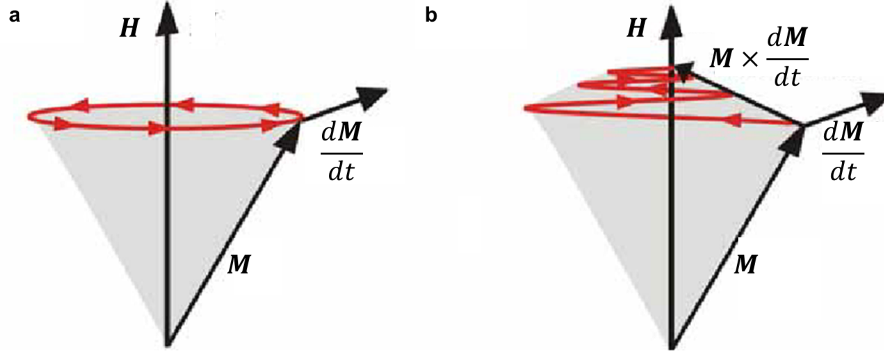

Figure 2.14: *(a) Magnetization precession around magnetic field (H) caused by the torque $d\boldsymbol{M}/dt$ (Eq. 2.30).* ***b*** *Dynamics of the magnetization in presence of a damping torque $\sim \boldsymbol{M} \times \frac{d\boldsymbol{M}}{dt}$ (Eq. 2.31). Adapted from Ref. [158].*

The minimization brings to the Brown problem:

$$\mathbf{m} \times \mathbf{H}_{eff} = 0 \tag{2.28a}$$

$$\left.\frac{\partial \mathbf{m}}{\partial \mathbf{n}}\right|_{\Omega} = 0 \tag{2.28b}$$

where $\mathbf{H}_{eff}$ is the effective magnetic field, accounting for the external magnetic field $\mathbf{H}_0$, the demagnetizing field $\mathbf{H}_D$ and the anisotropy field $\mathbf{H}_{an}$ defined above:

$$\mathbf{H}_{eff} = \mathbf{H}_0 + \mathbf{H}_{an} + \mathbf{H}_D \tag{2.29}$$

The exchange contribution is in general neglected for uniformly magnetized media. At equilibrium $\mathbf{M}$ is aligned to the effective field $\mathbf{H}_{eff}$.

Landau-Lifshitz-Gilbert equation

When the system is brought out of equilibrium, the magnetic torque $\boldsymbol{\tau} = \mathbf{M} \times \mathbf{H}_{eff}$ produces a time variation of the total angular momentum of the system ($\mathbf{J}$), opposite to $\mathbf{M}$ and scaled by the gyromagnetic ratio ($\gamma = g\mu_B/\hbar$). The dynamic equation reads:

$$\frac{\partial \mathbf{M}}{\partial t} = -\gamma \mathbf{M} \times \mathbf{H}_{eff} \tag{2.30}$$

The magnetization describes a perpetual precession around the field axis (Fig. 2.14**a**). In a real systems however, several processes as electron-phonon scattering, electron-magnon scattering and magnon-phonon scattering cause a loss of angular momentum. Losses quench the amplitude of the precession cone and bring the system to equilibrium (i.e. $\mathbf{M}$ parallel to $\mathbf{H}_{\text{eff}}$). A phenomenological damping torque has been added by Gilbert in order to describe losses. Hence, the dynamics is the described by the Landau-Lifshitz-Gilbert equation (LLG):

$$\frac{\partial \mathbf{M}}{\partial t} = -\gamma \mathbf{M} \times \mathbf{H}_{eff} + \frac{\alpha}{M_s} \mathbf{M} \times \frac{\partial \mathbf{M}}{\partial t} \tag{2.31}$$

Where α is a dimensionless damping constant (Gilbert damping). The action of the damping torque on $\mathbf{M}$ is clarified in Fig. 2.14**b**. The precession of $\mathbf{M}$ extinguishes within a time scale of $(1/\alpha\gamma H_{eff})$.

In other words, a magnetized medium is a damped harmonic oscillator characterized by its own resonance frequency. An external magnetic field oscillating at the resonance frequency would strongly amplify the precessional motion (ferromagnetic resonance condition).

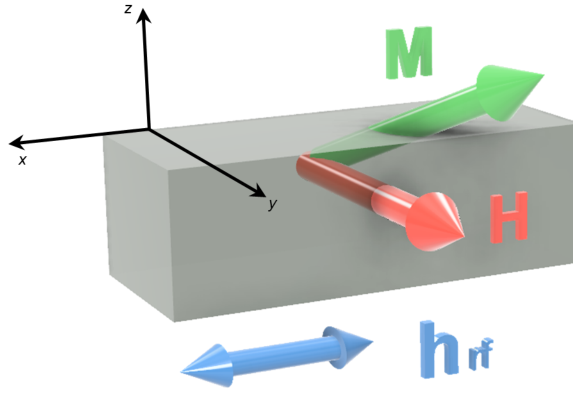

Figure 2.15: *Geometry of a ferromagnetic resonance experiment. The radio-frequency magnetic field* $\boldsymbol{h}_{rf}$ *makes the magnetization vector* $\boldsymbol{M}$ *precess around the equilibrium direction, set by the magnetic field* $\boldsymbol{H}$*. The amplitude of the excitation is maximum when* $\boldsymbol{H}$ *and* $\boldsymbol{h}_{rf}$ *are orthogonal.*

Ferromagnetic resonance

FMR was first observed by J. H. E. Griffhits in 1946 [159]. The resonance conditions can be derived by solving the LLG equation (Eq. 2.31) and determine the maximum amplitude of oscillation under given experimental conditions. Typically, magnetization resonance is achieved in presence of an external static field that sets the equilibrium state for $\mathbf{M}$ and a small radiofrequency field ($\mathbf{h}_{\mathrm{rf}}$) acting as a periodical excitation (Fig. 2.15).

In the following, the resonance condition is derived for a system in absence of damping, while the general solution will not be derived but directly presented.

The total magnetization ($\mathbf{M}_{tot}$) and the total field ($\mathbf{H}_{tot}$) can be expressed as the sum of an equilibrium static component and a time dependent oscillating perturbation:

$$\begin{cases} \mathbf{H}_{tot} = \mathbf{H}_0 + \mathbf{h}(\mathbf{r}, t) \\ \mathbf{M}_{tot} = \mathbf{M}_0 + \mathbf{m}(\mathbf{r}, t) \end{cases} \tag{2.32}$$

Where $|\mathbf{h}(\mathbf{r}, t)| << |\mathbf{H}_0|$ and $|\mathbf{m}(\mathbf{r}, t)| << |\mathbf{M}_0|$. By assuming $\mathbf{H}_{eff} = H_{eff}\mathbf{u}_y$ and $\mathbf{M}_0 = M_0\mathbf{u}_y$ and substituting quantities in Eq. 2.32 into the LLG equation (Eq. 2.31) with the approximation of small precession cone angle, the dynamical equation results:

$$\frac{\partial \mathbf{m}(\mathbf{r}, t)}{\partial t} = -\gamma M_0 \mathbf{u}_y \times \mathbf{h}(\mathbf{r}, t) + \mathbf{m}(\mathbf{r}, t) \times H_0 \mathbf{u}_y \tag{2.33}$$

The problem can be simplified assuming a periodic perturbation with angular frequency ω, $\mathbf{h}e^{-j\omega t}$, that will induce an oscillation of the magnetization the same frequency ($\mathbf{m}e^{-j\omega t}$). With this assumption, Eq. 2.33 can be linearized

$$j\omega \mathbf{m} = -\gamma \mathbf{u}_y \times (M_0 \mathbf{h} - H_0 \mathbf{m}) \tag{2.34}$$

and projected along the x, y, z directions of Fig. 2.15.

$$\begin{cases} j\omega m_x = -\gamma(M_0 h_z - H_0 m_z) \\ j\omega m_y = 0 \\ j\omega m_z = -\gamma(-M_0 h_x + H_0 m_x) \end{cases} \tag{2.35}$$

If Eq. 2.35 is inverted, the amplitude of the magnetization oscillation is expressed as function of the excitation through the Polder susceptibility tensor: $\mathbf{m} = \underline{\underline{\chi}}\mathbf{h}$. The Polder susceptibility is a complex quantity (with real and imaginary parts χ' and χ'', respectively):

$$\underline{\underline{\chi}} = \begin{pmatrix} \chi' & j\chi'' \\ -j\chi'' & \chi' \end{pmatrix} \tag{2.36}$$

With

$$\chi' = \frac{M_0 H_0 \gamma^2}{\gamma^2 H_0^2 - \omega^2} \tag{2.37a}$$

$$\chi'' = \frac{\omega M_0 H_0 \gamma}{\gamma^2 H_0^2 - \omega^2} \tag{2.37b}$$

The Polder susceptibility defines the precession cone angle and the two components play two different roles. The real part mainly describes the dephasing (ϕ_0) of $\mathbf{m}$ with respect to $\mathbf{h}_{\mathrm{rf}}$, which jumps by 180° at FMR [160]. The imaginary part instead is related to the absorption of the *rf* power by the FM system:

$$P_{abs} = \frac{1}{2}\omega h^2 \chi'' \tag{2.38}$$

Therefore, by measuring the power absorbed by the system we can probe χ''. It follows that the power absorption is maximum at resonance, when the amplitude of the oscillating magnetization is maximized. The resonance frequency ω_{res} maximizing the component χ'' in Eq. 2.37 results:

$$\omega_{res} = -\gamma H_0 = \frac{g\mu_B}{\hbar} H_0 \tag{2.39}$$

Adding the presence of demagnetizing energy, the static field acting on $\mathbf{M}$ is $\mathbf{H}_{eff}$ (Eq. 2.29). As discussed above, the demagnetizing field of a thin FM layer is perpendicular to the film plane $\mathbf{H}_{\mathrm{D}} = -M\mathbf{u}_{\mathrm{z}}$. This field will induce a change of m_{x} in Eq. 2.35 (and not of m_{z} which is parallel to $\mathbf{H}_{\mathrm{D}}$). The resonance condition in this case is given by the Kittel formula [161]:

$$\omega_{res} = \frac{g_{eff}\mu_B}{\hbar} \sqrt{(\mu_0 M_{eff} + H_0 + H_{an})(H_0 + H_{an})} \tag{2.40}$$

Where g_{eff} is the effective Landè factor, M_{eff} the effective magnetization accounting for possible surface anisotropy.

The Kittel formula is the fundamental equation of FMR. The resonance condition can be met by fixing the excitation frequency ω and tuning H_0 to the value H_{res} (the resonance field), that satisfies the equality 2.40. A FMR spectrum is acquired by sweeping the external field H_0 around resonance.

If now we consider the effect of *damping*, real and imaginary components of the Polder susceptibility do not diverge at resonance. The real part is a purely antisymmetric function of H_{eff}, while the imaginary part is a symmetric Lorentzian function centered at H_{res}:

$$\chi'' = \frac{\chi_{max}\Delta H^2}{\Delta H^2 + (H_{eff} - H_{res})^2} \tag{2.41}$$

With a full width at half maximum ΔH linked to the damping coefficient α:

$$\Delta H = \frac{\alpha}{\gamma\mu_0}\omega \tag{2.42}$$

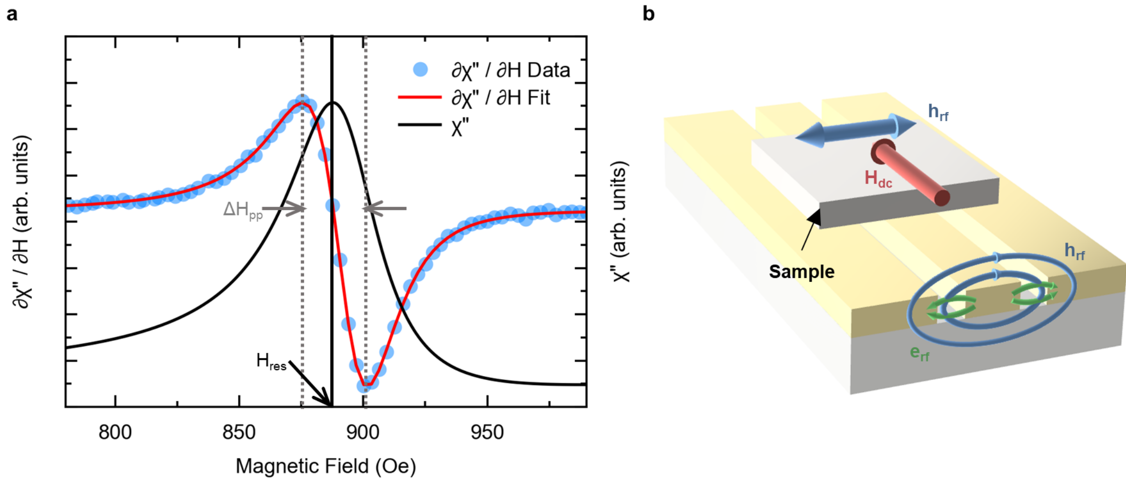

Figure 2.16: *Example of FMR spectrum of $Co_{40}Fe_{40}B_{20}$(15 nm) thin film grown by Magnetron sputtering on Si substrate. The rf excitation frequency was 10 GHz. The excitation frequency is constant and the resonance condition is achieved by sweeping the external magnetic field. Light blue points represent the measured absorbed power, the red line the fitting curve with the model in Eq. 2.45. As result of the lock-in modulation, the absorbed power is proportional to the derivative of the imaginary part of the magnetic susceptibility ($\partial\chi''/\partial H$). The integration of the spectrum retrieves the Lorentzian line-shape of χ'', with a resonance field $H_{res} = 893$ Oe and a peak line-width $\Delta H = 22$ Oe.* ***b*** *Schematics of the micro-stripline used for the measurement of FMR and its characterization over a broad band of frequencies. The magnetic rf field* $\mathbf{h}_{rf}$ *lays in the sample plane and perpendicular to the wave-guide axis. Its intensity is strongly non-homogeneous in space as shown by the field lines. The electric counterpart* $\mathbf{e}_{rf}$ *is much less intense and it is created between the wires. The dc magnetic field is applied in-plane along the wave-guide axis.*

This is the second characteristic equation of FMR. For a inhomogeneous FM, such as a polycrystalline material, one has to take into account an additional contribution ΔH_0, that arises from the local variation of the amplitude and orientation of saturation magnetization (called 'inhomogeneous broadening'):

$$\Delta H = \frac{\alpha\omega}{\gamma} + \Delta H_0 \tag{2.43}$$

Inhomogeneous broadening is the result of collective response of different grains with slightly different magnetization and related resonance fields.

As an outgrowth, the FMR constitutive equations (Eq. 2.40 and 2.43) of FMR provide information about static and dynamic properties of the FM, as anisotropy field, saturation magnetization and Gilbert damping. Understanding the magnetic behaviour of a FM film is also necessary for the quantification of spin-to-charge conversion by spin pumping (Sec. 2.3).

Measurement of a FMR spectrum

The measurement of a FMR spectrum requires a lock-in detection, in order to increase the signal-to-noise ratio. The small *ac* field is added to $\mathbf{H}_0$, with a frequency $\omega_0 << \omega_{ref}$ (typically 1 kHz). If $\mathbf{H}_{0,ac} = \mathbf{H}_0 + h_{ac}e^{j\omega_0 t}$, the susceptibility is corrected by the first order Taylor expansion. For example, χ'' results:

$$\chi''(\mathbf{H}_0 + h_{ac}e^{j\omega_0 t}) = \chi''(\mathbf{H}_0) + j\omega_0 h_{ac}e^{j\omega_0}\frac{\partial\chi''}{\partial H} \tag{2.44}$$

The absorbed power is hence proportional to the derivative of χ'' with respect to the field ('differential absorption'), as clear from Eq. 2.38 and Eq. 2.44. The typical setup is described in Sec. .

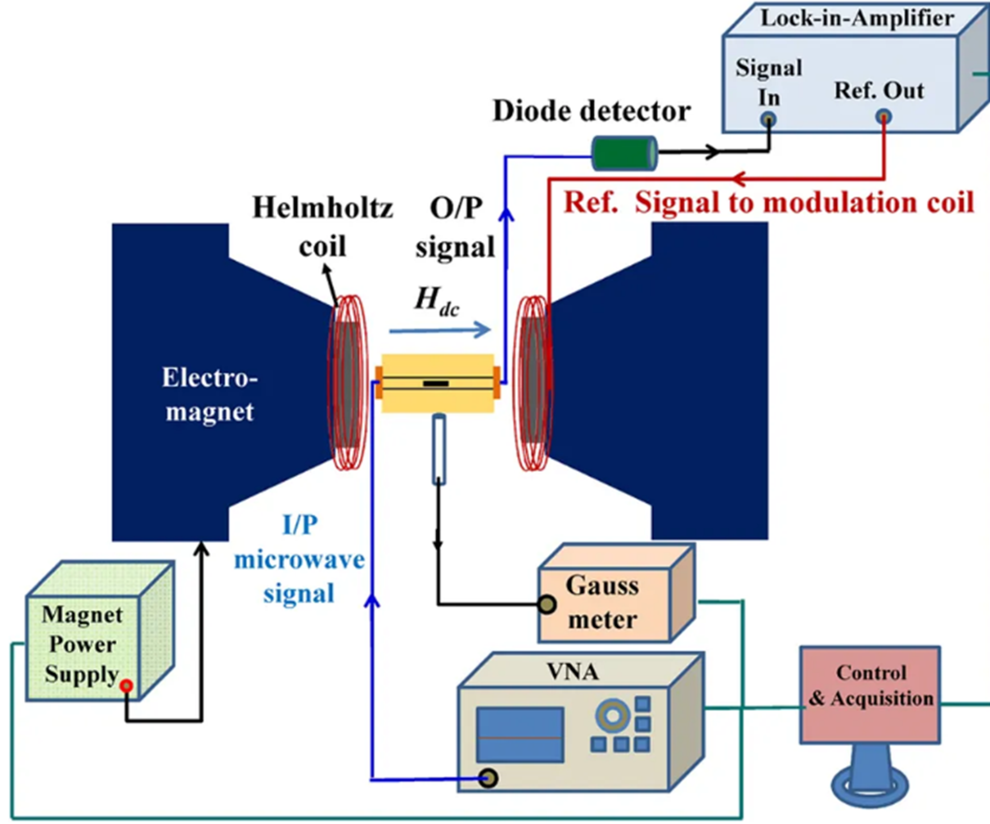

Figure 2.17: *Schematics of a common braodband FMR setup based on VNA-microstriplines. Adapted from Ref. [162].*

The differential absorption spectrum can be fit with analytical models, in order to estimate the material's parameters. The formula employed in this work is based on the intrinsic FMR line-shape (Eq. 2.41) corrected by experimental non-idealities. In the complex notation

$$\frac{\partial \chi''}{\partial H} = \Im\left(A \frac{\frac{\Delta H}{4} e^{-j\phi}}{(H_0 - H_{res} + j\Delta H)^2} \right) + B \tag{2.45}$$

A is the amplitude of the absorbed power, while B and ϕ are experimental offset introduced by the lock-in modulation and experimental asymmetry of the line-shape (2 rad in our apparatus), respectively.

An example of measurement and fit of the FMR spectrum of a $Co_{40}Fe_{40}B_{20}$ thin film is shown in Fig. 2.16. As expected, the line-shape of the differential absorption is the derivative of a Lorentzian, with a zero at the resonance field H_{res}. The distance between the positive and negative peaks (peak-to-peak line-width, ΔH_{pp}) is related to the non-derivated Lorentzian by: $\Delta H_{pp} = (2/\sqrt{3})\Delta H$.

Broad Band detection of Ferromagnetic Resonance

Collecting FMR spectra for different values of ω and the trends of H_{res} and ΔH allows for the determination the magnetic properties of the FM. This kind of measurement is called 'broadband FMR'. More precisely, the following quantities can be extracted:

- H_{res} versus $\omega = 2\pi f$ is fit by the Kittel formula (Eq. 2.40). The uniaxial anisotropy field, the effective Landè factor and the effective saturation magnetization are the free parameters.

- Gilbert damping and inhomogeneous broadening are estimated by fitting ΔH_{pp} versus f with Eq. 2.43.

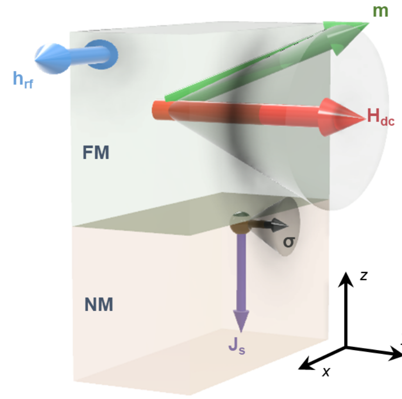

Figure 2.18: *Illustration of the spin injection from a FM (top layer), into an adjacent NM (bottom layer) by FMR. Both magnetization and spin vectors ($\boldsymbol{m}$ and $\boldsymbol{\sigma}$) describe a precession cone angle around $\boldsymbol{H}_{dc}$ at rf frequency.*
.

Broadband FMR is therefore a powerful magnetometry tool that provides a complete picture of the behaviour of a FM.

Typical setups employed for broadband excitation make use of microstriplines [163], combined with a broadband microwave source. A microstripline consists of a signal wire separated by a dielectric material from a grounded metallic plate (Fig. 2.16**b**). It can convey microwave signals in a wide range of frequencies. A power source injects the microwave intensity in the stripline by means of a Vector Network analyser (VNA). The power transmitted to the end of the line is detected by a broadband diode. When a FM sample is placed on top of the microstripline, a magnetic field $\mathbf{h}_{rf}$ is generated by an electric field $\mathbf{e}_{rf}$ mostly confined between the wire and the ground plate, as depicted in Fig. 2.16**b**. $\mathbf{h}_{rf}$ is preferentially oriented in the film plane and orthogonal to the stripline axis. The *dc* magnetic field $\mathbf{H}_0$ is applied by two coils along the stripline axis. The two orthogonal fields induce magnetization precession. As discussed above, the saturating field is modulated at a low frequency (1 kHz) and the lock-in detection provides the differential absorption spectrum. The complete setup is shown in Fig. 2.17.

2.3.2 Spin transfer via spin pumping at ferromagnetic resonance

Spin current injection

Tserkovnyak *et al.* [164] demonstrated that the magnetization of a thin FM film with thickness t_{F} excited at its FMR can inject a spin current into an adjacent non-magnetic (NM) conducting layer (thickness t_{NM}). Spin pumping is the reciprocal effect of the spin torque.

In the case of a precessing magnetization, an extra term ($\Delta\alpha^{SP}$) adds to the intrinsic Gilbert damping (α_0):

$$\alpha = \alpha_0 + \Delta\alpha^{SP} \tag{2.46}$$

Thus, the LLG equation becomes:

$$\frac{\partial \mathbf{M}}{\partial t} = -\gamma \mathbf{M} \times \mathbf{H}_{eff} + \frac{\alpha_0}{M_s}\mathbf{M} \times \frac{\partial M}{\partial t} + \frac{\Delta\alpha^{SP}}{M_s}\mathbf{M} \times \frac{\partial M}{\partial t} \tag{2.47}$$

The extra-damping $\Delta\alpha^{SP}$ describes the additional relaxation channel of the magnetization, due to spin injection into the NM. The efficiency of the injection is related to $\Delta\alpha^{SP}$. The latter can be estimated by subtracting to the total damping constant the intrinsic damping coefficient of the ferromagnet in absence of the NM (α_{in}).

The instantaneous $\boldsymbol{\sigma}$-polarized spin current generated by a precessing FM and injected into the adjacent NM layer is derived in Ref. [164, 165] and it depends on the precession motion of the magnetization [166]:

$$j^0_{spin}\boldsymbol{\sigma}(t) = \frac{\hbar}{8\pi}\Re\{2g^{\uparrow\downarrow}\}\mathbf{m} \times \frac{\partial \mathbf{m}}{\partial t} \tag{2.48}$$

This means that the injected spin current is maximum at FMR, when the vector product $\mathbf{m} \times \frac{\partial \mathbf{m}}{\partial t}$ describing the amplitude of the precession cone is maximum (Fig. 2.18).

The polarization $\boldsymbol{\sigma}$ in Eq. 2.48 is always perpendicular to both $\mathbf{m}$ and its time derivative, so it describes a precession cone with a constant projection along $\mathbf{H}_0$ (Fig. 2.18). Then, it is clear that a FM system oscillating at its FMR generates a *dc* spin current polarized along the *dc* field direction and propagating normal to the interface.

The quantity $g^{\uparrow\downarrow}$ in Eq. 2.48 is the interface spin-mixing conductance per unit area, that depends on the reflection coefficients of spin up and spin down electrons at the interface [164]. $g^{\uparrow\downarrow}$ encodes the efficiency of the spin injection, thus it depends on the extra-damping $\Delta\alpha^{SP}$ [103]. With the assumption that the NM is a good spin-sink and there is not back-reflection in the FM layer (i.e. the thickness t_{NM} is much larger than the spin diffusion length λ_s), the relation between $g^{\uparrow\downarrow}$ and $\Delta\alpha^{SP}$ is linear (Eq. 2.49) [167]:

$$g^{\uparrow\downarrow} = \frac{4\pi M_{eff} t_F}{g_L \mu_B}\Delta\alpha^{SP} \tag{2.49}$$

The *dc* spin current is obtained integrating $j^0_{spin}\boldsymbol{\sigma}(t)$ in the period of the *rf* excitation.

The calculation performed by K. Ando *et al.* [168] brings to the following expression of j^0_{spin}, which depends on the *rf* amplitude and frequency and on the magnetic response of the FM:

$$j^0_{spin} = \frac{g^{\uparrow\downarrow}\gamma^2\hbar h^2_{rf}}{8\pi\alpha^2}\left[\frac{4\pi M_{s,eff}\gamma + \sqrt{(4\pi M_{s,eff}\gamma)^2 + 4\omega^2}}{(4\pi M_{s,eff}\gamma)^2 + 4\omega^2}\right] \tag{2.50}$$

The estimation of the injected spin current is crucial for the extraction of the spin-to-charge conversion efficiency.

Spin pumping in a resonant cavity

FMR can also be achieved in a microwave cavity (or *rf* cavity), a hollow resonator that can host an electromagnetic radiation oscillating at the cavity resonance frequency in the microwave spectral region. The *rf* magnetic field is strongly amplified by the quality factor (*Q*) and its intensity is orders of magnitude larger than the one obtained with striplines. Thus, not only the signal-to-noise ratio of FMR spectrum is strongly improved, but more importantly the higher power absorption by the FM yields to a more efficient spin injection efficiency. Differently from striplines, the amplitude of the *rf* magnetic field can be precisely obtained from the injected power *P* as follows:

$$h_{rf} = 0.2\sqrt{\frac{PQ}{500}} \tag{2.51}$$

The denominator is specific for our MS5 loop gap cavity and it depends on the distribution of the field inside the cavity. A precise measurement of h_{rf} is of fundamental importance for the estimation of the spin injected current and hence the determination of the spin Hall angle of the material (Eq. 2.50).

Another advantage comes from the fact that $\mathbf{e}_{rf}$ and $\mathbf{h}_{rf}$ take well defined directions within the volume occupied by the sample. The sample is placed in the center of the cavity, where the amplitude of $\mathbf{h}_{rf}$ is maximized and the $\mathbf{e}_{rf}$ is zero. As it will be clear afterwards, a vanishing

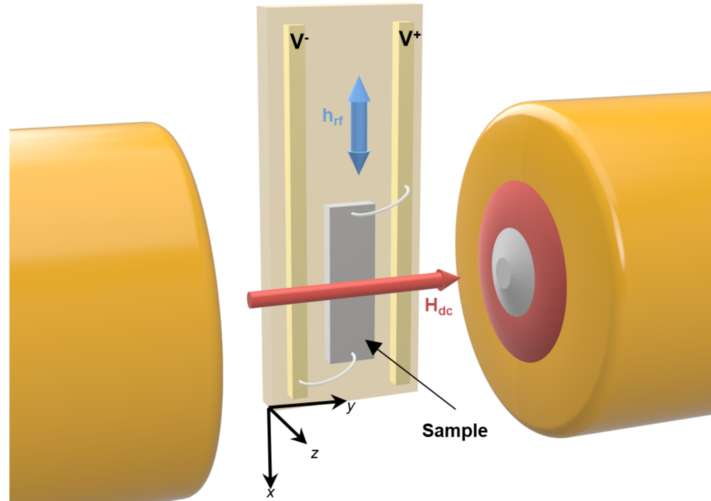

Figure 2.19: *Illustration of the setup of a spin pumping experiment. The static magnetic field $\mathbf{H}_{dc}$ is generated between two electromagnets. The sample is glued on a printed circuit board between two Cu stripes, connected to the positive and negative electrodes of a voltmeter. The top and bottom edges of the sample are wired to the V^- and V^+, respectively. The spin current pumped by FMR is polarized along y parallel to $\mathbf{H}_{dc}$ and propagates along z; the charge current from spin conversion flows along x, the longitudinal axis of the sample and develops a dc voltage. Having a small sample width reduces the noise of the voltage measured, whereas a large value of the length increases the signal level over the noise.*

electric field in the sample is of crucial importance for spin pumping in order to avoid spurious contributions to the measurement of spin-to-charge conversion.

For these arguments, spin pumping experiments presented in this work were a resonant *rf* cavity. The setup employed consists of a Brucker EPR 300E cavity, a S5 loop gap cavity with resonance frequency around 9.75 GHz. The cavity is placed between the coils of an electromagnet which serves for the application of the saturating magnetic field H_0. The sample is placed in the cavity as described in Fig. 2.19. The radiofrequency source is a Gunn diode which injects a microwave into a circulator. The circulator directs the intensity to the cavity: part of the injected power is absorbed by the cavity, the rest reaches the detector. The FMR spectrum is measured in a way very similar to the case of microstriplines. A *dc* saturating magnetic field is swept in order to meet the resonance condition, at which the power absorbed by the cavity is maximized. The field is modulated through a pair of Helmholtz coils and a lock-in detection yields to the differential FMR spectrum, that is modelled using Eq. 2.45.

The samples employed in this work are shaped into elongated stripes of 0.4×0.8 mm^2 area and they are glued on a PCB with two copper lines for the electric detection of spin-to-charge conversion. The magnetic field $\mathbf{H}_0$ is applied in plane and transverse to the sample, the field $\mathbf{h}_{rf}$ is in the direction longitudinal to the bar.

Measurement of the spin-to-charge conversion

The spin current injected in the NM material by FMR (Eq. 2.50) is converted into a charge current via spin-to-charge conversion mechanisms (ISHE and IREE, Sec. 1.3.2 and 1.3.3). The intensity I_c provides a first indication of the efficiency of the spin-to-charge conversion of the NM (e.g. the spin Hall angle θ_{SHE}). It can be measured by a rather simple electrical measurement. As visible in Fig. 2.19, an open-circuit voltage drop forms between the edges of the sample $V_{sp} = V^+ - V^-$, connected to the positive and the negative electrodes of a voltage-meter. The voltage is related to I_c via the electrical resistance *R* (Ohm's law):

$$I_c = V_{sp}/R \tag{2.52}$$

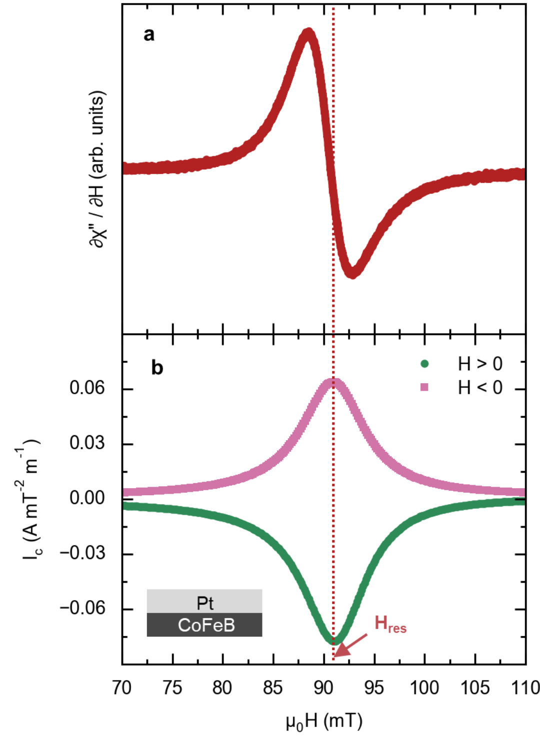

Figure 2.20: *Spin pumping measurement of Pt(15 nm) grown by sputtering on top of a CoFeB(15 nm)/Si.* ***a*** *Differential absorption FMR spectrum of CoFeB versus the static field H.* ***b*** *Charge current production (i_c) measured simultaneously to the FMR spectrum. The negative peak is recorded when H> 0 (green data), the positive peak when H< 0 (pink data). The inversion of the dc field sign corresponds to the inversion of the polarization of the pumped current.*

In our experiments V_{sp} was measured with a Keithley Nanovoltmeter and a two-probes setup was used to measure the resistance between the two electrodes (R). An example of a spin pumping measurement is shown in Fig. 2.20. A spin current is pumped by FMR of a CoFeB(15 nm) film into an adjacent Pt(15 nm) layer, a well known reference material with large and positive spin Hall angle of about 6 % [63]. Panel **a** shows the FMR of CoFeB, panel **b** the current acquired during the field sweep of the *dc*. I_c describes a *symmetric* peak with a maximum intensity at H_{res}. This behaviour is expected because FMR condition is where spin injection is mostly efficient. The current peak in negative for positive fields, positive in the opposite case. The direction of H defines the spin polarization $\boldsymbol{\sigma}$ of the pumped spin current: switching its sign (keeping the same propagation direction of $\mathbf{j}_\text{s}$) corresponds to an inversion of the charge current (Eq. 1.20). Note that I_c is normalized to h_{rf}^2, as the spin pumped current is proportional to the *rf* intensity (Eq. 2.50). Normalization allows to compare different measurements.

Determination of the spin Hall angle

In the following, we will provide the fundamental steps to estimate quantitatively the spin Hall angle of a NM by spin pumping.

The spin current injected at the interface diffuses in the NM, according to the spin diffusion model described in Sec. 1.17. The 1D spin diffusion equation along the axis normal to the surface yields to the spin current density profile:

$$\mathbf{j}_{spin}(z) = \mathbf{j}^0_{spin} \frac{\sinh\left(\frac{z-t_{NM}}{\lambda_s}\right)}{\sinh\left(\frac{t_{NM}}{\lambda_s}\right)} \tag{2.53}$$

The spin current density $\mathbf{j}_{spin}(z)$ decays exponentially in the NM within a length scale of the order of the spin diffusion length.

The charge current density produced by ISHE is:

$$\mathbf{J}_c^{ISHE}(z) = \theta_{SHE} \frac{2e}{\hbar} \mathbf{j}_s(z) \times \boldsymbol{\sigma} \tag{2.54}$$

I_c can be computed integrating Eq. 2.54 within the NM. Defining *W* the width of the slab in the transverse direction (0.4 mm in this work), the current results:

$$I_c = W\theta_{SHE}\lambda_s J^0_{spin} \tanh\frac{t_{NM}}{2\lambda_s} \tag{2.55}$$

This is the output of a spin pumping measurement: the current is a function of the spin Hall angle and the spin diffusion length that can be extracted by properly estimating $j_{\text{spin}}{}^0$ and fitting the thickness dependent behaviour.

Spurious effects in spin pumping measurements

The open circuit voltage measured at the edges of the ferromagnetic layer can contain spurious contributions in addition to the spin-to-charge one. The voltage signal would be a combination of the ISHE signal, spin rectification and thermal effects, as discussed in the following.

- **Thermal effects**. The power absorption at FMR is accompanied by a heating of the sample in which a thermal gradient develops. Different thermo-electric effects such as Anomalous Nernst (ANE) and Spin-Seebeck (SSE) can couple the thermal gradient to spurious spin or charge current contributions. ANE and SSE are hard to identify, as they generate an open loop voltage showing a symmetric peak at resonance as ISHE (the thermal gradient is maximum at resonance). P. Noel *et al.* [169] recently developed a protocol that allows to separate thermal from ISHE contributions. By inserting a thick insulating barrier between the FM and the NM layers to prevent the spin injection to occur, only ANE in the FM can be observed (both ISHE and SSE are related to the spin current). Then, ISHE can be epurated from SSE exploiting their different time-scales: spin-to-charge conversion occurs in the nanosecond range, thermal effects develop in the second. In absence of SSE slow and fast FMR sweeps would produce the same peak of I_c; vice-versa, SSE would increase the I_c of a slower scans more than a fast one.

- **Spin-rectification effects**. The field $\mathbf{h}_{rf}$ induces a non-vanishing electric field in the cavity $\mathbf{e}_{rf}$. A *rf* current $I_{rf}\cos(\omega t)$ thus flows in the sample. Given *R* the longitudinal resistance of the slab, a voltage drop $V(t)$ is generated at the edges according to Ohm's law:

$$V(t) = R(t)I_{rf}\cos(\omega t) \tag{2.56}$$

  The resistance is not constant, because the Anisotropic MagnetoResistance (AMR) of the FM adds a *rf* modulation to the the intrinsic resistance R_0. Indeed, the instantaneous magnetization $\mathbf{m}(t)$ rotates along the field axis with a precession cone angle θ (Fig. 2.18), shifted in time by the FMR dephase ϕ_0. It follows that the angle $\psi(t)$ between $\mathbf{m}(t)$ and the direction of the current (i.e. *x* axis) oscillates with ω, as well as the AMR contribution to the resistance:

$$R(t) = R_0 - \Delta R_{AMR} \sin^2(\psi(t)) \tag{2.57}$$

Replacing the expression of $R(t)$ in Ref. 2.56, the resulting $V(t)$ displays a *dc* component proportional to ΔR_{AMR}, as first observed in Nickel by Egan *et al.* [170]. In the generic case when the magnetic field and the slab axis describe an angle α, the *dc* voltage is written as [166]:

$$V_{dc,AMR} = \Delta R_{AMR} I_{rf} \frac{\sin(2\theta)}{2} \frac{\sin(2\alpha)}{2} \cos(\phi_0) \tag{2.58}$$

The AMR voltage is only due to the FM, hence it can be measured even in absence of NM layer under ISHE, as shown in Ref. [171]. From Eq. 2.58 it is clear that the expected AMR voltage should approach be zero when $\alpha = 90$ (i.e. in the geometry of this work, Fig. 2.19). For this reason, spin pumping in resonant cavity represents the best option, as the electric field amplitude has a node at the center.

In principle, ISHE ($V_{dc,ISHE}$) can be distinguished from AMR ($V_{dc,AMR}$) contributions because of their different line-shapes at FMR. While $V_{dc,ISHE}$ describes a symmetric peak at H_{res}, $V_{dc,AMR}$ is an antisymmetric function. The sign change at resonance is caused by the jump of the dephase angle ϕ_0= 180° (Eq. 2.58). Nonetheless, the coexistence of symmetric and antisymmetric AMR contributions in the V_{DC} peak was observed in thin film of CoFeB in Ref. [103] and it was attributed to current dissipation in the sample that reduces the phase jump. As a consequence, disentangling spin-rectification from ISHE contributions cannot be done just by separating symmetric and antisymmetric contributions, but exploiting the different dependency of these two effects on the angle α is required [170].

2.4 Growth of GeTe-based Heterostructures

This section includes information on the growth of the samples employed in this experimental work.

Thin films of epitaxial and quasi single crystalline GeTe were used for the study of the ferroelectric behaviour of this material in Ch. 3, or the spectroscopic investigation of its spin-textured bands by SARPES in Sec. 4.1. Epitaxial heterostructures based on GeTe/Fe bilayers for Spin-charge interconversion experiments by spin pumping (Sec. 4.2).

High-quality films of α-GeTe(111) were epitaxially grown on Si(111) by Molecular Beam Epitaxy (MBE) and provided by the group of R. Calarco (Paul-Drude-Institut für Festkörperelektronik, Germany, Berlin). The thickness of the samples examined in this work ranges between 5 nm and 50 nm.

Despite the quite large lattice mismatch between GeTe(111) and Si(111) of about 11% [128, 172], epitaxy is achieved by employing substrates with ad-hoc surface reconstruction Si(111)-$(\sqrt{3}\sqrt{3})R30°$-Sb. The role of Sb is to passivate the dandling bonds of Si(111) surface and minimize the interaction between the two compounds which takes the form of a weak Van Der Waals interaction, thus favoring the so called Van Der Waals Epitaxy [173]. As checked by in-situ High Energy Electron Diffraction (RHEED), the growth is two-dimensional immediately after the growth onset, with a complete relaxation of the in-plane lattice parameter to the bulk value after two bilayers. The sample surface was protected from oxidation and contamination by the in-situ deposition of a suitable capping layer with thickness of the about of 10-20 nm. The material of the capping layer is chosen depending on the final use of the sample:

- A **insulating Si_3N_4** capping layer is suitable for the ferroelectric characterization by PFM, because it reduces the current flowing between the tip and GeTe avoiding heating and sample

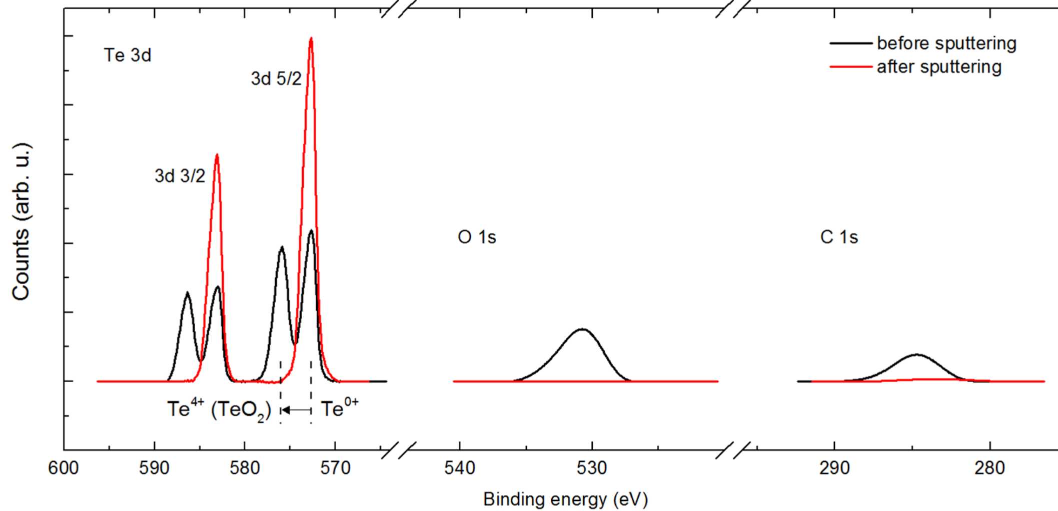

Figure 2.21: *Al-$K\alpha$ XPS spectra describing the removal of oxygen and contaminants from the Te capping layer. Before sputtering (black data), the Te_{3d} intensity accounts for one SOC split doublet of the metallic states (Te^{0+}) and one replica shifted by $\sim$3.2 eV towards larger binding energies, as expected from oxide states of TeO_2 (Te^{4+}). After sputtering, the chemically shifted doublet is removed, and the intensities of the oxygen and carbon peaks are dramatically reduced. The buried GeTe surface is thus correctly recovered, clean from oxygen and carbon contaminants.*

damage during domains writing. More in general, Si_3N_4-capped samples are used for applications not requiring the bare surface with the as-grown quality, as SARPES. Indeed, Si_3N_4 can be removed by wet etching methods and the subsequent exposure to air would immediately lead to oxidization of the surface. The oxide at the surface cannot be removed without desorbing or damaging the GeTe layer with sputtering and/or annealing the sample in UHV.

- An amorphous **metallic Te** capping layer with $\sim$20 nm thickness can be also used to protect GeTe against oxidation: only a thin layer of TeO_2 of $\sim$1-2 nm forms on top of Te, as demonstrated experimentally by X-Ray Photoemission Spectroscopy (XPS), Fig. 2.21. Differently from Si_3N_4, Te is removable in UHV by a suitable recipe involving low energy sputtering and relatively low temperatures, so that the ordered and clean as-grown surface of GeTe can be recovered. The surface recovering recipe will be described in detail in the Sec. 2.4.2. Reprepared Te-capped GeTe samples were employed in this work for the spin-resolved mapping of the bands by SARPES (Sec. 4.1). Moreover, epitaxial Fe was grown on recovered GeTe samples for spin pumping FMR investigation (Sec. 4.2).

2.4.1 Growth by Molecular Beam Epitaxy (MBE)

Molecular Beam Epitaxy (MBE) is a technique for the growth of epitaxial thin films of different materials, including metals, insulators and semiconductors. Thanks to very low rates of evaporation in UHV ($p < 10^{-5}$ mbar), with precise control of the beam fluxes, the kinetics of the growth can be controlled and optimized to obtain high quality film with a certain stochiometry. The material is evaporated from a Knudsen cell (rod shape or crucibles depending on the evaporation temperature) is provoked by an electron beam, generated by thermoionic emission from a filament of tungsten. The beam flux and the deposition is controlled by the intensity of the electron beam, hence by the power on the target. Up to seven deposition cells are available simultaneously in the MBE apparatus used in this work, allowing the growth of heterostructures involving layers of different materials (e.g. the GeTe/Fe/Au heterostructures employed for spin pumping in Sec. 4.2) and the co-evaporation of different materials for the deposition of complex compounds (e.g. $Ge_xIn_yTe_z$ and heterostructures realized in Ch. 5).

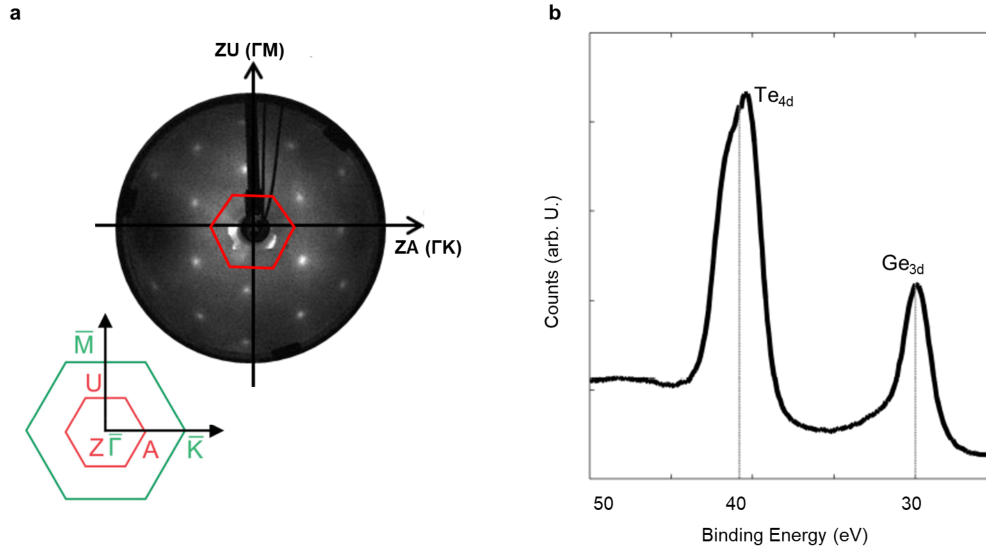

Figure 2.22: ***a*** *Hexagonal LEED pattern of a GeTe/Si surface after annealing at 250°C. The crystallographic orientation of the sample are indicated, highlighting the correspondence between the* ΓM *(*ΓK*) surface direction with the ZU (ZA) bulk one [60] (sec. 1.4). The Wigner-Seitz cell is drawn in red on the spectrum.* ***b*** *Al-*$K\alpha$ *XPS spectrum of GeTe, providing the atomic composition of the recovered sample. The ratio of the* Te_{4d} *and* Ge_{3d} *intensities normalized to the relative photoemission cross-section reveals a stoichiometric sample with 51% content of Ge (49 % of Te), with a variability of about 1% depending on instrumental uncertainty and fitting accuracy.*

2.4.2 Decapping protocol

The clean and ordered as-grown surface of GeTe can be recovered in UHV from a Te-capped GeTe thin film. In this work, an ad-hoc protocol was developed for such a purpose, exploiting a UHV cluster available in Polifab equipped with preparation and characterization tools (e.g. sputtering, annealing, X-ray Photoemission Spectroscopy, Low-Energy Electron Diffraction).

In most cases, annealing in vacuum is used for the desorption of capping layers, as well as of superficial oxide and contaminants. However, a direct desorption of the Te-capping layer by annealing is always accompanied by diffusion of oxygen atoms from the topmost TeO_2 layer to the interface with GeTe, where they preferentially bond to Ge. This was confirmed by XPS on several samples (data not shown). Further annealing to desorb oxygen from Ge-oxide would require temperature of ∼600-700°C, much higher than the evaporation point of the GeTe (∼300°C).

To solve this issue, a preliminary sputtering is performed prior annealing, to remove the TeO_2 layer thus avoiding oxygen diffusion and the formation of Ge-oxide.

The surface treatment protocol requires two sequential steps:

- **Oxide removal**. A soft sputtering of the capping layer by Ar^+ ions with energy ∼1100 eV removes the oxidized topmost part of the Te capping layer (the Ar-pressure is $\sim 10^{-8}$ Torr). The final and initial surface qualities can be checked by comparing the XPS spectra, as in the example of Fig. 2.21. Oxygen and carbon intensities drop to zero after the sputtering (red curve), concurrently with the chemically shifted Te_{3d} doublet of the Te^{4+} oxidation state.

- **Desorption of Te and surface recovery**. An annealing at about 250°C is performed in UHV to desorb the Te capping. This temperature ensures a highly ordered surface keeping the sample stoichiometry intact. The crystallographic quality of the surface can be checked either by Low or High Energy Electron Diffraction (RHEED or LEED, respectively) that provide the reciprocal space image of the film surface. An example of a clear LEED pattern of the recovered GeTe surface is shown in Fig. 2.22**a**. The sample stoichiometry instead is measured by XPS, as shown in Fig. 2.22**b**. The fractional amount of the Ge ($C_{Ge}/(C_{Ge} + C_{Te})$) is

retrieved from the ratio of the normalized intensity of Te_{4d} and Ge_{3d} peaks, as follows:

$$\frac{C_{Ge}}{C_{Ge}+C_{Te}}=\frac{\left(\frac{I}{\sigma\lambda_{IMFP}T}\right)_{Ge3d}}{\left(\frac{I}{\sigma\lambda_{IMFP}T}\right)_{Ge3d}+\left(\frac{I}{\sigma\lambda_{IMFP}T}\right)_{Te4d}} \tag{2.59}$$

The intensities are normalized to the cross-sections (σ) that depend on the specific photon energy and the inelastic mean free path of the electrons (λ_{IMFP}) discussed in Eq. 2.18. T is the analyser transmission function that depends on the electrons' kinetic energy. In the case shown here, the film stoichiometry is Te 49 $\%$ and Ge 51 $\%$, as at its grown status.

CHAPTER 3

Control of ferroelectricity in the semiconductor GeTe

Tuning the Rashba effect and the spin-charge interconversion mechanisms of FERSC in devices relies on the possibility to switch the ferroelectric state by electric fields. As commonly believed [116, 118], switching the polarization in small gap semiconductors such as GeTe is not achievable because the external field that is applied for the ferroelectric reversal would be screened by the free carriers of the semiconductor, within a thickness determined by the Debye screening length in the accumulation regime or by the depletion width in the depletion regime (respectively of about 1 nm in *p* and 3.5 nm for a free charge density of $3 \cdot 10^{20}$ cm^{-2} as GeTe). Based on this argument, GeTe has been considered as a polar metallic system or a ferroelectric in more general sense [116]. On the other hand, in the last years several attempts of electric switching have been made on other conducting systems, even in polar metals. For instance, ferroelectric switching has been observed in the two-dimensional polar metal WTe_2, sufficiently thin to let the field penetrate the whole film and induce the polarization reversal [174].

Similarly, GeTe is a narrow gap semiconductor falling in between a polar metal and a ferroelectric oxide, as it is prone to become degenerate depending on the surface preparation and the density of Ge vacancies. The possibility of switching GeTe by means of an electric gate has never been proved so far because its sizable conductivity makes the electric control of the polarization state very hard if performed with traditional *I-V* techniques widely employed for oxides as PUND (Sec. 2.1.1). For this reason, switching of GeTe films was first observed at the nanoscale by A. V. Kolobov *et al.* [112] in 2013 by means of Piezoresponse Force Microscopy (PFM), presented in Sec. 2.1.2. PFM was also used by W. X. Zhou *et al.* [175] to investigate the coexistence of electrically switchable spontaneous polarization and metallicity in bulk WTe_2, validating the concept of a “metallic ferroelectricity” at least at the nanoscale. In Sec. 3.1, we demonstrate and refine the results of A. V. Kolobov [112], adopting resonance-enhanced PFM. We defined protocols, rules and methods to avoid artifacts when measuring ferroelectric materials with very low piezoresponse such as GeTe and identified pulsed *dc* spectroscopy as the mode of choice (see Sec. 2.1.2). Then, we write ferroelectric domains down to the nanoscale.

In a long term vision which sees GeTe integrated in electronic circuits, the polarization control must be achieved over a larger scale (typically in the micrometer range) with respect to the local excitation of the PFM ($\sim 50 - 100$ nm). However, the possibility of such "macroscopic switching"

is still under debate. In Sec. 3.2 we investigate the control of ferroelectricity of GeTe films by means of micrometric gate electrodes. The problem must be tackled from both a conceptual and a technical points of view.

The conceptual issue is related to the screening operated by the large density of free carriers which is thought to prevent the switching. However we should recall that GeTe is not a metal. Hence, being in between a metal and an oxide, GeTe can react to an external electric field taking advantage from the mechanisms typical of both types of material, namely the screening via free charges and the inversion of the polarization. In a ferroelectric oxide, a uniformly polarized film displays a net surface polarization charge density at the surfaces perpendicular to the polarization vector. When an external field is applied, the material preferably aligns the polarization vector in such a way that polarization charges could partially screen the applied field (in other words, the depolarizing field described in Sec. 1.1 partially screens the external field). In this view, ferroelectric switching and movement of free charges are coexisting phenomena in semiconductors, rather than competing.

From the technical side, electric fields involve intense electric currents between the metallic electrodes (the resistivity of GeTe is rather low respect to standard oxides). High current densities cause heating and eventually damage the film. They can even induce other kinds of modifications not related to polarization switching such as the crystalline-amorphous phase-change transformation, a well-established phenomenon in GeTe. Most importantly, intense currents hinder the the read-out of the polarization state, that would hardly rely on the detection of the switching currents as with PUND (Sec. 2.1.1). PUND is suitable only for slightly doped materials, whose relatively low leakage current can be removed in order to extract the polarization one. For these reasons, one milestone achieved in the present work and presented in Sec. 3.2.1 is the development of an innovative *I-V* technique for writing and monitoring the ferroelectric state in GeTe thin films, based on the concept of the Ferroelectric-Shottky diode proposed by P. W. M. Blom in Ref. [176] and originally adopted for the wide gap FE semiconductor $BiFeO_3$ [177]. The basic idea is based on the fact that polarization charges modify the width of the depletion region, which in turn influences the resistance of the semiconductor/metal junction. The bistable behaviour of the resistance is also named *bipolar resistive switching* or *ferroresistive switching*. We also studied the actual inversion of FE domains during the electrical gating by means of PFM (Sec. 3.2.2), so as to validate the ferroresistive switching and clarify the physical mechanisms.

3.1 Ferroelectricity at the nanoscale: Piezoresponse Force Microscopy

The first observation of ferroelectricity in GeTe was carried out by Raman scattering experiments [113, 178]. This technique probes phonon softening at the transition temperature but it allows neither for recording nor for switching between the two remnant polarization states. The switching requires an external excitation source (e.g. external electric field or heat shocks) that provides the lattice with enough energy to overcome the barrier separating the two polarization states. As mentioned, I-V methods cannot be performed in materials with non-negligible conductivity. To circumvent this limitation, Piezoresponse Force Microscopy (PFM) [45] can be employed as the premier non-destructive technique for characterization of ferroelectric semiconducting materials with spatial resolution down to the nanometer scale [134]. PFM is suitable for semiconducting ferroelectrics since the AFM tip is used as a movable top electrode and its nanometric size drastically limits the current flow when a voltage is applied to it and the reading of the ferroelectric state is performed by sensing the piezoelectric response rather than the current. PFM characterization of GeTe thin films is discussed in the following with the use of pulsed *dc* hysteresis technique introduced in Sec. 2.1.2. Domains writing and reading with fine control down to the nanometer scale are also shown.

3.1.1 Switching spectroscopy PFM in GeTe

The characteristic signature of a ferroelectric material is given by the presence of a hysteresis loop of the polarization versus the external electric field. In a semiconducting ferroelectric material, it can be measured by the pulsed *dc* spectroscopy, as described in Sec. 2.1.2. The strong electrostatic tip-sample interaction can be strongly reduced in the measurement of the piezoelectric signal. The working principle is recalled in Fig. 3.1**a**. A train of poling voltage pulses is applied to the tip (V_{dc}) while the sample is properly grounded, typically by conductive Ag paste. The 'SET' operation writes a defined ferroelectric state at a given V_{tip}. The piezoelectric response is always collected at remanence ('READ' time window), so that the component of the electrostatic interaction proportional to V_{dc} expressed in Eq. 2.13 is zero and constant for all the point collected. The piezoelectric response is obtained as the tip deflection induced by the oscillating driving voltage (V_{ac}), namely the X and Y signals of the lock-in demodulation. The PFM amplitude and phase signals are computed from X and Y after background subtraction as defined by the protocol in Sec. 2.1.2.

For example, a measurement on a GeTe thin film is shown in Fig. 3.1. We chose the value of the excitation frequency close to the tip-sample contact resonance (f ~280 kHz in this case), to benefit from the internal amplification of the tip deflection (see Sec. 2.1.2). The behaviour of the amplitude (A) and phase (Φ) versus the tip bias V_{tip} are reported in panels **b** and **c**.

A describes a typical butterfly shape with saturation at large bias voltages and strong decrease at the coercive field (i.e. mixture of domains underneath the tip). Eventually, the amplitude signal can be converted in the piezoelectric coefficient d_{33}, by using Eq. 2.10. Here we provide the estimation of d_{33} in GeTe, with an AFM sensitivity $S\sim$ 200 nm/V calibrated on the force versus distance curve considering the nominal elastic constant of the cantilever ($k \sim 3$ N/m). As other resonant systems, the quality factor Q is estimated from the resonance peak described by A versus the f i.e. the resonance frequency normalized to the peak line-width). We measured $Q \sim 100$ (data not shown). The calculation with Eq. 2.10 performed on the data shown in Fig. 3.1**a** returns a $d_{33}\sim$ 3 pm/V at saturation as indicated in the plot. This value is comparable with other studies in the literature (1.5 pm/V in Ref. [179], 0.1-2 pm/V in Ref. [180]), and way smaller than oxides (100-500 pm/V for PZT ceramics [180]).

The PFM phase follows the hysteresis loop of the polarization orientation, showing 180° jumps at the coercive voltages (about 3-5 V). The first point of the loop corresponding to V_{tip}= 0 V is used to identify the native ferroelectric state of the sample at that specific location, by comparison with the PFM signal obtained in the saturated states. Performing this measurement on a significant number of points on the surface, these information can be recovered also with spatial resolution.

3.1.2 Nanopatterning of domains in GeTe

The AFM tip can be used also to write and map ferroelectric domains patterns as introduced in Sec.2.1.2. The flexibility of positioning the tip on specific sample locations is of great interest for technology. Indeed, scaling of modern in-memory computing technologies would require the control of the material and its physical properties down to nanometric sizes.

The stability of ferroelectric domains at the nanoscale was demonstrated in 2012 in GeTe nanometer crystals as reported in Ref. [118]. We achieved the patterning of nanometer-size domains on epitaxial GeTe thin films by means of the biased tip of the AFM [181]. The extreme difficulty of writing over a strongly semiconducting material is related to the intense current flow during poling, which provokes modifications of the sample surface (burning, electro-chemical reactions), besides a fast degradation of the tip quality. To overcome this issue, we optimized the writing step tuning the speed of the scan to minimize the time spent by the tip in each point, but giving the polarization enough time to switch. Concerning the reading, the main obstacle is the poor piezoelectric signal which may be surmounted by the electrostatic background and tip modifications during the scan. For this reason, PFM is preferentially recorded at near the contact resonance frequency. Nonethe-

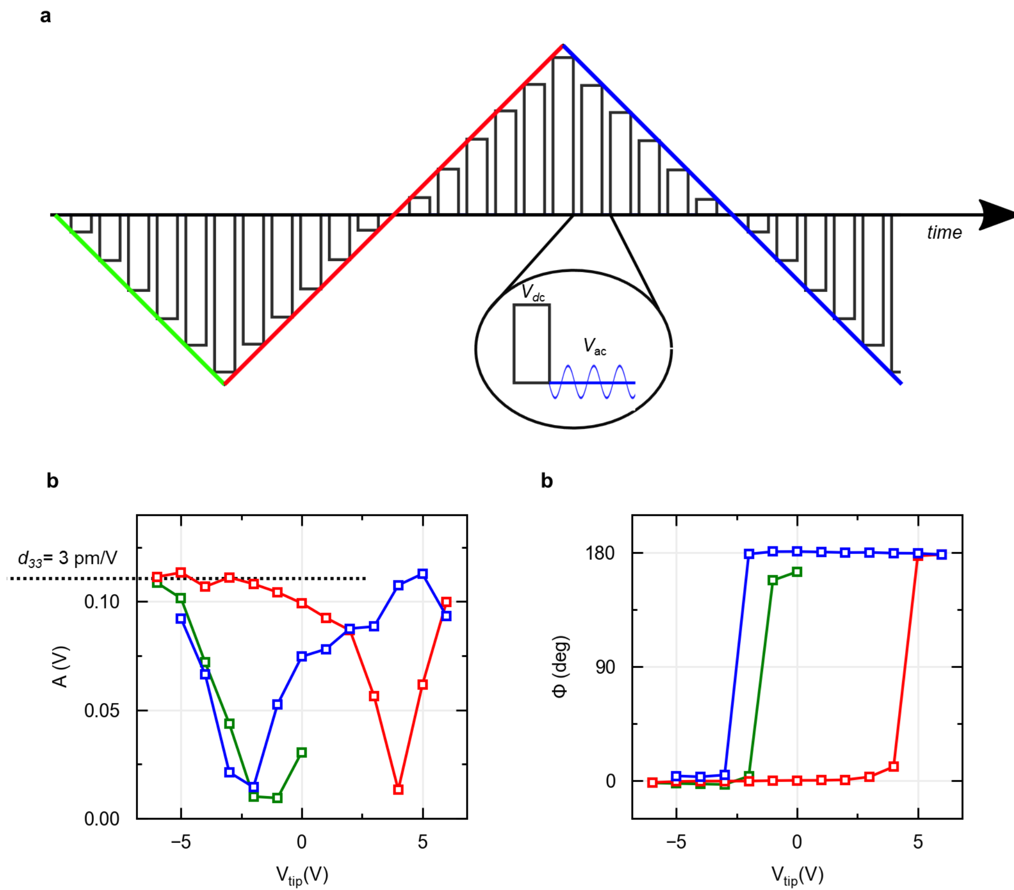

Figure 3.1: *Pulsed DC hysteresis PFM on epitaxial GeTe(20 nm)/Si(111).* ***a*** *Sketch of the pulsed dc measurement.* ***b*** *PFM amplitude and* **c** *PFM phase versus tip voltage. A driving voltage V_{ac}= 2 V and resonance excitation frequency (280 kHz) were adopted for the measurement. For details about the growth refer to Sec. 2.4.*

less, the drawback of resonant measurements is the a strong cross-talking between the topographic and the PFM signals, due to the local modification of the resonance frequency during the scan.

Fig. 3.2 reports one example of nanopatterning. As shown in panel **a**, the pattern consists in the writing of parallel lines with inward polarization in a uniform pristine outward sample. The lines are written by moving the tip with applied positive voltage (10 V). The PFM mapping of the domain distribution is reported in panels **b-c**: alternation of inward lines have been stabilized with a natural lateral size that results from the relaxation of domains for the specific speed of the moving tip. The optimization of the scan speed and stiffness of the tip-sample contact lead to a lateral size which is really within the dimension of the tip and the resolution of the AFM. This proves that the ferroelectric patterning can be pushed to nanometric scale.

Because of the correlation between ferrolectricity and Rashba spin texture discussed in Sec. 4.1, crafting ferroelectricity in GeTe has practical impact not only in nonvolatile memory devices but also in reconfigurable spin-logic, where the functionality is dictated by the geometry of the domains [181]. The pattern realized as in Fig. 3.2 could act as a Rashba filter, with spin dependent scattering at the ferroelectric domain boundaries.

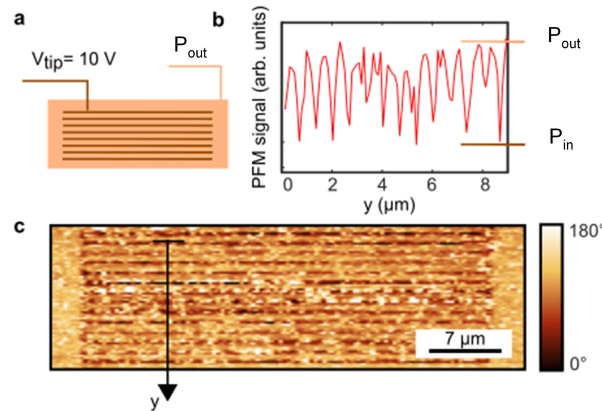

Figure 3.2: *PFM domains patterning at the nanoscale.* ***a*** *Sketch of the writing procedure to write a sequence of inward domains on a uniform outward area. 300 nm wide stripes of inward polarization are drawn by scanning the tip with V_{tip}= 10 V. The distance between the lines is 600 nm.* ***b*** *PFM phase measured scanning along the direction perpendicular to the lines (y).* ***c*** *PFM phase map of the ferroelectric polarization distribution. Adapted from Ref. [181].*

3.2 Ferroelectric switching via macroscopic gate

For sake of the realization of devices based on GeTe, the ferroelectric state has to be controlled by a gate electrode. Demonstrating the switching in GeTe films requires the development of a suitable technique.

As a matter of fact, standard methods as Dynamic I-V characteristic and PUND [182] described in Sec. 2.1.1 are not suitable since the reading operation is performed by probing the displacement current originating from the change of the surface charge sign during polarization reversal. This current is normally of 0.3 μA for an insulating ferroelectric with P= 30 $\mu C/cm^2$ (i.e. the nominal value for $BaTiO_3$) and electrode area of A= (100 $\mu m)^2$. For GeTe, the current registered during the switching pulse is about 10^5 times larger, thus preventing the monitoring of the polarization one. In this section, we propose a new method to solve this issue. We carried out this investigation in Polifab with Luca Nessi and Simone Petrò.

3.2.1 Reading the ferroelectric state: bipolar resistive switching

Although conduction current in GeTe capacitors is considered as the main limitation to the control of the FE switching by means of PUND (Sec. 2.1.1), we propose a change of perspective. Polarization charges in GeTe modify the distribution of the free charges and the electrostatic potential profile of the heterostructure, as pictorially explained in Fig. 3.3. The inversion of FE charges translates into a modification of the bands profile, so that the conduction properties are influenced by the ferroelectric state. In this view, the conduction current, as well as the resistance of the metal/GeTe junction, becomes the key for reading the FE state in semiconductors.

Influence of ferroelectricity on GeTe/metal junctions

When a semiconductor is interfaced with another material (e.g. a metal or another semiconductor), the electronic bands in the system experience a bending inside the semiconductor as a result of the electrostatic potential barrier at the interface (i.e. different positioning of the Fermi energy respect to the vacuum level). Thermodynamic equilibrium is reached thanks to the the motion of free charges from the two sides of the junction. In the the semiconductor, free carriers can accumulate

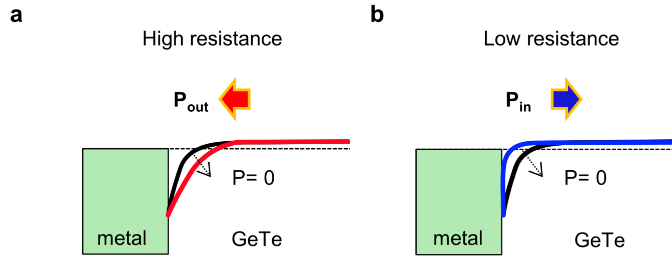

Figure 3.3: *Schematic idea of the energy bands profiles in a metal-semiconductor in the presence of ferroelectric remanent polarization. **a** The polarization vector points towards the metal. **b** The polarization points towards the semiconductor.*

or deplete in a defined region adjacent to the interface to compensate the difference of the Fermi levels. The IV curve will be then affected by the band profile at the interface. In the case of a GeTe/metal heterojunction a Ohmic contact was usually obtained, due to the high density of free carriers of the semiconductor ($p > 10^{19}$ cm^{-3}). The depletion width inside a non-polar semiconductor in contact with a metal (X_{d}) can be expressed as follows:

$$X_{\mathrm{d}} = \sqrt{\frac{2\epsilon_0\epsilon_r\Phi_B}{qN}} \tag{3.1}$$

Where ϵ_0 is the dielectric permeability in vacuum, ϵ_r the relative dielectric permeability ($\epsilon_r = 36$ in GeTe), Φ_i is the potential barrier height due to the difference in the work functions of the two materials (in general of the order of 1 V), N is the density of dopants that can be assumed equal to the density of free carriers ($p = 3 \cdot 10^{20}$ cm^{-3}). Such a large doping concentration generates a very narrow depletion width, $X_{\mathrm{d}} \sim 3$ nm, in GeTe as given by Eq. 3.1. For this reason, we ascribe the dominant conduction mechanism to the tunneling of carriers across the barrier Φ_B and the process occurs in both directions so the contact displays a Ohmic behaviour. The specific contact resistivity (ρ_c) can be expressed as:

$$\rho_c = \rho_{c,0} \exp\left(\frac{2\Phi_B}{h}\sqrt{\frac{\epsilon_s m^*}{N}}\right) \tag{3.2}$$

Where $\rho_{c,0}$ is a constant depending on the metal and the semiconductor. In Eq. 3.2, ρ_c depends on the barrier height Φ_B and the dielectric constant ϵ_s. In the following, the modulation of the conduction properties is explained in terms of dependence of Φ_B and ϵ_s on the FE polarization.

The impact of polarization on the transport properties of metal/semiconductor heterojunctions is investigated in [183, 184]. Volume polarization charges in the depletion layer arise from an inhomogeneous remanent polarization, induced by the internal electric field determining the actual band-bending. Two different methods were adopted in Ref. [183,184] to determine the bands profile of a ferroelectric semiconductor/metal junction. However, the effect of surface polarization charges was not included in those models, but it was used in order to explain the physical mechanism governing oxides tunnel junctions [185–188]. In the following, the interplay between both kinds of polarization charges and the conduction properties will be investigated.

H. Matsuura [183] developed an analytical model for the calculation of the bands profile in wide-gap ferroelectric/metal Shottky junctions. According to this model, a significant widening of the depletion region respect to non-polar semiconductors is derived from the modified Poisson equation [184] containing a polarization dependent term. The increase of the depletion width can be explained in terms of an increase of the effective dielectric constant. However, this analytic approach is not valid for degenerate semiconductors for which Fermi-Dirac distribution has to be considered when deriving charge transport equations [189]. A more general model was proposed

by P. W. M. Blom in Ref. [176], who derived the transport properties of ferroelectric Shottky diodes by means of a self-consistent model. The basic assumption is that the barrier height is constant and only the effective dielectric constant of the material is dependent on the polarization (Eq. 3.5). This model is suitable even for highly doped semiconductors since no assumptions are made on the free charge thermodynamic distribution, including GeTe.

Such a model predicts a bistable and hysteretic behaviour of the conduction of metal/semiconductor Shottky barrier by deriving a polarization dependent depletion width, which dominates the transport properties of the junction. Experimental investigations and theoretical calculations have been performed on $La_{0.5}Sr_{0.5}CoO_3$/$PbTiO_3$/Au heterostructure reported in Ref. [176]. The low voltage characteristic switches between Shottky and Ohmic behaviour, as a result of a wider or narrower depletion region when polarization is opposite or parallel to the built-in field, respectively.

The ferroelectric dependent band-bending is computed starting from the Gauss law:

$$\nabla \cdot \mathbf{D} = \rho_{free} \tag{3.3}$$

Where **D** is the dielectric displacement, related to the electric field **E** and the polarization vector **P** as:

$$\mathbf{D} = \epsilon_0 \mathbf{E} + \mathbf{P} \tag{3.4}$$

The dielectric permittivity is defined in general as:

$$\epsilon_0 \epsilon_r = \partial D / \partial E \tag{3.5}$$

Inserting Eq. 3.5 in Eq. 3.3, a generalized Poisson equation results in:

$$\nabla \cdot \mathbf{E} = \rho_{free} / (\epsilon_0 \epsilon_r) \tag{3.6}$$

With an effective dielectric constant ϵ_r

$$\epsilon_r = 1 + \epsilon_0^{-1} \partial P / \partial E \tag{3.7}$$

Since in a FE material the relation between *P* and *E* is strongly nonlinear, ϵ_r is not constant with the external electric field. For this reason, a self-consistent approach must be adopted. The hysteretic dependence of *P* versus *E* can be accounted in the single domain case by using [176]:

$$P(E) = \epsilon_0(\epsilon_{r\infty} - 1)E + P_0 \frac{\tanh(E + E_c)}{\tanh(E_c)} \tag{3.8}$$

From Equations 3.6 and considering that **P** = **D** - ϵ_0**E**, the polarization charge density results

$$\rho_p = -\partial P / \partial x = -\epsilon_r^{-1}(\epsilon_r - 1)\rho_{free} \tag{3.9}$$

Thus, ρ_p takes a opposite sign with respect to the space-charge. For a *p* semiconductor under the depletion approximation, it can be expressed as $\rho_p = qN_A$. The net charge $\rho_{free} + \rho_p$ is responsible for the electric field profile and the band bending. Since the total charge is reduced with respect to a non-polar semiconductor, then a wider depletion layer is expected. Moreover, the calculated ρ_p depends on the ferroelectric state, through the polarization dependent $\epsilon_r(P)$.

Similarly, σ_p at the surface can affect the conduction properties. As investigated in Ref. [190] in the case of molecular dipoles, surface polarization charges induce a shift of the surface potential of the semiconductor depending on their polarity, thereby modifying both the contact barrier height with the metal electrode and the depletion width in the semiconductor as shown in Fig. 3.3.

Therefore, both volume and surface polarization charges are predicted to cause a modulation of the electrical resistance of the metal/semiconductor junction with the ferroelectric state.

Furthermore, other possible mechanisms might concur to this effect. For instance, the field produced by σ_p penetrates not only in the semiconductor but also into the metal electrode within the

Thomas Fermi length [186]. The imperfect screening can lead to an asymmetric modulation of the bands profile, depending on the orientation of **P** [191], as in ferroelectric tunneling junctions [187]. Finally, in displacive ferroelectrics as GeTe [112], $BaTiO_3$, $PbTiO_3$ [192], the displacement of the ions upon polarization switching can modify the interface at the microscopic scale and the junction barrier height [192].

The determination of the precise microscopic explanation for a ferroelectric resistive modulation goes beyond the scope of this thesis, as it will require further investigations based on other experimental and computational tools.

Bipolar resistive switching

In order to investigate the concept of ferroelectric-induced switching of the resistivity in GeTe, we conceived separate writing and reading operations (Figure 3.4**a**-**b**):

- **Writing operation**: a writing voltage rectangular pulse is applied between the top and the bottom electrodes of a capacitor structure. The amplitude and the sign of the writing pulse is set to stabilize a well defined ferroelectric state (e.g. a positive pulse with amplitude larger than the coercive voltage V_c stabilizes a inward FE state, if applied to the top electrode).
- **Reading operation**: a voltage ramp is applied to the capacitor while the current is registered by an amperometer. The maximum voltage applied is required to be well below the voltage needed for the FE switching (V_c), so that the ferroelectric state that is stabilized in the device is not perturbed by the reading operation. As a result of the ferroelectric modulation of the band-bending in the heterostructure explained in the previous section, the FE state can be deduced by the shape of the low-voltage I-V characteristic of the capacitor.

The time separation between writing and reading operations represents one first improvement to traditional memories encoding the information as ferroelectric polarization, such as Ferroelectric Random Access Memories (FeRAM). FeRAMs are commercially available devices with fast write speed, low power consumption and large endurance [193]. However, the reading operation is executed simultaneously to the writing pulse, by detecting the polarization switching current peak. Therefore, reading the state previously stored in the capacitor can be performed only by applying a writing pulse that brings the system to a known polarization state [194], so that the initial state has to be restored after reading. On the contrary, the method proposed in the present work allows for non-destructive reading of the FE state, thus making way for increased endurance performances.

A sketch of the devices is depicted in Fig. 3.4**a**-**b**: squared Ti contacts of 40 μm side were evaporated on the bare surface of GeTe(18 nm) to act as top-electrodes; the back-electrode is not employed because the high resistivity of the Si substrate ($p = 2 \cdot 10^{15}$ cm^{-3} for Si) and a lateral one was realized with Ag paste at the edges of the sample, in order to reduce the required switching voltage. The advantage of this geometry also called "top-bottom measurement" is that only the GeTe/top electrode interface contributes on the observed RS. This is fundamental in order to have some insight into the underlying physical mechanism starting from symmetry and sign considerations.

In Fig. 3.4**c**, two low-voltage characteristics were obtained with the reading operation, adopting a maximum voltage of V_{max}= 1 V. The blue (red) curve is measured after the application of a writing pulse of +10 V (-10 V) to the top electrode, which stabilizes an inward (outward) polarization in the GeTe film. The IV curves are linear with a different slope for the two polarization states. When sequential pulses are applied with a voltage level sweeping from V= -10 V to V= +10 V and from V= +10 V back to V= -10 V, the conductance describes a hysteresis loop (Fig. 3.4**d**). The loop is quite similar to the ferroelectric hysteresis measured by PFM (Fig. 3.1**c**), in terms of switching voltage ($\sim$ 4 V). This indicates that the conductance variation is possibly due to ferroelectricity.

Consistently, when a top-top configuration is adopted instead of a top-bottom (as depicted in Fig. 3.5**a**), the switching amplitude is drastically reduced due to the fact that the variation of the

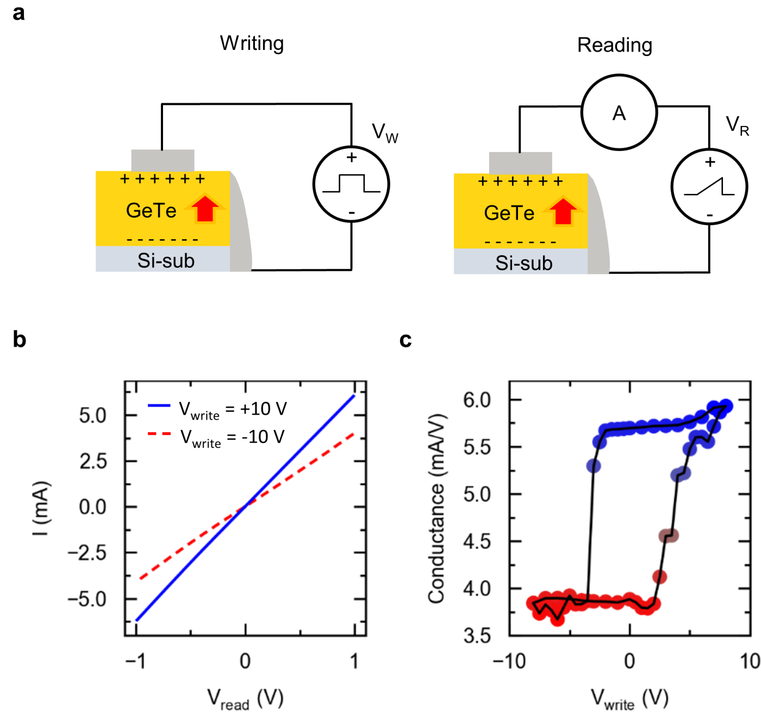

Figure 3.4: *Schematics of the writing **a** and reading **b** procedure. The sample is contacted to the negative pole of the source-measure unit by means of a lateral contact made by Ag paste, whereas the writing and reading voltage is applied to the top electrode (V_{write} and V_{read}, respectively). The writing operation consists in a rectangular voltage pulse, the reading operation by the collection of the IV at voltages much lower than the coercive one, avoiding perturbations of the stored state. **c** Current-voltage characteristics acquired with the reading step; the red curve is measured after V_{write}= -10 V, the blue one after +10 V applied to the top electrode. The pulse duration is of 10 ms. **d** Low-voltage conductance (V_{max}= 1 V) versus V_{write}. The hysteresis loop resembles the ferroelectric response acquired by PFM in Sec. 3.1. Both writing and reading operations are performed by means of a source-measure unit (Keithley K2600 or equivalent).*

resistance is expected to be opposite for the two pillars, apart from unavoidable random asymmetries in actual devices. This is shown in Fig. 3.5**b**, where the amplitude of the top-top loop is decreased by one order of magnitude respect to the top-bottom one. In addition, the coercive voltage is nearly doubled, as expected for the doubling of the thickness of GeTe involved in the new switching geometry. Finally, the sign of the top-top hysteresis loop can be reversed with respect to the top-bottom depending on the asymmetry involved. The unpredictability of the sign and the reduced amplitude of the resistance loop makes the top-top configuration less suitable as gating configuration with respect to the top-bottom one. Note that the distance between the pads does not influence the measured resistance, because it is mostly dominated by the GeTe/contact interface resistances.

The sign of the top-bottom loop is compatible with a ferroresistive switching in GeTe. As calculated by P. W. M. Blom *et al.* in Ref. [176], when polarization, **P**, is parallel (antiparallel) to the electric field in the depletion region, **E**, the depletion layer is narrowed (widened) with respect to the non-ferroelectric case. This means that in a *p* semiconductor like GeTe, where the space-charge field points inwards, the inward (outward) FE state corresponds to high (low) conduction (Fig. 3.3). This is compatible to what is reported in Fig. 3.4 where the high conduction is measured for positive writing voltages (i.e. inward state). Moreover, a positive surface polarization charge (P_{out}) would lead to a wider depletion layer and an increase of the metal-semiconductor barrier, so as to guarantee the charge neutrality of the system. Conversely, a negative charge P_{in} would narrow the depletion layer and decrease the effective barrier for crossing carriers. Therefore, P_{out}

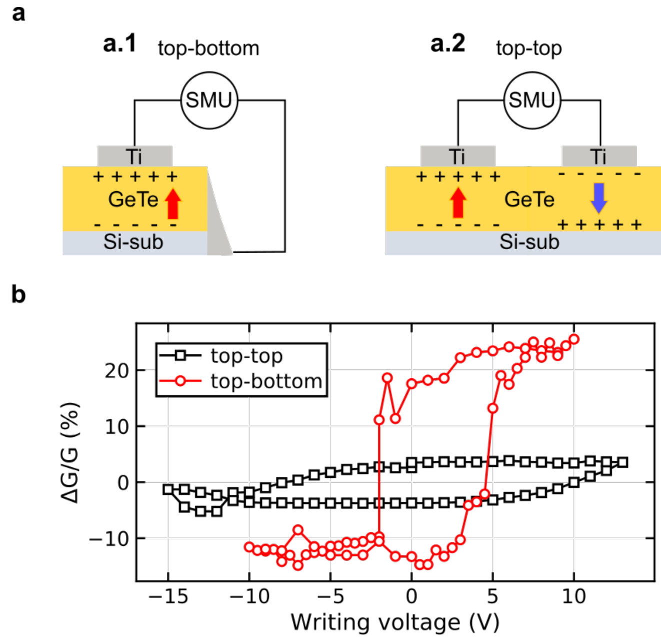

Figure 3.5: ***a*** *Sketch of the top-bottom (**a.1**) and top-top **a.2** configurations adopted for the measurement of resistive switching.* ***b*** *Percentage modulation of the conductance ($\Delta G/G$) versus the writing voltage level in the top-top (black square dots) and top-bottom (red circular dots) configurations, measured in GeTe(5 nm)/Si_xN_y(10 nm).*

state gives rise to low conductivity state, whereas P_{in} produces a high conduction level. This is compatible with what is observed in Fig. 3.4 and 3.5.

Other mechanisms of the resistive switching

So far, we assumed that the resistive switching (RS) is potentially ascribed to the change in the depletion region width or even in the Schottky barrier height operated by the inversion of the FE polarization. Nevertheless, in the last decades an intensive investigation of resistive switching in a plethora of different systems lead to different concepts of nanoscale non-volatile memory devices (resistive switching random access memories, RRAMs) to be integrated in state-of-the-art CMOS technology [195].

Several mechanisms were identified as responsible of the RS besides the ferroelectric one, which we should in principle consider as other possible explanations to our effect. Here the most widespread ones are reviewed.

- Phase-change resistive switching in transition metals chalcogenides [196–198]. The reversible transition between amorphous and crystalline phase leads to resistance variation with ON/OFF ratio of and this opened the field to Phase-change RAMs technology (PC-RAMs).
- Valence change and thermochemical switching, in binary oxides (e.g. HfO_2, TiO_2 [199]): the voltage-induced migration of the oxygen atoms results in a change of the valence of the metal ions in the metal oxide. This leads to the formation of a conducting filament (set state), that can be disrupted by inverting the polarity of the applied voltage (reset state);
- Homogeneous oxygen ion movement, in complex oxide compounds as $BiFeO_3$ [200]: the weakly bound oxygen atoms can move over the whole device area when the writing voltage is applied, thus modulating the Shottky barrier at the interface with the metal and leading to a change of the *I*-*V* curve;
- Metal ions movement from the contact across an insulating layer, that can form a conducting path. This concept was exploited in electrochemical memories (ECMs) [201];

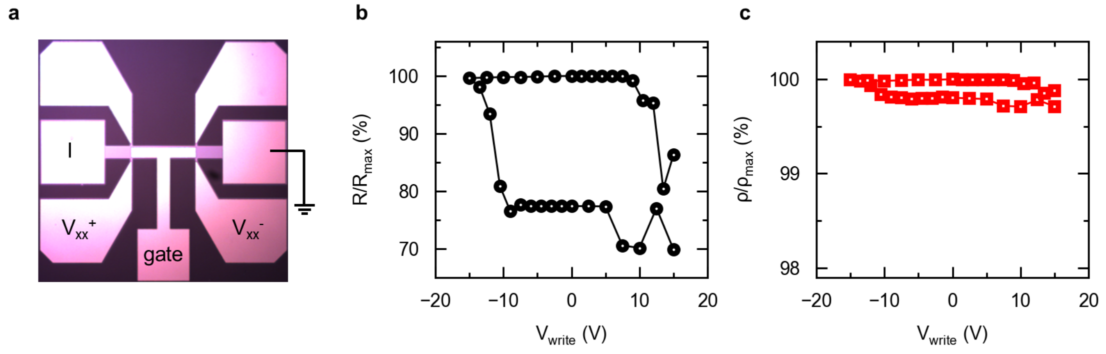

Figure 3.6: ***a*** *Picture of a Hall bar device patterned by optical lithography on GeTe/Si. The gate is used for electrical poling of the channel of GeTe. The pad I is used to inject a current, while the lateral contacts (V_{xx+} and V_{xx-}) are used to measure the resistivity of the channel below the gate.* ***b*** *Resistive switching of the gate/GeTe contact.* ***c*** *Resistivity of the GeTe channel versus V_{write}.*

- Ion migration in chalcogenides (e.g. GeSbTe [202]) or in transition metals oxides (e.g. HfO_x [203]): the conductive ions migrate towards one of the two metallic contacts depending on the polarity of the applied voltage. The movement of the metallic ions can lead to formation/disruption of conducting filament, hence to the resistive switching.

Among the aforementioned mechanisms, phase-change transformation, metal ions movement and ion migration are highlighted as other possible contributions for bipolar resistive switching in GeTe, in addition to the ferroelectric induced one proposed in the present work. Contrary to the effect presented in this study, phase-change RS is unipolar with respect to the writing pulse (i.e. set and reset operations can occur both at positive or negative voltages) and it involves much larger current densities than the one developed in our measurements (1 MA/cm^2 for the phase-change switching [198], 1 kA/cm^2 in our measurements). Moreover, set and reset pulses require different time duration to allow the switching kinetics during amorphization (fast process) or crystallization (slow process) of the material. For those reasons, phase-change transitions can be excluded as possible contributions to the resistive switching observed in GeTe (3.4). To further exclude a contribution of phase changes, we investigated the resistivity of a GeTe channel underneath a gate upon the ferroelectric poling. The Hall bar device employed is shown in Fig. 3.6**a**. During poling, the voltage is applied between the gate and one of the lateral contacts implementing the top-top configuration. The two lateral contacts (V_{xx+} and V_{xx-}) were used for monitoring the longitudinal resistivity versus the poling voltage, with a current flowing between the electrode *I* and the one connected to ground. Both the resistance of the gate/GeTe junction and the longitudinal resistivity of the channel were measured after each poling pulse and reported for comparison in Fig. 3.6**b**-**c**. The RS of the gate/GeTe junction behaves as expected for the top-top configuration described in Fig. 3.5**c**, with an ON/OFF ratio of about 20 % and a coercive voltage of ∼10 V. On the other hand, the longitudinal resistivity of the channel changes of just 0.2 %. This means that the RS is mainly ascribed to the modulation of the local band bending of GeTe at the interface with the gate, rather than a modification of the material in the volume. If a phase change transformation had happened in GeTe, the resistivity would have changed by two orders of magnitude between the amorphous and crystalline states [204, 205]. Therefore we can reasonably exclude the phase-change mechanism in our structure.

Concerning the other effects, we observed the bipolar RS also when a Si_xN_y protective layer is introduced between GeTe and the metal contact or when changing the metal employed as a gate (Au, Cr, Ti, Fe). Such a robustness makes embodiment and migration of oxygen from air in the metal structure or metal-ions migration inside the GeTe layer less probable [202]. However, migration of Ge or Te ions in GeTe can be considered as possible origin of the resistance variation,

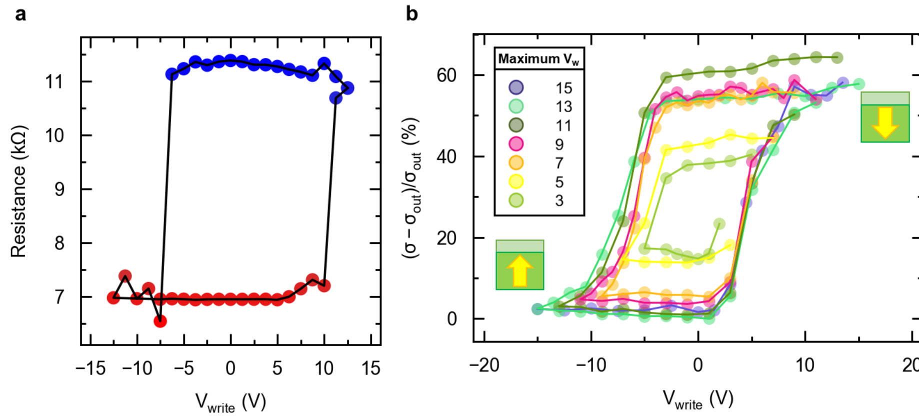

Figure 3.7: ***a*** *Resistive switching loop measured in top-top configuration at 20 K.* ***b*** *Minor loops of the resistive switching. Writing voltage sweeps are performed with different maximum voltages: 15 V, 13 V, 11 V, 9 V, 7 V, 3 V. When the maximum voltage approaches or is lower than the coercive voltage (V_c = ± 5 V), the system switches between unsaturated states. Minor loops behaviour is typical of ferroelectric systems.*

due to the compatibility with symmetry (bipolar RS), ON/OFF ratio and switching voltages with the observed data. Further microscopic investigations are needed at this point in order to associate the resistive switching to ferroelectricity. A first hint against ion migration is the insensitivity to the temperature, which is not compatible with the reduced mobility of the ionic species expected at low temperatures. Indeed, Fig. 3.7**a** shows that the ON/OFF ratio of RS at 20 K is the same as at room temperature, thus indicating that ion-migration could play a minor role.

An indirect signature of ferroelectric induced RS comes from the presence of minor hysteresis loops, i.e. the possibility of reducing the resistance variation by sweeping the writing voltage between progressively smaller voltage levels (Fig. 3.7**b**). Intermediate conductance levels can be precisely tuned by controlling the maximum writing voltage amplitude. This behaviour has been recently proposed as a technological solution for the realization of ferroelectric memristors [127, 187], to be interconnected to artificial neural networks [206].

The minor loops behaviour and the negligible variation of the longitudinal resistivity are first indications of the possible ferroelectric origin of the RS. To unambiguously associate the resistive switching to ferroelectricity and eventually exclude ion migration, we designed a suitable experiment based on the visualization of the FE domains distribution upon poling, the topic of the next section (Sec. 3.2.2).

3.2.2 Ferroelectric domains: a microscopic view

We visualized the ferroelectric behaviour of GeTe during the electric switching of the resistance. This approach has already been tested as powerful method for real time imaging of FE domains of FTJs based on ferroelectric oxides ($Pb(Zr_{0.2}Ti_{0.8})O_3$ in Ref. [207], $BiFeO_3$ in Ref. [127, 177]). In the present study, this experiment represents the key for understanding if ferroelectric switching is feasible in GeTe by means of gate pulses.

Ad-hoc capacitors were fabricated out of a Si_xN_y(10 nm)/GeTe(50 nm)/Si sample, with the following features (Fig. 3.8):

- A square Au(5 nm)/Ti(5 nm) pad was patterned on GeTe surface by means of optical lithography, with a lateral size of 30 μm (comparable to the contacts employed in the measurements of Sec. 3.2.1). The metallic pad served as top electrode to control the FE polarization of GeTe underneath. The thickness of the pad was made just 10 nm in order to guarantee a robust coupling between the AFM tip and the GeTe surface: in this way the piezoelectric deformation can be sensed despite the small d_{33} of GeTe.

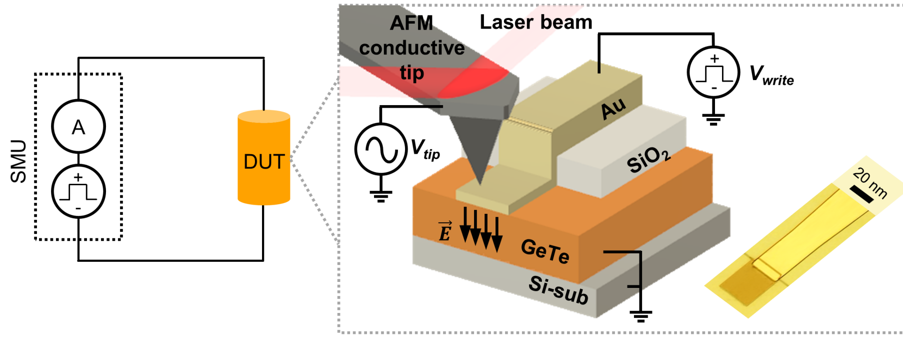

Figure 3.8: *Sketch of the setup realized for cross-experiment resistive switching and PFM. The gating requires a source-measure unit (SMU) that can provide a writing voltage and sense the current during the reading operation. In the dotted box, sketch of the sample patterning. The structure has been realized by optical lithography and a top view optical image of the obtained device is displayed.*

- A thicker and wider Au track (thickness of 200 nm, width of 200 μm) electrically connects the square pad to an external source-measure unit (SMU) and it is isolated from the GeTe film by 120 nm of SiO_2.

In the dotted box in Fig. 3.8, a sketch of the device structure is reported together with optical microscopy image of the final device.

For this experiment we adopted the top-bottom configuration as in Fig. 3.4. The voltage pulses were applied to the thicker electrode in contact with the thin gate (top contact), with the GeTe sample brought to ground by Ag-paste (bottom contact). Notably, the conductive tip was not suitable for poling the sample, because the high current density provided by a such large area and flowing through the tip would have damaged its metallic coating. To preserve its capability to map the FE domains, the tip was raised above the surface just by few micrometers during poling. Such a slight lift allowed to break the electric tip-sample contact and avoid intense current flow through the tip, and at the same time it guarantees that the scanned area is the approximately the same after each pulse. After a given writing pulse (V_{write}), the low-voltage IV was measured in order to check the resistive state of the heterojunction. Then, the SMU was disconnected from the sample and the tip was lowered on the electrode to map the distribution of the FE domains with V_{ac}. These operations were performed after each voltage pulse along the voltage loop. The result of the experiment is summarized in Fig. 3.9.

In Fig. 3.9**a** the resistance versus V_{write} is overlapped with the PFM phase averaged over the entire scan area. The RS and PFM loops show a similar hysteretic behaviour with two saturating states and a coercive voltage of about 3.5 V, compatible with the ferroelectric loop acquired by PFM on the uncovered Si_xN_y/GeTe surface nearby and the pulsed *dc* loop of Fig. 3.1. The modulation of the resistance is of 78 % (on the average state). The overlap of the two curves indicates that vertical resistance and FE state are linked. Four selected images are reported in panel **b**, referred to the points A (V = +8 V), B (V = -1 V), C (V = -2 V), D (V = -8 V), in order to appreciate the evolution of the FE domains with the pulses. The images are acquired off-resonance (70 kHz) to ensure reliable PFM contrast, by avoiding topography correlation and artifacts. The PFM scan area was of 0.7×0.2 μm^2, positioned at 5 μm distance from the edge with the thicker Au track connected to the voltage supply (see Fig. 3.8). In state A, the polarization state is mainly inwards, that corresponds to $\Phi = 0°$. Applying negative gate voltages, the inward domain progressively reduces (states B and C) and a uniform outward state is obtained with V = -8 V (state D). The switchable polarization computed from the distribution of the domains of the PFM phase maps is of about 70 %. The asymmetry of the switching is visible also as a slight shift of the hysteresis loop (about 1.2 V), compatible with the different work function of the electrodes or with built-in fields

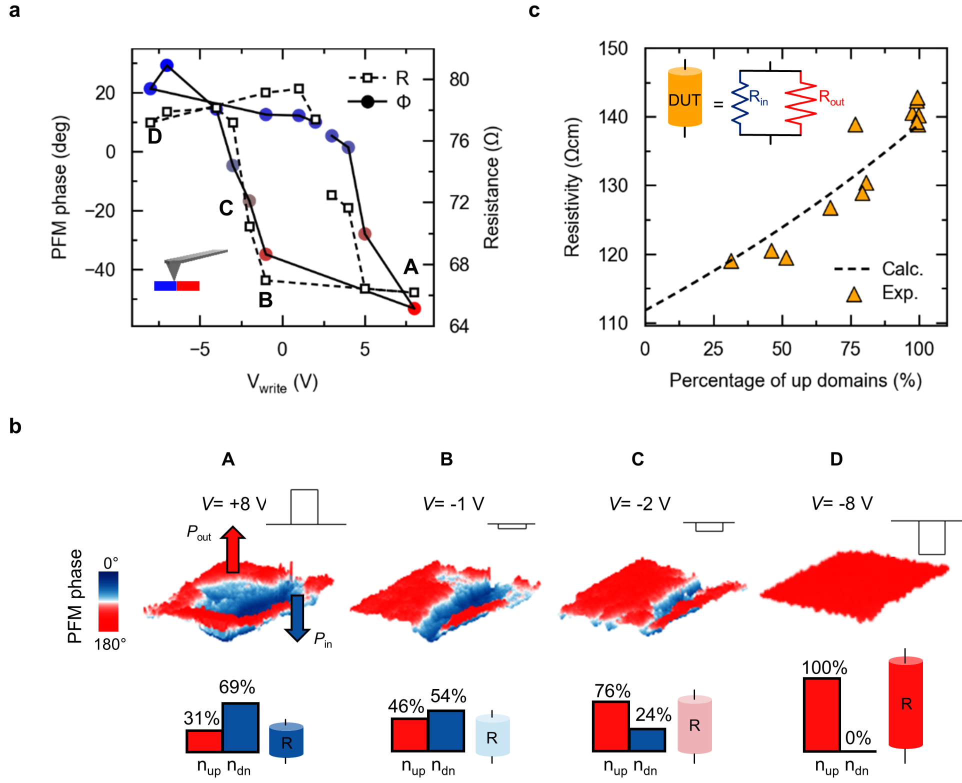

Figure 3.9: ***a*** *Resistance (squared black markers) and PFM phase (coloured circular markers) are plotted against the amplitude of the writing voltage pulse. The overlap between the two curves is signature of ferroelectric induced resistive switching. Points A (V = +8 V), B (V = -1 V), C (V = -2 V), D (V = -8 V) corresponds to PFM images reported in panel b.* ***b*** *PFM maps related to points A, B, C, D. The scan size is 0.7 x 0.2 μm^2, modulation amplitude 2 V and frequency 70 kHz. The phase value has been normalized to the range 0°-180°, thus not accounting for the contribution from the system inherent background noise [139]. Blue state (0°) represents the inward FE polarization, the red one (180°) represents the outward state. Below each map, the histograms of up and down populations are reported. As the writing voltage sweeps from +8 V to -8 V, the PFM contrast switches from inward to outward and the resistance from the low state to the high state.* ***c*** *Resistivity trend with the percentage of up domains calculated from the PFM maps as explained in panel b. The orange dots are experimental data, the gray-dashed line is calculated from the parallel resistance model described in Eq. 3.11 and sketched in the top of the present graph.*

at the GeTe interfaces caused by interfacial dipoles that favour the preferential growth of outward ferroelectric domains. Previous theoretical and experimental works [114, 181] further confirm the tendency of an outward FE state, which is also justified by the higher energy of formation of the inward state with respect to the outward.

Correlating the resistance change with the amount of switched domains, we can explore more about the physical model behind (Fig. 3.9**c**). The dependence of the resistivity versus the percentage of outward domains extracted from the collected PFM maps has been fitted assuming the parallel resistance model. The overall resistance is modelled as the parallel of outward (R_{up}) and inward (R_{dn}) resistances. R_{up} and R_{dn} are estimated introducing a FE-dependent resistivity (ρ_{up} or ρ_{dn}) and the corresponding percentage of coverage (n_{up} or n_{dn}). In other terms:

$$R_{\text{up, dn}} = \frac{\rho_{\text{up, dn}} \cdot t}{n_{\text{up, dn}} \cdot A} \text{ where } n_{\text{up}} + n_{\text{dn}} = 1 \tag{3.10}$$

In Eq. 3.10, A is the total area of the contact ($30 \cdot 30\ \mu\text{m}^2$) and t is the thickness of GeTe. The parallel resistance model can be then be formulated as follows:

$$\frac{1}{R} = \frac{1}{R_{\text{up}}} + \frac{1}{R_{\text{dn}}} = \left(\frac{n_{\text{up}}}{\rho_{\text{up}}} + \frac{n_{\text{dn}}}{\rho_{\text{dn}}}\right) \cdot \frac{t}{A} = \frac{t}{\rho_{\text{eff}} A} \tag{3.11}$$

From Eq. 3.11 we extracted the effective resistivity of GeTe (ρ_{eff}) that is expected for a given distribution of domain measured by PFM. The experimental resistivity agrees very well with the simple parallel conduction model (dashed line in panel **c**), suggesting once again that resistive switching in metal/GeTe junctions results from the nucleation and propagation of outward and inward FE domains.

The experiment demonstrates that ferroelectric switching can be achieved at micrometer scale in GeTe, and controlled through the resistance of the GeTe/gate interface. This is the fundamental step enabling the non-volatile electric control of spin in GeTe. Hereafter, the gating method based on bipolar resistive switching of GeTe/metal surface developed in the present work represents also a new technique adaptable to other ferroelectric semiconductors, thus filling the need for a reliable, simple and cheap alternative to PFM that allows for writing and reading different FE states and can work at the scale of several μm.

3.2.3 Performances of ferroelectric Shottky devices

Amplitude, endurance, speed and power consumption of GeTe memory devices

A statistical analysis on different samples with different GeTe thickness or different spacer with the metal contact revealed that the amplitude of the resistance modulation (i.e. the ON/OFF ratio $(R_{high} - R_{low})/R_{low}$) can vary between 10 % and 100 %. The variability can be ascribed to an incomplete ferroelectric switching under the contact area. As calculated in Ref. [114] and demonstrated in our previous work in Ref. [181], GeTe films possess a preferred polarization state depending on the surface termination. The reversed state instead is less stable from the energetic point of view, so that it is likely that the system is not switched completely and it could only reach a multi-domain configuration. As demonstrated in the previous section (Sec. 3.2.2), this could be actually the case, where the ON/OFF ratio of 31% is accompanied by partial switching to the inward state, the less favoured state for a 50 nm GeTe capped with Si_xN_y. In some cases, the ON/OFF ratio can reach even 250%, depending on the history of the gating pulses. The unfavored FE state can be fully observed by forcing the system with a train of hundreds of several writing voltage pulses. The maximum modulation of the current achieved is shown in Fig. 3.6**a**. In Sec. 4.2 of Ch. 4, we investigate the switching of GeTe in a metal/Si/GeTe/metal heterostructure. In that case, RS is dominated by the Si/GeTe interface showing a larger potential barrier than the GeTe/metal junction. The recorded ON/OFF ratio of the loop shown in Fig. 4.17 reaches $\sim 10^4$ %. This suggests that the amplitude of the resistance modulation can be increased by properly control the relative doping of the semiconductor and gate electrode.

A key parameter for integration of GeTe as a ferroelectric semiconductor in actual technologies requires a high cycling endurance, i.e. the possibility of writing and erasing different polarization states many times. The endurance of a ferroelectric-based memory is limited by the fatigue of the ferroelectric [208, 209]. Two main mechanisms have been identified to produce ferroelectric fatigue. As explained by E. L. Colla in Ref. [210], FE domain walls can be pinned by charged defects that can be created during the poling pulses, thus reducing the switchable polarization. Moreover, nucleation of domains can be suppressed by the trapped charges that are injected by the large electric field during polarization switching, from the metal gate into the film [211]. In the GeTe-memory device in Fig. 3.4 and described in Sec. 3.2.1, the endurance was tested by applying several repetitions of +V_{sat} and -V_{sat}. In Fig. 3.10 the device stability is shown up to 2000 cycles, by applying +V_{sat}= 10 V and -V_{sat}= -10 V. The maximum endurance achieved in GeTe films is of the order of 10^4 cycles, value comparable to flash memories [212]. This makes GeTe a suitable material to be employed in novel semiconductor based ferroelectric memories.

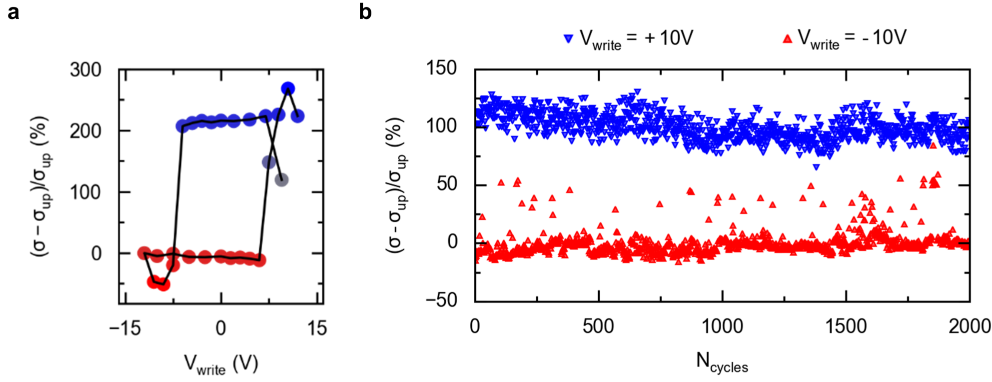

Figure 3.10: *Low-voltage conductance level measured at remanence (V_{max}= 1 V) versus the number of multiple repetitions of the sequence V_{pulse}= +10 V and V_{pulse}= -10 V. This measurement tests the endurance of the system, i.e. the number of writing/erasing cycles can be performed before the switchable polarization is reduced by fatigue.*

For what concerns the power consumption, the power needed to pole a 5 nm thick GeTe layer is:

$$P_{pol} = V \cdot I = \frac{V^2}{R} \cong \frac{(10^2)}{5000} = 20 \text{ mW} \tag{3.12}$$

Which per unit area (A) results:

$$\frac{P_{pol}}{A} \cong \frac{20 \text{ mW}}{(40 \ \mu\text{m})^2} = 0.5 \text{ mW}/\mu\text{m}^2 \tag{3.13}$$

As discussed in Sec. 3.2.1, the time duration of the writing pulse (t_{write}) is set to hundreds of 100 μs to get an effective writing/erasing of the ferroelectric element. As a consequence, the energy consumption is calculated as:

$$\frac{E_{pol}}{A} = \frac{P_{pol}}{A} \cdot t_{write} \cong 0.5 \text{ mW}/\mu\text{m}^2 \cdot 100\mu s = 50 \text{ nJ}/\mu\text{m}^2 \tag{3.14}$$

The energy consumption is the bottleneck that limits the integration of GeTe in nowadays technologies, where the energy required per cell is about 10^6 times lower.

Comparison with other technologies

The state-of-the-art nonvolatile technology employed in memory cards and solid-state drives is represented by the NAND flash memories, developed by Toshiba at the end of 1980s. This technology allows the fastest writing/erasing performances compared to other nonvolatile RAMs, with the highest storage density [213]. However, the endurance is limited to 10^4 programming/erasing cycles. An alternative widely explored in the last decades is represented by Ferroelectric RAMs [208]. It is basically a Dynamic RAM (DRAM) in which the dielectric is a ferroelectric material. FeRAMs endurance is limited by the fatigue of the ferroelectric material introduced in the above paragraph, reaching up to 10^{12} cycles [208]. Moreover, a much lower power consumption is required during the writing operation. The main drawbacks of FeRAMs are represented by the the destructive reading, low storage density and high cost compared to flash. Reading is performed by monitoring the polarization switching current, the same concept exploited in PUND technique (Sec. 2.1.1). In this sense, the reading process is destructive and it requires the memorized state to be restored after every operation. A technological alternative to FeRAMs that employs still ferroelectric materials in order to keep the high endurance performance is represented by Ferroelectric Tunnel Junctions (FTJs) [187, 214]. In the latter, the reading operation is separated from the writing, similarly to NAND flash. A voltage pulse is applied to the ferroelectric layer in order to write/erase a defined

state in the cell, while the quantum mechanical tunneling current is measured at relatively low voltages to read the stored state. Nevertheless, with the miniaturization of the electronic devices, ultra-thin ferroelectric layers are required in order to realize a FTJ with significant readout currents. High-quality films few monolayers thick represent a limitation to the development of FTJs, due to the high cost of the growth process and the need of high-precision electronic circuit for reading the state. In this view, the ferroelectric control of charge transport in GeTe proposed in this work represents an alternative to quantum-tunneling across ferroelectric oxides, since the readout current is significantly larger due to its high doping. The main drawback is then represented by the much higher power writing/erasing operations (as discussed in the previous paragraph). A reduction of the power consumption could be achieved by introducing high-κ dielectric layers between GeTe and the electrodes in order to limit the current flow during the writing process.

In all ferroelectric based memories the retention is limited by the depolarization field that might induce a back-flipping of the polarization state [195]. Due to the high doping level, the depolarizing field is effectively screened in the film thus reducing the effect of back-flipping. This could indicate that GeTe could be employed as material for long retention time.

From the energy consumption point of view, the energy required for the switching of a GeTe-based memory cell is 10^6 times higher than the one required for NAND flash [213, 215]. Towards a reduction of the power consumption, the memory cells based on GeTe have to be scaled down to few nanometers size (15 nm is the lateral size of state-of-the-art miniaturized memory devices). This solution requires process engineering although it could be ideally a valid solution, since ferroelectric behaviour in GeTe has been observed in nanometric crystals in Ref. [118]. Nevertheless, a more effective solution would be the possibility of reducing the doping level of GeTe, so as to reduce the current densities involved in the ferroelectric switching. In the present work, GeTe crystals has been grown with doping of In atoms to substitute Ge atoms and reduce the vacancies (i.e. the amount of p free charges), as reported in Ch. 5.

3.3 Conclusions

In this chapter we experimentally demonstrated that the ferroelectric switching of a degenerate semiconductor as GeTe can be achieved at the macroscale, despite the high density of free carriers. This is also the first experimental evidence that GeTe behaves as a proper ferroelectric and not only as a polar material. The nondestructive readout of the ferroelectric state relies on the ferroelectric resistive switching effect. From a technological perspective, ferroresistive switching represents a simple, reliable and fast technique to reconfigure and control the memory state. The control of ferroelectricity in GeTe is the premise for the nonvolatile tuning of the Rashba effect and spin-charge conversion investigated in Ch. 4. Although GeTe is not competitive purely for memory applications, ferroresistive devices represent an innovative concept and a real step towards the electrical reconfigurability of spin transport in a CMOS compatible multifunctional material.

CHAPTER 4

Ferroelectric control of the spin physics in GeTe

The ferroelectric state in a FERSC material is intrinsically linked to the spin-orbit coupling, with the emergence of a *giant intrinsic bulk Rashba effect at room temperature*, without any external electric field. From theoretical calculations (Sec. 1.4), the coupling between ferroelectricity and Rashba effect in GeTe is reflected on the spin texture: the chirality of the Rashba sub-bands is predicted to be opposite for the two polarization states (inward and outward). Demonstrating this concept experimentally was the task of the work presented in the first section of this chapter (Sec. 4.1). The experiment combines engineered sample preparation recipes, ferroelectric characterization by PFM and spin resolved probing of the electronic bands by SARPES. The final picture summarized in Fig. 4.11 is compared with the theoretical expectations (Fig. 4.6) to establishing the link between ferroelectricity and the Rashba effect.

The interest in Rashba materials is motivated mostly by their implications on spin-charge interconversion mechanisms, namely the intrinsic spin Hall effect (Sec. 1.3.2) and the Rashba Edelstein effect (Sec. 1.3.3). In GeTe, the ferroelectric control of the Rashba SOC would lead to a spin-charge conversion manipulated through the ferroelectric state. *Nonvolatile and switchable spin-charge conversion in a single semiconducting material* would make up the lack of non-magnetic platforms operating at room temperature for low-power spin computing devices as the one proposed by Intel [9]. In the second part of this chapter (Sec. 4.2), the behaviour of spin-to-charge conversion in GeTe upon ferroelectric switching is harnessed by taking advantage of the macroscopic gating achieved in Ch. 3 and designing a spin pumping setup with in-situ monitoring of the ferroelectric state (Fig. 4.16). Based on the spin pumping measurements, theoretical calculations carried out by our coworkers J. Sławińska, S. Picozzi *et al.* lead to a better understanding of the physical origin of the conversion mechanisms separating spin Hall and Rashba Edelstein contributions.

4.1 Ferroelectric control of the Rashba spin texture in GeTe

Probing the interplay between ferroelectricity and Rashba effect requires a spectroscopic investigation of the electronic bands and the control of the ferroelectric state of the sample. A powerful technique allowing for the direct mapping of the Rashba spin texture is Spin- and Angle- Resolved PhotoEmission Spectroscopy (SARPES). As discussed in Sec. 2.2, (S)ARPES can be performed

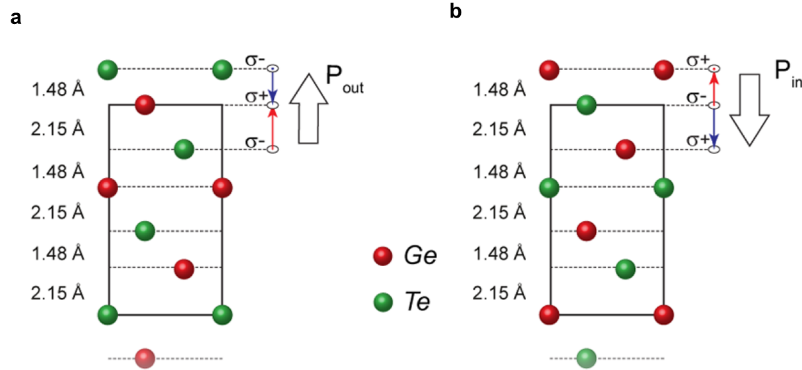

Figure 4.1: *Correlation between ferroelectric polarization and surface termination in GeTe.* ***a-b'*** *Sketch of the atomic planes along (111) and unrelaxed interlayer distances of Ge- and Te-terminated GeTe, respectively. The net polarization* $\boldsymbol{P}_{out}$*-*$\boldsymbol{P}_{in}$ *results from the different interatomic dipoles indicated with blue and red arrows. Adapted from Ref. [181].*

only in UHV environment, on clean surfaces. In Sec. 2.4.2 it is shown how an ordered and clean surface of GeTe can be obtained in vacuum from Te-capped samples, with sputtering and thermal annealing, thus allowing for the probing of the Rashba states by SARPES. The work carried by M. Liebmann *et al.* [60] already showed a Rashba splitting and a rotating spin texture on GeTe. Nevertheless, the polarization state of the sample was fixed and checked by PFM aftwerwards. In-situ switching of the polarization represents a hard task, as SARPES is a surface sensitive technique and a top electrode cannot be employed. Recently, J. Krempaský *et al.* [216] proposed to use Au mesh as a top electrode and collect the photoelectron intensity from its uncovered parts, to show the in-situ switching. This solution is however quite demanding in terms of sample preparation and does not ensure that polarization of the uncovered areas under the mesh effectively switches.

In this work we first investigated the possibility of preparing different samples in UHV, controlling their spontaneous polarization state. As discussed more in details in Sec. 4.1.1, the termination of the surface plays a key role in the stabilization of different polarization states. This possibility would circumvent the issues related to an in-situ switching and favor SARPES investigation of different polarization states. SARPES measurements on GeTe films were performed at the Advanced Photoelectric Effect experiments (APE) beam-line of the Elettra Syncrotron in Trieste (Basovizza). In Sec. 4.1.2 and 4.1.3, detection of bulk Rashba states and their spin texture by (S)ARPES on GeTe samples specifically prepared with different termination will be discussed, so as to correlate the spin chirality of the bands with the termination and the ferroelectric state.

4.1.1 Control of the polarization by surface termination

An alternative solution to the in-situ switching would be the possibility of preparing samples in UHV, spontaneously showing either uniform outward or uniform inward ferroelectric states.

From energetic arguments, different ferroelectric phases can be stabilized in a film of GeTe(111) depending on its surface termination, namely on the atomic specie of the topmost atomic layer. As introduced in Sec. 1.4, GeTe(111) is formed by the alternation of Ge and Te planes with non-equivalent spacing, thus leading to a net ferroelectric dipole. Among all cases (outward or inward polarization and Ge or Te surface termination), the most energetically favored are those in which the surface breaks the longer bond rather than the shorter one. This is shown in Fig. 4.1, in which Ge terminated surface is stabilized with inward polarization ($\mathbf{P}_{\text{in}}$, panel **a**), and the Te terminated is associated with the outward ($\mathbf{P}_{\text{in}}$, panel **a'**). This simplified picture was also supported by more complete Density Functional Theory (DFT) calculations, discussed in details in Ref. [181]. It follows that the ferroelectric state can be in principle set by controlling the termination of the

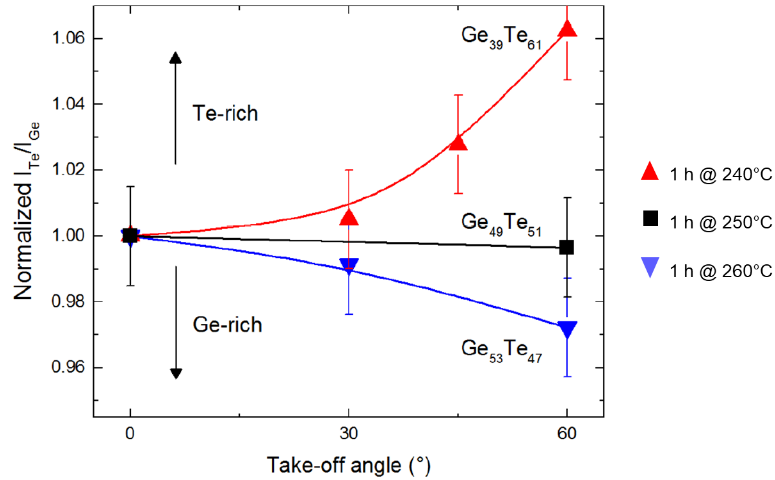

Figure 4.2: *XPS for three Te-capped GeTe sample re-prepared with different thermal budgets:1 hour at 260°C (red), 250°C (black) and 240°C (blue). The ratio between Te 4d and Ge 3d peaks intensities (normalized to their cross section and analyser transmission) is plotted versus the photoelectron take-off angle from the surface normal. The ratio I_{Te4d}/I_{Ge3d} is normalized to the value obtained at 0°. Adapted from Ref. [181].*

surface, which in turn is much easier to manipulate with UHV surface treatments (e.g. sputtering and annealing). For instance, Te has has a much higher vapour pressure and thus is quite more volatile than Ge. Therefore, the surface composition would lack of Te when annealed at relatively high temperatures with an average stoichiometry leaning towards a Ge-terminated surface (or more properly a Ge-rich surface). On the contrary, lower thermal budgets would favor the Te termination.

The study of the surface chemical composition versus the annealing temperature was performed in Polifab and then reproduced at the beamline prior to SARPES.

Samples are obtained in UHV from Te-capped GeTe films grown in Paul-Drude-Institut für Festkörperelektronik, Germany, Berlin). The surface preparation protocol described in Sec. 2.4.2 requires two steps:

- A mild sputtering with Ar^+ removes the oxidized topmost part of the Te capping layer to avoid the diffusion of oxygen towards the interface with GeTe during a subsequent heating.

- The residual metallic Te capping layer is then desorbed by thermal annealing with $T\sim 250°$, while monitoring the evolution of the surface order by LEED. The stoichiometry of samples can be checked by XPS (Al-$\kappa\alpha$ X-ray source in our lab or high energy synchrotron radiation at the beam-line). As shown in Ref. [217], the minimum temperature for an ordered surface with a clear LEED pattern is $\sim$240°C. On the other side, temperature larger than $\sim$260°C would induce the evaporation of Te from the sample and lead to strongly off-stoichiometric sample. Therefore, the temperature range is limited to a narrow window ($\sim$240-260°C).

In this study, various samples were prepared applying different thermal budgets (i.e. temperature and duration of the annealing step) and the obtained Ge and Te content at the surface was monitored by XPS. Fig. 4.2 shows the ratio of the normalized Te_{4d} and Te_{3d} intensities (i.e. the ratio between Te and Ge concentrations in the probed volume), versus the take-off angle of the photoemitted electrons and for different values of the annealing temperature (within the available range of $\sim$240-260°C, the annealing time was fixed at 1 hour). After an annealing at 240°C, the ratio increases with the collection angle (i.e. decreasing the probing depth). In other words, the content of Te close to the surface increases with respect to its percentage in the "bulk". On the contrary, when a lower temperature of 260°C is adopted for the desorption, the Te/Ge intensity ratio decreases with the take off angle, thus indicating a Ge-rich surface.

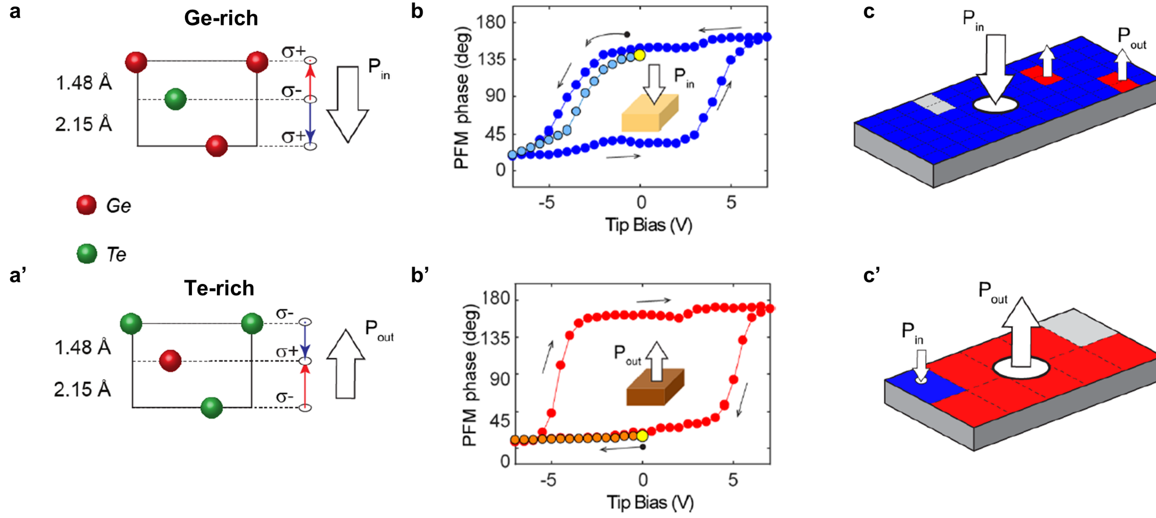

Figure 4.3: *GeTe(111) surfaces with opposite spontaneous polarization.* ***a-a'*** *Sketch of the surface termination and expected ferroelectric polarization of Ge-rich and Te-rich samples, respectively.* ***b-b'*** *PFM phase hysteresis loops representative of Ge and Te rich samples, measured with the pulsed DC technique. The yellow points indicate the pristine ferroelectric states.* ***c-c'*** *maps of the spontaneous polarization of Ge and Te rich samples, respectively. Adapted from Ref. [181].*

PFM was performed on the grown samples in order to investigate the correlation between the surface termination of the samples and their spontaneous ferroelectric state (Fig. 4.3). The pristine polarization of both both Ge- and Te- rich samples was probed by means of a statistical study of the pulsed *dc* spectroscopy, performed over a mesh of points on the surface (Sec. 2.1.2). Panels **b**-**b'** of Fig. 4.3 display the point hysteresis loops relative to Ge- and Te- rich samples, respectively. Those loops were chosen as representative of the overall behaviour of the samples. The pristine polarization on the specific location on the sample can be inferred by comparing the initial value of the PFM signal (yellow dot) to the two saturation levels reached at tip bias of ± 7 V. The two loops indicate an inward polarization ($\mathbf{P}_{in}$) for the Ge-rich sample, an outward state ($\mathbf{P}_{out}$) for the Te-rich one. The distribution of the pristine state is drawn in Fig. 4.3**c**-**c'**. Grey areas indicate indefinite polarization. Despite few reversed domains, both samples displays a uniform polarization ($\mathbf{P}_{in}$ for Ge-rich, $\mathbf{P}_{out}$ for Te-rich). The presence of residual domains with opposite polarization is probably related to some non-uniformity in the desorption of Te during the annealing. The PFM study demonstrated that the different Ge or Te surface content of the samples are associated to opposite polarization states.

For the SARPES investigation described in the following, two 20 nm thick samples with by Ge-rich (S_{Ge}) and a Te-rich (S_{Te}) surfaces were prepared at APE-Elettra with 1 hour of thermal annealing at 260°C and 240°C, respectively. The stoichiometries checked by *in-situ* normal emission XPS with 800 eV photon energy were $Ge_{53}Te_{47}$ for S_{Ge} $Ge_{39}Te_{61}$ for S_{Te}, in good agreement with the values shown in Fig. 4.2 for large take off angles. Indeed, the escape depth of analysed electrons at normal incidence with photon energy $h\nu = 800$ eV is about ~ 17 Å, quite similar to the one obtained with Al-$\kappa\alpha$ at $\theta \sim 60°$. The polarization of the two samples, checked by PFM after the spectroscopic measurements, was $\mathbf{P}_{out}$ for Te-rich and $\mathbf{P}_{in}$ for Ge-rich as expected. Thus, the spin texture of the Rashba states measured by SARPES can be correlated to the ferroelectric state.

4.1.2 Surface and bulk Rashba states in GeTe by ARPES

Contrary to the more spread 2D Rashba systems, the special feature of GeTe is the giant Rashba spin-splitting of the bulk valence bands (Sec. 1.4.2), which was calculated by S. Picozzi and

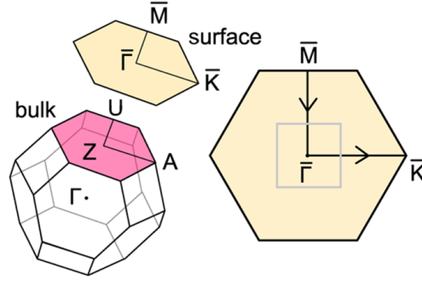

Figure 4.4: *Representation of the Brillouin zone of bulk and surface lattices. Adapted from Ref. [181]*

coworkers [11, 12, 114] by DFT. Such a giant effect would allow to achieve an electrically tunable spin-charge interconversion in a bulk system, rather than in a 2D fashion. On one side, interface-driven SOC at Rashba interfaces leads to much larger values of the conversion efficiency with respect to bulk systems (usually lower than 10 %) [17, 54, 218]. On the other hand, the exploitation of surface states in actual devices is strongly limited by their sensitivity to the detailed structure an quality of the surface and by the necessity of *ad-hoc* growth apparatus. In the case of GeTe, bulk states are instead an intrinsic property, robust against surface treatments, as will be shown for Ge-rich (S_{Ge}) and Te-rich (S_{Te}) samples. The presence surface states can partially contribute to the spin transport in GeTe, for instance determining the efficiency of the spin injection at the interface. Their effect on spin-charge conversion would become much more relevant only in ultra-thin films (thickness lower than 5 nm).

Here we investigated the bulk and surface Rashba states of Ge- rich and Te- rich samples, by combining DFT calculations with ARPES measurements. This was the preliminary step for the onward SARPES detection of the spin texture of the bulk bands (Sec. 4.1.3).

Density Functional Theory calculations

As introduced in Sec. 1.4.2, the Rashba bands splitting involves electronic states close to the high symmetry point Z of the reciprocal space. Fig. 4.4 shows the bulk First Brillouin Zone (FBZ) of GeTe. The splitting is different according to the crystallographic axis. Two non-equivalent directions ZA and ZU can be identified in the (111) plane, which defines the film plane (we will refer to it as the ZAU plane). In Fig. 4.4, the bulk ZU and ZA axes correspond to the ΓM and ΓK surface directions of the projected Brillouin zone. The ferroelectric polarization is along the (111) direction, parallel to ΓZ in the reciprocal space. In the following, k_x (k_y) axis refer to ZA (ZU) in the reciprocal space, corresponding to ΓM (ΓK).

DFT calculated bands dispersion along ΓM (ZU) and ΓK (ZA) are presented in Fig. 4.5, for Te- and Ge-terminated surfaces with outward and inward polarization, respectively. In the next, they will be compared to the ARPES measurements of S_{Te} and S_{Ge}. In panels **a-a'** the color indicates the surface (yellow) or bulk (pink) character of the bands, obtained by projecting the spectral function on the surface layers and on the bulk of a semi-infinite GeTe crystal. The spin polarization of the electronic states is reported in panels **b-b'**. The axis for the projection of the spin polarization is in the ZAU plane and perpendicular to the wave-vector according to the theory of Rashba effect (Sec. 1.2). Green and orange colors indicate a negative or positive sign of the spin polarization. Comparing S_{Ge} and S_{Te}, the shape of the bulk Rashba sub-bands near the Fermi level (E_B= 0 eV) is not affected by the different termination neither by the different polarization. For those states, the sign of the spin polarization is inverted depending on the ferroelectric state (as green and orange bands are swept in panels **b-b'** of Fig. 4.5). The inversion of the spin rotation is more evident in the constant energy maps (CEM) of the bulk bands obtained by cutting the complete bands structure at a fixed energy. Fig. 4.6**a-b** reports the CEM at E_B= 0.5 eV for S_{Ge} and S_{Te}. As result of the non-

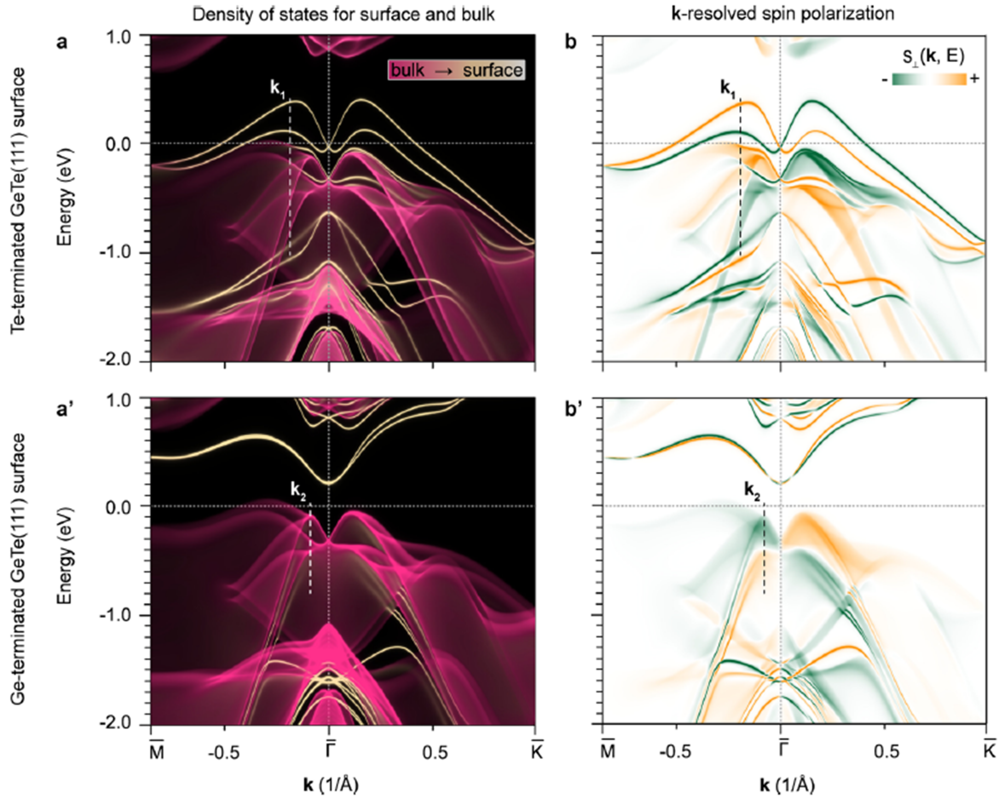

Figure 4.5: ***a*** *Density of states of Te-terminated sample with outward polarization, along the surface directions* Γ*M and* Γ*K (corresponding to the bulk directions ZA and ZU, as shown in panel* ***d****). The states are projected on bulk (pink) and surface (yellow) principal layers calculated by Density Functional Theory (DFT) for a semi-infinite GeTe(111) surface surface.* ***b*** *k-resolved spin polarization of the states calculated in panel* ***a****. For simplicity, only the in-plane components perpendicular to the wave-vector* ***k*** *is plotted. According to the theory of the Rashba effect (Sec. 1.2), the in-plane component parallel to* ***k*** *is absent.* ***c*** *Schematic picture of the spin texture of the main bulk Rashba bands obtained from panels* ***a*** *and* ***b*** *at -0.5 eV binding energy. The in-plane projection of the spin are drawn with black arrows.* ***a'c'*** *Similar calculations performed for a Ge-terminated sample, with inward polarization. The wave-vectors* $\mathbf{k}_1$ *and* $\mathbf{k}_2$ *were selected for spin resolved experiments. Adapted from Ref. [181].*

isotropic splitting of the bands, the two Rashba energy contours emerge with a hexagonal shape, reflecting the symmetry of the six-fold crystal (Sec. 1.4.2). The spin polarization of the states is drawn on the CEM by black arrows. The chiral spin texture is opposite for inward or outward polarization (panels **a** and **b**). This is the main concept of FERSC. A different picture is predicted for surface states, which are clearly affected by the termination of the surface. By comparing panels **a** and **a'** of Fig. 4.5, only S_{Te} displays surface branches at at the Fermi level. On the contrary, those states are suppressed in S_{Ge}.

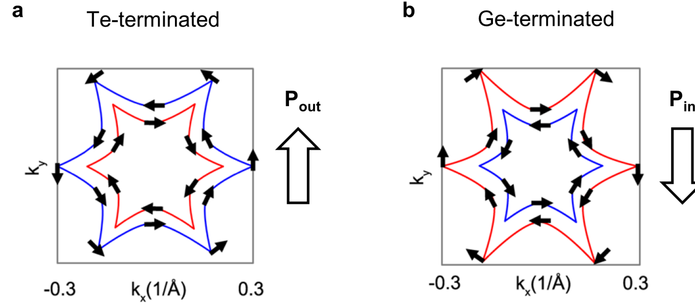

Figure 4.6: ***a*** *Schematic picture of the spin texture of the main bulk Rashba bands of* S_{Te} *with outward polarization, obtained from Fig. 4.5**a**-**b** at -0.5 eV binding energy. The in-plane projection of the spin is represented with black arrows.* ***b*** *Similar calculation for* S_{Ge}*, with inward polarization. The theoretical CEM predict the inversion of the bulk spin texture upon polarization reversal. Adapted from Ref. [181].*

ARPES measurements

In the following we will compare the experimental bands of S_{Te} and S_{Ge} with the calculated ones, identifying bulk and surface structures. In ARPES experiments, electrons with a certain $\kappa_\perp$ normal to the sample surface are photo-emitted depending on the photon energy ($h\nu$), according to Eq. 2.23. Then, by resolving the electrons by their photo-emission angle along the dispersing direction of the analyser, the intensity spectrum maps the bands dispersion along the in-plane wave-vector $\kappa_\|$ projected on the analyser axis (Sec. 2.2.2).

In order to probe the electronic states near the Z point, the value of $h\nu$ must be properly selected according to Eq. 2.23. For convenience, the expression of $\kappa_\perp$ is reported here:

$$k_\perp = \sqrt{\frac{2m}{\hbar^2}(h\nu - \Phi - E_B + V_0)} \tag{4.1}$$

Assuming that we want to collect electrons with kinetic energy in the range 15-25 eV, a $k_\perp = 3\Gamma Z = 2.73\text{Å}^{-1}$ would correspond to $h\nu$= 18 eV (considering V_0= 15 V, ϕ= 4.3 eV and E_B= 0 from previous measurements and calculations). This is also supported by ARPES dispersion along ZA acquired with different $h\nu$ (i.e. k_z), shown in Fig. 4.7.

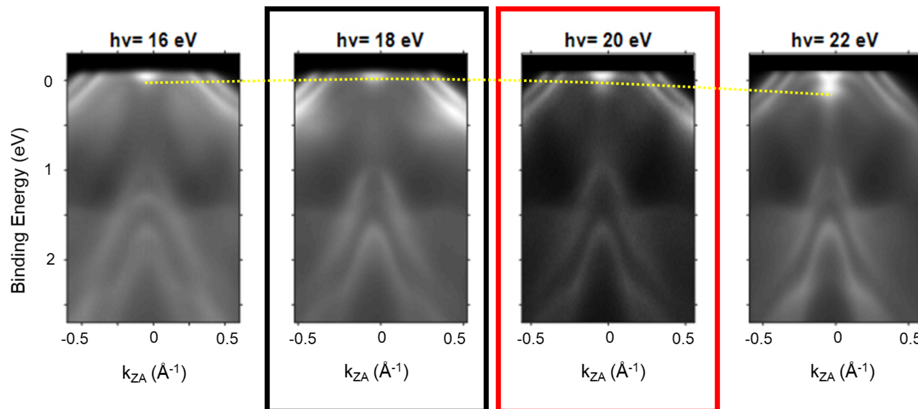

Figure 4.7: *Bands dispersion of* S_{Te} *along ZA at different photon energies (*$h\nu$*). The black box embraces the measurement at* $h\nu$*= 18 eV, which corresponds to a normal emission from Z (the valence band is located at the lowest position in binding energy in agreement with theoretical calculations). The red box highlights the bands at the photon energy chosen for the ARPES and SARPES investigation of* S_{Te} *and* S_{Ge}*.*

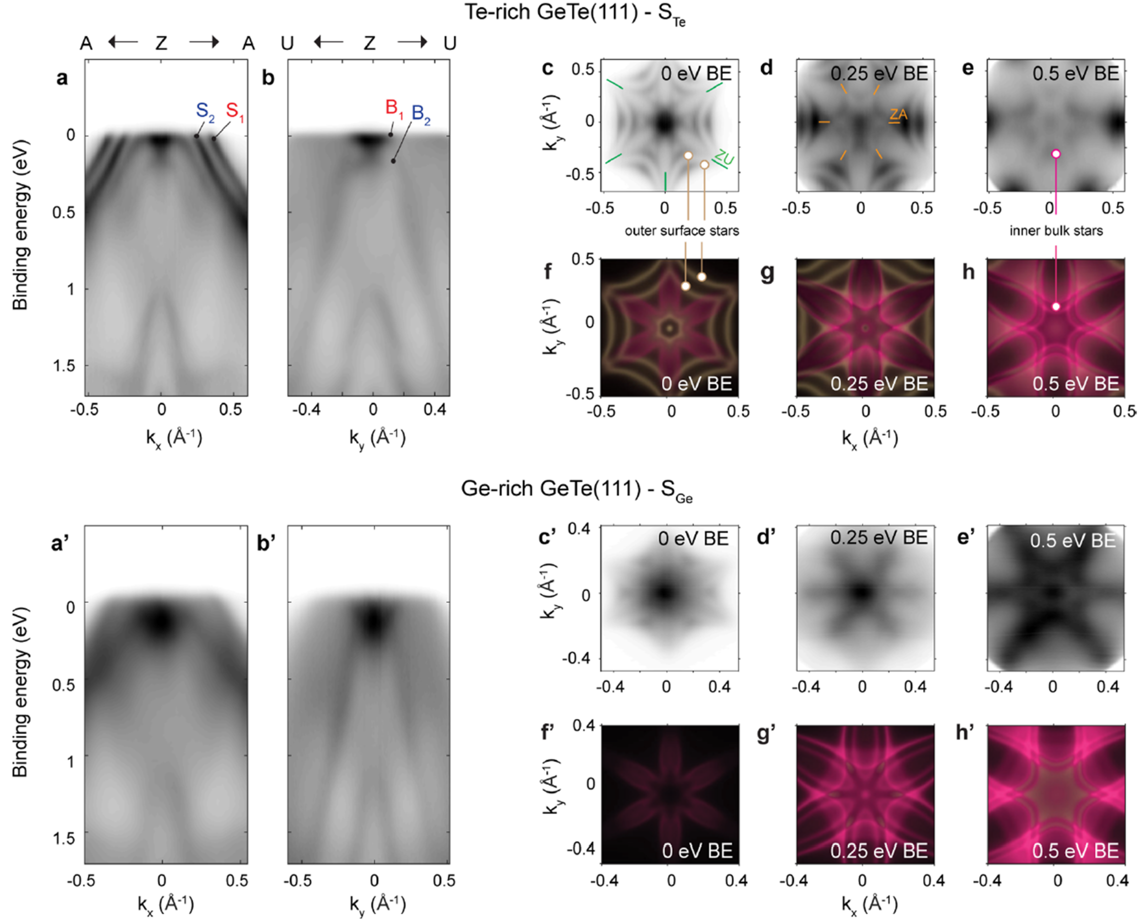

Figure 4.8: *ARPES measurements of Te-rich (S_{Te}) and Ge-rich (S_{Ge}) samples. Panels* **ah** *are referred to S_{Te} displaying outward polarization,* **a'-h'** *to S_{Ge} polarized inwards.* **a-a'**, **b-b'**, *Bands dispersion measured along the high symmetry directions of the first Brillouin zone, ZA (k_x) and ZU (k_x). (**c-e**) Constant energy maps of S_{Te} at 0, 0.25, and 0.5 eV binding energy, compared with the Corresponding calculated maps (**f-h**), where yellow and pink states indicate surface and bulk states, respectively. Panels* **c'-h'** *are the equivalent of* **c-h** *but referred to S_{Ge}. Adapted from Ref. [181]*

The Fermi level cuts the bands outlining that GeTe is a *p*-doped degenerate semiconductor (Sec. 1.5). The yellow dotted line indicates the evolution of some bulk features from $h\nu$= 16 eV to $h\nu$= 22 eV. The crossing of the bulk bands is higher in binding energy at $h\nu$= 18 eV, while it drops below the Fermi level for higher or lower values of $h\nu$. It follows that 18 eV is the energy which excites electrons from Z. In agreement with previous studies on GeTe [60], we used $h\nu$= 20 eV (red rectangle) for our investigation, as it allows to better appreciate the Rashba features which instead are cut by the Fermi level at 18 eV. The shift of $\sim$0.07 Å^{-1} from Z is small enough for a comparison of the data with the calculated bands.

The result of ARPES measurements at $h\nu$= 20 eV along ZA (k_x) and ZU (k_y) on both S_{Te} and S_{Ge} are shown in Fig. 4.8. Panels **a-h** and **a'-h'** refer to S_{Te} and S_{Ge}, respectively.

In the dispersion along ZA of S_{Te} (panel **a**), intense surface Rashba bands can be distinguished near the Fermi level (S_1 and S_2). This this is also clear from the theoretical calculations of Fig. 4.5**a**, where similar bands of surface character can be identified. Besides, this type of bands were already measured by ARPES in Ref. [60] and superimposed to the calculated ones. Along ZU instead (panel **b**), those bands are not visible for k_x< 0.5 Å^{-1} and only the bulk structures B_1 and B_2 are present. The symmetry of surface states can be better appreciated from the CEM in panels **c-e**. In the cuts at 0 eV an 0.25 eV (panels **c-d**), a pair of outer Rashba split bands with sixfold symmetry is oriented with "arms" along the ZU directions (green lines), where S_1 and S_2 cross the

Fermi level at large momenta. These features are also present in the calculated maps (panels **f-h**), where the yellow states are related to surface (pink states to bulk ones). At 0.25 eV (panels **d-e**), a couple of bulk Rashba split bands appears at smaller momenta corresponding to B_1 and B_2. The bulk states have the same hexagonal symmetry, which is rotated by 30 ° with respect to the surface states (i.e. with arms along ZA, indicated by orange ticks in panel **d**). This picture is confirmed by theoretical CEM, where the outer "star" is of surface nature, the inner features are ascribed to bulk states (panels **g-h**). A completely different scenario is found for S_{Ge} (Fig. 4.8**a'-h'**). In agreement with theory in Fig. 4.5, the surface bands S_1-S_2 are not visible at the Fermi level, neither in the bands dispersion of panels **a'** and **b'** nor in the constant energy maps (panels **c'-h'**). On the contrary, only the bulk bands B_1 and B_2 are observed in the carpets and they quite similar to those of S_{Te} (along ZU where they are more visible). This is confirmed by the absence of the outer star in the constant energy maps. Besides, the features measured at 0.25 eV (panel **d'**) reflect the symmetry of bulk Rashba states, showing a similar star as the inner one of S_{Te} (panels **d-e**).

The ARPES investigation thus allowed to verify that Te- and Ge- rich samples have a bands structures reproducing those calculated by DFT for Te- and Ge- terminated surfaces with outward and inward polarization. Moreover, the identification of the bulk Rashba states in S_{Te} and S_{Ge} is the fundamental ingredient for the mapping of the spin texture in the two cases.

4.1.3 Spin-resolved ARPES of bulk Rashba bands

This work goes beyond the work done by M. Liebmann, C. Rinaldi *et al.* [60], in which the the spin texture was mapped only for surface states. We mapped the bulk states depending on their wave-vector and spin orientation by SARPES. The 3D reconstruction of the spatial orientation of the photo-emitted electron's spin is performed through the combined use of two orthogonal VLEED detectors (see Sec. 2.2.3 for more details). The magnetization of the polarimeter sets the quantization axis for the spin, and it can be fixed either in-plane (x, y) or out-of-plane (z). Hence, one of the two detectors is sensitive to P_x and P_z, the other one to P_y and P_z. The value of the polarization along one defined direction can be obtained by subtracting the intensities at

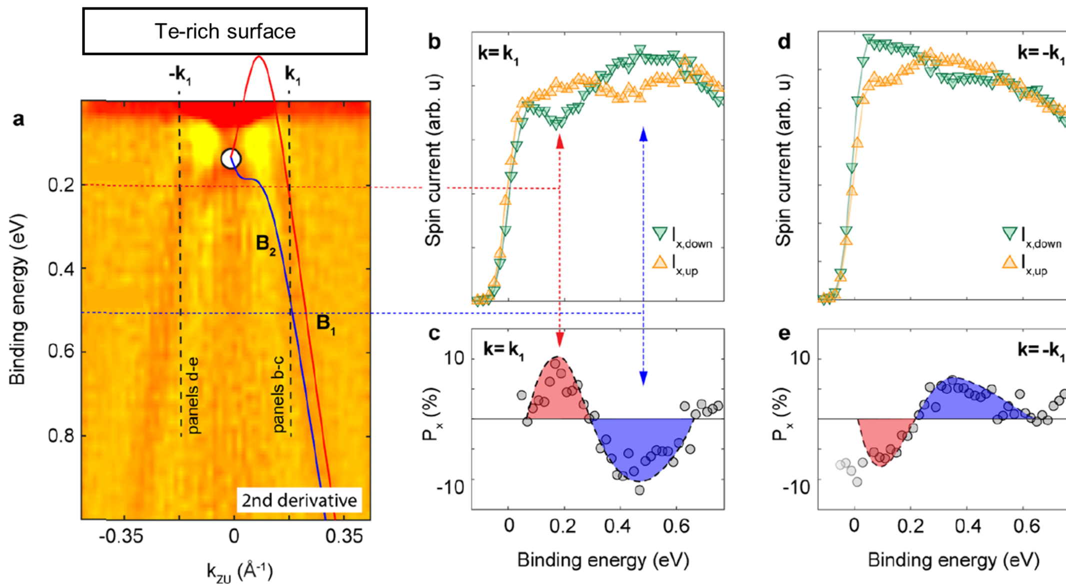

Figure 4.9: *SARPES of Te-rich surface.* ***a*** *Bands dispersion along ZU obtained by second derivative of ARPES carpet.* ***b*** *SARPES measurement of spin current at wave-vector* $\boldsymbol{k}_1$ *indicated by dashed lines in panel* ***a***. ***c*** *corresponding calculated spin polarization. The magnetization axis of the polarimeter is set along x to filter electrons' spin projection along ZA. Red and blue arrow highlight the peaks of* P_x *which correspond to the intersections of* $\boldsymbol{k}_1$ *with* B_1 *and* B_2*, respectively.* ***d-e*** *SARPES measurement of* P_x *performed at* -$\boldsymbol{k}_1$*. Adapted from Ref. [181].*

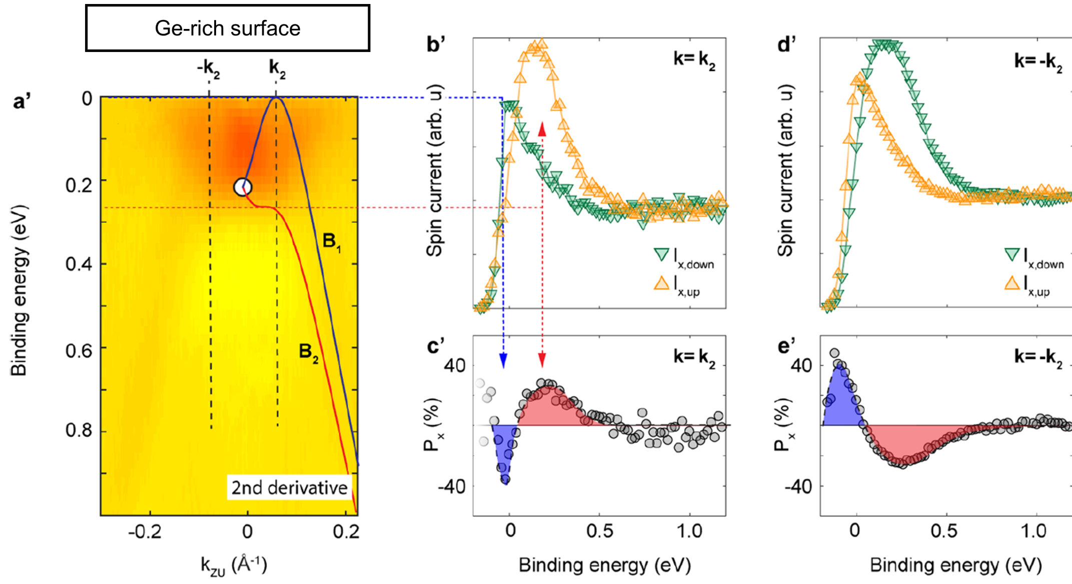

Figure 4.10: *SARPES of Ge-rich surface.* ***a*** *Bands dispersion along ZU obtained by second derivative of ARPES carpet.* ***b*** *SARPES measurement of spin current at wave-vector* $\mathbf{k}_2$ *indicated by dashed lines in panel* ***a****.* ***c*** *corresponding calculated spin polarization. The magnetization axis of the polarimeter is set along x axis to filter electrons' spin projection along ZA. Red and blue arrow highlight the peaks of* P_x *which correspond to the intersections of* $\mathbf{k}_2$ *with* B_1 *and* B_2*, respectively.* ***d-e*** *SARPES measurement of* P_x *performed at -*$\mathbf{k}_1$*. Adapted from Ref. [181].*

a given wave-vector and energy (I^+ and I^-), for two opposite orientations of the magnetization. This method allows to eliminate experimental asymmetries. The calculation of the polarization is discussed more in details in Sec. 2.2.3.

The spin filtered spectra (I_+ and I_-) of both S_{Te} and S_{Ge}, are shown in Fig. 4.9 and Fig. 4.10, respectively. The wave-vector is fixed along the direction ZU (i.e. along k_y), along which bulk bands can be better distinguished from surface states. Indeed we have previously discovered that, while S_{Ge} shows only bulk states around the Fermi level, in S_{Te} surface states are present and along ZU they are pushed to wave-vectors larger than the probed window. The bands dispersion along ZU of S_{Te} and S_{Ge} are superimposed to the main calculated bulk bands B_1 and B_2 (panel **a** of Fig. 4.9 and Fig. 4.10). This process is helped by computing the second derivative of the spectrum, as typically done in ARPES in order to enhance the contrast of the bands with respect to the noisy background. The superposition of the bands permits to assign the measured spin polarization signals to specific positions of the wave-vector along ZU. Spin polarized intensities of S_{Te} and S_{Ge} were measured at $\pm\mathbf{k}_1$ and $\pm\mathbf{k}_2$, respectively. These values are also reported in Fig. 4.5, for a direct comparison with the DFT calculated bands. Due to the orthogonality between the spin and the wave-vector in Rashba systems (Sec. 1.2), only the in-plane polarization P_x was expected to be different from zero. Hence, the spin resolved photoemitted current was measured versus the electrons binding energy, by setting the magnetization of the VLEED polarimeter along ZA (x axis).

In S_{Te} (Fig. 4.9), spin polarized intensities and spin polarization for $\mathbf{k}_1$ (-$\mathbf{k}_1$) are shown in panels **b** and **c** (**d** and **e**). Two distinguishable peaks at about 0.1 eV and 0.5 eV binding energy are visible in the spin-resolved intensity spectra in panels **b** and **d** and in the corresponding polarization P_x in panels **c** and **e**. The peaks are associated to B_1 and B_2, as clear from the intersections of dashed lines in panel **a** with the theoretical bands. According to the spin texture of Rashba bands, spin polarization of B_1 and B_2 is opposite and each band inverts its polarization at opposite wave-vectors ($\pm\mathbf{k}_1$). By assigning an arrow (red for $\mathbf{B}_1$ and blue for B_2), the results of Fig. 4.9 are summarized in a schematic spin texture on the CEM shown in Fig. 4.11**a**: for a Te-terminated sample ($\mathbf{P}_{out}$) the

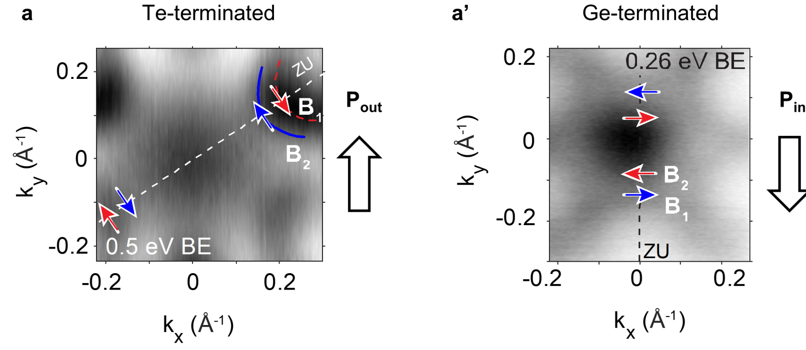

Figure 4.11: ***a** and **a'** Constant energy maps with spin texture of B_1 and B_2 of Te- and Ge-rich surfaces. Arrows are oriented along ZA and the orientation is obtained from the sign of the calculated spin polarization (P_x) of Fig. 4.9 and Fig. 4.10. Adapted from Ref. [181].*

sense of circulation of spins is clockwise for the outer band and counterclockwise for the inner one, in agreement with theory (Fig. 4.6**a**).

The experiment was repeated on S_{Ge} (Fig. 4.10), for which electrons' spin was probed at the wave-vectors $\pm\mathbf{k}_2$. The peaks of the spin polarization P_x of B_1 and B_2 have opposite sign compared to those of S_{Te} (panels **c'**,**e'**). Therefore, the circulation of the Rashba contours of S_{Ge} shown in Fig. 4.11**a'** is inverted with respect to S_{Te}. This is the crucial result of this investigation, which established experimentally a connection between the chirality of spin texture of the bulk Rashba states of GeTe and its ferroelectric state.

For the sake of completeness, the spin components P_y and P_z were also measured by SARPES to perform the full vectorial reconstruction of the spin and confirm that the spin information is fully contained in the P_x signal. The case of S_{Ge} is presented in Fig. 4.12. According to what expected, the spin is mainly oriented in the ZAU plane (P_z= 0) and it is orthogonal to the wave-vector (P_y= 0). Finally, the absence of surface states in S_{Ge} allows to estimate the Rashba splitting (E_R) as the energy separation between the two peaks of P_x. We obtained a value of $E_R\sim$ 200 meV, in nice agreement with the giant Rashba spin splitting predicted by S. Picozzi (E_R= 250 meV [12]). The Rashba splitting is giant compared to 2DEG or other bulk polar materials as summarized in Table 4.1. Such large value emerges from the strong SOC experienced by the free charges in the crystal combined with the ferroelectric polarization. Hence, the related spin-charge interconversion mechanisms (SHE and REE) are expected to be also giant.

Material	E_R (meV)
GeTe (bulk)	200
BiTeI (bulk)	100
Bi(111) (surface)	14
Au(111) (surface)	2.1

Table 4.1: *Rashba energy splitting (E_R) for different systems.*

To sum up, we developed a surface preparation method as a tool to control the spontaneous polarization (outward or inward) at the surface of GeTe in a UHV environment depending on the termination of the sample. The SARPES investigation on two samples with different termination demonstrate the ferroelectric switching of the spin texture in GeTe, in agreement with DFT calculations. Based on the demonstration that the ferroelectric state can be controlled by electric fields either applied with a tip or by a macroscopic gating (Ch. 3), the remanent switching of the spin texture can be now achieved in devices with electric fields. For instance, a biased AFM tip can be used to write nanometric regions with opposite spin textures. The domains pattern shown in Fig. 3.2 is an example of a spatially periodic SOC system, in which the transmission of a charge current

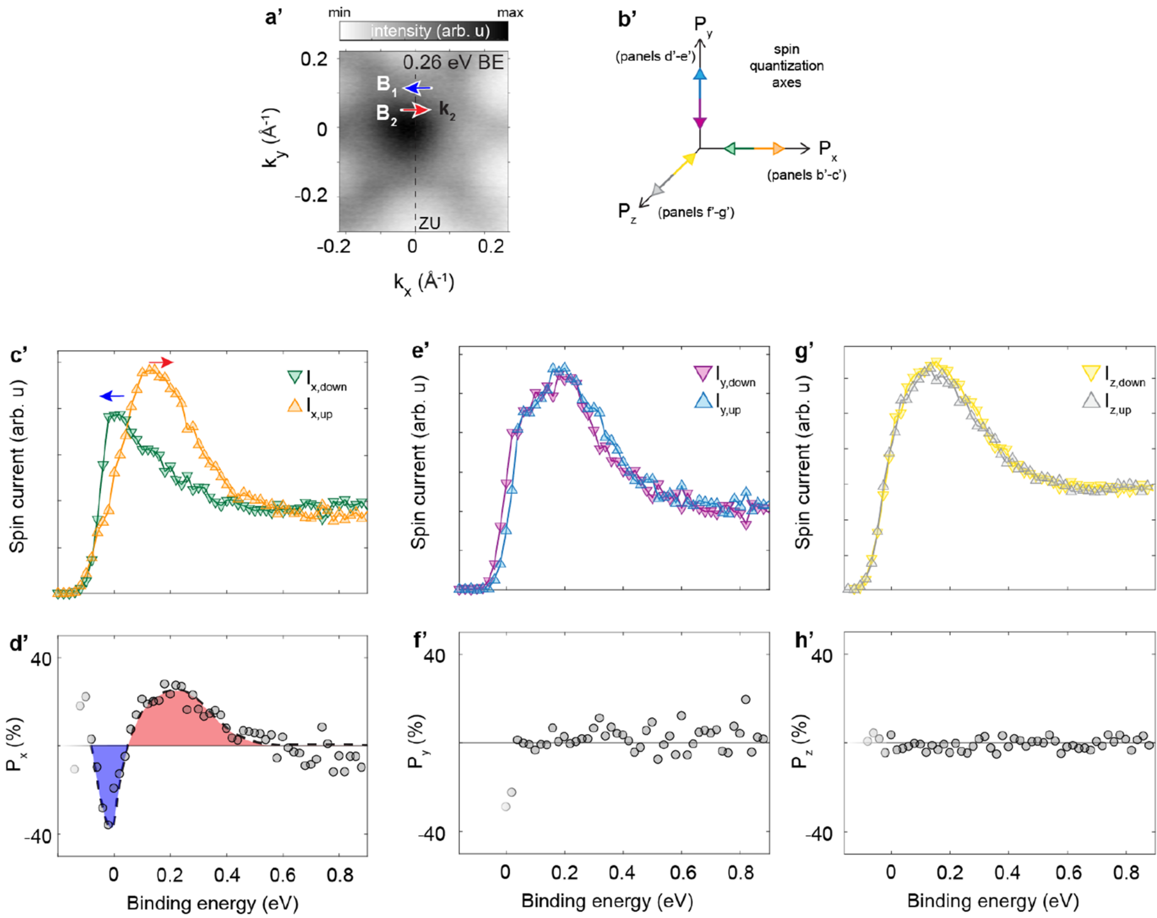

Figure 4.12: *3D reconstruction of the spin in S_{Ge} by SARPES. **a'** Constant energy map for E_B= 0.26 eV. $\boldsymbol{k}_2$ is the wave-vector chosen for the measurement of the spin polarization. **b'** Reference frame for the spin polarization that is formed via the combined operation of the two VLEED. The spin filtered intensities and the computed spin polarization are shown in panels **c'-d'** for quantization axis along x, **e'-f'** along y and **g'-h'** along z.*

flowing perpendicularly to the ferroelectric stripes would depend on its spin polarization (parallel or perpendicular to the stripes) [219, 220]. This is just an example of how ferroelectricity can be exploited as a buffer for designing SOC patterns and manipulate the carrier transport in the material within a reconfigurable nano-device.

However, the relevance of the concept of FERSC goes much further. Rashba SOC triggers spin-charge conversion mechanisms, including Intrinsic Spin Hall Effect [77] and Rashba Edelstein Effect [100] (Sec. 1.3.2 and Sec. 1.3.3, respectively). Spin charge conversion can be tuned through the Rashba parameter, hence via the external electric field. The main advantage of the bulk Rashba effect of GeTe with respect to a 2DEG is clearly related to the remanence and of the Rashba spin texture and its inversion upon ferroelectric switching, properties that would be reflected in the spin-charge interconversion. From the device perspective, GeTe could be used used for low-power generation, manipulation or detection of spin currents controlled by ferroelectricity.

The experimental investigation of spin-to-charge conversion in GeTe as well as its modulation upon ferroelectric switching is the subject of the next two sections.

4.2 Investigation of spin-to-charge conversion

In this work we employed spin pumping by ferromagnetic resonance for the investigation of spin-to-charge conversion, such as Inverse Spin Hall Effect (ISHE) and Inverse Rashba Edelstein Effect (IREE). The technique is based on the injection of a spin current from a ferromagnetic layer excited at its resonance frequency into the material under investigation, and a simple electrical detection of the charge current produced (the details of the technique can be found in Sec. 2.3.2).

For this kind of measurements we employed a Fe/GeTe/Si heterostructures, in which the Fe layer was used as a spin injector. At the same time, Fe served as a metallic top contact for the electrical gating. The following section deals with the fundamental aspects regarding the growth and the quality of epitaxial Fe/GeTe bilayers, in view of spin pumping measurements. The growth of the samples was carried out by Alessandro Novati in Polifab, and we performed spin pumping experiments in Spintec (CEA, Grenoble), with Paul Noël, Laurent Vila and Jean-Philippe Attane.

4.2.1 Growth of Fe/GeTe heterostructures

Iron was selected as a ferromagnetic spin injector because of the relatively good lattice matching between bcc Fe(111) and GeTe ($a_{\text{Fe, bcc}}$= 2.8665 Åand a_{GeTe}= 4.174 Å, with a strain ϵ= 2.9 %), the fundamental ingredient for epitaxy. The deposition was performed by in UHV by Molecular Beam Epitaxy (MBE, Sec. 2.4.1) on clean GeTe samples obtained with well-established procedure presented in Sec. 2.4. As demonstrated in our work in Ref. [221], the deposition of Fe tends to suppress Rashba surface states of GeTe [221]. This would allow to study the polarization dependent bulk Rashba spin-charge conversion effect, the ultimate goal of this work.

The growth direction and the crystalline quality of the Fe layer are checked by comparing the LEED patterns of the Te-terminated GeTe surface (panel **a** of Fig. 4.13) and the one after the deposition of 5 nm of Fe (panel **b** of Fig. 4.13). The diffraction pattern of Fe reflects the hexagonal symmetry of the GeTe surface, thus indicating an epitaxial Fe layer exposing the (111) surface. The samples are protected against oxidation by a 3 nm-thick Au layer.

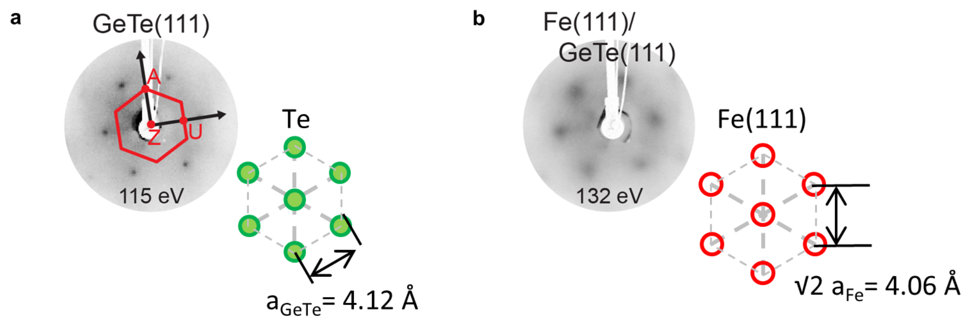

Figure 4.13: *LEED patterns of* ***a*** *GeTe(111) surface and* ***b*** *Fe(111)/GeTe(111). The thickness of Fe layer is 5 nm, the thickness of GeTe is 75 nm. Adapted from Ref. [217].*

The spin current pumped from Fe at FMR into GeTe is strongly dependent on the magnetic properties of Fe, including the effective saturation magnetization (M_{eff}) and the Gilbert damping (α) that can be measured by broadband FMR (Sec. 2.3.1).

Due to the in-plane anisotropy of the hexagonal (111) surface of Fe on GeTe, one might expect a different FMR response if the magnetization is along ZA or ZU. Therefore, the measurements were performed on a Fe(15 nm)/GeTe(20 nm) sample, cut in elongated stripes with longitudinal axis along ZA (ZU) and static magnetic field along ZU (ZA). The result is summarized in Fig. 4.14.

Panel **a** shows the FMR curves measured with different *rf* frequencies (f), referred to the sample axis along ZU (the same experiment was carried out for a sample along ZA). The resonance field (H_{res}) and the peak-to-peak line-width (ΔH_{pp}) of each spectrum were extracted by fitting the data

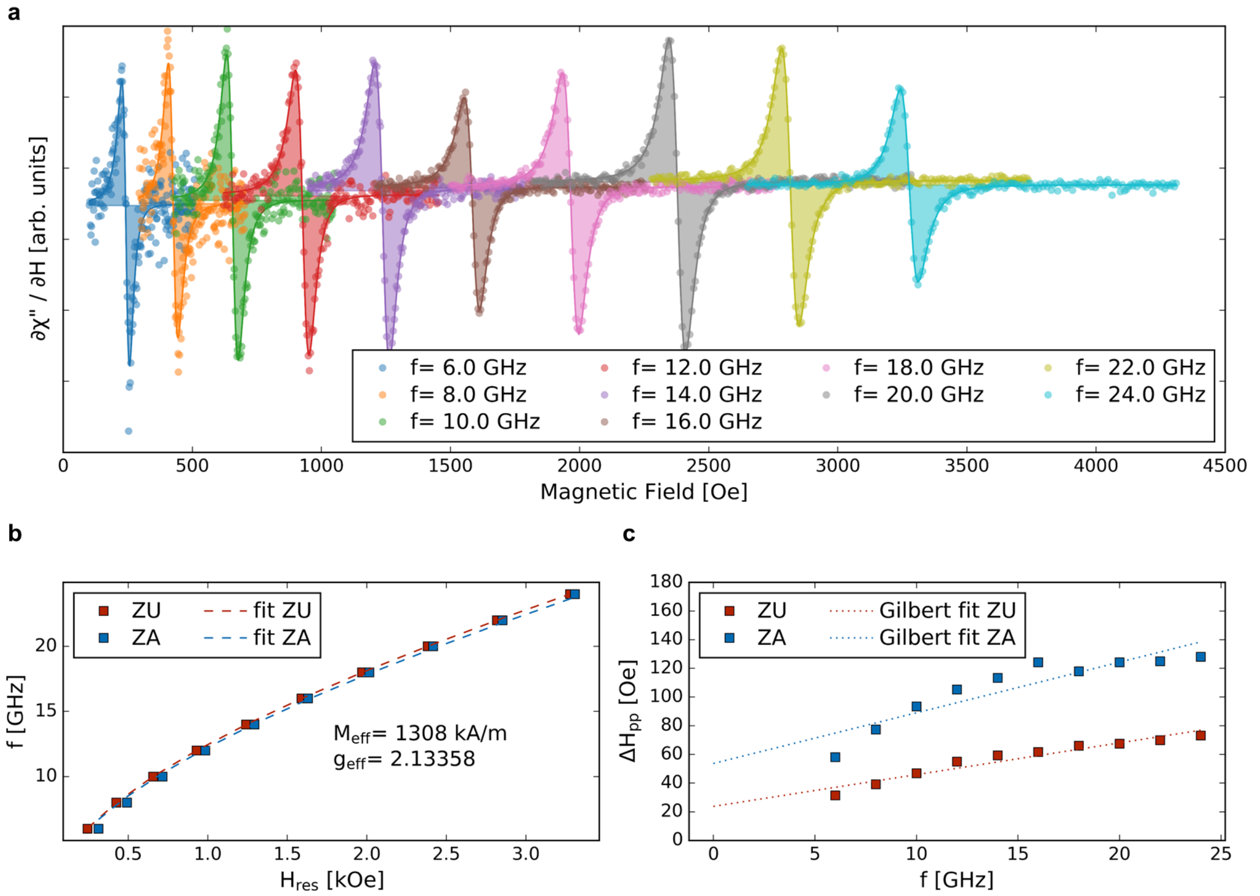

Figure 4.14: ***a*** *FMR spectra at different rf frequencies measured on Si/GeTe(15 nm)/Fe(20 nm)/Au(3 nm) along ZU with the broadband FMR setup described in Sec. 2.3.1.* ***b*** *Excitation frequency (f) versus resonance field (H_{res}) for both ZA and ZU directions. Data are fitted by the Kittel formula (Eq. 2.40) giving similar result for the two directions. The average value of effective saturation magnetization (M_{eff}) and effective g factor are reported in the graph.* ***c*** *Peak-to-peak line-width of the FMR spectra (ΔH_{pp}) versus rd frequency for both ZA and ZU directions.*

with an anti-Lorentzian line-shape, as explained in Sec. 2.3.1. H_{res} and ΔH_{pp} versus f are reported in panels **b**-**c**. H_{res} is well fit by the Kittel formula (Eq. 2.40), which gives M_{eff}= 1308 kA/m and g factor g_{eff}= 2.13, in quite good agreement with Ref. [222] and VSM data (not shown). The FMR line-width (panel **c**) cannot be fit with Eq. 2.43, as it clearly increases non-linearly with f. This is often related to two-magnons scattering. Nonetheless, the expression of ΔH_{pp} for two-magnons scattering derived in Ref. [223, 224] is not suitable to fit our experimental data.

A nonlinear line-width can be also caused by the magneto-crystalline anisotropy [225], which is indeed detected by VSM measurements. Our data quite well reproduce the frequency dependence reported in Ref. [225], suggesting anisotropic damping as the leading mechanism.

The main outcome is that the estimation of the spin current injected into GeTe from Fe is not straightforward, because of the complex dynamics of the magnetization. The damping parameter of Fe/GeTe could be extracted with the model developed by L. Chen *et al.* [225], provided that anisotropy, demagnetization and surface anisotropy fields are known. For such a purpose, the full in-plane and out-of-plane angular dependence of the FMR will be carried out in the future. Moreover, as discussed in Sec. 2.3.2, the extra-damping related to the spin injection is obtained by subtracting the damping to the one of a Fe/Si reference system. Anyhow, epitaxial Fe(111) on Si(111)-$(\sqrt{3}\sqrt{3})R30°$-Sb substrates requires the engineering of the growth conditions (e.g. to avoid the formation of silicates at the interface) and at the moment they cannot be prepared in our UHV systems. Finally, the expression of the charge current by ISHE is proportional to the product

between the spin Hall angle and the spin diffusion length by Eq. 2.55. Hence, the estimation of the spin Hall angle would be based on the study of the spin pumping measurement versus the thickness of GeTe, which could be reduced by the annealing. The growth of a reference sample and the accurate calibration of the thickness of GeTe needed for such study will be subjects of further investigations beyond the present work.

For these reasons, it is not possible at this stage to quantitatively estimate the spin Hall angle of GeTe. Nevertheless, the efficiency of spin-charge conversion can be inferred at a first order approximation from the intensity of the produced charge current to be compared with that of reference systems, such as CoFeB/Pt. In the following, we consider the charge current produced during a spin pumping FMR experiment as the efficiency of spin-to-charge conversion in GeTe.

4.2.2 Spin pumping in Fe/GeTe bilayers

Based on the **k**-anisotropy and the ferroelectric dependence of the Rashba spin texture, we can expect that the spin-to-charge conversion efficiency in GeTe is a function of both the polarization state ($\mathbf{P}_{out}$ or $\mathbf{P}_{in}$) and the crystallographic direction (ZA or ZU).

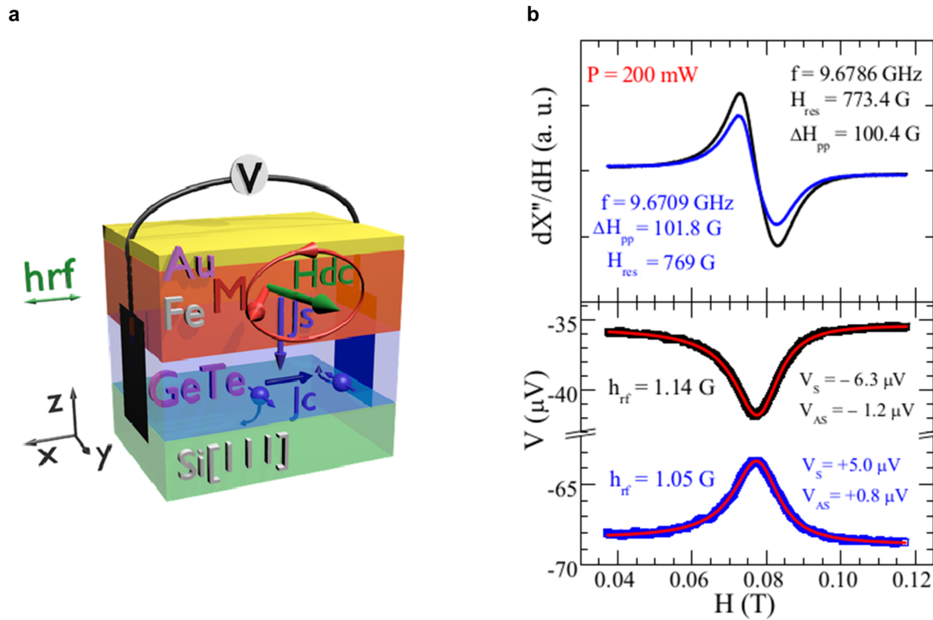

Figure 4.15: ***a*** *Sketch of spin pumping experiment performed on Au(3 nm)/Fe(5 nm)/GeTe(75 nm)/Si. The dc magnetic field is applied in plane and transverse to the sample, while the rf filed is aligned with the axis of the slab.* ***b*** *FMR (top) and spin pumping open loop voltage (bottom) acquired on the same sample as in panel* ***a****. The experiment is performed with positive (black and red curves) and negative (blue and purple curves) saturating magnetic field with fixed power of the rf source of about 200 mW.*

A first study of spin pumping was carried out in 2016 by C. Rinaldi *et al.* [217] on a Fe/GeTe bilayer at its pristine polarization state. The sketch in Fig. 4.15**a** reminds the geometry of the experiment. The ferromagnetic resonance of Fe is excited by a magnetic field perturbation $\mathbf{h}_{rf}$. In general, $\mathbf{h}_{rf}$ is orthogonal to a static saturating magnetic field ($\mathbf{H}_{dc}$). A spin current is generated by Fe when the ferromagnetic resonance condition is met. The FMR frequency is tuned to the excitation frequency by setting the *dc* field at the value H_{res}, provided by the Kittel formula (Eq. 2.40). The generated spin current is injected through the interface ($\mathbf{j}_s$), with spin polarization along the *dc* field (y). Eventually, a charge current produced by ISHE or IREE $\mathbf{j}_c$ flows in GeTe along the longitudinal axis x. In a open-loop configuration, the current leads to a voltage between the two opposite edges of the slab, detected by a voltmeter (Sec. 2.3.2). The role of the crystallographic direction was investigated on slabs with longitudinal axis either along ZA or along ZU. In such a

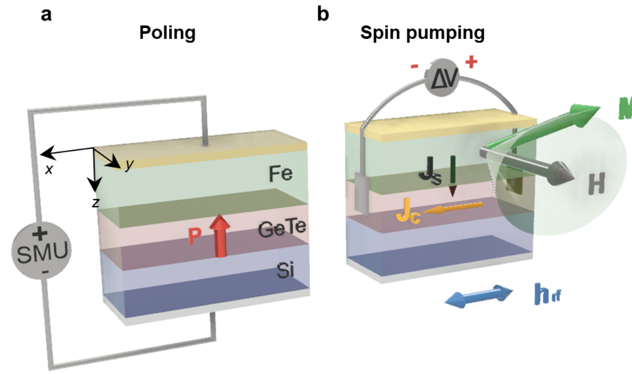

Figure 4.16: *Sketch of the setup needed for the experiment on Au(3 nm)/Fe(15 nm)/GeTe(20 nm)/Si, combining ferroelectric switching of GeTe and detection of ISHE at remanence by spin pumping.* ***a*** *the electrical circuit employed for macroscopic gating of GeTe. The back-electrode is made by Ag-paste below the Si substrate, while the Fe/Au bilayer serves as top-electrode. A positive (negative) voltage applied to the back-contact stabilizes an outward (inward) polarization.* ***b*** *Spin pumping from Fe into GeTe and detection of lateral open loop voltage.*

way, the direction of the produced charge current was set along the two non-equivalent directions (while the spin current was fixed by the geometry of the experiment). Fig. 4.15**b** reports the result of the room temperature experiment on a slab oriented along ZA [217]. The plot reports the FMR spectra in the top panel, and the open loop voltage (recorded simultaneously) in the bottom panel, for two opposite directions of the saturating field (i.e. of the polarization of the spin current). The shape of the peak voltage is mostly symmetric, as expected from ISHE and IREE signals. The negligible asymmetric component of the recorded peaks indicate that spin-charge conversion signal could play a dominant role over spurious spin-rectification effects. The sign of the peak depends on the direction of the *dc* field, being negative for $H>0$ and positive for $H<0$. The peak inversion is in line with the symmetry of spin-charge conversion (the charge current is proportional to the vector product between the spin current and the spin polarization vector as stated by Eq. 2.54). On the other hand, similar experiments performed on a slab oriented along ZU revealed a negligible current production, which could be interpreted as a preliminary indication of a some anisotropy in the system.

This was the first evidence that spin-to-charge conversion in GeTe is feasible. Nonetheless this experiment was not conclusive, since spin-charge conversion was performed without controlling the ferroelectric state of GeTe with a gate. The objective of this thesis is to study spin-to-charge conversion as function of the polarization state.

4.2.3 Gating Inverse Spin-Hall Effect

The control of the ferroelectric state of GeTe opens the way to the investigation of the tunability of the spin-charge interconversion. In this work, spin pumping was performed as function of the ferroelectric state controlled by means of a electric gating. According to the concepts developed in Ch. 3, the polarization can be monitored by the resistive modulation of the heterostructure (ferroresistive switching).

Combined resistive switching and spin pumping experiment

The experiment was conceived in two sequential steps, represented in Fig. 4.16.

The first one is the setting of a certain polarization state (panel **a**), that is performed by a short writing voltage pulse ($t_{\mathrm{pulse}} \sim 5$ ms) between the top Au/Fe electrode and the bottom Ag contact. The ferroelectric state is monitored through the resistance between these two electrodes, as in Ch. 3. In this geometry of the electrodes, the resistive switching (RS) of the heterostructure is controlled by

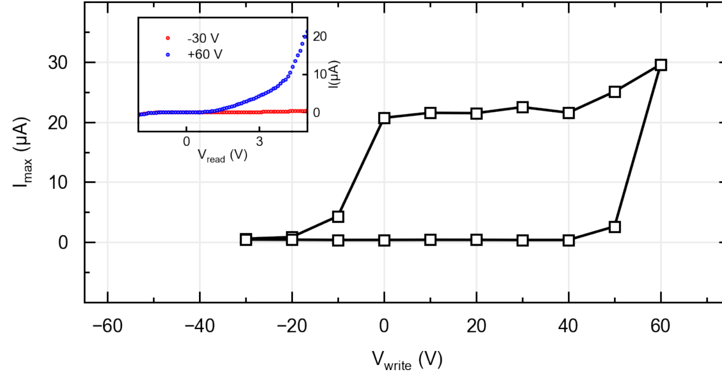

Figure 4.17: ***a*** *Current-voltage curves of the heterostructure Au(3 nm)/Fe(15 nm)/GeTe(20 nm)/Si measured at remanence after the application of two saturating voltage pulses (V_{sat}^{+} = 30 V, V_{sat}^{-} = -80 V).* ***b*** *Top-bottom resistive loop of Si/GeTe/Fe/Au heterostructure. The maximum forward bias is plotted versus the writing voltage.*

the interfacial resistances of Si/GeTe and the GeTe/Fe. Between those interfaces, Si/GeTe junction is expected to give the major contribution. Indeed, the marked difference of doping of the two materials (p= 3 · 10^{20} cm^{-3} for GeTe while p= 2 · 10^{15} cm^{-3} for Si) and the larger difference between their work functions/electron affinities (χ_{GeTe}= 4.8 eV, $\chi_{Si111} \sim$ 4 eV, $\phi_{Fe111} \sim$ 4.81 eV) lead to a Shottky barrier and a rectifying I-V curve, as observed for these samples (inset of Fig. 4.17).

The RS loop of Au/Fe/GeTe/Si heterostructure is shown in Fig. 4.17**b**, where the maximum forward current is plotted versus the writing voltage level. In this structure, the bias needed for the ferroelectric switching is of the order of tens of volts and it is asymmetric with respect to the writing voltage, since V_c^+ = -20 V and V_c^- = 50 V. Such asymmetry reflects the one of the current-voltage characteristic of the diode, thus confirming that ferroelectric switching requires a minimum amount of energy that depends on the power (i.e. on the product $V \cdot I$, as calculated in Eq. 3.14). Therefore, we can ascribe the resistive switching to the foerroelectric one, without further PFM investigations.

The possibility of controlling the polarization of GeTe by means of bipolar RS through the Si substrate allows not only to apply a perfectly vertical electric field that is needed for proper FE switching but most importantly it allows for the measurement of the spin-to-charge conversion by means of spin pumping technique (Fig. 4.16**b**).

Initially, the experiments were run at T= 100 K in He-saturated cavity, in order to avoid oxidation of the Fe layer with poling. Then, the temperature behaviour is measured to see whether the effect is workable at room temperature. Note that the spin-to-charge conversion measured by spin pumping at 100 K is expected to be of the same order of magnitude as at room temperature, because ferroelectricity is stable up to 700 K.

Polarization dependence of the ISHE

Combining resistive switching and spin pumping experiments on GeTe/Fe epitaxial bilayers, we investigated the ferroelectric control of spin-to-charge conversion and the influence of the crystal direction.

Fig. 4.18 reports the investigation of FMR (panels **a** and **c**) and charge current production (panels **b** and **d**) versus FE polarization, for slabs oriented along ZA and ZU. As evident in panel **b**, the current peak is higher in the two saturated states $\mathbf{P}_{out}$ and $\mathbf{P}_{in}$ compared to the the signal obtained from the unpoled sample (green line). The sign of the charge current changes according to the FE polarization, while the signal from the pristine sample indicates a coexistence of outward and inward domains to be associated with a low spin pumping signal. For the low conductivity state corresponding to $\mathbf{P}_{out}$ (see Fig. 4.17), the spin pumping peak is negative when the charge current is produced along ZA (panel **b**), with a normalized current production of -0.011 A · mT^2 · m^{-1}. When

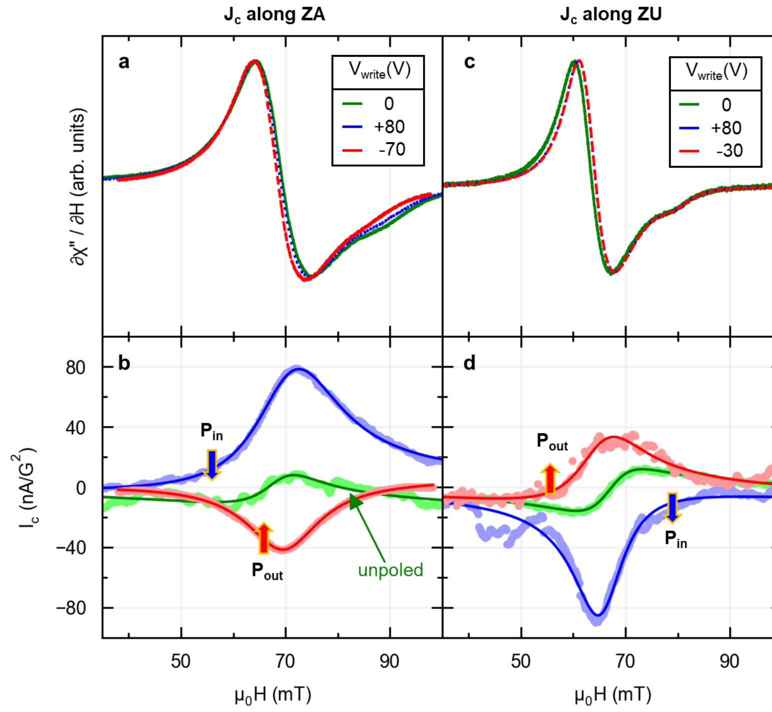

Figure 4.18: ***a*** *FMR spectra and* ***b*** *spin pumping spectra for a GeTe/Fe sample after the application of different poling pulses. The green curve is referred to the pristine state, blue to inward (negative writing voltage) and red to outward (positive writing voltage). The spin current injected is polarized along ZU while the charge current* $\boldsymbol{J_c}$ *is along ZA. The spin pumping peak is positive for the inward, negative in the outward polarization. The small amplitude measured in the initial state is associated to a multi-domain ferroelectric state.* ***c-d*** *Reports a similar experiment as in* ***a-b****, but in this case* $\boldsymbol{J_c}$ *is generated along ZU from a spin current polarized along ZA. The spin pumping peaks are inverted with respect to panel* ***b****, thus indicating the influence of the current direction on the measured signal.*

the ferroelectric polarization is switched to the inward state (high conductivity), the charge current along ZA is positive and equal to 0.019 $A \cdot mT^2 \cdot m^{-1}$. Upon several poling pulses, the current production can be eventually increased up to a maximum value 0.059 $A \cdot mT^2 \cdot m^{-1}$, comparable to the one observed in Pt(15 nm)/CoFeB(15 nm)/Al(3 nm) as shown in Fig. 4.19**a**. This suggests a more uniform polarization state of the GeTe channel with respect to the case presented in Fig. 4.18. Indeed, the electric gating over millimetric areas likely leads to non-uniform polarization states.

To improve the results shown in Fig. 4.18 and obtain larger values of produced current with fully polarized samples, similar measurements can be performed in nanopatterned structures. Alternatively, in Ch. 5 we investigate the possibility of reducing the strong *p*-doping character of GeTe, which would yield to a reduction of the switching currents and favor the FE switching.

Hence, since the current production can reach the same order of magnitude as reference materials in spin orbitronics like Pt, GeTe can be used for its high spin-charge conversion efficiency, but with the precious advantage offered by its reconfigurability by means of the FE polarization. In addition, the result suggests that the current production previously measured on a pristine sample [217] and discussed in Sec. 4.2.2 was low because associated to a non-uniformly polarized sample. For instance, the value of I_c= -0.07 $A \cdot mT^2 \cdot m^{-1}$ for H> 0 s along ZA suggests a multiple domains state, with a slight predominance of outward polarization (negative sign).

We probed the temperature dependence of the produced charge current. Fig. 4.19**b** shows that the amplitude of the produced charge current keeps almost constant from 100 K up to about 300 K. Therefore, spin-charge conversion in GeTe can be exploited in actual architectures operating at room temperature.

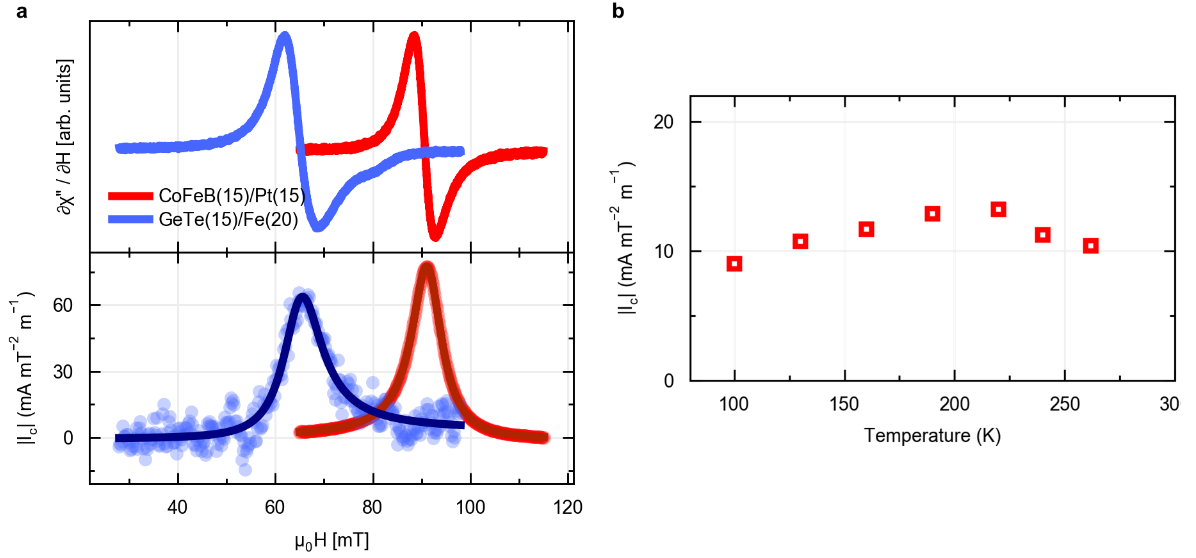

Figure 4.19: ***a*** *Comparison of spin pumping of Pt and polarized GeTe. FMR (top panel) and current production (bottom panel) for CoFeB(15 nm)/Pt(15 nm) and Fe(20 nm)/GeTe(15 nm). The charge current production upon poling reached up to 66 mA $\cdot$ mT^{2} $\cdot$ m^{-1}, a value comparable with that obtained for Pt (77 mA $\cdot$ mT^{2} $\cdot$ m^{-1}).* ***b*** *Temperature dependence of the amplitude of the current production from 100 K up to 270 K.*

The inversion of the spin pumping peak with the FE polarization is the first experimental demonstration that ferroelectricity governs the spin-to-charge conversion via the Rashba bands structure, thus suggesting an intrinsic origin of the effect. Indeed, any other spurious contributions to the spin signal originated from spin-dependent thermoelectric effects in GeTe (e.g. spin Seebeck effect) or AMR phenomena are not expected to reverse neither with voltage pulses nor with FE polarization. The dependence on the crystallographic direction is gained by comparing the measurements with slabs along ZA (Fig. 4.18**a**) and ZU (Fig. 4.18**b**). In the second case the positive (negative) peak is associated to $\mathbf{P}_{\text{out}}$ ($\mathbf{P}_{\text{in}}$). This result is exactly the opposite to what measured along ZA.

4.2.4 Ferroelectric dependent spin Hall conductivity

In order to understand the physical origin of the spin-to-charge conversion in GeTe observed in our measurements, *ab initio* calculations of the spin Hall effect were carried out by our coworkers J. Sławińska, S. Picozzi *et al.* (Sec. 4.2.4).

They investigated the dependence of the spin Hall conductivity (defined in Sec. 1.3.2) of GeTe on the ferroelectric state and on the crystallographic directions.

In a solid, the spin Hall conductivity takes a tensorial expression. σ_{ij}^{k}, where *i* is the direction of the charge current, *j* the propagation direction of the spin current and z the spin polarization axis. The intrinsic spin Hall conductivity is computed with the Kubo formula involving the spin Berry curvature (Eq. 1.23), which in turn depends on the Hamiltonian of the system. Therefore, the construction of a proper Hamiltonian is fundamental.

In two recent works [226, 227], the spin Hall conductivity has been computed from the Hamiltonian of a bulk infinite GeTe. Due to the symmetry of the crystal, σ_{ij}^{k} is function of only four independent components:

$$\sigma_{ij}^{x} = \begin{pmatrix} \sigma_{xx}^{x} & 0 & 0 \\ 0 & -\sigma_{xx}^{x} & \sigma_{yz}^{x} \\ 0 & -\sigma_{zx}^{y} & 0 \end{pmatrix} \sigma_{ij}^{y} = \begin{pmatrix} 0 & -\sigma_{xx}^{x} & \sigma_{yz}^{x} \\ -\sigma_{xx}^{x} & 0 & 0 \\ \sigma_{zx}^{y} & 0 & 0 \end{pmatrix} \quad \sigma_{ij}^{y} = \begin{pmatrix} 0 & \sigma_{xy}^{z} & 0 \\ -\sigma_{xy}^{z} & 0 & 0 \\ 0 & 0 & 0 \end{pmatrix} \tag{4.2}$$

Starting from this expression and considering the case a charge current *x* axis along ZA and *y* along ZU and a spin current polarized along z in both cases, the retrieved spin Hall components are opposite: $\sigma_{zy}^{x} = -\sigma_{zx}^{y}$. This is a signature of the asymmetry of the crystal, the same asymmetry found in the bands structure.

Moreover, the components emerging from the Berry phase calculation are unaffected by the ferroelectric state of GeTe. However, the role of the surface can be crucial, because it incorporates the polarization charges which create an internal electric field (Sec. 1.1). To observe the effect of the polarization-driven electric field, σ_{ij}^{k} was computed modelling GeTe as a truncated system with a well defined polarization, as shown in Fig. 4.20**a**. A suitable real space Hamiltonian was built for an equivalent solid (panel **b**) in which both the electronic properties of the bulk and the matrix elements of the surface slab are retained. In such a way, the macroscopic electric field inside the film could be included in the calculation. The spin polarized bands structure born of such built Hamiltonian show similar Rashba behaviour as for the infinite solid, with opposite spin polarized bands for $\mathbf{P}_{\text{out}}$ (Fig. 4.20**d**) and $\mathbf{P}_{\text{in}}$ (Fig. 4.20**e**). For this system, the four independent elements of the tensor were calculated for both polarizations, as function of the binding energy (Fig. 4.20**f**). It is evident that the spin Hall conductivity components in this case strongly depends on the FE polarization, both in magnitude and sign. In our experiments, the conduction occurs near the Fermi level, approximately in the middle of the grey panel. In this relatively wide energy region, the component σ_{zx}^{y} takes two opposite values for $\mathbf{P}_{\text{in}}$ and $\mathbf{P}_{\text{out}}$. Opposite values are therefore expected for the other component, σ_{zy}^{x}.

4.2.5 Comparison with calculated spin Hall conductivity

The aim of this section is to provide an interpretation for the dependencies of the measured charge current production on both **k** and **P** (Fig. 4.18). As a first step, we should consider that both intrinsic ISHE and IREE could be responsible mechanisms for an intrinsic-type spin-to-charge conversion in GeTe.

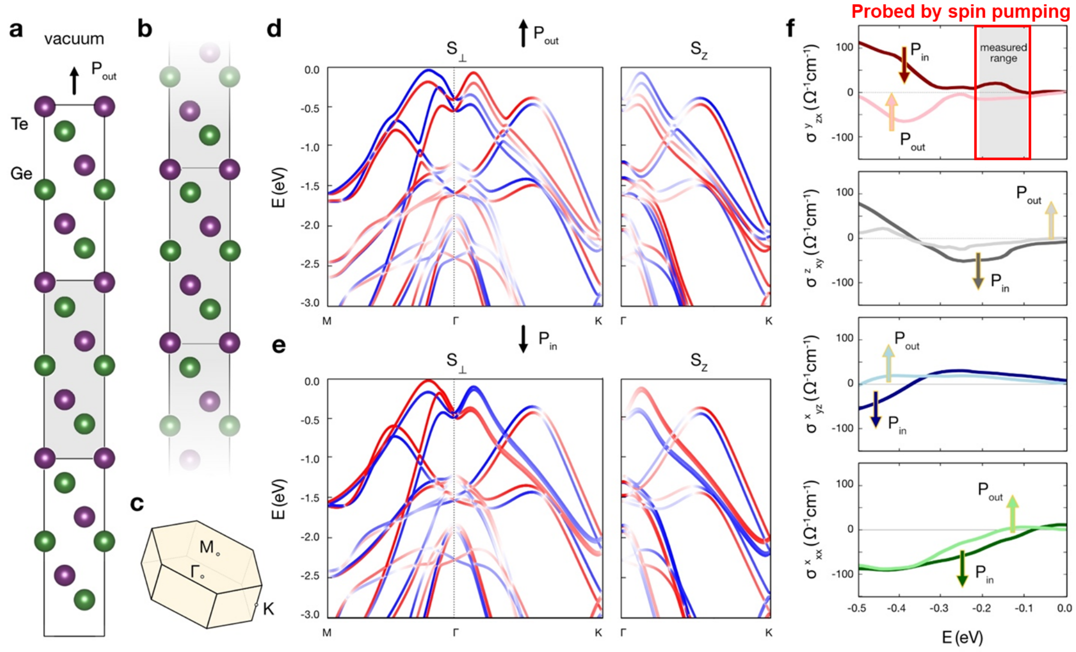

Figure 4.20: ***a*** *Ferroelectric GeTe surface modelled as a slab consisting of three hexagonal bulk unit cells and a large vacuum region. Two opposite signs of polar displacement were included (*$\boldsymbol{P}^{out}$ *and* $\boldsymbol{P}^{in}$*).* ***b*** *Bulk GeTe constructed by applying periodic boundary conditions to the central part of the surface slab defined as the shaded area in panel* ***a****.* ***d****(****e****) Spin polarized bands structure calculated for* $\boldsymbol{P}^{out}$ *(*$\boldsymbol{P}^{in}$*).* ***f*** *Intrinsic spin Hall conductivity components. The component* σ^{y}_{zx} *is the one probed experimentally by spin pumping. Spin Hall conductivity components are modulated by the FE state, eventually with sign changes depending on the crystallographic direction and the energy of the system*

A sketch of IREE is presented in Fig. 4.21. When a spin accumulation is produced by spin pumping in a Rashba system, the two Fermi surfaces are displaced coherently. This results in a net charge current perpendicular to both spin current and spin polarization. Of course, a change of Rashba bands chirality upon FE switching is expected to invert the sign of the charge current accordingly. However in IREE, the sign of j_c does not depend on the crystallographic orientation of the slab. Two slabs elongated either along the ZA or along ZU would lead to charge currents with the same sign, as shown pictorially in Fig. 4.21. This scenario does not reproduce the inversion between ZA and ZU of our experimental data (Fig. 4.18).

This means that IREE is not the only mechanism responsible for spin-to-charge conversion in GeTe.

Concerning intrinsic spin Hall effect, the calculated spin Hall conductivity tensor for the bulk in Ref. [226, 227] and for the thin film system discussed in Sec. 4.2.4 envisage specific asymmetries of the different components with respect to the crystallographic direction. With a spin pumping experiment it is possible to measure one component of the tensor. For charge current along ZA (ZU) the component is σ^{y}_{zx} (σ^{x}_{zy}), where z is the direction of propagation of the spin current, x (y) the polarization of the spin current and y (x) the charge current direction. To be comparable with the theoretical calculations, x is ZA and y is ZU. Both methods (i.e. purely bulk and truncated system calculations) predict the sign inversion between ZA and ZU ($\sigma^{y}_{zx} = -\sigma^{x}_{zy}$), in agreement with the measurements. Concerning the dependence on the polarization state, the purely bulk calculations fails to predict the sign change with **P**. This model indeed is not suitable to reproduce the experiments, since it treats an infinite bulk system. Indeed, not accounting for the symmetry breaking by the interfaces leaves behind the presence of the polarization surface charges. As discussed in Sec. 4.2.4, the electric field produced by the surface charges is the element carrying the role of ferroelectricity, which is retained in the truncated system. In this framework, the component σ^{y}_{zx} shown

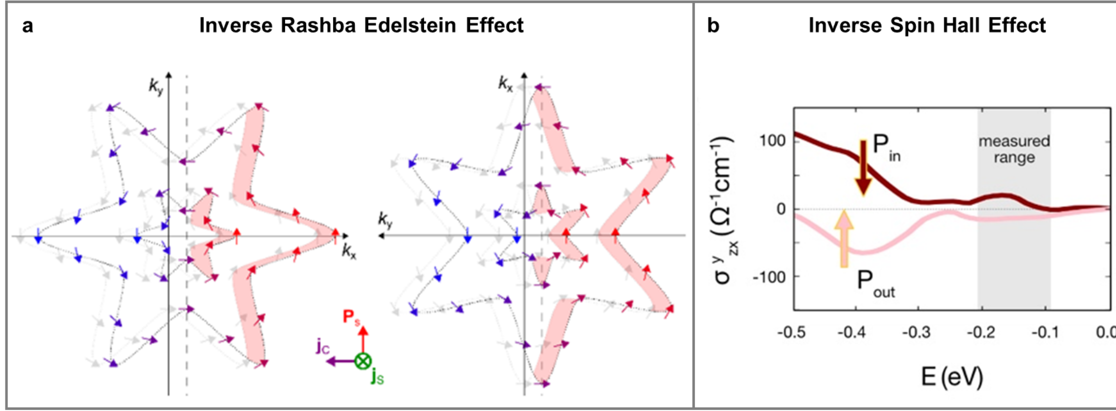

Figure 4.21: ***a*** *Sketch of the inverse Rashba Edelsteing effect (IREE) applied to the six-fold Rashba Fermi contours of GeTe. In agreement with the notation employed for ARPES,* k_x *(*k_y*) indicates the bulk direction ZA (ZU). Due to spin pumping, a spin accumulation is formed in GeTe which induces the displacement of the Fermi surfaces by* Δk *and the formation of a charge current the spin current and its polarization. Panel* ***a*** *(*$\boldsymbol{b}$*) corresponds to the production of charge current along ZA (ZU).* ***b*** *Spin Hall conductivity component* σ^y_{zx}*, corresponding to a spin pumping experiment with charge current produced along ZA. The ferroelectric polarization modifies the spin Hall conductivity and eventually inverts its sign, depending on the energy of the free carriers. The grey area highlights the region probed by spin pumping. At this energy, the doping corresponds to that of the p-degenerate GeTe.*

in Fig. 4.21**b** is modulated by the FE state. In the energy range marked with the grey panel (which corresponds to the experimental doping of GeTe), σ^y_{zx} (i.e. current along ZA) has an opposite sign for $\mathbf{P}_{\text{out}}$ and $\mathbf{P}_{\text{in}}$. The sign is also compatible with the measured spin pumping peaks, being positive for $\mathbf{P}_{\text{in}}$ and negative for $\mathbf{P}_{\text{out}}$ (with this experimental geometry, the sign of the spin pumping peak is the same as the conversion efficiency). The calculations also suggest a possible asymmetry of spin-to-charge signals, as found in the experiments.

The excellent matching between the experimental curves and the theoretical calculations of the spin Hall conductivity is a strong indication that spin-charge conversion is dominated by intrinsic spin Hall effect, remanent and switchable with ferroelectricity. The truncated model also suggests that the sign of SHE is controlled by the electric field generated by the polarization charges at the surface.

4.3 Conclusions

By way of conclusion, we demonstrated the fundamental concept of FERSC, the ferroelectric control of Rashba effect and spin-to-charge conversion. In particular, we calibrated a suitable sample preparation strategy that allowed to control the surface termination and the pristine polarization of GeTe thin films. SARPES measurements of inward and outward samples lead to counter spin textures of the bulk electronic bands, in agreement with the DFT calculations. This experiment established the link between ferroelectricity and Rashba effect in GeTe. In the second part of the chapter we investigated the effect of ferroelectric switching on the spin-charge conversion. Spin pumping measurements of epitaxial Fe/GeTe bilayers and theoretical DFT calculations revealed a remanent conversion and reversible with the ferroelectric polarization. The sign change of the conversion with the crystallographic direction allowed to exclude IREE as the main responsible mechanism. On the contrary, it is a direct signature of intrinsic SHE as predicted by DFT calculations. We also showed that this effect can operate up to room temperature, a necessary ingredient for the realization of devices.

CHAPTER 5

Control of the doping in FERSC: Indium doped GeTe

The ferroelectric control of charge and spin transport in GeTe achieved in this work (Ch. 3 and Ch. 4) is the first demonstration of the great potential of FERSC for spintronic applications: spin currents can be controlled in a nonvolatile way by changing the ferroelectric configuration of the material.

Nevertheless, to fully exploit the semiconductive behaviour of such compounds in transistors, a solution for the compensation of the natural doping of GeTe must be found.

To this aim, here we propose the use of In-doped GeTe, epitaxially grown by MBE as described in Sec. 5.1. We investigate the properties of such alloy in terms of ferroelectricity (Sec. 5.2.1), Rashba effect (Sec. 5.2.2) and doping (Sec. 5.2.3). The growth and characterization of InGeTe was carried out with Paolo Maria Caldera, Luca Nessi, Simone Petrò and Alessandro Novati.

5.1 Growth of InGeTe

In this section we provide information about the growth of InGeTe epitaxial thin films. Two different approaches were adopted:

- Epitaxy on GeTe/Si substrates (Sec. 5.1.1). The decapped GeTe surface represents the 'natural' substrate because the two compounds are supposed to own very similar lattice constants. Samples of InGeTe/GeTe/Si exhibited high quality surface lattices, suitable for the detection of its Rashba bands structure by means of SARPES (Sec. 5.2.2).

- Epitaxy on BaF_2 (Sec. 5.1.2). The growth conditions defined for homoepitaxial samples were adopted for InGeTe epitaxy on BaF_2 substrates. Due to the insulating behaviour of the substrate, the samples were suitable for the ferroelectric characterization by PFM and ferroelectric resistive switching (Sec. 5.2.1) and the quantification of the carriers' concentration by Hall measurements (Sec. 5.2.3).

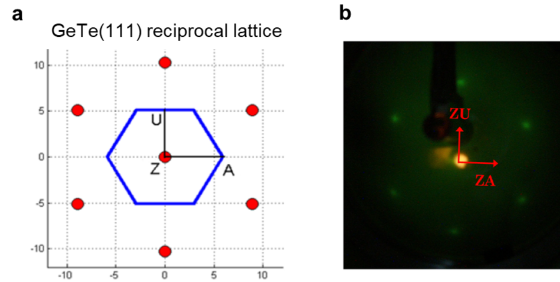

Figure 5.1: ***a*** *Representation of the reciprocal lattice of a GeTe(111) surface.* ***b-c*** *LEED patterns after deposition of* $In_{0.03}Ge_{0.43}Te_{0.54}$*(20 nm) on a GeTe(15 nm)/Si substrate.*

5.1.1 Epitaxy on GeTe/Si

The growth of 20 nm thick epitaxial InGeTe films was performed by MBE (Sec. 2.4.1), through co-deposition from GeTe crystals and In cells (Fig. 5.1**a**). A temperature of 245 (± 5) °C during growth guaranteed the formation of the ordered lattice structure.

The stoichiometry of the sample is calculated according to Eq. 2.59, as the ratio of the XPS Al-$K\alpha$ peaks of the core levels Ge3d, Te4d and In4d. The intensity of each peak is normalized by its cross-section, the inelastic mean free path and the transmission of the electron analyser. The similar values of the binding energy of the peaks of Ge3d, Te4d and In4d (i.e. of λ_{IMFP} and T) limit the error on the result of Eq. 2.59 and the relatively large value of $\lambda_{IMFP} \sim 3$ nm permits to observe the "bulk" stoichiometry.

A certain composition of the sample can be obtained by properly tuning the In/GeTe fluxes ratio We discovered that the In content of the grown compound (η_{In}) is proportional to the ratio $\frac{r_{In}}{r_{GeTe}}$.

Thanks to the possibility of tuning the stoichiometry of the film, we realized a series of InGeTe samples with increasing In content in order to compensate the p-type doping of GeTe, with η_{In} from 3 % up to 20 %. *In-situ* LEED was performed after the deposition of each sample, to check the crystallographic quality of the surface. Hexagonal LEED patterns of the Ge(In)Te(111) surface $In_{0.03}Ge_{0.43}Te_{0.54}$ is reported Fig. 5.1**b**. We observed similar patterns in samples with up to 10% of In. The LEED disappears when η_{In}= 20%, indicating In content exceeding the maximum solubility of the compound.

The crystallographic structure of InGeTe films is retrieved by X-Ray Photoelectron Diffraction (XPD) patterns reported in Fig. 5.2. Performing angular dependence XPS measurements, it is possible to identify the directions with high density of atoms in a line. As reported in Fig. 5.2**c** (top panel), the angular dispersion of the photoelectron intensity of Ge3d, Te4d and In3d$_{\frac{3}{2}}$ of $In_{0.05}Ge_{0.49}Te_{0.48}$ along ZA and ZU directions shows specific peaks that quite well reproduce the diffraction pattern computed for the GeTe(111) lattice [128] sketched in Fig. 5.2**b**. The XPD data highlight that In atoms in InGeTe substitute vacancies in the lattice of GeTe. In agreement with LEED investigation, XPD pattern can be observed up to η_{In}= 10 %. Finally, in the bottom panel of Fig. 5.2**c**, we show that the XPD pattern is lost for η_{In}= 20 % with the formation of a precipitated In layer covering the surface (this is evident from the strong attenuation of Ge and Te intensities and the angle dependence of the In peak). This also means that the actual percentage of substitutional In is lower than 20 %, which was computed assuming a single uniform InGeTe layer. Hence we can conclude that the maximum solubility of In is larger than 10 % and lower than 20 %. This limit also sets the maximum reduction of the free carriers. This range is comparable with the one that can be extracted from Ref. [130]. In that work, M. S. Lubell *et al.* studied the enhancement of solubility of In in GeTe upon increasing the density of Bi_2Te_3 neutral vacancies. The solubility of In reaches a saturation value of 1.2 % with 6 % of neutral vacancies. Now, if we assume that part of In forms In_2Te_3 introducing neutral vacancies as done by Bi, and another part substitutes Ge compensating

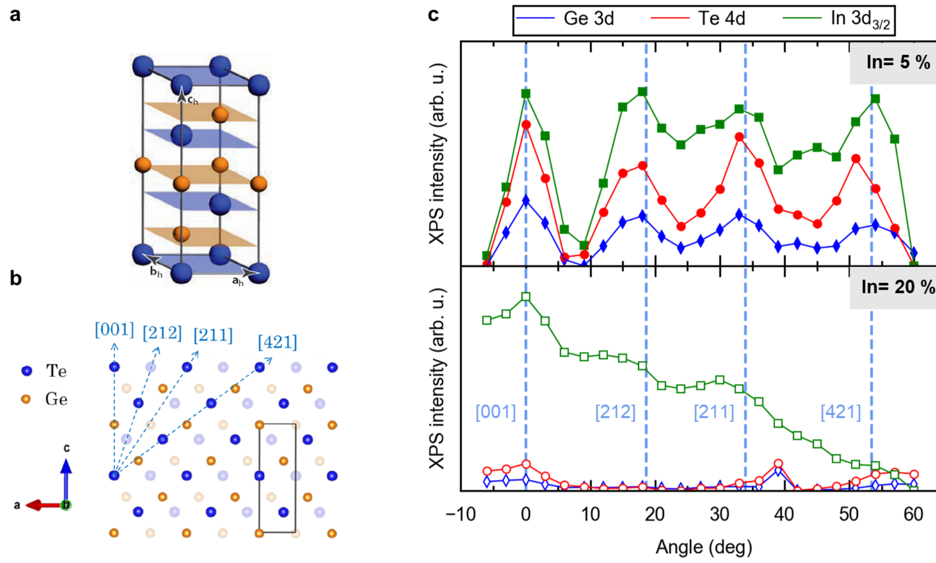

Figure 5.2: ***a*** *GeTe cell in the rhombohedral setting representation of the lattice.* ***b*** *Representation of the GeTe lattice plane [010].* ***c*** *XPD spectra acquired along ZU from* $In_{0.05}Ge_{0.49}Te_{0.48}$ *(top panel) and* $In_{0.20}Ge_{0.30}Te_{0.50}$ *(bottom panel). The XPS peaks Te4d, Ge3d,* $In3d_{3/2}$ *are monitored as function of the collection angle.*

the doping, the total amount of In is $\eta_{In,max} = 6\% \cdot 2 + 1.2\% = 13.2\%$ (multiplication by 2 is due to the fact that two atoms of In are required for one neutral vacancy). The substitutional doping represents the fundamental achievement for compensation of free carriers in GeTe, provided that the resulting compound keeps ferroelectricity and Rashba effects.

5.1.2 Epitaxy on BaF_2

We grew InGeTe films also on insulating BaF_2 substrates. $BaF_2(111)$ was chosen due to (i) the relatively reduced lattice mismatch with GeTe (3.5 %), (ii) electrical insulation which allows for measurement of the carriers concentration via Hall effect, and (iii) the need of a relatively simple preparation prior evaporation of Ge(In)Te by MBE.

The atomic pattern of a $BaF_2(111)$ cleaved surface is shown in Fig. 5.3**a**-**b**. The hexagonal arrangement of the (111) surface quite well reproduces the epitaxial GeTe surface (Sec. 1.4). Moreover the in-plane lattice parameter of $BaF_2(111)$ *a*= 4.38 Å is very closed to that of GeTe, *a*= 4.23 Å, so that just a 3.5 % tensile strain will be exerted on the grown film. Annealing at 500 °C of BaF_2 in UHV environment for one hour ensures complete desorption of oxygen atoms from the surface [228]. Moreover, the annealing favors surface ordering.

The deposition of 20 nm thick GeTe and InGeTe films was performed at 245 °C as explained in detail in Sec. 5.1.1. To achieve a large degree of compensation, a 10 % In doped sample was grown with r_{GeTe}= 0.5 nm/min and r_{In}= 0.05 nm/min (as we calibrated that $\eta_{In} = -11.3 + 226.1 \cdot \frac{r_{In}}{r_{GeTe}}$, with an error of about 3 %). The final stoichiometry of $In_{0.10}Ge_{0.42}Te_{48}$ was measured by XPS as explained above. After growth, the crystal quality was checked *in-situ* by RHEED; exploiting high energy electron beam (*E*= 30 kV) it is possible to observe the crystal order of the surface lattice avoiding distortions eventually derived from the charging of the Ge(In)Te layer on the insulating substrate. In Fig. 5.3, some RHEED patterns acquired along ZU from BaF_2/GeTe (panel **c**) and $BaF_2/Ge_{0.42}In_{0.10}Te_{48}$ are shown (panel **d**). The presence of RHEED diffraction lines indicates a epitaxial type growth of the film. The spacing between the lines (indicated in red) is proportional to the reciprocal vector k_{ZU} as represented in Fig. 5.3**e**. Performing RHEED along ZA and ZU, the obtained ratio k_{ZU}/k_{ZA} of InGeTe was consistent with the values of GeTe. However, the spots along the RHEED lines are signs of a 3D arrangement of the topmost atomic layers. Hence the

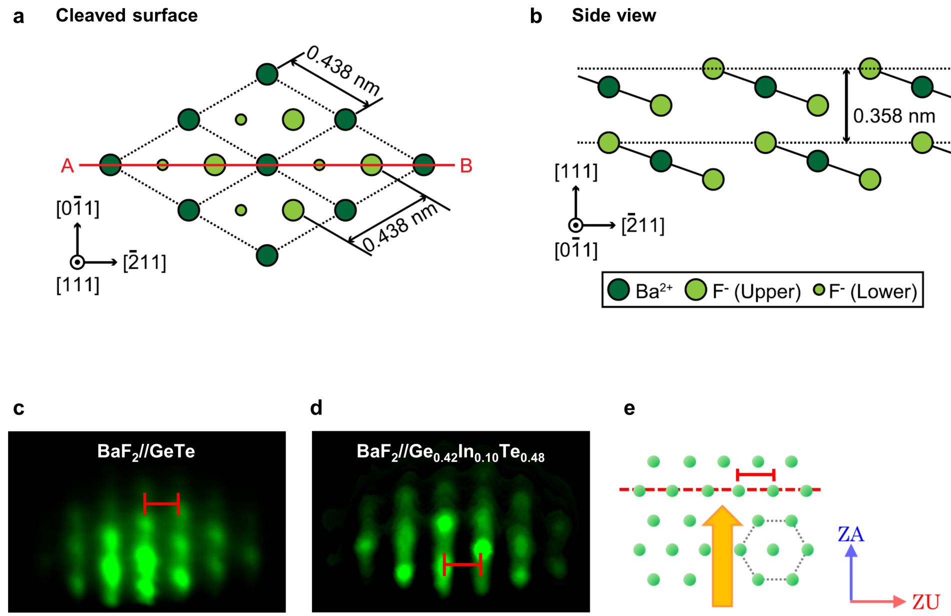

Figure 5.3: ***a*** *Crystal structure of BaF_2(111) cleaved surface.* ***b*** *Sketch of the surface projected along the direction (011). Adapted from Ref. [228].* ***c-d*** *RHEED patterns of GeTe/BaF_2-InGeTe/BaF_2 along the crystallographic direction ZU at 30 keV.* ***e*** *Sketch of the (111)-surface reciprocal lattice. The direction of the incoming electrons is highlighted in orange. The spacing between the RHEED lines in* ***c-d*** *and the atomic layers in* ***c*** *is represented by the red bar.*

crystallographic quality of the grown film is reduced with respect to homoepitaxial films, likely due to the tensile strain exerted by the substrate. Nonetheless, InGeTe/BaF_2 films were the suitable choice for the investigation of ferroelectricity (checked by PFM and ferroresistive switching) and free carriers' concentration (measured by Hall effect).

5.2 In-doped GeTe as a FERSC

In this section, the three physical properties of FERSC are investigated in In-doped GeTe. We will focus the attention on the samples with In concentrations approaching the solubility limit ($\sim$10 %), for which we expect the maximum effect on the doping. (i) In Sec. 5.2.1, ferroelectricity is probed by PFM and by the bipolar resistive switching of InGeTe/gate junctions, as reported in Ch. 3 for GeTe. (ii) In Sec. 5.2.2, SARPES measurements are presented in order to study the possible impact of In on the Rashba splitting as well as on the position of the Fermi level with respect to the valence band maximum. (iii) Finally, electrical characterization of the free carriers density of InGeTe is reported in Sec. 5.2.3.

5.2.1 Ferroelectricity of InGeTe

The ferroelectric behaviour of InGeTe was investigated on films grown on BaF_2 rather than on Gete/Si (Sec. 5.1.2), where the ferroelectric response of InGeTe is mixed to that of GeTe film underneath.

We probed the ferroelectric response of a 10 % In doped 20 nm-thick InGeTe/BaF_2, both by PFM and the resistive switching with gate contacts, as done for GeTe. Similarly to undoped GeTe films (Fig. 3.1), PFM switching shown in Fig. 5.4**a**-**b** follows a good hysteresis loop. The amplitude (A) describes a butterfly shaped loop, the phase (Φ) switches between 0 ° and a 180 °, corresponding to outward and inward polarization. The coercive voltage is nearly doubled with respect to GeTe (Fig. 3.1). The enhancement of the activation energy for the switching indicates an increased stability of

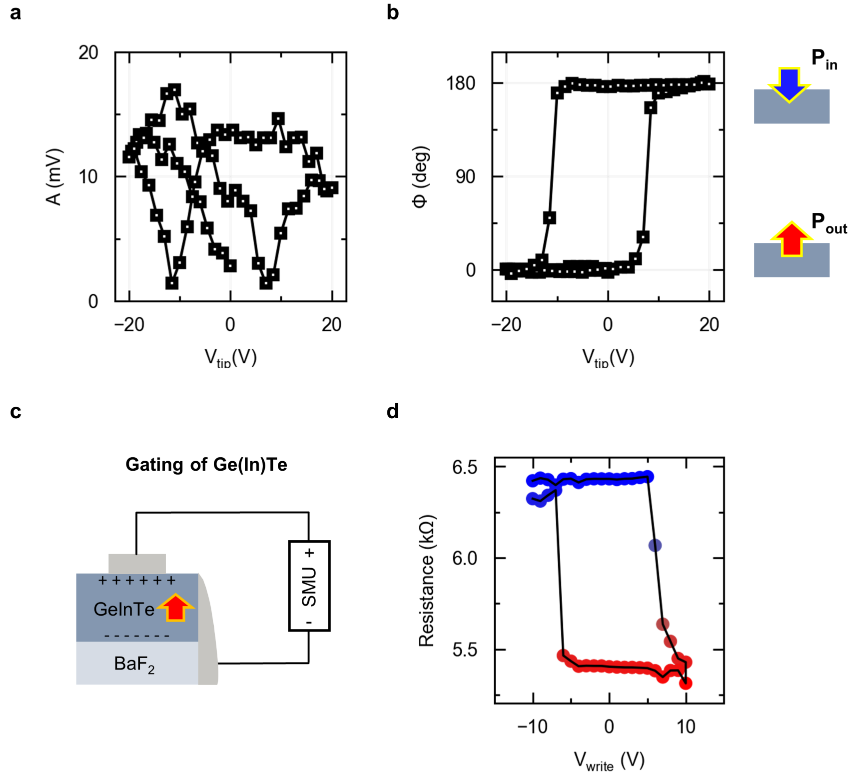

Figure 5.4: ***a-b*** *Pulsed dc PFM hysteresis acquired on the surface of InGeTe(20 nm)/BaF$_2$ with 10 % of In content. The top electrode is provided by the conductive tip of the AFM while the sample is grounded through lateral electrode made by Ag paste. Amplitude* ***a*** *and* ***b*** *phase signals are retrieved after background subtraction, as described in Sec. 2.1.2. The excitation frequency was 61 kHz, much lower than the tip-sample resonance frequency ($\sim$ 280 kHz). The amplitude of the excitation voltage was 4 V, lower than the coercive voltage ($\sim$ 10 V).* ***c*** *Sketch of the top-bottom configuration adopted for gating of InGeTe samples. Both writing and reading procedures are performed by a Source-Measure Unit (SMU).* ***d*** *Ferroelectric modulation of the vertical resistance by sweeping the amplitude of the writing voltage pulse from -10 V to +10 V and from +10 V back to -10 V.*

the ferroelectric state. Moreover, a reduction of system inherent background in PFM measurements already suggests a possible reduction of the free carriers concentration concentration, thus a possible compensation of the doping (Sec. 2.1.2). Macroscopic switching was achieved at larger scales of the order of 10-100 μm with gate contacts, by exploiting the bipolar resistive switching (Ch. 3). The ferroelectric state was monitored by the resistance of the InGeTe/gate junction. The remarkable similarity of the bipolar resistive loop (Fig. 5.4**d**) with the PFM response further confirms that the resistance variation is related to a change of the ferroelectric domains configuration below the electrode. When compared with GeTe (Fig. 3.4), we observe a decrease of the read current of InGeTe/gate by a factor ~ 35, pointing towards a more intrinsic film.

Both PFM and resistive switching measurements revealed that the GeTe preserves its ferroelectric behaviour when In dopants are introduced in the lattice.

5.2.2 Rashba effect of InGeTe

In analogy with the investigation of GeTe films (Sec. 4.1.2), the Rashba splitting of the bulk electronic bands of InGeTe was probed by SARPES (Sec. 2.2.3). The bands were observed in InGeTe films on GeTe/Si, with a high crystallographic quality of the In-doped GeTe layer (Sec. 5.1.1). After the growth, InGeTe samples were protected by 10-20 nm of amorphous Te capping and examined at Elettra Synchrotron (Basovizza, Trieste, Italy). Immediately before SARPES, samples were decapped so that the stoichiometric clean and ordered surface was recovered in UHV

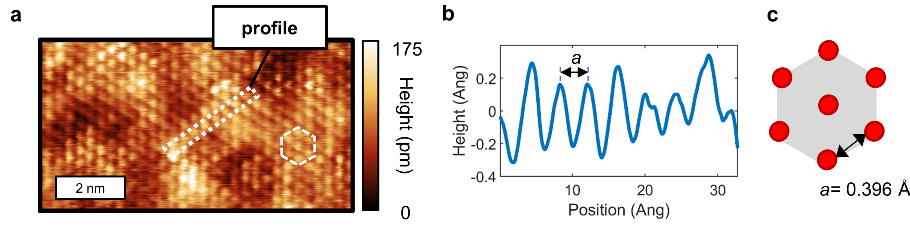

Figure 5.5: ***a*** *High resolution STM of* $In_{0.10}Ge_{0.42}Te_{0.48}$*(20 nm)/GeTe(15 nm)/Si acquired at Elettra (APE beamline) after in-situ recovering of the surface.* ***b*** *Height profile corresponding to the scan enclosed by the black square on the image in panel* ***a****.* ***c*** *Representation of hexagonal (111) surface lattice with indication of the measured lattice constant (a= 3.96 Å).*

following the same method developed in Sec. 2.4.2. The stoichiometry of the samples was mapped by XPS, revealing a uniform distribution of In content. The *in-situ* Scanning Tunneling Microscopy (STM) image with atomic resolution of the surface topography of $In_{0.10}Ge_{0.42}Te_{0.48}$ in Fig. 5.5**a**, confirms that the crystallographic quality of the sample is fully recovered by decapping. Atoms are placed in a hexagonal pattern with a spacing of about 3.96 Å, as extracted from the height profile in Fig. 5.5**b**. Because the atomic positions are approximately unaltered, electrons from the Z point could be probed by ARPES within the same photon energy range employed for the undoped samples (15-25 eV, Sec. 4.1.2). ARPES spectra along ZA acquired with $h\nu$= 18, 20 and 22 eV are reported in Fig. 5.6. Close to the Fermi level, we can observe Rashba bands of bulk origin that disperse with $h\nu$ (i.e. on k_z). As done for GeTe, we adopted $h\nu$= 20 eV in order to quantitatively estimate and compare the Rashba parameters of In-doped and undoped GeTe.

The bulk nature of the bands can be also evinced from the constant energy maps (CEM) in the ZA-ZU plane, shown in panel **a** of Fig. 5.7. Similarly to GeTe, sixfold shaped contours stem from the symmetry of the (111) surface (Sec. 1.4). At a binding energies of 0.7 eV, only bulk bands with "arms" along ZA are detected in the wave-vector window of k< 0.5 Å^{-1}, while surface ones would be encountered at much larger values of k and would be rotated along ZU. Such symmetry further confirms that In atoms substitute defects of the lattice of GeTe (i.e. they occupy empty sites left by Ge vacancies) which keeps an hexagonal crystal structure. Panels **b** and **c** of Fig. 5.7 show the dispersion of the bands of InGeTe along ZA, probed the ARPES and SARPES, respectively. A typical Rashba-like bands splitting is found in the carpet (panel **b**), with two parabolic bands shifted

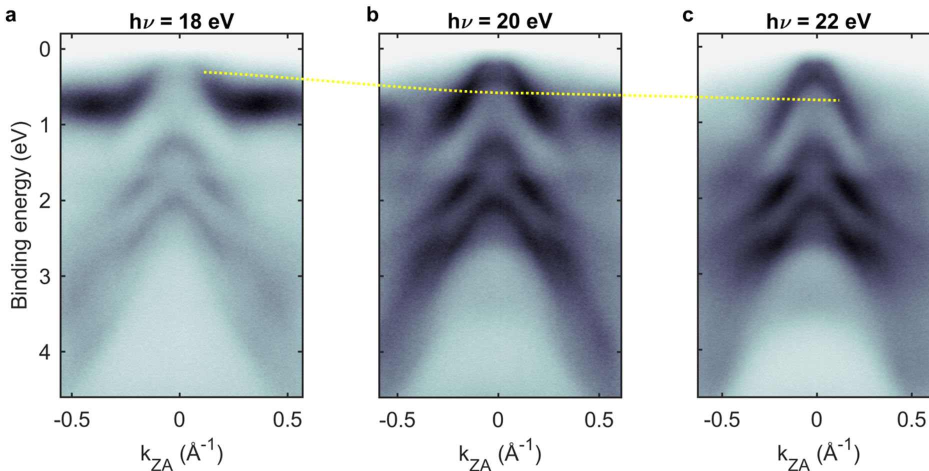

Figure 5.6: *Bands dispersion of* $In_{0.10}Ge_{0.42}Te_{0.48}$*(20 nm)/GeTe(15 nm)/Si acquired with hν= 18 eV* ***a****, 20 eV* ***b*** *and 22 eV* ***c****.*

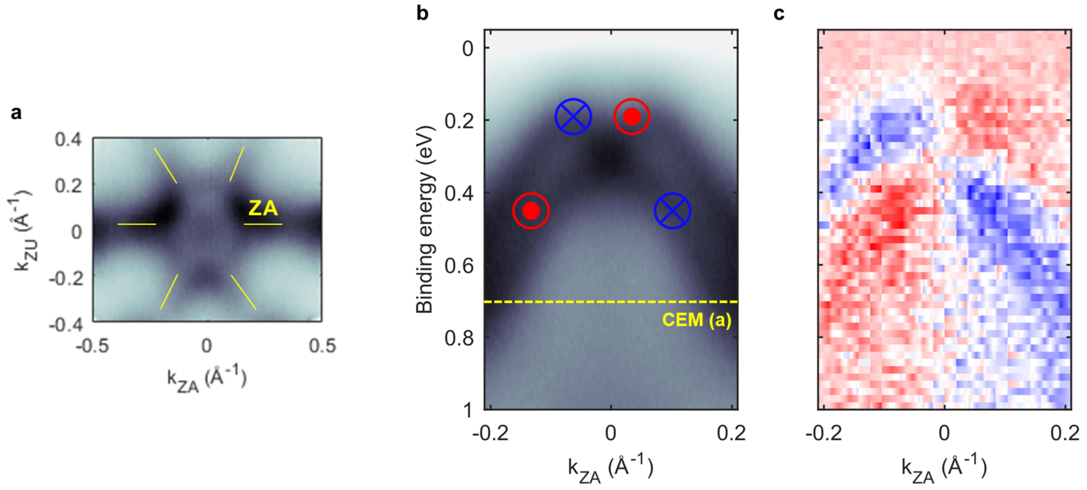

Figure 5.7: ***a*** *Constant energy map (CEM) at binding energy of -0.7 eV, showing bands elongated along ZA.* ***b*** *Bands dispersion along ZA at hν= 20 eV of GeTe(15 nm)/$Ge_{0.42}In_{0.10}Te_{0.48}$ surface.* ***c*** *Map of the spin polarization along ZU direction.*

laterally in the **k** space. The Rashba nature of the bands is also confirmed by the spin polarization along ZU (panel **c**), in agreement with the spin texture expected for a Rashba system (Eq. 1.13). The resulting spin texture is drawn on the bands dispersion in panel **b**, highlighting the in-plane rotation of the spin typical of a Rashba system. Furthermore, a maximum energy splitting $E_R\sim$ 0.085 eV encountered at the Rashba wave-vector $k_R\sim$ 0.07 $\mathring{A}^{-1}$ can be extracted from the bands dispersion (see Sec. 1.2 for more theoretical details). Similarly, we extracted the values of E_R and k_R for GeTe (Fig. 4.8) and the result is summarized as follows:

Sample	k_R ($\mathring{A}^{-1}$)	E_R (eV)
GeTe	0.14	0.2
InGeTe	0.07	0.085

Table 5.1: *Rashba wave-vector (k_R) and energy splitting (E_R) for intrinsic GeTe and 10 %-In-doped GeTe.*

The Table 5.1 allows for a direct comparison of the Rashba effect observed in the undoped and In-doped compounds. Both the Rashba wave-vector and energy splitting are reduced by a factor of 2 when the sample is doped with 10 % of In. In other words, the Rashba coefficient of the In-doped GeTe ($\alpha_{R,InGeTe}$) can be estimated as:

$$\alpha_{R,InGeTe} \sim \frac{\alpha_{R,GeTe}}{2} = \frac{4.8 \text{ eV}\mathring{A}}{2} = 2.4 \text{ eV}\mathring{A} \tag{5.1}$$

Nonetheless, such value is still quite large compared to other Rashba systems observed at metallic surfaces or interfaces (e.g. Au(111) [229], Bi and Sb surfaces [230]). This opens the route to a sizeable conversion between charge and spin currents in a FERSC with different doping. To understand the effect of In on the doping, we can compare the position of the Fermi level observed in GeTe and InGeTe. As shown in Fig. 5.8**a-b** at 20 eV, the valence bands of InGeTe are pushed to higher binding energies by ~ 250 meV with respect to the Fermi level. The angle-integrated spectra in Fig. 5.8**c** display a net Fermi edge for GeTe (red data) and a smooth vanishing intensity at E_F for InGeTe. This is the experimental evidence that In atoms mitigate the strong *p* doping of GeTe, bringing it from a metallic to a more semiconductive state. The shift of the Fermi level obtained from ARPES experiments is also predicted by DFT calculations. The bands structure of In-doped GeTe was computed by our collaborators S. Picozzi *et al.*, for different values of In concentration

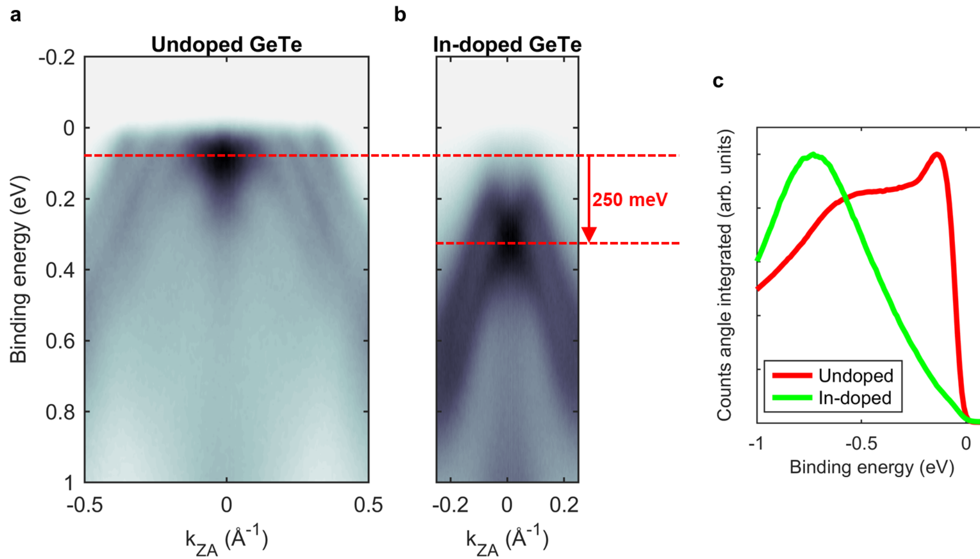

Figure 5.8: *Comparison between carpet of undoped GeTe (**a**) and $In_{0.10}Ge_{0.42}Te_{0.48}$/GeTe(15 nm)/Si (**b**), with $h\nu$ = 20 eV. The red dashed lines indicate the energy position of the bulk Rashba bands in the two cases, showing a shift of 250 meV towards higher binding energies upon doping. **c** Comparison between the angle-integrated photoelectron intensity versus binding energy for In-doped (green data) and undoped (red data) GeTe, near the Fermi level (E_B= 0).*

up to 12.5 %. In Fig. 5.9, valence bands structure and lattice supercell composed by 8 unit cells of undoped GeTe (green box) are compared with those of In-doped crystals with 6.25 % (orange box) and 12.5 % (red box) absolute concentrations. As discussed before, GeTe displays a rhombohedral distorted unit cell (symmetry group *R*3*m* [12, 114]) with associated bulk bands (B_1 and B_2). Both the bands dispersion and the supercell (panels **a**-**b**) are drawn along the (001 plane). Te atoms are represented in yellow, Ge in blue and In in pink. The introduction of one In atom in the lattice cell leads to a new compound ($In_1Ge_7Te_8$, i.e. 6.25 % of In) with the same relaxed crystal structure as GeTe (*R*3*m*, panel **d**) and expected comparable ferroelectric behaviour. The In atom occupies the central position of the unit cell, i.e. it substitutes vacant Ge atoms in the cell as demonstrated experimentally by XPD spectra (Fig. 5.2). Bulk Rashba bands were also obtained as clear in panel **c**. Although, In atoms might introduce additional electronic states near the gap (In_1 and In_2 in the valence band and In_{CB} in the conduction one). Higher In concentrations alter the crystal structure. In the case of $In_2Ge_6Te_8$ (12.5 % of In), the crystal symmetry is reduced to *Pm*-6. Three different possible structures can be achieved depending on the position of the In atoms in the lattice. Independently on the distribution of In, bulk Rashba bands are preserved (panels **e**-**h**-**k**), while the In-related bands substantially change. When four In atoms are placed within the (001) plane of the supercell (panels **f**-**g**), the different planes alternating along the (001) direction shift to minimize the overall energy. In other words, the interaction between In adjacent atoms is also minimized thus leading to light In-bands as reported in the diagram of panel **e** and a shift of the Fermi level occurs towards the conduction band. Such landscape predicts the Fermi level shift observed in our ARPES measurements of $In_{0.1}Ge_{0.42}Te_{0.48}$. We can argue that this structure is compatible with a reduction of the density of free holes operated by In dopants. Theoretically, other arrangements of In were also explored. When two In atoms occupy empty Ge sites in the (001) supercell plane (panels **h**-**i**-**j**), their proximity in the whole lattice is increased. The enhanced interaction between In atoms introduces stronger In bands crossing the Fermi level at wave-vectors comparable to those of bulk Rashba states. This is even more evident in the case of a single In atom in the (001) plane (panels **k**-**l**-**m**) and the intense conduction bands at the Fermi level, probably due to the formation of In-atoms columns along the (001) direction. This explains the absence of the Fermi level shift in

panels **h-k** and the appearance of intense metallic In bands, which are not observed in our ARPES measurements. Therefore, these two scenarios can be excluded in the interpretation of the results shown here.

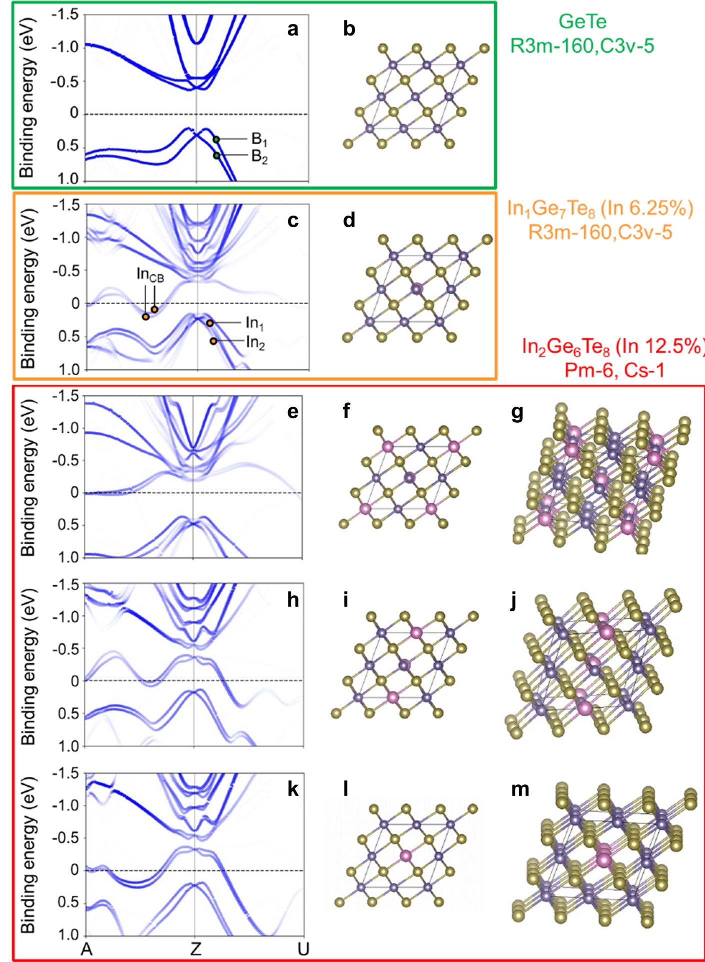

Figure 5.9: *Theoretical DFT calculations of valence and conduction bands for In-doped GeTe with different In concentrations.* ***a*** *Bands dispersion of undoped GeTe along ZA and ZU and* ***b*** *(001) plane of the lattice supercell composed by 8 unit cells, employed for the calculations. The bulk Rashba bands are marked as B_1 and B_2. Ge atoms are drawn in blue, Te in yellow and In in pink.* ***c-d*** *Same as panels* ***a-b*** *for a 6.25 % In doped GeTe. In bands (In_{CB} and In_1-In_2 are visible in the bands diagram).* ***e-m*** *DFT calculations of 12.5 % In-doped GeTe.* ***e-f-g*** *are bands dispersion, 2D view of the (001) plane and 3D view of the lattice structure. Four In atoms are occupy Ge vacant sites in the (001) supercell plane.* ***h-i-j*** *As in* ***e-f-g*** *when only two In atoms are placed in the cell.* ***k-l-m*** *are obtained with one In atom.*

5.2.3 Concentration of carriers

In the previous section we demonstrated that the compensation of the Ge vacancies in GeTe by substitution with In atoms produces a new semiconductor, where the ferroelectricity and the Rashba effect are still present. The partial compensation of the vacancies was demonstrated indirectly by the dip of the Fermi level in the bands gap (Fig. 5.8). Here a direct probing of the free carriers' concentration is provided by Hall measurements on $In_{0.10}Ge_{0.42}Te_{0.48}/BaF_2$. The insulating substrate guarantees the currents flowing only in the In-doped GeTe layer. As shown in Fig. 5.10**a**, a simple detection of the Hall effect can be performed using four electrodes created by Ag paint on the corners of the sample. The area of the contacts was at least one order of magnitude smaller than that of the entire sample. The Hall effect was observed by injecting a current I between two opposite contacts (by means of V_{xy}) with a magnetic field B perpendicular to the film plane. The Hall voltage (V_H) was then sensed across the other electrodes (i.e. a Hall current is generated perpendicularly to I). By sweeping the amplitude of B, the Hall voltage increases linearly as shown in Fig. 5.10**b**. The positive slope of the Hall voltage versus the applied field indicates a p-type doping of the material. Assuming holes as carriers, the Lorentz force $F = e\mathbf{v} \times \mathbf{B}$ with $\mathbf{v}$ is the drift velocity of the carriers gives rise to a lateral voltage (Hall voltage, V_H). The Hall resistance R_H is defined as:

$$R_H = \frac{V_H t}{IB} = \frac{1}{e \cdot p} \tag{5.2}$$

Where t is the thickness of the layer, e is the charge unity and p the density of free holes. By inverting Eq. 5.2, a free holes' concentration of $\sim 2 \cdot 10^{20}$ cm^{-3} is extracted from the Hall resistance of the InGeTe sample. Although the insertion of In in the lattice does not change the GeTe doping type, the high density of free carriers is reduced by a factor 4 ($p \sim 8 \cdot 10^{20}$ cm^{-3} for our undoped GeTe films). The decrease of holes' concentration is in line with the shift of the Fermi level towards the band gap found with the ARPES (Sec. 5.2.2). Besides, the value of the free carriers' concentration achieved is in good agreement with what reported in Ref. [130] for single crystals of GeTe where In was employed as a solute metal.

The mitigation of the spontaneous doping of GeTe thin films represents an important step in the direction of semiconductor devices.

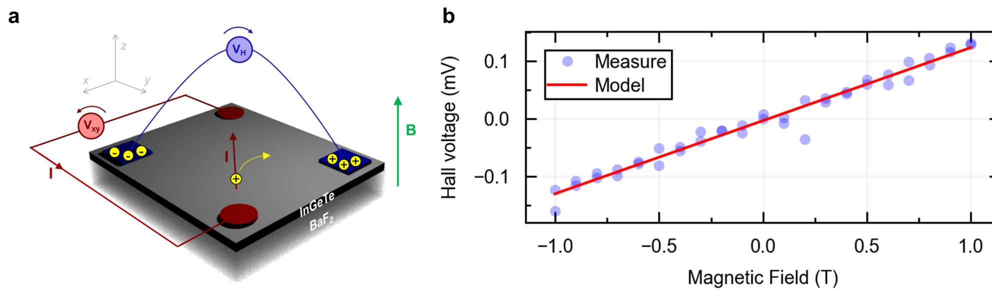

Figure 5.10: ***a*** *Sketch of the measurement of the Hall coefficient of In-doped GeTe samples on BaF_2. A current is injected by V_{xy} between two contacts at the opposite corners of a square, the Hall voltage is created perpendicularly when a magnetic field is applied normal to the sample plane.* ***b*** *Hall voltage from a 10 % In-doped InGeTe(20 nm)/BaF_2.*

5.3 Conclusions

In this chapter we achieved the mitigation of the strong *p*-type doping of GeTe. Indium-doped epitaxial GeTe films were grown on GeTe/Si and BaF_2 substrates, up to the solubility limit (between 10 and $20\ \%$). Indium atoms are responsible for a partial charge compensation in GeTe, due to its increased valency (3+) with respect to Ge vacancies (2+). Furthermore, it increases the solubility of In in the GeTe matrix. Characterization by SARPES revealed that while Rashba splitting is reduced by a factor ~ 2 with respect to GeTe, the valence band is shifted by $\sim$250 meV towards higher binding energies, a direct signature of the doping effect. Moreover, by PFM and resistive switching we observed that the ferroelectric phase of In-doped GeTe is stable and it involves switching currents reduced by a factor ~ 35. This demonstrates that In-doped GeTe is a FERSC material with a lower concentration of free the carriers, also confirmed by the increased of the Hall resistance by a factor 4. This is a first path towards the realization of ferroelectric spin-based transistors.

Conclusions and Perspectives

The work presented in this thesis was devoted to the investigation of the ferroelectric control of Rashba and spin transport in a FERSC material.

In **Chapter 3**, we achieved the ferroelectric switching of the *p*-degenerate semiconductor GeTe by means of a micrometric gate. We developed an innovative current-voltage method to monitor the polarization state upon poling, based on the resistive switching of the GeTe/gate interface. While the polarization is set by voltage pulses exceeding the coercive value, the remanent state is read out in non-destructive way by measuring the polarization dependent resistivity of the GeTe/gate junction at low voltages. Indeed, we showed that polarization charges at the interface modify the depletion region in the semiconductor so that the current-voltage characteristic of the junction depends on the orientation of the polarization vector. From a technological point of view, this method is a big step beyond commercial FeRAMs, in which the reading operation destroys the ferroelectric state that must be restored afterwards [194]. The resistive switching of GeTe/gate shows high cycling endurance up to 10^4, comparable to flash memories. The ON/OFF ratio of GeTe/metal can be pushed up to about 250 % for the complete inversion of the polarization state. Moreover, different doping between GeTe and the gate materials could pump the ON/OFF ratio, for instance up to $\sim 10^4$ % with a GeTe/Si interface. Moreover, we demonstrated that such modulation is correlated to the switching of the ferroelectric domains underneath the gate electrode, that we closely mapped by PFM. Despite the common belief that high density of free carriers would prevent ferroelectric inversion, we provided evidence of the effective switching in degenerate or almost degenerate semiconductor. We can explain our results based on energy arguments: a semiconductor can react to an external electric field and minimize the electrostatic energy, both by switching its polarization state and by moving free carriers. This demonstration opens the route to the exploitation of ferroelectric semiconductors in devices relying on "classical" resistive switching, i.e. charge transport, or spin transport.

In **Chapter 4** we demonstrated the interplay between ferroelectricity and spin physics in GeTe. By SARPES, we established the inversion of the spin texture of the bulk Rashba bands with the polarization. On the spin transport side, we achieved a remanent spin-to-charge conversion in such ferroelectric SOC system, by spin pumping experiments and theoretical DFT calculations. The sign of the conversion efficiency is reversed by gating the ferroelectric state, resembling the behaviour of the spin texture. The efficiency is also reversed when the charge current flows along the two non-equivalent crystallographic directions ZA and ZU. We demonstrated by DFT calculations of the spin Hall conductivity tensor that this is direct consequence of the symmetry of the crystal. The observations can be explained in terms of intrinsic spin Hall rather than Rashba Edelstein effect. Remarkably, tunable spin-charge conversion can be operated up to room temperature, a head start on other electrically tuned systems as 2DEG and topological materials [17, 18, 65, 85, 86, 231].

The experimental investigation presented here also boosted the theoretical understanding of the spin-charge conversion mechanisms available in a Rashba-ferroelectric crystal, something almost unexplored before.

In this thesis we demonstrated that GeTe represents the first example of a system allowing for spin-charge conversion, dynamically controlled by the nonvolatile ferroelectric state. Although it is a degenerate semiconductor, GeTe provides a particularly good starting point for material engineering or for the search of less doped FERSC compounds in which the conduction can be switched on or off by a gate.

In **Chapter 5** we proposed a route towards the reduction of the strong *p*-type doping of GeTe. We grew InGeTe epitaxial films and proved that 10 % of substitutional In approaches the limit of solubility. Such alloy leads to a mitigation of the carriers concentration with respect to GeTe, reduced by a factor ~ 4. This translates in an increased InGeTe/gate contact resistance and a significant reduction of the switching current by a factor ~ 35. Finally, ARPES measurements revealed a shift of ~250 meV of the valence band around Z towards higher binding energies, a direct signature of the doping effect. The Rashba splitting is preserved with a reduction of the Rashba coefficient of ~ 2 with respect to undoped GeTe, in agreement with DFT calculations. Therefore, InGeTe alloys are a first path for the implementation of FERSC concept in a transistor.

In the future, we will also explore GeTe films with thickness of few monolayers, where carriers' quantum confinement is predicted to boost the spin-charge conversion efficiency, due to reduced momentum scattering and long mean free paths for both charge and spin [232]. Moreover, confinement is predicted to lead to a significant increase of the band gap, so that the ferroelectric control by gate will involve lower switching currents and low power. Recently, attention has been put on atomic-thick SnTe, a chalcogenide supporting an intrinsic spin helix valence electronic state [233, 234], in principle accessible by a robust room temperature ferroelectricity [235, 236].

Ferroelectric-driven spin devices based on engineered FERSC materials could represent an innovative concept of spintronics operating without ferromagnets which exploits the nonvolatile ferroelectric state as memory variable. The remanent electric gating of the spin-charge interconversion could represent the missing link towards tunable spin torque applications such as memories, oscillators or magnonic circuits, as well as advanced spin-orbit logic like the MESO-device architecture proposed by Intel [9]. Both memory (ferroelectricity) and the reading (spin orbit coupling) functionalities can be provided by a single layer of FERSC, thus removing the need for technological scaling and high density memories. Remarkably, FERSC are CMOS-compatible multifunctional materials allowing for electric reconfigurability of spin-based logic circuits [10].

Bibliography

[1] Gordon E Moore. Cramming more components onto integrated circuits, reprinted from electronics, volume 38, number 8, april 19, 1965, pp. 114 ff. *IEEE solid-state circuits society newsletter*, 11(3):33–35, 2006.

[2] Ralph K Cavin, Paolo Lugli, and Victor V Zhirnov. Science and engineering beyond moore's law. *Proceedings of the IEEE*, 100(Special Centennial Issue):1720–1749, 2012.

[3] Igor L Markov. Limits on fundamental limits to computation. *Nature*, 512(7513):147–154, 2014.

[4] Xiaowei Xu, Yukun Ding, Sharon Xiaobo Hu, Michael Niemier, Jason Cong, Yu Hu, and Yiyu Shi. Scaling for edge inference of deep neural networks. *Nature Electronics*, 1(4):216, 2018.

[5] Mohammad Kazemi and Mark F Bocko. Design rules for scalability in spin-orbit electronics. *Scientific reports*, 9(1):1–9, 2019.

[6] Robert A Nawrocki, Richard M Voyles, and Sean E Shaheen. A mini review of neuromorphic architectures and implementations. *IEEE Transactions on Electron Devices*, 63(10):3819–3829, 2016.

[7] Daniele Ielmini and H-S Philip Wong. In-memory computing with resistive switching devices. *Nature Electronics*, 1(6):333–343, 2018.

[8] Daniele Ielmini. Brain-inspired computing with resistive switching memory (rram): Devices, synapses and neural networks. *Microelectronic Engineering*, 190:44–53, 2018.

[9] Sasikanth Manipatruni, Dmitri E Nikonov, Chia-Ching Lin, Tanay A Gosavi, Huichu Liu, Bhagwati Prasad, Yen-Lin Huang, Everton Bonturim, Ramamoorthy Ramesh, and Ian A Young. Scalable energy-efficient magnetoelectric spin–orbit logic. *Nature*, 565(7737):35, 2019.

[10] Sasikanth Manipatruni, Dmitri E Nikonov, and Ian A Young. Beyond cmos computing with spin and polarization. *Nature Physics*, 14(4):338, 2018.

[11] Silvia Picozzi. Ferroelectric rashba semiconductors as a novel class of multifunctional materials. *Frontiers in Physics*, 2:10, 2014.

[12] Domenico Di Sante, Paolo Barone, Riccardo Bertacco, and Silvia Picozzi. Electric control of the giant rashba effect in bulk gete. *Advanced Materials*, 25(4):509–513, 2013.

[13] Hania Djani, Andres Camilo Garcia-Castro, Wen-Yi Tong, Paolo Barone, Eric Bousquet, Silvia Picozzi, and Philippe Ghosez. Rationalizing and engineering rashba spin-splitting in ferroelectric oxides. *npj Quantum Materials*, 4(1):1–6, 2019.

[14] Hosik Lee, Jino Im, and Hosub Jin. Harnessing the giant out-of-plane rashba effect and the nanoscale persistent spin helix via ferroelectricity in snte thin films. *arXiv preprint arXiv:1712.06112*, 2017.

[15] Jongyeon Kim, Ayan Paul, Paul A Crowell, Steven J Koester, Sachin S Sapatnekar, Jian-Ping Wang, and Chris H Kim. Spin-based computing: Device concepts, current status, and a case study on a high-performance microprocessor. *Proceedings of the IEEE*, 103(1):106–130, 2014.

[16] Sergey Dushenko, Masaya Hokazono, Kohji Nakamura, Yuichiro Ando, Teruya Shinjo, and Masashi Shiraishi. Tunable inverse spin hall effect in nanometer-thick platinum films by ionic gating. *Nature communications*, 9(1):1–7, 2018.

[17] E Lesne, Yu Fu, S Oyarzun, JC Rojas-Sánchez, DC Vaz, H Naganuma, G Sicoli, J-P Attané, M Jamet, E Jacquet, et al. Highly efficient and tunable spin-to-charge conversion through rashba coupling at oxide interfaces. *Nature materials*, 15(12):1261, 2016.

[18] Diogo C Vaz, Paul Noël, Annika Johansson, Börge Göbel, Flavio Y Bruno, Gyanendra Singh, Siobhan Mckeown-Walker, Felix Trier, Luis M Vicente-Arche, Anke Sander, et al. Mapping spin–charge conversion to the band structure in a topological oxide two-dimensional electron gas. *Nature materials*, 18(11):1187–1193, 2019.

[19] Muzhi Wang and Mina Rais-Zadeh. Development and evaluation of germanium telluride phase change material based ohmic switches for rf applications. *Journal of Micromechanics and Microengineering*, 27(1):013001, 2016.

[20] Joseph Valasek. Piezo-electric and allied phenomena in rochelle salt. *Physical review*, 17(4):475, 1921.

[21] Joseph Valasek. Piezo-electric activity of rochelle salt under various conditions. *Physical Review*, 19(5):478, 1922.

[22] Shepard Roberts. Dielectric and piezoelectric properties of barium titanate. *Physical Review*, 71(12):890, 1947.

[23] RV Schmidt and IP Kaminow. Metal-diffused optical waveguides in linbo3. *Applied Physics Letters*, 25(8):458–460, 1974.

[24] Ronald E Cohen. Origin of ferroelectricity in perovskite oxides. *Nature*, 358(6382):136, 1992.

[25] Wei Li and Li-Jun Ji. Perovskite ferroelectrics go metal free. *Science*, 361(6398):132–132, 2018.

[26] TS Böscke, J Müller, D Bräuhaus, U Schröder, and U Böttger. Ferroelectricity in hafnium oxide: Cmos compatible ferroelectric field effect transistors. In *2011 International Electron Devices Meeting*, pages 24–5. IEEE, 2011.

[27] Ping-Ping Shi, Si-Qi Lu, Xian-Jiang Song, Xiao-Gang Chen, Wei-Qiang Liao, Peng-Fei Li, Yuan-Yuan Tang, and Ren-Gen Xiong. Two-dimensional organic-inorganic perovskite ferroelectric semiconductor with the fluorinated aromatic spacers. *Journal of the American Chemical Society*, 2019.

[28] JF Scott. [3d] nano-scale ferroelectric devices for memory applications. *Ferroelectrics*, 314(1):207–222, 2005.

[29] Xingqiang Liu, Yueli Liu, Wen Chen, Jinchai Li, and Lei Liao. Ferroelectric memory based on nanostructures. *Nanoscale research letters*, 7(1):285, 2012.

[30] Zhang Shoubai, Guo Xiaoyun, and Xu Juntao. The application of ferroelectric materials in micro-electro-mechanic systems (mems). *Ferroelectrics*, 232(1):175–184, 1999.

[31] Husein Irzaman and Renan Prasta Jenie. *Ferroelectrics and Their Applications*. BoD–Books on Demand, 2018.

[32] Kenji Uchino. Ferroelectric devices and piezoelectric actuators. *DEStech Publ*, 2017.

[33] Alfredo Vázquez Carazo. *Novel piezoelectric transducers for high voltage measurements*. Universitat Politècnica de Catalunya, 2000.

[34] N Izyumskaya, Ya Alivov, and H Morkoc. Oxides, oxides, and more oxides: high-κ oxides, ferroelectrics, ferromagnetics, and multiferroics. *Critical Reviews in Solid State and Materials Sciences*, 34(3-4):89–179, 2009.

[35] Daniel Sando, A Barthélémy, and M Bibes. Bifeo3 epitaxial thin films and devices: past, present and future. *Journal of Physics: Condensed Matter*, 26(47):473201, 2014.

[36] Francesco Calavalle. *Electrospun polymer nanofibers for electromechanical transduction investigated by scanning probe microscopy*. PhD thesis.

[37] Premi Chandra and Peter B Littlewood. A landau primer for ferroelectrics. In *Physics of ferroelectrics*, pages 69–116. Springer, 2007.

[38] J.F. Scott. *Ferroelectric Memories*. Springer Series in Advanced Microelectronics. Springer Berlin Heidelberg, 2013.

[39] Premala Chandra, M Dawber, PB Littlewood, and JF Scott. Scaling of the coercive field with thickness in thin-film ferroelectrics. *Ferroelectrics*, 313(1):7–13, 2004.

[40] Philip W Anderson. Absence of diffusion in certain random lattices. *Physical review*, 109(5):1492, 1958.

[41] W Cochran. Crystal stability and the theory of ferroelectricity. *Advances in Physics*, 9(36):387–423, 1960.

[42] Andrei L Kholkin, Nikolay A Pertsev, and Alexander V Goltsev. Piezoelectricity and crystal symmetry. In *Piezoelectric and Acoustic Materials for Transducer Applications*, pages 17–38. Springer, 2008.

[43] Dragan Damjanovic. Hysteresis in piezoelectric and ferroelectric materials. *The science of hysteresis*, 3:337–465, 2006.

[44] Raffaele Resta and David Vanderbilt. Theory of polarization: a modern approach. In *Physics of Ferroelectrics*, pages 31–68. Springer, 2007.

[45] M Abplanalp, LM Eng, and P Günter. Mapping the domain distribution at ferroelectric surfaces by scanning force microscopy. *Applied Physics A: Materials Science & Processing*, 66:S231–S234, 1998.

[46] Takeshi Shigenari. Raman spectra of soft modes in ferroelectric crystals. *Ferroelectric Materials: Synthesis and Characterization*, page 1, 2015.

[47] Jan Petzelt and Stanislav Kamba. Far infrared and terahertz spectroscopy of ferroelectric soft modes in thin films: A review. *Ferroelectrics*, 503(1):19–44, 2016.

[48] M Verwerft, G Van Tendeloo, J Van Landuyt, and S Amelinckx. Electron microscopy of domain structures. *Ferroelectrics*, 97(1):5–17, 1989.

[49] Angelika Reichmann, Armin Zankel, Herbert Reingruber, Peter Pölt, and Klaus Reichmann. Direct observation of ferroelectric domain formation by environmental scanning electron microscopy. *Journal of the European Ceramic Society*, 31(15):2939–2942, 2011.

[50] Sava A Denev, Tom TA Lummen, Eftihia Barnes, Amit Kumar, and Venkatraman Gopalan. Probing ferroelectrics using optical second harmonic generation. *Journal of the American Ceramic Society*, 94(9):2699–2727, 2011.

[51] Supriyo Bandyopadhyay and Marc Cahay. *Introduction to spintronics*. CRC press, 2015.

[52] Aurelien Manchon, Hyun Cheol Koo, Junsaku Nitta, SM Frolov, and RA Duine. New perspectives for rashba spin–orbit coupling. *Nature materials*, 14(9):871–882, 2015.

[53] VE Degtyarev, SV Khazanova, and AA Konakov. Effect of electric field on the ratio between the rashba and dresselhaus parameters in iii–v heterostructures. *Semiconductors*, 51(11):1409–1414, 2017.

[54] A Ohtomo and HY Hwang. A high-mobility electron gas at the laalo 3/srtio 3 heterointerface. *Nature*, 427(6973):423, 2004.

[55] AF Santander-Syro, O Copie, T Kondo, F Fortuna, S Pailhes, R Weht, XG Qiu, F Bertran, A Nicolaou, A Taleb-Ibrahimi, et al. Two-dimensional electron gas with universal subbands at the surface of srtio 3. *Nature*, 469(7329):189, 2011.

[56] KV Shanavas. Overview of theoretical studies of rashba effect in polar perovskite surfaces. *Journal of Electron Spectroscopy and Related Phenomena*, 201:121–126, 2015.

[57] Mikaël Kepenekian, Roberto Robles, Claudine Katan, Daniel Sapori, Laurent Pedesseau, and Jacky Even. Rashba and dresselhaus effects in hybrid organic–inorganic perovskites: from basics to devices. *ACS nano*, 9(12):11557–11567, 2015.

[58] A Crepaldi, LAGT Moreschini, G Autes, C Tournier-Colletta, S Moser, N Virk, H Berger, Ph Bugnon, YJ Chang, K Kern, et al. Giant ambipolar rashba effect in the semiconductor bitei. *Physical review letters*, 109(9):096803, 2012.

[59] Henriette Maaß, Hendrik Bentmann, Christoph Seibel, Christian Tusche, Sergey V Eremeev, Thiago RF Peixoto, Oleg E Tereshchenko, Konstantin A Kokh, Evgueni V Chulkov, Jürgen Kirschner, et al. Spin-texture inversion in the giant rashba semiconductor bitei. *Nature communications*, 7:11621, 2016.

[60] Marcus Liebmann, Christian Rinaldi, Domenico Di Sante, Jens Kellner, Christian Pauly, Rui Ning Wang, Jos Emiel Boschker, Alessandro Giussani, Stefano Bertoli, Matteo Cantoni, et al. Giant rashba-type spin splitting in ferroelectric gete (111). *Advanced Materials*, 28(3):560–565, 2016.

[61] R Adhikari, M Matzer, A Tarazaga Martin-Luengo, MC Scharber, and A Bonanni. Rashba semiconductor as spin hall material: Experimental demonstration of spin pumping in wurtzite n-gan: Si. *Physical Review B*, 94(8):085205, 2016.

[62] Kunihiko Yamauchi, Paolo Barone, and Silvia Picozzi. Bulk rashba effect in multiferroics: a theoretical prediction for bicoo3. *arXiv preprint arXiv:1910.06758*, 2019.

[63] J-C Rojas-Sánchez, N Reyren, P Laczkowski, W Savero, J-P Attané, C Deranlot, M Jamet, J-M George, Laurent Vila, and H Jaffrès. Spin pumping and inverse spin hall effect in platinum: the essential role of spin-memory loss at metallic interfaces. *Physical review letters*, 112(10):106602, 2014.

[64] G Zahnd, Laurent Vila, VT Pham, M Cosset-Cheneau, W Lim, A Brenac, P Laczkowski, A Marty, and JP Attané. Spin diffusion length and polarization of ferromagnetic metals measured by the spin-absorption technique in lateral spin valves. *Physical Review B*, 98(17):174414, 2018.

[65] Hiroyasu Nakayama, Yusuke Kanno, Hongyu An, Takaharu Tashiro, Satoshi Haku, Akiyo Nomura, and Kazuya Ando. Rashba-edelstein magnetoresistance in metallic heterostructures. *Physical review letters*, 117(11):116602, 2016.

[66] Yang Lv, James Kally, Delin Zhang, Joon Sue Lee, Mahdi Jamali, Nitin Samarth, and Jian-Ping Wang. Unidirectional spin-hall and rashba- edelstein magnetoresistance in topological insulator-ferromagnet layer heterostructures. *Nature communications*, 9(1):111, 2018.

[67] T Valet and A Fert. Theory of the perpendicular magnetoresistance in magnetic multilayers. *Physical Review B*, 48(10):7099, 1993.

[68] Michel I Dyakonov. *Spin physics in semiconductors*, volume 1. Springer, 2017.

[69] Cui-Zu Chang and Mingda Li. Quantum anomalous hall effect in time-reversal-symmetry breaking topological insulators. *Journal of Physics: Condensed Matter*, 28(12):123002, 2016.

[70] M Idrish Miah. Observation of the anomalous hall effect in gaas. *Journal of Physics D: Applied Physics*, 40(6):1659, 2007.

[71] AA Bakun, BP Zakharchenya, AA Rogachev, MN Tkaohuk, and VG Fleisher. Observation of a surface photocurrent caused by optical orientation of electrons in a semiconductor.

[72] JE Hirsch. Spin hall effect. *Physical Review Letters*, 83(9):1834, 1999.

[73] Mikhail I Dyakonov and VI Perel. Current-induced spin orientation of electrons in semiconductors. *Physics Letters A*, 35(6):459–460, 1971.

[74] Yuichiro K Kato, Roberto C Myers, Arthur C Gossard, and David D Awschalom. Observation of the spin hall effect in semiconductors. *science*, 306(5703):1910–1913, 2004.

[75] P Laczkowski, M Cosset-Cheneau, W Savero-Torres, VT Pham, G Zahnd, H Jaffrès, N Reyren, J-C Rojas-Sànchez, A Marty, L Vila, et al. Spin-dependent transport characterization in metallic lateral spin valves using one-dimensional and three-dimensional modeling. *Physical Review B*, 99(13):134436, 2019.

[76] MI D'yakonov and VI Perel. Possibility of orienting electron spins with current. *Soviet Journal of Experimental and Theoretical Physics Letters*, 13:467, 1971.

[77] Jairo Sinova, Sergio O Valenzuela, J Wunderlich, CH Back, and T Jungwirth. Spin hall effects. *Reviews of Modern Physics*, 87(4):1213, 2015.

[78] MI Dyakonov. Spin hall effect. *International Journal of Modern Physics B*, 23(12n13):2556–2565, 2009.

[79] Takashi Kimura, Y Otani, T Sato, S Takahashi, and S Maekawa. Room-temperature reversible spin hall effect. *Physical review letters*, 98(15):156601, 2007.

[80] Tomas Jungwirth, Jörg Wunderlich, and Kamil Olejník. Spin hall effect devices. *Nature materials*, 11(5):382, 2012.

[81] Yasuhiro Niimi and YoshiChika Otani. Reciprocal spin hall effects in conductors with strong spin–orbit coupling: a review. *Reports on Progress in Physics*, 78(12):124501, 2015.

[82] Takeshi Seki, Yu Hasegawa, Seiji Mitani, Saburo Takahashi, Hiroshi Imamura, Sadamichi Maekawa, Junsaku Nitta, and Koki Takanashi. Giant spin hall effect in perpendicularly spin-polarized fept/au devices. *Nature materials*, 7(2):125, 2008.

[83] Hui Zhao, Eric J Loren, HM Van Driel, and Arthur L Smirl. Coherence control of hall charge and spin currents. *Physical review letters*, 96(24):246601, 2006.

[84] NP Stern, S Ghosh, G Xiang, M Zhu, Nitin Samarth, and DD Awschalom. Current-induced polarization and the spin hall effect at room temperature. *Physical review letters*, 97(12):126603, 2006.

[85] Vanessa Sih, RC Myers, YK Kato, WH Lau, AC Gossard, and DD Awschalom. Spatial imaging of the spin hall effect and current-induced polarization in two-dimensional electron gases. *Nature Physics*, 1(1):31, 2005.

[86] Joerg Wunderlich, Bernd Kaestner, Jairo Sinova, and Tomas Jungwirth. Experimental observation of the spin-hall effect in a two-dimensional spin-orbit coupled semiconductor system. *Physical review letters*, 94(4):047204, 2005.

[87] Robert Karplus and JM Luttinger. Hall effect in ferromagnetics. *Physical Review*, 95(5):1154, 1954.

[88] Michael Victor Berry. Quantal phase factors accompanying adiabatic changes. *Proceedings of the Royal Society of London. A. Mathematical and Physical Sciences*, 392(1802):45–57, 1984.

[89] Arno Böhm, Hiroyasu Koizumi, Qian Niu, Joseph Zwanziger, and Ali Mostafazadeh. *The geometric phase in quantum systems: foundations, mathematical concepts, and applications in molecular and condensed matter physics*. Springer, 2003.

[90] Ganesh Sundaram and Qian Niu. Wave-packet dynamics in slowly perturbed crystals: Gradient corrections and berry-phase effects. *Physical Review B*, 59(23):14915, 1999.

[91] Edurne Sagasta, Yasutomo Omori, Miren Isasa, Martin Gradhand, Luis E Hueso, Yasuhiro Niimi, YoshiChika Otani, and Fèlix Casanova. Tuning the spin hall effect of pt from the moderately dirty to the superclean regime. *Physical Review B*, 94(6):060412, 2016.

[92] Shuichi Murakami. Intrinsic spin hall effect. In *Advances in Solid State Physics*, pages 197–209. Springer, 2005.

[93] Jairo Sinova, Dimitrie Culcer, Qian Niu, NA Sinitsyn, T Jungwirth, and Allan H MacDonald. Universal intrinsic spin hall effect. *Physical review letters*, 92(12):126603, 2004.

[94] EM Hankiewicz and Giovanni Vignale. Spin-hall effect and spin-coulomb drag in doped semiconductors. *Journal of Physics: Condensed Matter*, 21(25):253202, 2009.

[95] R Dingle. Luminescent transitions associated with divalent copper impurities and the green emission from semiconducting zinc oxide. *Physical Review Letters*, 23(11):579, 1969.

[96] A Fert, A Friederich, and A Hamzic. Hall effect in dilute magnetic alloys. *Journal of Magnetism and Magnetic Materials*, 24(3):231–257, 1981.

[97] J Smit. The spontaneous hall effect in ferromagnetics i. *Physica*, 21(6-10):877–887, 1955.

[98] P Laczkowski, Y Fu, H Yang, J-C Rojas-Sánchez, P Noel, VT Pham, G Zahnd, C Deranlot, S Collin, C Bouard, et al. Large enhancement of the spin hall effect in au by side-jump scattering on ta impurities. *Physical Review B*, 96(14):140405, 2017.

[99] Y Niimi, M Morota, DH Wei, Cyrile Deranlot, M Basletic, A Hamzic, Albert Fert, and Y Otani. Extrinsic spin hall effect induced by iridium impurities in copper. *Physical review letters*, 106(12):126601, 2011.

[100] SD Ganichev, EL Ivchenko, VV Bel'Kov, SA Tarasenko, M Sollinger, Dieter Weiss, Werner Wegscheider, and Wilhelm Prettl. Spin-galvanic effect. *Nature*, 417(6885):153, 2002.

[101] Ka Shen, Giovanni Vignale, and Roberto Raimondi. Microscopic theory of the inverse edelstein effect. *Physical review letters*, 112(9):096601, 2014.

[102] J Wunderlich, AC Irvine, Jairo Sinova, Byong Guk Park, LP Zârbo, XL Xu, B Kaestner, V Novák, and T Jungwirth. Spin-injection hall effect in a planar photovoltaic cell. *Nature Physics*, 5(9):675, 2009.

[103] J-C Rojas-Sanchez, M Cubukcu, A Jain, C Vergnaud, C Portemont, C Ducruet, A Barski, A Marty, L Vila, J-P Attané, et al. Spin pumping and inverse spin hall effect in germanium. *Physical Review B*, 88(6):064403, 2013.

[104] Victor M Edelstein. Spin polarization of conduction electrons induced by electric current in two-dimensional asymmetric electron systems. *Solid State Communications*, 73(3):233–235, 1990.

[105] Diogo Castro Vaz, Agnès Barthélémy, and Manuel Bibes. Oxide spin-orbitronics: New routes towards low-power electrical control of magnetization in oxide heterostructures. *Japanese Journal of Applied Physics*, 57(9):0902A4, 2018.

[106] S Dushenko, Hiroki Ago, K Kawahara, T Tsuda, S Kuwabata, T Takenobu, T Shinjo, Y Ando, and M Shiraishi. Gate-tunable spin-charge conversion and the role of spin-orbit interaction in graphene. *Physical review letters*, 116(16):166102, 2016.

[107] Talieh S Ghiasi, Alexey A Kaverzin, Patrick J Blah, and Bart J van Wees. Charge-to-spin conversion by the rashba-edelstein effect in 2d van der waals heterostructures up to room temperature. *arXiv preprint arXiv:1905.01371*, 2019.

[108] SK Bahl and KL Chopra. Amorphous versus crystalline gete films. iii. electrical properties and band structure. *Journal of Applied Physics*, 41(5):2196–2212, 1970.

[109] Pierre Noé and Françoise Hippert. Structure and properties of chalcogenide materials for pcm. In *Phase Change Memory*, pages 125–179. Springer, 2018.

[110] Alexander V Kolobov, Junji Tominaga, and Paul Fons. Phase-change memory materials. In *Springer Handbook of Electronic and Photonic Materials*, pages 1–1. Springer, 2017.

[111] J Goldak, CS Barrett, D Innes, and W Youdelis. Structure of alpha gete. *The Journal of Chemical Physics*, 44(9):3323–3325, 1966.

[112] AV Kolobov, DJ Kim, A Giussani, P Fons, J Tominaga, R Calarco, and Alexei Gruverman. Ferroelectric switching in epitaxial gete films. *APL Materials*, 2(6):066101, 2014.

[113] EF Steigmeier and G Harbeke. Soft phonon mode and ferroelectricity in gete. *Solid State Communications*, 8(16):1275–1279, 1970.

[114] Volker L Deringer, Marck Lumeij, and Richard Dronskowski. Ab initio modeling of α-gete (111) surfaces. *The Journal of Physical Chemistry C*, 116(29):15801–15811, 2012.

[115] Bart J Kooi and Beatriz Noheda. Ferroelectric chalcogenides—materials at the edge. *Science*, 353(6296):221–222, 2016.

[116] Malcolm E Lines and Alastair M Glass. *Principles and applications of ferroelectrics and related materials*. Oxford university press, 2001.

[117] Dominic Lencer, Martin Salinga, Blazej Grabowski, Tilmann Hickel, Jörg Neugebauer, and Matthias Wuttig. A map for phase-change materials. *Nature materials*, 7(12):972, 2008.

[118] Mark J Polking, Myung-Geun Han, Amin Yourdkhani, Valeri Petkov, Christian F Kisielowski, Vyacheslav V Volkov, Yimei Zhu, Gabriel Caruntu, A Paul Alivisatos, and Ramamoorthy Ramesh. Ferroelectric order in individual nanometre-scale crystals. *Nature materials*, 11(8):700, 2012.

[119] Filip Kadlec, Christelle Kadlec, Petr Kužel, and Jan Petzelt. Study of the ferroelectric phase transition in germanium telluride using time-domain terahertz spectroscopy. *Physical Review B*, 84(20):205209, 2011.

[120] Pavan Nukala, Mingliang Ren, Rahul Agarwal, Jacob Berger, Gerui Liu, AT Charlie Johnson, and Ritesh Agarwal. Inverting polar domains via electrical pulsing in metallic germanium telluride. *Nature communications*, 8:15033, 2017.

[121] Nicola A Spaldin and Manfred Fiebig. The renaissance of magnetoelectric multiferroics. *Science*, 309(5733):391–392, 2005.

[122] Ramaroorthy Ramesh and Nicola A Spaldin. Multiferroics: progress and prospects in thin films. *Nature materials*, 6(1):21, 2007.

[123] MS Bahramy, R Arita, and N Nagaosa. Origin of giant bulk rashba splitting: Application to bitei. *Physical Review B*, 84(4):041202, 2011.

[124] K Ishizaka, MS Bahramy, H Murakawa, M Sakano, T Shimojima, T Sonobe, K Koizumi, S Shin, H Miyahara, A Kimura, et al. Giant rashba-type spin splitting in bulk bitei. *Nature materials*, 10(7):521, 2011.

[125] Won Young Choi, Hyung-jun Kim, Joonyeon Chang, Suk Hee Han, Adel Abbout, Hamed Ben Mohamed Saidaoui, Aurélien Manchon, Kyung-Jin Lee, and Hyun Cheol Koo. Ferromagnet-free all-electric spin hall transistors. *Nano letters*, 18(12):7998–8002, 2018.

[126] Jörg Wunderlich, Byong-Guk Park, Andrew C Irvine, Liviu P Zârbo, Eva Rozkotová, Petr Nemec, Vít Novák, Jairo Sinova, and Tomás Jungwirth. Spin hall effect transistor. *Science*, 330(6012):1801–1804, 2010.

[127] André Chanthbouala, Vincent Garcia, Ryan O Cherifi, Karim Bouzehouane, Stéphane Fusil, Xavier Moya, Stéphane Xavier, Hiroyuki Yamada, Cyrile Deranlot, Neil D Mathur, et al. A ferroelectric memristor. *Nature materials*, 11(10):860, 2012.

[128] Alessandro Giussani, Karthick Perumal, Michael Hanke, Peter Rodenbach, Henning Riechert, and Raffaella Calarco. On the epitaxy of germanium telluride thin films on silicon substrates. *physica status solidi (b)*, 249(10):1939–1944, 2012.

[129] AV Kolobov, J Tominaga, P Fons, and T Uruga. Local structure of crystallized gete films. *Applied physics letters*, 82(3):382–384, 2003.

[130] MS Lubell and R Mazelsky. Carrier compensation in germanium telluride. *Journal of The Electrochemical Society*, 110(6):520–524, 1963.

[131] Xinyue Zhang, Juan Li, Xiao Wang, Zhiwei Chen, Jianjun Mao, Yue Chen, and Yanzhong Pei. Vacancy manipulation for thermoelectric enhancements in gete alloys. *Journal of the American Chemical Society*, 140(46):15883–15888, 2018.

[132] Charles Baldwin Sawyer and CH Tower. Rochelle salt as a dielectric. *Physical review*, 35(3):269, 1930.

[133] Greta Radaelli, Daniela Petti, E Plekhanov, I Fina, P Torelli, BR Salles, Matteo Cantoni, Christian Rinaldi, D Gutiérrez, G Panaccione, et al. Electric control of magnetism at the fe/batio 3 interface. *Nature communications*, 5:3404, 2014.

[134] Anna N Morozovska, Sergei V Svechnikov, Eugene A Eliseev, Stephen Jesse, Brian J Rodriguez, and Sergei V Kalinin. Piezoresponse force spectroscopy of ferroelectric-semiconductor materials. *Journal of Applied Physics*, 102(11):114108, 2007.

[135] Alexei Gruverman, Orlando Auciello, and Hiroshi Tokumoto. Imaging and control of domain structures in ferroelectric thin films via scanning force microscopy. *Annual review of materials science*, 28(1):101–123, 1998.

[136] LM Eng, H-J Güntherodt, G Rosenman, A Skliar, M Oron, M Katz, and D Eger. Nondestructive imaging and characterization of ferroelectric domains in periodically poled crystals. *Journal of applied physics*, 83(11):5973–5977, 1998.

[137] Sergei V Kalinin, Brian J Rodriguez, Stephen Jesse, Junsoo Shin, Arthur P Baddorf, Pradyumna Gupta, Himanshu Jain, David B Williams, and Alexei Gruverman. Vector piezoresponse force microscopy. *Microscopy and Microanalysis*, 12(3):206–220, 2006.

[138] H Khassaf, N Khakpash, F Sun, NM Sbrockey, GS Tompa, TS Kalkur, and SP Alpay. Strain engineered barium strontium titanate for tunable thin film resonators. *Applied Physics Letters*, 104(20):202902, 2014.

[139] Elisabeth Soergel. Piezoresponse force microscopy (pfm). *Journal of Physics D: Applied Physics*, 44(46):464003, 2011.

[140] T Jungk, A Hoffmann, and E Soergel. Consequences of the background in piezoresponse force microscopy on the imaging of ferroelectric domain structures. *Journal of microscopy*, 227(1):72–78, 2007.

[141] Nina Balke, Stephen Jesse, Qian Li, Petro Maksymovych, M Baris Okatan, Evgheni Strelcov, Alexander Tselev, and Sergei V Kalinin. Current and surface charge modified hysteresis loops in ferroelectric thin films. *Journal of Applied Physics*, 118(7):072013, 2015.

[142] Stephen Jesse, Arthur P Baddorf, and Sergei V Kalinin. Switching spectroscopy piezoresponse force microscopy of ferroelectric materials. *Applied physics letters*, 88(6):062908, 2006.

[143] Wentao Zhang, Guodong Liu, Jianqiao Meng, Lin Zhao, Haiyun Liu, Xiaoli Dong, Wei Lu, JS Wen, ZJ Xu, GD Gu, et al. High energy dispersion relations for the high temperature bi 2 sr 2 cacu 2 o 8 superconductor from laser-based angle-resolved photoemission spectroscopy. *Physical review letters*, 101(1):017002, 2008.

[144] Jin Mo Bok, Jong Ju Bae, Han-Yong Choi, Chandra M Varma, Wentao Zhang, Junfeng He, Yuxiao Zhang, Li Yu, and XJ Zhou. Quantitative determination of pairing interactions for high-temperature superconductivity in cuprates. *Science advances*, 2(3):e1501329, 2016.

[145] Pedram Roushan, Jungpil Seo, Colin V Parker, Yew San Hor, David Hsieh, Dong Qian, Anthony Richardella, M Zahid Hasan, Robert Joseph Cava, and Ali Yazdani. Topological surface states protected from backscattering by chiral spin texture. *Nature*, 460(7259):1106, 2009.

[146] PK Das, D Di Sante, F Cilento, C Bigi, D Kopic, D Soranzio, A Sterzi, JA Krieger, I Vobornik, J Fujii, et al. Electronic properties of candidate type-ii weyl semimetal wte2. a review perspective. *Electronic Structure*, 1(1):014003, 2019.

[147] Baiqing Lv, Tian Qian, and Hong Ding. Angle-resolved photoemission spectroscopy and its application to topological materials. *Nature Reviews Physics*, 1(10):609–626, 2019.

[148] M Pl Seah and WA Dench. Quantitative electron spectroscopy of surfaces: A standard data base for electron inelastic mean free paths in solids. *Surface and interface analysis*, 1(1):2–11, 1979.

[149] Timothy J Gay and FB Dunning. Mott electron polarimetry. *Review of scientific instruments*, 63(2):1635–1651, 1992.

[150] Koichiro Yaji, Ayumi Harasawa, Kenta Kuroda, Sogen Toyohisa, Mitsuhiro Nakayama, Yukiaki Ishida, Akiko Fukushima, Shuntaro Watanabe, Chuangtian Chen, Fumio Komori, et al. High-resolution three-dimensional spin-and angle-resolved photoelectron spectrometer using vacuum ultraviolet laser light. *Review of Scientific Instruments*, 87(5):053111, 2016.

[151] Riccardo Bertacco and Franco Ciccacci. Fe/mgo (001) single-crystal films for electron polarimetry. *Journal of magnetism and magnetic materials*, 196:134–135, 1999.

[152] Riccardo Bertacco, Michele Merano, and Franco Ciccacci. Spin dependent electron absorption in fe (001)-p (1× 1) o: A new candidate for a stable and efficient electron polarization analyzer. *Applied physics letters*, 72(16):2050–2052, 1998.

[153] Riccardo Bertacco, Davide Onofrio, and Franco Ciccacci. A novel electron spin-polarization detector with very large analyzing power. *Review of scientific instruments*, 70(9):3572–3576, 1999.

[154] Chiara Bigi, Pranab K Das, Davide Benedetti, Federico Salvador, Damjan Krizmancic, Rudi Sergo, Andrea Martin, Giancarlo Panaccione, Giorgio Rossi, Jun Fujii, et al. Very efficient spin polarization analysis (vespa): new exchange scattering-based setup for spin-resolved arpes at ape-nffa beamline at elettra. *Journal of synchrotron radiation*, 24(4):750–756, 2017.

[155] Taichi Okuda, Koji Miyamoto, Akio Kimura, Hirofumi Namatame, and Masaki Taniguchi. A double vleed spin detector for high-resolution three dimensional spin vectorial analysis of anisotropic rashba spin splitting. *Journal of Electron Spectroscopy and Related Phenomena*, 201:23–29, 2015.

[156] Moritz Hoesch, M Muntwiler, VN Petrov, M Hengsberger, L Patthey, M Shi, M Falub, T Greber, and J Osterwalder. Spin structure of the shockley surface state on au (111). *Physical Review B*, 69(24):241401, 2004.

[157] William Fuller Brown. *Micromagnetics*. Number 18. interscience publishers, 1963.

[158] Jakob Walowski and Ketrzyn Im. Non-local/local gilbert damping in nickel and permalloy thin films diplomarbeit vorgelegt von. 01 2020.

[159] JHE Griffiths. Anomalous high-frequency resistance of ferromagnetic metals. *Nature*, 158(4019):670, 1946.

[160] Y Guan, WE Bailey, E Vescovo, C-C Kao, and DA Arena. Phase and amplitude of element-specific moment precession in ni81fe19. *Journal of Magnetism and Magnetic Materials*, 312(2):374–378, 2007.

[161] Charles Kittel. Ferromagnetic resonance. 1951.

[162] Xin Fan, Sangcheol Kim, Xiaoming Kou, James Kolodzey, Huaiwu Zhang, and John Q Xiao. Microwave phase detection with a magnetic tunnel junction. *Applied Physics Letters*, 97(21):212501, 2010.

[163] Ivan S Maksymov and Mikhail Kostylev. Broadband stripline ferromagnetic resonance spectroscopy of ferromagnetic films, multilayers and nanostructures. *Physica E: Low-dimensional Systems and Nanostructures*, 69:253–293, 2015.

[164] Yaroslav Tserkovnyak, Arne Brataas, and Gerrit EW Bauer. Enhanced gilbert damping in thin ferromagnetic films. *Physical review letters*, 88(11):117601, 2002.

[165] Yaroslav Tserkovnyak, Arne Brataas, Gerrit EW Bauer, and Bertrand I Halperin. Nonlocal magnetization dynamics in ferromagnetic heterostructures. *Reviews of Modern Physics*, 77(4):1375, 2005.

[166] O Mosendz, V Vlaminck, JE Pearson, FY Fradin, GEW Bauer, SD Bader, and A Hoffmann. Detection and quantification of inverse spin hall effect from spin pumping in permalloy/normal metal bilayers. *Physical Review B*, 82(21):214403, 2010.

[167] J Foros, Georg Woltersdorf, B Heinrich, and A Brataas. Scattering of spin current injected in pd (001). *Journal of applied physics*, 97(10):10A714, 2005.

[168] Kazuya Ando, Saburo Takahashi, Junichi Ieda, Yosuke Kajiwara, Hiroyasu Nakayama, Tatsuro Yoshino, Kazuya Harii, Yasunori Fujikawa, M Matsuo, S Maekawa, et al. Inverse spin-hall effect induced by spin pumping in metallic system. *Journal of applied physics*, 109(10):103913, 2011.

[169] Paul Noël, Maxen Cosset-Cheneau, Victor Haspot, Vincent Maurel, Christian Lombard, Manuel Bibes, Agnès Barthelemy, Laurent Vila, and Jean-Philippe Attané. Do thermal effects always contribute to spin pumping signals? *arXiv preprint arXiv:1905.00771*, 2019.

[170] WG Egan and HJ Juretschke. Dc detection of ferromagnetic resonance in thin nickel films. *Journal of Applied Physics*, 34(5):1477–1484, 1963.

[171] MV Costache, SM Watts, CH Van Der Wal, and BJ Van Wees. Electrical detection of spin pumping: dc voltage generated by ferromagnetic resonance at ferromagnet/nonmagnet contact. *Physical Review B*, 78(6):064423, 2008.

[172] Peter Rodenbach, Raffaella Calarco, Karthick Perumal, Ferhat Katmis, Michael Hanke, André Proessdorf, Wolfgang Braun, Alessandro Giussani, Achim Trampert, Henning Riechert, et al. Epitaxial phase-change materials. *physica status solidi (RRL)–Rapid Research Letters*, 6(11):415–417, 2012.

[173] Atsushi Koma, Kazumasa Sunouchi, and Takao Miyajima. Fabrication and characterization of heterostructures with sub-nanometer thickness. *Microelectronic Engineering*, 2(1-3):129–136, 1984.

[174] Zaiyao Fei, Wenjin Zhao, Tauno A Palomaki, Bosong Sun, Moira K Miller, Zhiying Zhao, Jiaqiang Yan, Xiaodong Xu, and David H Cobden. Ferroelectric switching of a two-dimensional metal. *Nature*, 560(7718):336, 2018.

[175] Pankaj Sharma, Fei-Xiang Xiang, Ding-Fu Shao, Dawei Zhang, Evgeny Y Tsymbal, Alex R Hamilton, and Jan Seidel. A room-temperature ferroelectric semimetal. *Science advances*, 5(7):eaax5080, 2019.

[176] PWM Blom, RM Wolf, JFM Cillessen, and MPCM Krijn. Ferroelectric schottky diode. *Physical Review Letters*, 73(15):2107, 1994.

[177] An Quan Jiang, Can Wang, Kui Juan Jin, Xiao Bing Liu, James F Scott, Cheol Seong Hwang, Ting Ao Tang, Hui Bin Lu, and Guo Zhen Yang. A resistive memory in semiconducting bifeo3 thin-film capacitors. *Advanced Materials*, 23(10):1277–1281, 2011.

[178] T Chatterji, S Rols, and UD Wdowik. Dynamics of the phase-change material gete across the structural phase transition. *Frontiers of Physics*, 14(2):23601, 2019.

[179] JJ Gervacio-Arciniega, E Prokhorov, FJ Espinoza-Beltran, and G Trapaga. Characterization of local piezoelectric behavior of ferroelectric gete and ge2sb2te5 thin films. *Journal of Applied Physics*, 112(5):052018, 2012.

[180] R. Proksch and S. Kalinin. Piezoresponse force microscopy with asylum research AFMs. page 22.

[181] Christian Rinaldi, Sara Varotto, Marco Asa, Jagoda Slawinska, Jun Fujii, Giovanni Vinai, Stefano Cecchi, Domenico Di Sante, Raffaella Calarco, Ivana Vobornik, et al. Ferroelectric control of the spin texture in gete. *Nano letters*, 18(5):2751–2758, 2018.

[182] JF Scott, LD McMillan, and CA Araujo. Switching kinetics of lead zirconate titanate sub-micron thin-film memories. *Ferroelectrics*, 93(1):31–36, 1989.

[183] Hideharu Matsuura. Calculation of band bending in ferroelectric semiconductor. *New Journal of Physics*, 2(1):8, 2000.

[184] Simon M Sze and Kwok K Ng. *Physics of semiconductor devices*. John wiley & sons, 2006.

[185] H Kohlstedt, A Petraru, K Szot, A Rüdiger, P Meuffels, H Haselier, R Waser, and V Nagarajan. Method to distinguish ferroelectric from nonferroelectric origin in case of resistive switching in ferroelectric capacitors. *Applied Physics Letters*, 92(6):062907, 2008.

[186] Massimiliano Stengel, David Vanderbilt, and Nicola A Spaldin. Enhancement of ferroelectricity at metal–oxide interfaces. *Nature materials*, 8(5):392, 2009.

[187] Vincent Garcia and Manuel Bibes. Ferroelectric tunnel junctions for information storage and processing. *Nature communications*, 5:4289, 2014.

[188] Fei Mo, Yusaku Tagawa, Takuya Saraya, Toshiro Hiramoto, and Masaharu Kobayashi. Scalability study on fcrroclcctric-hfo 2 tunnel junction memory based on non-equilibrium green function method with self-consistent potential. In *2018 IEEE International Electron Devices Meeting (IEDM)*, pages 16–3. IEEE, 2018.

[189] Shinji Odanaka. Multidimensional discretization of the stationary quantum drift-diffusion model for ultrasmall mosfet structures. *IEEE Transactions on Computer-Aided Design of Integrated Circuits and Systems*, 23(6):837–842, 2004.

[190] Raymond T Tung. The physics and chemistry of the schottky barrier height. *Applied Physics Reviews*, 1(1):011304, 2014.

[191] M Ye Zhuravlev, Renat F Sabirianov, SS Jaswal, and Evgeny Y Tsymbal. Giant electroresistance in ferroelectric tunnel junctions. *Physical Review Letters*, 94(24):246802, 2005.

[192] H Kohlstedt, NA Pertsev, J Rodríguez Contreras, and R Waser. Theoretical current-voltage characteristics of ferroelectric tunnel junctions. *Physical Review B*, 72(12):125341, 2005.

[193] JF Scott. Applications of modern ferroelectrics. *science*, 315(5814):954–959, 2007.

[194] Walter Hartner, Günther Schindler, and Frank Hintermaier. Ferroelectric random access memory (feram) having storage capacitors with different coercive voltages, 2002. US Patent 6,438,019.

[195] Stefan Slesazeck and Thomas Mikolajick. Nanoscale resistive switching memory devices: a review. *Nanotechnology*, 30(35):352003, 2019.

[196] Simone Raoux, Wojciech Wełnic, and Daniele Ielmini. Phase change materials and their application to nonvolatile memories. *Chemical reviews*, 110(1):240–267, 2009.

[197] Andrea L Lacaita and Dirk J Wouters. Phase-change memories. *Physica status solidi (a)*, 205(10):2281–2297, 2008.

[198] Geoffrey W Burr, Matthew J Breitwisch, Michele Franceschini, Davide Garetto, Kailash Gopalakrishnan, Bryan Jackson, Bülent Kurdi, Chung Lam, Luis A Lastras, Alvaro Padilla, et al. Phase change memory technology. *Journal of Vacuum Science & Technology B, Nanotechnology and Microelectronics: Materials, Processing, Measurement, and Phenomena*, 28(2):223–262, 2010.

[199] B Govoreanu, GS Kar, YY Chen, V Paraschiv, S Kubicek, A Fantini, IP Radu, L Goux, S Clima, R Degraeve, et al. 10× 10nm 2 hf/hfo x crossbar resistive ram with excellent performance, reliability and low-energy operation. In *2011 International Electron Devices Meeting*, pages 31–6. IEEE, 2011.

[200] Tiangui You, Nan Du, Stefan Slesazeck, Thomas Mikolajick, Guodong Li, Danilo Burger, Ilona Skorupa, Hartmut Stocker, Barbara Abendroth, Andreas Beyer, et al. Bipolar electric-field enhanced trapping and detrapping of mobile donors in bifeo3 memristors. *ACS applied materials & interfaces*, 6(22):19758–19765, 2014.

[201] Debanjan Jana, Sourav Roy, Rajeswar Panja, Mrinmoy Dutta, Sheikh Ziaur Rahaman, Rajat Mahapatra, and Siddheswar Maikap. Conductive-bridging random access memory: challenges and opportunity for 3d architecture. *Nanoscale research letters*, 10(1):188, 2015.

[202] Daniele Ielmini. Resistive switching models by ion migration in metal oxides. In *Nanoscale Applications for Information and Energy Systems*, pages 169–202. Springer, 2013.

[203] Stefano Larentis, Federico Nardi, Simone Balatti, David C Gilmer, and Daniele Ielmini. Resistive switching by voltage-driven ion migration in bipolar rram—part ii: Modeling. *IEEE Transactions on Electron Devices*, 59(9):2468–2475, 2012.

[204] Matthias Wuttig and Noboru Yamada. Phase-change materials for rewriteable data storage. *Nature materials*, 6(11):824, 2007.

[205] Dushyant Tomer and Ronald Coutu. A phase change material for reconfigurable circuit applications. *Applied Sciences*, 8(1):130, 2018.

[206] Sung Hyun Jo, Ting Chang, Idongesit Ebong, Bhavitavya B Bhadviya, Pinaki Mazumder, and Wei Lu. Nanoscale memristor device as synapse in neuromorphic systems. *Nano letters*, 10(4):1297–1301, 2010.

[207] Daniel Pantel, Silvana Goetze, Dietrich Hesse, and Marin Alexe. Room-temperature ferroelectric resistive switching in ultrathin pb (zr0. 2ti0. 8) o3 films. *ACS nano*, 5(7):6032–6038, 2011.

[208] Betty Prince. Ferroelectric rams. *Emerging Memories: Technologies and Trends*, pages 1–67, 2002.

[209] Yuri A Genenko, Julia Glaum, Michael J Hoffmann, and Karsten Albe. Mechanisms of aging and fatigue in ferroelectrics. *Materials Science and Engineering: B*, 192:52–82, 2015.

[210] EL Colla, Seungbum Hong, DV Taylor, AK Tagantsev, N Setter, and Kwangsoo No. Direct observation of region by region suppression of the switchable polarization (fatigue) in pb (zr, ti) o 3 thin film capacitors with pt electrodes. *Applied physics letters*, 72(21):2763–2765, 1998.

[211] Alexander K Tagantsev, I Stolichnov, EL Colla, and N Setter. Polarization fatigue in ferroelectric films: Basic experimental findings, phenomenological scenarios, and microscopic features. *Journal of Applied Physics*, 90(3):1387–1402, 2001.

[212] Sparsh Mittal and Jeffrey S Vetter. A survey of software techniques for using non-volatile memories for storage and main memory systems. *IEEE Transactions on Parallel and Distributed Systems*, 27(5):1537–1550, 2015.

[213] Christian Monzio Compagnoni, Akira Goda, Alessandro S Spinelli, Peter Feeley, Andrea L Lacaita, and Angelo Visconti. Reviewing the evolution of the nand flash technology. *Proceedings of the IEEE*, 105(9):1609–1633, 2017.

[214] Evgeny Y Tsymbal and Hermann Kohlstedt. Tunneling across a ferroelectric. *Science*, 313(5784):181–183, 2006.

[215] Rino Micheloni, Luca Crippa, and Alessia Marelli. *Inside NAND flash memories*. Springer Science & Business Media, 2010.

[216] J Krempaskỳ, Stefan Muff, Jan Minar, Nicolas Pilet, Mauro Fanciulli, AP Weber, Eduardo B Guedes, Marco Caputo, Elisabeth Müller, Valentine V Volobuev, et al. Operando imaging of all-electric spin texture manipulation in ferroelectric and multiferroic rashba semiconductors. *Physical Review X*, 8(2):021067, 2018.

[217] Christian Rinaldi, JC Rojas-Sánchez, RN Wang, Y Fu, S Oyarzun, L Vila, Stefano Bertoli, Marco Asa, Lorenzo Baldrati, Matteo Cantoni, et al. Evidence for spin to charge conversion in gete (111). *APL Materials*, 4(3):032501, 2016.

[218] AD Caviglia, M Gabay, Stefano Gariglio, Nicolas Reyren, Claudia Cancellieri, and J-M Triscone. Tunable rashba spin-orbit interaction at oxide interfaces. *Physical review letters*, 104(12):126803, 2010.

[219] XB Xiao, XM Li, and YG Chen. Electron transport of a quantum wire with spatially periodic spin–orbit coupling. *Physica B: Condensed Matter*, 404(21):4159–4161, 2009.

[220] SJ Gong and ZQ Yang. Spin filtering implemented through rashba spin-orbit coupling and weak magnetic modulations. *Journal of Applied Physics*, 102(3):033706, 2007.

[221] Jagoda Sławińska, Domenico Di Sante, Sara Varotto, Christian Rinaldi, Riccardo Bertacco, and Silvia Picozzi. Fe/gete (111) heterostructures as an avenue towards spintronics based on ferroelectric rashba semiconductors. *Physical Review B*, 99(7):075306, 2019.

[222] Sergio Machado Rezende, JAS Moura, FM De Aguiar, and Wido Herwig Schreiner. Ferromagnetic resonance of fe (111) thin films and fe (111)/cu (111) multilayers. *Physical Review B*, 49(21):15105, 1994.

[223] Kh Zakeri, J Lindner, I Barsukov, R Meckenstock, M Farle, U Von Hörsten, H Wende, W Keune, J Rocker, SS Kalarickal, et al. Spin dynamics in ferromagnets: Gilbert damping and two-magnon scattering. *Physical Review B*, 76(10):104416, 2007.

[224] K Lenz, H Wende, W Kuch, K Baberschke, Kálmán Nagy, and András Jánossy. Two-magnon scattering and viscous gilbert damping in ultrathin ferromagnets. *Physical Review B*, 73(14):144424, 2006.

[225] L Chen, S Mankovsky, S Wimmer, MAW Schoen, HS Körner, Matthias Kronseder, Dieter Schuh, Dominique Bougeard, H Ebert, Dieter Weiss, et al. Emergence of anisotropic gilbert damping in ultrathin fe layers on gaas (001). *Nature Physics*, 14(5):490, 2018.

[226] Wenxu Zhang, Zhao Teng, Huizhong Zeng, Jakub Zelezny, Hongbin Zhang, and Wanli Zhang. Tunning spin hall conductivities in gete by ferroelectric polarization. *arXiv preprint arXiv:1907.07919*, 2019.

[227] Haihang Wang, Priya Gopal, Silvia Picozzi, Stefano Curtarolo, M Buongiorno Nardelli, and J Slawinska. Spin hall effect in prototype rashba ferroelectrics gete and snte. *arXiv preprint arXiv:1907.03979*, 2019.

[228] Naritaka Kobayashi, Ryuzo Kawamura, Hiroshi Y Yoshikawa, and Seiichiro Nakabayashi. Investigation on nanoscale processes on the baf2 (111) surface in various solutions by frequency modulation atomic force microscopy. *Journal of Applied Physics*, 119(21):214308, 2016.

[229] Shi-Jing Gong, Chun-Gang Duan, Yan Zhu, Zi-Qiang Zhu, and Jun-Hao Chu. Controlling rashba spin splitting in au (111) surface states through electric field. *Physical Review B*, 87(3):035403, 2013.

[230] A Takayama, T Sato, S Souma, and T Takahashi. Rashba effect in antimony and bismuth studied by spin-resolved arpes. *New Journal of Physics*, 16(5):055004, 2014.

[231] P Noël, C Thomas, Y Fu, L Vila, B Haas, PH Jouneau, S Gambarelli, T Meunier, P Ballet, and JP Attané. Highly efficient spin-to-charge current conversion at room temperature in strained hgte surface states. *arXiv preprint arXiv:1708.05470*, 2017.

[232] C Zucchetti, M-T Dau, F Bottegoni, C Vergnaud, T Guillet, Alain Marty, C Beigné, S Gambarelli, A Picone, A Calloni, et al. Tuning spin-charge interconversion with quantum confinement in ultrathin bismuth films. *Physical Review B*, 98(18):184418, 2018.

[233] Moh Adhib Ulil Absor and Fumiyuki Ishii. Intrinsic persistent spin helix state in two-dimensional group-iv monochalcogenide m x monolayers (m= sn or ge and x= s, se, or te). *Physical Review B*, 100(11):115104, 2019.

[234] Hosik Lee, Jino Im, and Hosub Jin. Emergence of the giant out-of-plane rashba effect and tunable nanoscale persistent spin helix in ferroelectric snte thin films. *Applied Physics Letters*, 116(2):022411, 2020.

[235] Kai Chang, Junwei Liu, Haicheng Lin, Na Wang, Kun Zhao, Anmin Zhang, Feng Jin, Yong Zhong, Xiaopeng Hu, Wenhui Duan, et al. Discovery of robust in-plane ferroelectricity in atomic-thick snte. *Science*, 353(6296):274–278, 2016.

[236] Kai Liu, Jinlian Lu, Silvia Picozzi, Laurent Bellaiche, and Hongjun Xiang. Intrinsic origin of enhancement of ferroelectricity in snte ultrathin films. *Physical review letters*, 121(2):027601, 2018.